COMPUTATIONAL MODELLING OF DIMETHYL ETHER SEPARATION AND STEAM REFORMING IN FLUIDIZED BED REACTORS

FRANCIS AWURUM ELEWUWA

Doctor of Philosophy

ASTON UNIVERSITY

FEBRUARY 2016

Aston University

Computational Modelling of Dimethyl Ether Separation and Steam Reforming in Fluidized Bed Reactors

Francis Awurum Elewuwa

Doctor of Philosophy

2016

THESIS SUMMARY

This study presents a computational fluid dynamic (CFD) study of Dimethyl Ether (DME) gas adsorptive separation and steam reforming (DME-SR) in a large scale Circulating Fluidized Bed (CFB) reactor. The CFD model is based on Eulerian-Eulerian dispersed flow and solved using commercial software (ANSYS FLUENT). Hydrogen is currently receiving increasing interest as an alternative source of clean energy and has high potential applications, including the transportation sector and power generation. Computational fluid dynamic (CFD) modelling has attracted considerable recognition in the engineering sector consequently leading to using it as a tool for process design and optimisation in many industrial processes. In most cases, these processes are difficult or expensive to conduct in lab scale experiments. The CFD provides a cost effective methodology to gain detailed information up to the microscopic level.

The main objectives in this project are to: (i) develop a predictive model using ANSYS FLUENT (CFD) commercial code to simulate the flow hydrodynamics, mass transfer, reactions and heat transfer in a large scale dual fluidized bed system for combined gas separation and steam reforming processes (ii) implement a suitable adsorption models in the CFD code, through a user defined function, to predict selective separation of a gas from a mixture (iii) develop a model for dimethyl ether steam reforming (DME-SR) to predict hydrogen production (iv) carry out detailed parametric analysis in order to establish ideal operating conditions for future industrial application. The project has originated from a real industrial case problem in collaboration with the industrial partner Dow Corning (UK) and jointly funded by the Engineering and Physical Research Council (UK) and Dow Corning.

The research examined gas separation by adsorption in a bubbling bed, as part of a dual fluidized bed system. The adsorption process was simulated based on the kinetics derived from the experimental data produced as part of a separate PhD project completed under the same fund. The kinetic model was incorporated in FLUENT CFD tool as a pseudo-first order rate equation; some of the parameters for the pseudo-first order kinetics were obtained using MATLAB. The modelling of the DME adsorption in the designed bubbling bed was performed for the first time in this project and highlights the novelty in the investigations. The simulation results were analysed to provide understanding of the flow hydrodynamic, reactor design and optimum operating condition for efficient separation. Bubbling

bed validation by estimation of bed expansion and the solid and gas distribution from simulation agreed well with trends seen in the literatures. Parametric analysis on the adsorption process demonstrated that increasing fluidizing velocity reduced adsorption of DME. This is as a result of reduction in the gas residence time which appears to have much effect compared to the solid residence time. The removal efficiency of DME from the bed was found to be more than 88%.

Simulation of the DME-SR in FLUENT CFD was conducted using selected kinetics from literature and implemented in the model using an in-house developed user defined function. The validation of the kinetics was achieved by simulating a case to replicate an experimental study of a laboratory scale bubbling bed by Vicente et al [1]. Good agreement was achieved for the validation of the models, which was then applied in the DME-SR in the large scale riser section of the dual fluidized bed system. This is the first study to use the selected DME-SR kinetics in a circulating fluidized bed (CFB) system and for the geometry size proposed for the project. As a result, the simulation produced the first detailed data on the spatial variation and final gas product in such an industrial scale fluidized bed system.

The simulation results provided insight in the flow hydrodynamic, reactor design and optimum operating condition. The solid and gas distribution in the CFB was observed to show good agreement with literatures. The parametric analysis showed that the increase in temperature and steam to DME molar ratio increased the production of hydrogen due to the increased DME conversions, whereas the increase in the space velocity has been found to have an adverse effect. Increasing temperature between 200 ^{o}C to 350 ^{o}C increased DME conversion from 47% to 99% while hydrogen yield increased substantially from 11% to 100%. The CO_2 selectivity decreased from 100% to 91% due to the water gas shift reaction favouring CO at higher temperatures. The higher conversions observed as the temperature increased was reflected on the quantity of unreacted DME and methanol concentrations in the product gas, where both decreased to very low values of 0.27 mol% and 0.46 mol% respectively at 350 °C. Increasing the steam to DME molar ratio from 4 to 7.68 increased the DME conversion from 69% to 87%, while the hydrogen yield increased from 40% to 59%. The CO_2 selectivity decreased from 100% to 97%. The decrease in the space velocity from 37104 ml/g/h to 15394 ml/g/h increased the DME conversion from 87% to 100% while increasing the hydrogen yield from 59% to 87%. The parametric analysis suggests an operating condition for maximum hydrogen yield is in the region of 300 ^{o}C temperatures and Steam/DME molar ratio of 5.

The analysis of the industrial sponsor's case for the given flow and composition of the gas to be treated suggests that 88% of DME can be adsorbed from the bubbling and consequently producing 224.4t/y of hydrogen in the riser section of the dual fluidized bed system. The process also produces 1458.4t/y of CO_2 and 127.9t/y of CO as part of the product gas. The developed models and parametric

analysis carried out in this study provided essential guideline for future design of DME-SR at industrial level and in particular this work has been of tremendous importance for the industrial collaborator in order to draw conclusions and plan for future potential implementation of the process at an industrial scale.

Keywords: Hydrogen Production, Adsorption, Computational Fluid Dynamic (CFD), Process Simulation, Gas Separation, Steam Reforming, Fluidized Bed.

ACKNOWLEDGEMENT

My first acknowledgement will go to my creator, God Almighty (My Father) and my saviour Jesus Christ. They have being my guide, inspiration and strength all through the good and difficult times I encountered during my PhD.

I would like to thank my family and friends for their support and encouragement especially when I felt lonely and confused about my ideas.

I would like to thank my external supervisor, Dr Yassir Makkawi for his immense support and guidance both on academic and personal challenges. I was privileged to learn from him during my undergraduate studies. I am pleased about the continual relationship he maintained despite moving to another university.

I would like to thank my current supervisor Dr (Reader) Sotos Generalis, who kindly accepted taking over the project supervision after Dr Makkawi's departure. I thank him for his great support within a short time period I have worked with him. I am really grateful for the impact he made in organising the viva and ensuring my thesis was ready for submission in due time.

I would like to thank Dr Gregory Cartland Glover for his support particularly at the early stage of my work.

Finally, I would like to thank my industrial supervisor from Dow Corning Ltd, Dr Simon Acey for his support and assistance in providing valuable personnel from Dow corning to share ideas.

LIST OF FIGURES

LIST OF TABLE

NOMENCLATURE

A	Drag law constants (-)
A	D-A adsorption potential (mol/kJ)
A_1, A_2	pre-exponential term in the Arrhenius expression (s^{-1})
A_t	Cross sectional area of the bed (m^2)
a_T	Toth isotherm constant (L/mg)
a_S	Sips isotherm model constant (L/mg)
b	Equilibrium constant for Langmuir isotherm (mg/L)
B	Drag law constants (-)
B_1	pre-exponential term in the Arrhenius expression (s^{-1})
$C_\mu, C_{1\varepsilon}, C_{2\varepsilon}$	constants (-)
C_D	Decomposition reaction constant (-)
C_e	Equilibrium concentration (mg/L)
C_{H^+}	Concentration of vacant acid sites (mol/g-cat)
C_i	concentration of species (mol m^{-3})
C_0	Tracer initial concentration ($kmol/m^3$)
C_R	methanol steam reforming modification constant (-)
$C_{R_1^+}$	Total surface concentration of surface methoxy (-)
C_t	Tracer exiting concentration ($kmol/m^3$)
C_{WGS}	water gas shift reaction constant (-)
D	Diameter of the bed (m)
D_B	Bubble diameter (m)
D_{B0}	Initial bubble diameter (m)
D_{BM}	Maximum bubble diameter (m)
$D_{T,i,g}$	thermal diffusion coefficient (kg m^{-2} s^{-1})
d_s	particle diameter of solid phase (m)
E_i	activation energy of reaction (J mol^{-1})
E^0	Characteristic energy of adsorption (kJ/mol)
E_D	Decomposition activation energy (J/mol)
E_R	Methanol steam reforming activation energy (J/mol)
$e_{s_i s_j}$	particle-particle restitution coefficient (-)
$e_{s_i,w}$	particle-wall restitution coefficient (-)
$E(t)$	Residence time distribution function
F_o	Mass flowrate (kg/s)
g_0	radial distribution function (-)

g	gravity (m s^{-2})
h	Initial bed height (m)
H_{avg}	Average expanded bed height (m)
h_i	Volumetric heat transfer coefficient
H_{max}	Maximum expanded bed height (m)
H_{min}	Minimum expanded bed height (m)
H_s	Initial static bed height (m)
$G_{k,g}$	production of turbulent kinetic energy (kg m^{-1} s^{-2})
$\bar{\bar{I}}$	unit vector (-)
$\vec{J}_{i,g}$	diffusion flux of species i (kg m^{-2} s^{-1})
h_q	specific enthalpy of q phase (J kg^{-1})
K_f	Freundlich constant (-)
k_g	turbulence kinetic energy (m^2 s^{-2})
K_{eq}	water gas shift equilibrium constant (K^{-1})
K_i	Equilibrium coefficient of elementary step
k_i	Rate coefficient incorporating C_{H^+}
k_i'	Rate coefficients of an elementary step
k_{int}	Intraparticle diffusion rate constant (mol kg^{-1}-$min^{1/2}$)
k_R	methanol steam reforming rate constant (m^3 kg^{-1} s^{-1})
K_S	Sips isotherm constant (L/g)
K_T	Toth isotherm constant (mg/g)
k_{WGS}	water gas shift rate constant (mol m^{-3} s^{-1} K^{-1} pa^{-2})
m	Constant (-)
n	Constant (-)
P	pressure (pa)
P_i	partial pressures of gas components (bar)
$\dot{Q}$	Mass flowrate (kg/s)
q_e	Amount adsorbed per amount of adsorbent at equilibrium (mg/g)
Q_o	Maximum adsorption capacity (mg/g)
R	gas constant (J mol^{-1} K^{-1})
Re_s	Reynolds number of solid phase (-)
r_D	rate of methanol decomposition (mol m^{-3} s^{-1})
r_R	rate of reaction for methanol steam reforming (mol m^{-3} s^{-1})
r_{DME}	rate of reaction of DME (mol kg-cat^{-1} s^{-1})
Sc_t	Turbulent Schmidt number (-)

t	Toth isotherm constant (-)
T	temperature (°C)
$\bar{t_R}$	Mean residence time (s)
U_{mb}	Minimum bubbling velocity (m/s)
U_{mf}	Minimum fluidization velocity (m/s)
u_0	Fluidizing velocity (m/s)
V	D-A amount adsorbed in micropores (ml/g)
$\dot{V}$	Volumetric flowrate (m^3/s)
V_0	D-A maximum micropore adsorption (ml/g)
$v_{r,s}$	particle terminal velocity ($m\ s^{-1}$)
v	velocity ($m\ s^{-1}$)
$Y_{i,g}$	mass fraction of species i in the gas phase (-)
Z	Compressibility factor (-)

GREEK LETTERS

α	volume fraction (-)
β	affinity coefficient for Dubnin-Astakhov (-)
β	momentum exchange (drag) coefficient (kg m^{-3} s^{-1})
β_s	Sips isotherm model exponent (-)
$\gamma_{\theta_{s_i}}$	collisional energy dissipation (kg m^{-1} s^{-3})
θ_{s_i}	granular temperature of solid phase i (m^2 s^{-2})
$\kappa_{\theta_{s_i}}$	diffusion coefficient of granular energy (kg m^{-1} s^{-1})
$\mu_{l,g}$	viscosity of gas phase due to laminar flow (kg m^{-1} s^{-2})
$\mu_{t,g}$	viscosity of gas phase due to turbulent flow (kg m^{-1} s^{-2})
$\mu_{s_i,col}$	viscosity of solid phase i due to collision (kg m^{-1} s^{-1})
$\mu_{s_i,kin}$	viscosity of solid phase i due to kinetics (kg m^{-1} s^{-1})
ρ	densities respectively (kg m^{-3})
$\bar{\bar{\tau}}$	shear stress tensor (kg m^{-1} s^{-2})
$\sigma_k, \sigma_\varepsilon$	constants (-)
$\emptyset$	molar ratio of steam to methanol (-)
φ	specularity coefficient
$\bar{\bar{I}}$	Unit vector (-)

1. CHAPTER 1: INTRODUCTION AND BACKGROUND

1.1 Introduction

In industrial plants, products from chemical reactors often times are accompanied by undesired by-products. This effectively results in the application of technology or process to remove such unwanted by-products in order to obtain products of high quality. Removal of these unwanted products could sometimes be a difficult process depending on the chemical and physical properties of the desired and undesirable products. Usually products or chemicals with similar properties tend to be more difficult to separate because most techniques of separation rely on property differences as the driver for separation. Different separation techniques are available; the choice depends on the properties of the feed and products that requires separation. Some of the techniques include adsorption, distillation, chromatography and evaporation. Adsorption is a notable separation method and is the system of separation chosen for this research work. It is a process that measures the rate at which a molecule from a mixture is selectively allowed to settle on the surface/pores of an adsorbent and hence become separated from other molecules in the mixture. In this work, a mixture from a process containing methyl chloride (MeCl) and dimethyl ether (DME) are investigated with the latter being the by-product.

Dimethyl ether separation from methyl chloride is a difficult process, as both chemicals have close chemical and physical properties hence eliminating the use of certain technique like distillation. When the technique selected to separate the products is successfully executed, the effluent (DME) could serve as valuable feedstock for other processes or alternatively used directly in some processes. DME could be employed in direct use or as a supplement to other fuels. In this project the DME will be converted to hydrogen a renewable energy source. With the emergence of hydrogen powered cars and demand for no air pollutants or greenhouse gases emissions, hydrogen has become an essential fuel and future demand will certainly augment. Hydrogen is produced via the heating of the DME adsorbed onto an adsorbent with steam which effectively removes dimethyl ether from the adsorbent (desorption).

Desorption is a term applied in conjunction with adsorption which depicts the removal of adsorbed molecule on the surface/pores of the adsorbent. Adsorption and steam reforming processes could be performed in different media such as packed bed, slurry beds and fluidised beds. The process equipment selected for the proposed research is a dual fluidised bed (DFB) (also known as twin fluidised bed). This consist of two joint fluidised beds instead of the traditional one bed hence the name “dual”. The application of fluidised beds in the process industry encompasses many applications such as adsorption, conversion of syngas to methanol, crystalline silicon production, biomass/coal gasification and catalytic cracking. Justification of fluidised bed superiority to other process

equipment relies mainly on the effective contact between the fluid and solid which subsequently leads to higher mass and heat transfer.

Example of published work conducted for adsorption using fluidized beds include such as the work done by Song et al. [2] in which volatile organic compounds (VOC) emitted from industries were removed from air through adsorption of the VOC in a circulating fluidized bed system. Steam reforming on the other hand, has quite limited work using fluidized beds for the process. Though Vicente et al. [1] investigated the effects of operating conditions of DME steam reforming in a laboratory scale bubbling bed. In recent years, industrial companies, as well as academic researchers, engaging on process design and optimisation emphasise on cost reduction through computer simulation and theoretical analysis.

Computational fluid dynamics (CFD) modelling has been identified as one of the most reliable tool for this purpose. CFD codes, such as ANSYS FLUENT, CFX, MFIX and Barracuda, provide realistic insight into multiphase flow characteristics in process units before a prototype is built. In this project, the multiphase flow in the dual circulating fluidised bed under the proposed adsorption and steam reforming processes will be studied using ANSYS FLUENT (Ver. 14.5). The modelling work will include incorporation of appropriate sorption and steam reforming kinetic models in the CFD code through a user defined function (UDF). The mathematical equation for the sorption will be derived from experimental data (carried out as a separate Ph.D. project) [3].

1.2 Problem Description

Dow Corning Ltd, the sponsoring company has a real issue with an undesirable gas which is produced as a by-product in one of the intermediate processes to manufacture silicone a synthetic polymer. Methyl chloride is the intermediate chemical for the manufacture of silicone materials; it is produced conventionally through the synthesis of methanol and hydrochloric acid whereby by-product dimethyl ether (DME) is equally produced. The product contains mainly of methyl chloride and about 0.2-1wt% of DME (this data was from Dow Corning Ltd).

The company's current method of eliminating DME involves treatment of the product with liquid sulphuric acid. This process removes about 99% of the unwanted gas. Dimethyl sulphate and methyl hydrogen sulphate are products produced from current separation method when contacted with the sulphuric acid. The limitations encountered with the current process such as high capital cost, toxicity nature of sulphate by-product (waste) and the cost of sulphuric acid replenishment renders the technology ineffectual. The mixture being gases at the operating conditions with relatively close boiling points (24.9^{o}C for DME and 24^{o}C for MeCl) hindered the use of notable separation processes such as distillation. The proposed solution to the problem involves a process similar to thermal swing adsorption using a dual fluidised bed system (see Fig.1.1) to selectively adsorb one gas from the gas

mixture containing DME and methyl chloride. The choice of the geometry size was made to replicate commercially proven scale of a CFB reactor (e.g. PYROFLOW CFB system of Goodrich Co in Illinois U.S.A as reported by [4]).

The adsorption is proposed to take place in one fluidized bed while the entrained adsorbent, loaded with one of the two gases, undergoes thermal desorption in a second bed within the dual fluidized bed system. Ideally, DME is preferred to be selectively adsorbed by the adsorbent as it can undergo thermal separation from the adsorbent and effectively acting as feed for the steam reforming process to produce hydrogen-rich fuel gas. The proposed design has some similarities with Fluid Catalytic Cracking system (FCC) used in the oil and gas industries for breaking larger hydrocarbons fuels to lighter fuels; however, with this design, adsorption is the process instead of combustion. Currently there is no work that has been done on adsorption involving MeCl and DME mixture neither with such proposed system (dual fluidized bed) designed for the separation. The incorporation of hydrogen production is unique and further demonstrates the novelty of the proposed system.

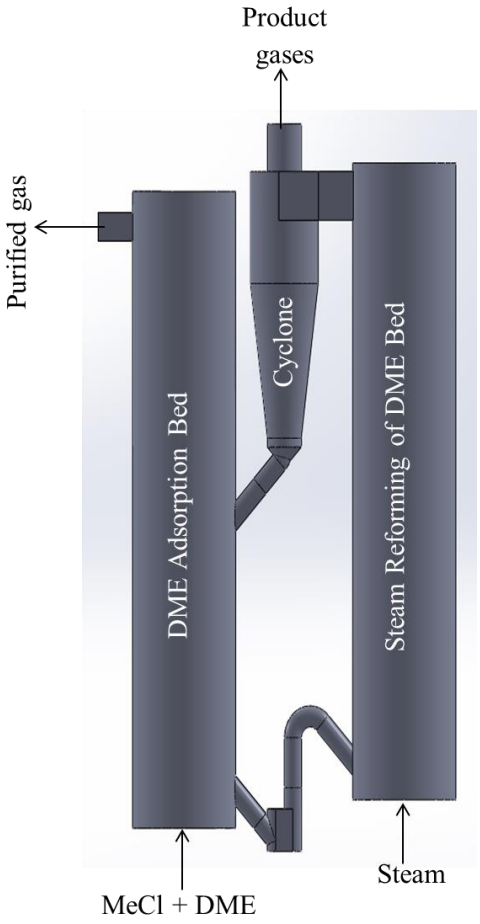

Fig. 1.1: Schematic diagram of the dual fluidized bed (DFB) system proposed for the project.

The DME adsorption in bubbling bed was conducted in similar approach as reported in the literature on the capture of CO_2 from flue gases [4–6]. For the DME adsorption, the interaction between the gas

and the selected adsorbent (Molecular Sieve 4A) was assumed to be a reaction. This was though suggested to be through physical interactions according to Lad and Makkawi [7]. The feed gas (MeCl and DME) was entering from the bottom at 0.48m/s fluidizing velocity, the adsorbent entering at bed height of 7m had mass flowrate of 20kg/s. the temperature of the system was at 25 ^{o}C.

The reactions selected for the DME steam reforming in the CFB system were DME hydrolysis reactions, methanol steam reforming, methanol decomposition and water gas shift reaction (WGSR). The two main criteria for the selected catalyst CuO/ZnO/AL_2O_3+ZSM-5 were availability of kinetics data and the presence of zeolite. The zeolite would be beneficial in the DFB coupled system as the DME adsorption adsorbent was a zeolite adsorbent (Molecular Sieve 4A). This is an area that needs further investigation experimentally to analyse the behaviour of the Molecular Sieve 4A in the CFB system for DME steam reforming. In this study, it was assumed that the Molecular Sieve 4A behaved like the ZSM-5 zeolite.

For the DME steam reforming in CFB the steam to DME molar ratio considered were 4:1, 5:1, 6:1 and 7.68:1. The catalyst mass flowrate considered were between 200kg/s - 2400kg/s for the industrial CFB and 10kg/s for the coupled DFB system. The temperature considered ranged between 200 ^{o}C – 350 ^{o}C.

1.3 Aims and Objectives

The project objectives are subdivided into the company objectives to satisfy specific industrial requirements and Ph.D. research objectives adding new scientific knowledge. The research idea proposed to the company is to investigate a novel selective separation and steam reforming of the unwanted gas (DME) in an industrial scale system using process simulation. The product of the steam reforming will be hydrogen-rich gas suitable to be used as a fuel. It should be noted that the experimental investigation in the area of discovering an appropriate sorbent material and sorption model for this novel separating process is currently conducted by another researcher as a separate PhD study [3].

Some of the Ph.D. aims and objective that have been planned to enable the fulfilment of the proposed project are listed below:

- Methodically comprehend the fundamentals of the processes that will assist in developing a model through FLUENT CFD code to simulate the flow hydrodynamics, mass transfer and heat transfer in a dual fluidised bed system.
- Implement a suitable adsorption models in the CFD code, through a user defined function, to predict selective separation of a gas from a mixture.
- Develop a model for the steam reforming of DME to predict hydrogen production in the clean fuel production unit which will potentially be integrated to the novel sorption unit.

- Analyse results in detail to establish ideal operating conditions and parameters to explain events in the systems.
- Recommendation of potential industrial scale-up processing necessary to create projected system in a real life operation

Some of the objectives that the sponsoring company desire to be achieved in the project include the following:

- Removes at least 99% of dimethyl ether impurity (DME) from a feed stock of methyl chloride
- Produces no toxic by-products that require transportation
- Has low capital cost and size
- Introduces no new compounds into the process
- Produces low levels of CO_2 not more than 2 tonnes/tonne DME removed
- Allows for recovering and re-using the DME
- Facilitate processing of 200,000 tonnes/year of MeCl feed

1.4 Research Approach

The solution to the issue encountered in the silicone manufacturing plant was approached by removing the undesired DME gas through bubbling bed in this study. The steam reforming CFB converts the DME to hydrogen rich gas. The simulations were conducted separately instead of the complete DFB system; this was because of the complexity of the DFB and the computational demand for CFD modelling. The results from the DME adsorption from the bubbling bed were then later coupled into the CFB system to complete the DFB loop. The industrial scale size selected for both the bubbling bed and CFB was to convince the industrial sponsor on the feasibility of implementing the DFB system in a commercial scale.

The simulations of the industrial scale CFB systems were conducted after validating the DME steam reforming kinetic models. The validation of the models was conducted by simulating an experimental work by Vicente [1]. The industrial CFB simulations were performed at assumed conditions mainly to support the proposed DFB commercial scale feasibility. For the coupling of DME adsorption from bubbling bed to CFB, the industrial CFB was scaled down to facilitate the industrial sponsor operating conditions.

1.5 Thesis Outline

This thesis is subdivided into 7 chapters to thoroughly elaborate on the different aspect of the project to enable full comprehension of the entire project.

Chapter 2: This will focus on the literature reviews on the modelling methodology utilised in this work. This will also include introductory to CFD and FLUENT general set-up, simulation set up for adsorption and steam reforming processes, model equations enabled for FLUENT and some

mechanism utilised such as heat transfer. FLUENT set-up for the bubbling and circulating including the meshing and geometry construction will be discussed. This chapter will also look into the residence time distribution of the solid using various methods as recommended from literature.

Chapter 3: In this chapter, the focus will be on the kinetics of adsorption and steam reforming process in FLUENT. The different methods that have been investigated and implemented in literature will be examined together with the evaluation of experimental data in determining of adsorption kinetics. The DME-SR selected kinetics from literature will be analysed and the method for implementation of the models into FLUENT explained.

Chapter 4: This chapter will look into the analysis of simulation results for DME adsorption in a bubbling bed; this will examine the performance of the bed in the adsorption of the gas. Parametric analysis of the adsorption process will be conducted to provide extensive understanding of the process and recommendation of suitable operating conditions.

Chapter 5: This chapter will cover the production of hydrogen through the process of steam reforming of DME using selected kinetics and catalyst from literature in the CFB system. Additionally a parametric analysis of the process to investigate the suitable operating conditions for the production of hydrogen will be provided.

Chapter 6: This chapter will investigate the redesigning of the original fluidized bed to analyse impact on the reactor performance. The coupling of DME adsorption to steam reforming process will be conducted to complete the DFB (Dual Fluidized Bed) system. The product gas composition from the industrial sponsor simulation would be analysed to predict hydrogen gas produced.

Chapter 7: This chapter will discuss the conclusions drawn from the various chapters and the provision of recommendations for future application of the kinetics and reactor design for the processes studied in the project.

1.6 Background

This section will briefly delve into the various aspects of the research work that will be investigated in the project. It has already been mentioned that the gas mixture will undergo two distinctive processes in this project, which are namely adsorption and steam reforming process. The medium in which these processes will be examined is the fluidized bed (bubbling and circulating bed). FLUENT CFD software that will be used in modelling the processes and equipment for the project will be discussed in chapter 2.

1.6.1 Adsorption as a separation technique

The two gas components in the mixture to be separated contain methyl chloride (MeCl) and dimethyl ether (DME). The chemical structure of these components are as follows:

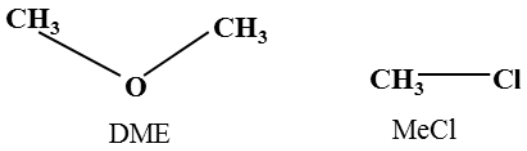

Fig. 1.2: Chemical structures for DME and MeCl.

MeCl is essentially used to produce silicone, agricultural chemicals and synthetic rubber. The gas is colourless with a mild odour and sweet taste at normal temperature and pressure. Dimethyl ether is the simplest of the ether group, it burns with a visible blue flame and unlike methane, an odorant is not necessary as it has a sweet ether-like odour.

Adsorption is a type of separation process which can be defined in its simplest form as the attachment of ions, molecules or atoms of a fluid (gas or liquid) onto the surface of a solid. Separation processes disintegrates mixtures containing different species of molecules into separate products based on the physical, chemical or thermal variation of the molecules. Separation is performed in industrial scale across several sectors such as the oil and gas, chemical and petrochemical sectors, it can also be in a small laboratory scale. There are other types of separation processes that exist apart from adsorption such as liquid-liquid extraction, leaching, drying, absorption, chromatography and distillation.

Separation process is instigated by differences between properties of components in the mixture to be separated. These requirements are different for each separation method, for example volatility is utilised in distillation, solubility for absorption and distribution coefficient for liquid extraction. In the adsorption process, molecules from the bulk fluid phase diffuse to the surface of the solid adsorbent where a distinctive adsorbed phase is formed. This is different from absorption process in which case the molecules from the gas or liquid enters into another bulk fluid. Sorption is a general term used to describe both adsorption and absorption process. During adsorption the solid adsorbent (the solid which provides the surface sites for the process) becomes saturated with the adsorbate (fluid that is adsorbed) over a period of time which then means the adsorbent will undergo desorption to remove the adsorbate from the solid.

There are various industrial adsorbents available that can be employed for the process such as zeolites, carbon, silicon and some treated (impregnated) adsorbents. The process of adsorption can be a physisorption process in which the force of attraction between the fluid and the surface of the solid are controlled by a weak Van der Waals (intermolecular forces). This is usually associated with the release of heat within the range of 20kJ mol^{-1} [8]. Adsorption can also be via a chemisorption process in

which case the fluid (gas or liquid molecules) forms a covalent bond with the solid surface when it is adsorbed and usually release heat in the region of 200kJ mol^{-1} [8].

1.6.2 Reforming process for hydrogen production

The continuous reliance on fossil fuel as energy source has steered the establishment of energy regulations to limit pollution of the atmosphere resulting from using fuels such as coal, diesel etc. Hydrogen is seen as a clean fuel and has the potential of powering cars as in hybrid cars and other mediums in which it performs well compared to other energy sources. It is definitely one of the energy options for the future. Production of hydrogen could be achieved via various sources such as natural gas, biomass, heavy hydrocarbons and dimethyl ether. Renewable sources such as biomass have also shown possibilities, though the technology is currently inefficient and expensive. Reforming is a major step in the fuels processing and it involves the conversion of fuels to hydrogen and carbon monoxide or carbon dioxide. There are three main reforming methods that are used in the industry to produce hydrogen. The advantages and disadvantages of the different reforming methods can be seen in

Table 1.1.

1.6.2.1 Steam reforming

Steam reforming can be defined as an endothermic reaction of steam with fuel in the presence of catalyst to produce hydrogen. Depending on the fuel utilised there could be various reaction that can occur spontaneously. Some of the hydrocarbon feed stock includes gases such as methane, DME, ethane, methanol, ethanol and acetone. It is a major industrial process for producing hydrogen with mainly carbon monoxide and carbon dioxide as the other by-products (syngas) [9,10].

Oxygen is not required for this process and lower operating temperature condition is favoured when compared to other reforming types. The operating temperatures however differ depending on the hydrocarbon fuel and catalyst to be used. For example, methanol temperature range of $>180^0$C, DME and other oxygen enriched hydrocarbon temperature $>500^0$C [9]. Catalyst selection range from the less expensive non-precious metals such as nickel to the more expensive precious metals from group VIII elements such as platinum and rhodium. Some conventional steam reforming process involves a step that removes carbon monoxide produced due to its contamination effects on the steam reforming catalyst [11]. The equation below is the general form of the steam reforming process reaction.

$$C_mH_n + mH_2O = mCO + \left(m + \frac{1}{2}n\right)H_2 \quad (1.1)$$

1.6.2.2 Partial oxidation

This process partially oxidizes the hydrocarbon with oxygen from air to produce hydrogen and carbon monoxide through an exothermic reaction. It equally accepts different sources, such as natural gas, propane, alcohols and liquid hydrocarbons. It is operated without the use of catalyst with operating

temperature between 1300ºC to 1500ºC. Though these high temperatures increase the rate of reaction, they also lead to the formation of carbon monoxide which might be a disadvantage for some processes. Hydrogen produced using PO (partial oxidation) method is lower than that produced by steam reforming because water, which is a source of hydrogen, is not used and introduction of nitrogen from air lowers the hydrogen partial pressure [10]. The exclusion of water removes the requirement of a generator which helps with the general design of the plant. A sub-type of this method operates at lower temperature (450ºC to 850ºC) and involves the use of catalyst which is referred to as Catalytic Partial Oxidation (CPO). Despite the temperature reduction for the CPO method, controlling temperature is extremely difficult due to exothermic nature of the process. The equation below is the general reaction for partial oxidation reformer

$$C_mH_n + \frac{1}{2}mO_2 = mCO + \frac{1}{2}H_2 \quad (1.2)$$

1.6.2.3 Autothermal reforming

This process is the combination of catalytic or non-catalytic partial oxidation process with steam reforming. A major advantage of this method is the optimisation of the energy requirement which is encouraged through the utilisation of the heat produced from the partial oxidation stage for the endothermic steam reforming stage. Hence this implies that two zones are present in the reactor with one section where partial oxidation occurs (thermal zone) and other section where endothermic reactions occur at reduced temperature (catalytic zone). Proper adjustment of the oxygen to carbon ratios is essential to ensure that the partial oxidation provides enough heat for the endothermic steam reforming section of the reactor, this efficiently will affect the reaction, temperature and product gas formation [12]. The equation below is a general form for autothermal reaction.

$$C_mH_n + \frac{1}{2}mH_2O + \frac{1}{4}mO_2 = mCO + \left(\frac{1}{2}m + \frac{1}{2}n\right)H_2 \quad (1.3)$$

Table 1.1: Advantages and disadvantages of the main types of reformer [12,13]

Reforming process	Advantages	Disadvantages
Steam reforming	• Oxygen not required • Lowest temperature • Best H_2/CO ratio • High efficiency • Cost effective for large unit • Most Popular technology	• Highest CO_2 emission • System is complex • Sensitive to natural gas qualities
Partial oxidation	• May not require catalyst • Simple system • Feed stock desulphurisation not required	• Low CO_2/H_2 ratio • Very high operating temperature • Soot formation/handling • Requires pure O_2

Reforming process	Advantages	Disadvantages
Autothermal	• Lower operating temperature • Lower oxygen requirement than partial oxidation	• Requires air or oxygen • Limited commercial validation

1.6.3 Fluidized bed

In various industrial applications, different technologies provide the platform for processes such as adsorption, chemical reaction and drying. Selecting a suitable technology can depend on certain criteria which could include as product specification, operating conditions, knowledge on technology and feed stock requirement. In the chemical industry, packed bed also called fixed bed is a very important technology, though some inefficiency limits the use of this technology such as heat and mass distribution leading to the formation of hotspot. Fluidised beds appears to be widely utilised in industrial applications such as chemical, environmental and energy, its popularity has often been accredited to the superior efficient mass & heat transfer between fluid and solids than the fixed beds [14–16]. The better mixing is as a result of increased interactions between the materials due to continuous movement in the bed initiated by the fluidising agent which could be liquid or gas phase. Despite the benefits that are associated with fluidized beds, the technology does possess some disadvantages as listed in the table below.

Table 1.2: Some selected advantages and disadvantages of fluidized beds [17]

Advantages	Disadvantages
Easy handling of the equipment as there are no moving parts	Erosion of pipes and vessels due to abrasion of particles
Suitability for large scale operation	Non-uniformity in residence time of solids in the bed as a result of rapid mixing
High heat and mass transfer rates between gas and solids	Brittle solids are pulverised and entrained by the gas and must be returned
Uniform temperature distribution due to intensive solid mixing	Expensive solids separation or gas purification is required
Circulations of solids makes it possible to remove large quantities of heat produced	Difficulties in scale-up

Fluidisation occurs when the drag force exerted on the solid particles by the fluidizing fluid (liquid or gas) flowing upwards is equivalent to the net weight of the solid particles in the bed; this phenomenon is called incipient fluidisation and leads to expansion of the bed. The fluid -particle mixture starts to behave like fluid-like state and the velocity at which incipient fluidization is reached is called the minimum fluidization velocity. Theoretically at the point of minimum fluidization velocity, the

frictional force between the fluid and the particle counterbalances the weight of the particles [18]. Fig. below shows a type of fluidised bed called circulating fluidised bed.

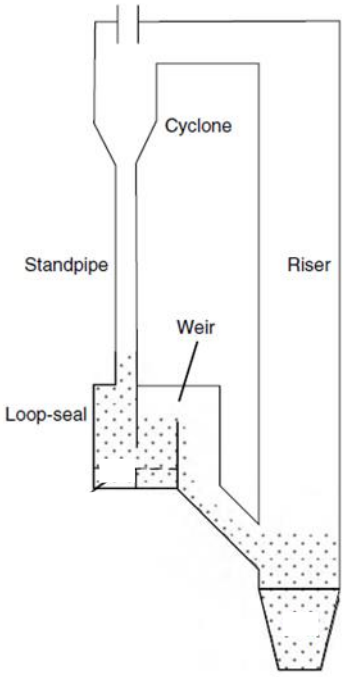

Fig. 1.3: Circulating fluidised bed system [18]

The expansion of the bed in relation to the increment of the fluidizing fluid is correlated with the pressure drop in the system which also helps in determining the minimum fluidizing velocity of the system. In Fig. 1.4 below, at zero fluidizing velocity, the system remains a packed bed with no pressure drop. Increasing the fluidizing velocity leads to increase of the pressure drop until the attainment of the minimum fluidization at which any further increase of the superficial fluid makes the bed to dilate while pressure drop remains constant [19,20].

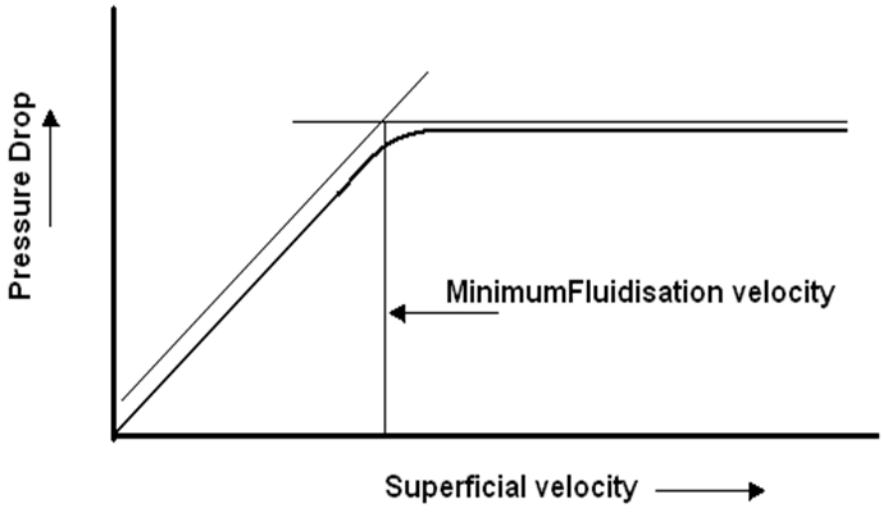

Fig. 1.4: Pressure drop against superficial velocity

A fluidized bed system could either be a liquid-solid or a gas-solid system. In a liquid-solid system, increment of flowrate above minimum fluidisation velocity usually result in a smooth progressive homogenous bed expansion with no gross flow instability, such bed is called homogenous fluidised bed. For gas-solid system, increment above minimum fluidisation velocity results in high instability with bubbling and channelling of gas apparent. In the gas-solid systems, the characteristics of the flow in the bed could differ depending on the size of the equipment and the properties of the gas and solid materials. This was initially illustrated by Geldart in 1973 where the behaviour of the solid fluidized by the gas is grouped into four categories resulting from the density differences between the solid & gas and by the mean particle diameter [16,21]. The table below shows the different flow regimes.

Table 1.3: Flow regime classification of the behaviours of a gas-solid system [22]

	Group C	Group A	Group B	Group D
Most obvious characteristics	Cohesive difficult to fluidise	Ideal for fluidisation. Exhibits range of non-bubbling fluidisation	Starts bubbling at U_{mf}	Coarse solids
Typical solids	Flour, Cement	Cracking catalyst	Building sand	Gravel, coffee, beans
Bed expansion	Low because of channelling	High	Moderate	Low
De-aeration rate	Initially fast then exponentially	Slow and linear	Fast	Fast
Bubble properties	No bubbles only channels	Bubbles split and coalesce. Maximum bubble size	No limit to size	No limit to size
Solids mixing	Very low	High	Moderate	Low
Gas backmixing	Very low	High	Moderate	Low
Spouting	No	No	Only in shallow beds	Yes even in deep beds
Particle size	<20µm	20-90µm	90-650µm	>650µm

Types of fluidized beds

There are different variations of fluidized beds that exist, they could be categorised based on the particle sizes and magnitude of the fluidising fluid velocity; these are described in the table below.

Table 1.4: Categories of fluidized beds that exits and its description [23]

Bed	Description
Bubbling bed	Formed when the fluidising fluid superficial velocity slightly increase beyond the minimum fluidisation velocity, this leads to vigorous particles movement in the bed without the bed expanding beyond the level attained at minimum fluidisation velocity.
Slugging bed	In gas-solid system when the gas bubbles coalesces and grow as it rises along the bed, the magnitude of bubbles increases and spreads across the vessel.
Spouted bed	Uniformly sized coarse particles when contacted by gas leads to spout of gas punching through the particle while moving the solids to the top of the bed
Turbulent bed	Fine particles are fluidised at sufficiently high fluidising flow rate to the extent that the solid terminal velocity is exceeded. Entrainment of solids becomes apparent.
Fast bed	Further increase of fluidising fluid velocity beyond the turbulent bed, fluidising gas carries the solids out of the bed.

Fluidized beds have various industrial applications; Fluid Catalytic Cracking (FCC) reactors are essential in the oil and gas industry in cracking of crude oil or higher carbon materials and are mainly fluidized beds. This represent an area that fluidized bed is most popular. Some of these applications are mentioned in Table below.

Table 1.5: Some industrial processes that apply fluidized beds [17]

Physical operations	Biotechnology applications	Gas-solid reactions	Catalytic gas-phase reactions
Adsorption	Biogas production	Combustion of coal and biomass	Catalytic cracking
Granulation	Solid-state fermentation	Municipal waste incineration	Fischer-Tropsch synthesis
Particle separation		Sewage sludge incineration	Methanol to gasoline
Solids blending		Reduction of iron oxide	Melamine from urea

2 CHAPTER 2: DEVELOPMENT OF CFD SIMULATION MODELS FOR FLUIDIZED BED REACTORS

2.1 Literature Review on CFD Modelling

Computational fluid dynamics (CFD) modelling is a theoretical approach that can be used to predict fluid flow, heat transfer and chemical reactions by solving complex sets of governing mathematical equations (conservation of mass, momentum and energy) over a discretised cells in a computer based simulation [24]. The CFD platform is based governing equation derived from Navier-Stokes equations and forms the platform in which CFD is built. CFD was initially popular in the aerospace industry where a virtual prototype was essential; however this is now standard tool for the development of new methods in wide range of engineering fields as seen in the table below.

Table 2.1: Various applications of CFD [25]

Applications	Sectors
Industrial	Aerospace, architecture, automotive, biomedical, chemical and process combustion, electronics and computers, glass manufacturing, petroleum, power, marine, mechanical, nuclear water reactors
Environmental	Atmospheric pollution, climate calculations, fire in the buildings, oceanic flows, pollution of natural waters safety
Physiological	Cardiovascular flows (heart, major vessels), flow in lungs and breathing passages

The main reason behind the growing interest on CFD is based on cost reduction for academic researchers and companies that have intentions of providing innovative solutions to remain competitive; however other advantages over experimental based approach exist as described in Table 2.2 below.

Table 2.2: Some advantages of CFD [25,26]

Advantages of CFD
• Reduction of cost of new designs and lead times • Ability to analyse systems that hinders performing controlled experiments • Practically unlimited level of detailed results • Ability to analyse systems under hazardous conditions at and beyond their normal performance limit • Enable evaluation of geometry changes at reduced time and cost compared to laboratory testing • Provides better understanding of flow distributions, weight losses, mass and heat transfer,

particulate separations etc.

CFD solver in multiphase flow involves calculating the mathematical representation of fluid flow (governing equation) derived from fundamental physical principles of conservation of mass, energy and momentum [27]. The nature of these equations are usually in the form of non-linear ODE (ordinary differential equation) or PDE (partial differential equation) which are difficult to be solved analytically. For this reason, an approximate solution is approached, this transforms the equations into simpler forms to reduce the mathematical and numerical complexity by discretizing the domain [28]. There are three main discretization methods that could be used: finite difference, finite volume and finite element. The CFD code FLUENT used for this project is based on the finite volume method. For this reason, only this method and the other most popular method (finite element) would be discussed. .

Finite Volume method

Finite volume discretization involves dividing the computational domain into cells that define the area of interest. In each control cell volume discretized, the integral form of the governing (conservation of mass, momentum and energy) and constitutive (chemical reactions, turbulence, particles transportation and radiation) equations are solved. The accuracy of the results depends on the size, shape and location of the control volumes together with inlet, outlet and wall boundary conditions. The finite differential method solves the multiphase systems in a differential form of the PDE; the computational domain is mainly divided into hexahedral grid of cells with solution obtained at each node points. The node points connect each individual cell.

Finite element method

The finite element method divides the computational domain into smaller domains and solution in each element is developed from the base functions [28]. The base functions describes the solution of the governing equations to be solved hence the final solution is iterated to be close to the base. This approach which is regarded as generic makes it suitable for complex domains with difficult problems. This implies that mesh refinement is not essential for producing accurate results as any cell size and geometry is permitted. The control volume method involves integrating of the governing equations of fluid flow over all the control volumes of the domain [26]. This feature differentiates control volume to the finite element method. This method is a preferred choice and is often applied in solid mechanics, though it has a drawback which is centred around its inability of solving local conservations [27].

Nowadays, there are various CFD codes for multiphase flow simulation such as FLUENT, CFX, Barracuda, Phoenics and MFIX. With the exception of the latter, all these software are available commercially. These codes usually have three main elements to analyse fluid flow; these are pre-processor, solver and post-processor. For the purpose of this project, ANSYS FLUENT code has been selected due to its wider use and recognized reliability for research and industrial applications in the in

the area of fluidization, namely gas-solid fluidized bed systems. Another popular code used for fluidized bed is Barracuda. This was not selected as a result of insufficient literature on fluidized beds using the software and is computationally intensive, particularly for dense fluidized beds with high solid volume fraction because it's based on Eulerian-lagrangian model.

Pre-processing involves constructing the geometry of interest (domain), grid generation or meshing (dividing of domain to elements/cells), selecting the physical and chemical phenomena that requires modelling and definition of fluid properties together with appropriate boundary conditions.
The FLUENT solver code involves using a suitable computer with considerable processor speed, inputting the boundary conditions and running the simulation until convergence is reached.
The post-processor generally evaluates the data obtained from the software and analysed either graphically or numerically.

2.2 Modelling of Multiphase Flow

In modelling multiphase flow, it is essential to initially understand the process flow regime. These are categorised into two phase systems such as gas-liquid or liquid-liquid flows, gas-solid flows, liquid-solid flows and three phase flow systems. In fluidized bed gas-solid systems, numerous researches have distinctively suggested two popular models for multiphase flow problems; these are Eulerian-Eulerian and Eulerian-Lagrangian (discrete phase model) methods. Selections of appropriate model are essential as this would give different results at considerably different computational time. The choice relies mainly on the objectives of the numerical simulation and the nature of the disperse phase 1.e whether it's a dense or dilute system. For instance, the Eulerian-Lagrangian is convenient to use for dilute flow as it tracks the solid through its path; hence it is time consuming especially if considering a large scale problem. The Eulerian-Eulerian, which is the method used in this project, is of interest due to the reported successful applications for processes involving gas-solid flow in fluidized bed systems and its ability to handle the variety of dense and dilute flows considered in this study. Further information on the Eulerian-Eulerian method is given below and literature examples of CFD studies based on this method can be found in [4,29].

2.2.1 Eulerian- Eulerian Model

This is suitable for a gas-solid flows (granular flows), gas-liquid and liquid-liquid flows. It has been applied to simulate process equipment such as fluidised beds, risers, bubble columns and suspension for undertaking some processes such as separation, evaporation, boiling and aeration [30]. In this model, both phases (dispersed and fluid) are treated as an interpenetrating continuum (fluid). The governing equations; continuity, momentum, energy and species equation are solved for each phase and the volume fractions are tracked. A single pressure field is used for all phases; interphase exchange coefficient (drag coefficient) and pressure are used in coupling the equations from each phase. Various drag laws can be selected in FLUENT (such as drag laws by Syamlal-O'Brien [31]

and Gidaspow [32] or through a user defined function written in C++ programming language. Commonly, the Kinetic Theory of Granular Flow (KTGF) is used to derive constitutive relations based on empirical information to describe the particle-particle interaction [28]. This modelling approach is particularly attractive as it is suitable for fast computation of realistic multiphase flow problems, as noted earlier.

2.3 CFD Modelling in ANSYS FLUENT

FLUENT and CFX codes are renowned commercial simulation tools from ANSYS for the analysis of fluid flow. The software is equally crucial in the design stages of process equipment and in the optimisation of existing processes. There are several simulation works that have commended the use of FLUENT software in accurately predicting flow behaviours in various applications ranging from engineering to non-engineering, some of these work include, Sikula et al, [33] who studied the thermal analysis of light pipes in buildings to control daylight into houses, Bose et al, [34] who studied effects of non-Newtonian behaviour of blood on magnetic drug targeting carrier for transporting drug molecules to a targeted site through the vascular system and Li et al, [35] who applied the two-phase model for gas-solid system for predicting the chemical reaction and hydrodynamics of ozone decomposition.

ANSYS FLUENT solver calculates the governing equations through a finite volume discretization method. This involves dividing the computational domain into cells in which the governing and constitutive equations are solved. On deciding that FLUENT is the suitable simulation tool, there are some pre-processor tools that could be utilised to build the geometry. Gambit, Solidworks and AutoCAD are some of these tools that can construct the geometry and then imported into ANSYS for meshing prior to FLUENT analysis. ANSYS do have its inbuilt tool for domain construction namely DesignModeler and ICEM CFD.

2.4 Mathematical Models

The model for this PhD work is based on a three dimensional (3-D) model. Kinetic theory of granular flow (KTGF) will be used to model a two-phase Eulerian-Eulerian multiphase model in FLUENT for both the bubbling bed for adsorption and the CFB bed for DME steam reforming (DME-SR). FLUENT code has various models and options to select in the user interface depending on the case to be simulated to enable accurate predictions. Some of the fundamental models that are solved are the governing and constitutive equations which provide understanding of the hydrodynamic behaviour for the beds. Equations in this section all apply to the bubbling and CFB beds unless otherwise stated.

2.4.1 Governing equations

These are mathematical statements that fundamentally define the physical principles in computational fluid dynamics which are each solved inside the finite control volume of the domain. These equations

are based on the three fundamental laws of conservation of mass, momentum and conservation of energy.

2.4.1.1 Conservation of mass

$$\frac{\partial}{\partial t}(\alpha_i \rho_i) + \nabla \cdot (\alpha_i \rho_i v_i) = S_i \qquad i\text{: solid } (s) \text{ or gas } (g) \tag{2.1}$$

where S_i, is the source term in which for the solid phase is zero because there was no creation of any solid from reactions , α_i is the volume fraction for either gas or solid, v_i is the velocity for either gas or solid and ρ_i is the density of either phase;

$$\sum_{j=1}^{n} \alpha_{s_j} + \alpha_g = 1 \tag{2.2}$$

where n is the number of solid phases which is one for bubbling bed and two for DME-SR, the where the subscript j=1 or 2 stands for the solid phases (catalysts and adsorbent).

2.4.1.2 Conservation of momentum

Gas phase

$$\frac{\partial}{\partial t}(\alpha_g \rho_g v_g) + \nabla \cdot (\alpha_g \rho_g v_g) = -\alpha_g \nabla P_g + \nabla \cdot \bar{\bar{\tau}}_g + \alpha_g \rho_g g - \sum_{j=1}^{n} \beta_{s_j} \left(v_g - v_{s_j}\right) \tag{2.3}$$

where g is acceleration due to gravity, $\beta_{s_i g}$ is the momentum exchange coefficient between gas and solid, P is the solid pressure and $\overline{\overline{\tau_g}}$ is the gas phase stress-strain tensor, S_{gs} is momentum transfer in the gas phase as a result of mass transfer between gas and solid phase and n is the number of solid phase which is 1 for bubbling bed and 2 for CFB.

Solid phase

$$\frac{\partial}{\partial t}(\alpha_{s_i} \rho_{s_i} v_{s_i}) + \nabla \cdot (\alpha_{s_i} \rho_{s_i} v_{s_i}) = -\alpha_{s_i} \nabla P_{s_i} + \nabla \cdot \bar{\bar{\tau}}_{s_i} + \alpha_{s_i} \rho_{s_i} g + \beta_{s_i}(v_g - v_{s_i}) + \sum_{j=1}^{n} \beta_{s_{i,j}} \left(v_{s_i} - v_{s_j}\right) \tag{2.4}$$

2.4.1.3 Kinetic fluctuation energy

This is also known as the granular temperature which represents the random kinetic fluctuation of particles. This results from the collisions of the particles with neighbouring particles; this is similar concept to the kinetic theory of gases in which gases moves freely and collides with the walls of the container.

$$\frac{3}{2}\left[\frac{\partial}{\partial t}(\rho_{s_i} \alpha_{s_i} \theta_{s_i}) + \nabla \cdot (\rho_{s_i} \alpha_{s_i} \theta_{s_i} v_{s_i})\right] = \left(-P_{s_i} \bar{\bar{I}} + \bar{\bar{\tau}}_{s_i}\right) : \nabla v_{s_i} + \nabla \cdot (k_{s_i} \theta_{s_i} \nabla \theta_{s_i}) - \gamma \theta_{s_i} + \varphi_{g s_i} \tag{2.5}$$

where θ is the granular temperature. The terms in the right side represent the generation of energy by the solid stress tensor, the diffusion of energy, the collisional dissipation of energy and the energy exchange between the gas and solid phase respectively.

2.4.1.4 Conservation equations of species transport in the gas phase

In the adsorption simulations, gas species are not created from chemical reactions while for the DME-SR simulations the kinetics evolve new species which are introduced into the species equations through the source terms.

$$\frac{\partial(\alpha_g \rho_g Y_{i,g})}{\partial t} + \nabla(\alpha_g \rho_g v_g Y_{i,g}) = -\nabla \cdot \alpha_g J_{i,g} + S_i \tag{2.6}$$

where $Y_{i,g}$=1,2,… n_g is the mass fraction of species i in the gas phase, $J_{i,g}$ is diffusion flux of species i, $D_{i,g}$ is the mass diffusion coefficient for species i in the gas phase, $D_{T,i,g}$ is the thermal diffusion coefficient and S_i is the source term which is zero for the bubbling bed simulation as mentioned

$$J_{i,g} = -\left(\rho_g D_{i,g} + \frac{\mu_t}{Sc_t}\right)\nabla Y_{i,g} - D_{T,i,g}\frac{\nabla T}{T} \tag{2.7}$$

2.4.2 Constitutive Equations

The governing equations mentioned have various relative equations that require computation before the governing equations are solved. These equations comprise the constitutive equations, in this section essential selected constitutive equations are elaborated.

2.4.2.1 Interphase momentum exchange coefficient

In fluidized bed systems, an essential model that requires appropriate selection is the interphase momentum exchange coefficient also known as drag model. This model represents the interaction between the fluid and the solid in the system, it's considered as one of the main parameters that characterises fluidized beds [36,37]. Theoretically, this is the force that the fluidizing velocity produces to counterbalance the gravitational force acting on the solids. There are two notable experimental methods of estimating the drag coefficient for the drag model, one is through packed bed pressure data and the other is using the terminal velocity of particles in fluidized bed in which the drag model is obtained as a function of void fraction and Reynolds Number [38–40].

There are various drag models available for FLUENT which are appropriate for different multiphase regimes. These models could be modified to further enhance suitability for the process through user defined functions [41]. Many researchers with different sets of priorities have produced work resulting in some inconsistencies regarding the appropriate drag model to select [40]. In FLUENT, the fluid-solid interphase momentum exchange coefficient has six models available for simulation purposes.

This include Syamlal-O'Brien model, Parameterized Syamlal-O'Brien model, Wen and Yu model, Gidaspow model, Huilin-Gidaspow model and Gibilaro model [41]. Gidaspow and Syamlal-O'Brien model are the most popular and often have been employed in modelling works with readily available literatures [42], for this reason the drag model for this work will be between these two models.

2.4.2.1.1 Syamlal-O'Brien model [43]

This model is based on the measurement of the terminal velocity of the solid particles in the fluidized bed s or settling beds, its correlations are a function of volume fraction and relative Reynolds Number [36,38]. Its drag function is represented in the equation below

Fluid-solid exchange coefficient

$$\beta_{gs_i} = \frac{3\alpha_{s_i}\alpha_g\rho_g}{4v_{r,s_i}^2 d_s} C_D\left(\frac{Re_{s_i}}{v_{r,s_i}}\right)\left|v_{s_i} - v_g\right| \tag{2.8}$$

where β_{gs_i} is the gas-solid interphase drag coefficient, C_D is the drag coefficient, v_{r,s_i} terminal velocity correlation, Re_{s_i} Reynolds number of solid phase, solid diameter

2.4.2.1.2 Parameterized Syamlal-O'Brien model [31]

In all the drag correlations, it is a known fact that the drag force depends on the local slip velocity and void fractions. Some of these properties which also include particle size distribution have not been considered in most drag models. However the knowledge of the minimum fluidization velocity which can be obtained experimentally or theoretically could enable better predictions [39], this have provided platform to adjust original drag models.

The formal Syamlal-O'Brien model have been reported to sometimes overestimate and underestimate the fluidized bed expansion based on certain conditions when compared to experimental data, though reasonable agreement in terms of solid distribution and bubble formations are maintained [42,44,45]. For this reason ANSYS have equally adjusted the original Syamlal-O'Brien model by introducing new parameters to enable the implementation of the minimum fluidizing velocity and void fraction entered in the user interface instead of creating a user defined function. This new adjusted model is called the Parameterized Syamlal-O'Brien model. This model was not considered due to lack of experimental data to validate its application in the CFD simulations.

Fluid-solid exchange coefficient

$$\beta_{gs_i} = \frac{3\alpha_{s_i}\alpha_g\rho_g}{4v_{r,s_i}^2 d_s} C_D\left(\frac{Re_{s_i}}{v_{r,s_i}}\right)\left|v_{s_i} - v_g\right| \tag{2.9}$$

The new parameters adjusted are programmed to change during iterations until an objective function is met which is;

$$\left\{U_{mf}^{experiment} - Re_{ts_i}\frac{\varepsilon_g\mu_g}{\rho_g d_s}\right\} \tag{2.10}$$

2.4.2.1.3 Gidaspow model [32]

This model aimed to cover whole range of void fraction which is a combination of the Wen and Yu drag model and the Ergun equation. When the void fraction of the fluid phase is less than or equal to 0.8, Ergun equation solves the interchange coefficient and when the void fraction of the fluid is greater than 0.8 Wen and Yu equation was used instead [44]. Its derivation is based on the pressure drop through a porous media.

When $\alpha_g > 0.8$ Fluid-solid exchange coefficient

$$\beta_{gs_i} = \frac{3}{4}C_D\frac{\alpha_{s_i}\alpha_g\rho_g|v_{s_i} - v_g|}{d_s}\alpha_g^{-2.65} \tag{2.11}$$

Drag function

$$C_D = \frac{24}{\alpha_g Re_{s_i}}\left[1 + 0.15\left(\alpha_g Re_{s_i}\right)^{0.687}\right] \tag{2.12}$$

When $\alpha_g \leq 0.8$ Fluid-solid exchange coefficient

$$\beta_{s_i g} = 150\frac{\alpha_{s_i}(1-\alpha_g)\mu_g}{\alpha_g d_s} + 1.75\frac{\rho_g\alpha_{s_i}|u_{s_i} - u_g|}{d_s} \tag{2.13}$$

The classical models of Syamlal-O'Brien and Gidaspow model have been reported to show quite similar characteristics when simulated, they have both overestimated/underestimated fluidized bed expansion for instance [36,40,46]. The modification of the Syamlal-O'Brien (parameterized Syamlal-O'Brien) model has shown that it improves hydrodynamic predictions for the fluidized bed [40]. Parameterized Syamlal-O'Brien model could have been a better choice but due to no experimental work is associated with this project, the Syamlal-O'Brien model will be selected as the best suitable choice as it has been reported that it correctly predict bed hydrodynamics to acceptable level [42,44,45]. Syamlal-O'Brien model was also observed to exhibit better predictions of bed hydrodynamics compared to Gidaspow model [38].

Solid shear stresses [41]

The force acting on the particles moves in directions described by the solid stress tensor. Solid stress tensor comprises of shear and bulk viscosities resisting the impact of deformation from the shear stresses which arises from the particle momentum exchange due to collisions of particles.

$$\bar{\bar{\tau}}_{s_i} = \alpha_{s_i}\mu_{s_i}\left(\nabla v_{s_i} + \nabla v_{s_i}^T\right) + \alpha_{s_i}\left(\lambda_{s_i} - \frac{2}{3}\mu_{s_i}\right)\nabla\cdot v_{s_i}\bar{\bar{I}} \tag{2.14}$$

where $\bar{\bar{\tau}}_{s_i}$ is the solid shear stress, μ_{s_i} solid shear viscosity, λ_{s_i} solid phase bulk viscosity, $\bar{\bar{I}}$ is unit vector

Solid shear viscosity

Solids shear viscosity consists of three components in the form of collisional, kinetic and frictional parts, the frictional part is optional and only applicable in a system with very dense dispersed phase associated with packed beds. In such system kinetic theory of granular flow is ineffective due to non-collision of particles as the solid are closely packed.

However, the frictional part was initially considered but was neglected due to computational time as it required considerably low time-step to avoid divergence.

$$\mu_{s_i} = \mu_{s_i,col} + \mu_{s_i,kin} \tag{2.15}$$

where $\mu_{s_i,col}$ is the collisional viscosity and $\mu_{s_i,kin}$ the kinetic viscosity

Collisional viscosity [47]

$$\mu_{s_i,col} = \left(\frac{4}{5}\alpha_{s_i}\rho_s d_s g_{0s_i}(1+e_{s_i})\sqrt{\frac{\theta_{s_i}}{\pi}}\right) \tag{2.16}$$

where g_{0s_i} is radial distribution function, e_{s_i} coefficient of restitution, θ_{s_i} is the granular temperature

Kinetic viscosity [47]

There are two models proposed for this computation in FLUENT (Gidaspow and Syamlal-O'Brien). Syamlal-O'Brien was selected to correlate with the drag model for the system.

$$\mu_{s_i,kin} = \left(\frac{\alpha_{s_i}\rho_s d_s\sqrt{\pi\theta_{s_i}}}{6(3-e)g_{0s_i}e_{s_i}}\left[1+\frac{2}{5}(1+e_{s_i})(3e_{s_i}-1)g_{0s_i}\alpha_{s_i}\right]\right) \tag{2.17}$$

Solid phase bulk viscosity

This accounts for the resistance of particles to compression and expansion as shear stress acts on the solids from neighbouring solids via collisions and according to [48] is derived as follows;

$$\lambda_s = \left(\frac{4}{3}\alpha_{s_i}\rho_s d_p g_{0s_i}(1+e_{s_i})\sqrt{\frac{\theta_{s_i}}{\pi}}\right) \tag{2.18}$$

Radial distribution function

As previously mentioned that substantially high dispersed phase volume fraction would render the KTGF ineffective. The radial distribution function serves as a correction factor to enhance the probability of particle collisions when the granular phase becomes dense. Equation (2.20) is for the bubbling bed simulation where only one solid phase is used while equation (2.19) is applicable for the CFB as it has two solids involved. The selected equation for the radial distribution was according to [48].

$$g_{0s_is_i} = \left[1 - \left(\frac{\alpha_{s_i}}{\alpha_{s_i,max}}\right)^{1/3}\right]^{-1} + \frac{1}{2} d_{s_i} \sum_{j=1}^{n} \frac{\alpha_{s_j}}{d_{s_j}} \tag{2.19}$$

where $\alpha_{s,max}$ is the packing limit and its equation for binary solid mixture can be found in [49].

$$g_{0,s_is_j} = \frac{d_{s_j} g_{0,s_is_i} + d_{s_i} g_{0,s_js_j}}{d_{s_i} + d_{s_j}} \tag{2.20}$$

Solid phase pressure

This is the pressure exerted on the wall of the domain due to presence of particles. Solids pressure is generated from the collision of the solids within the compressibility regime of the granular flow, this is the state at which the solid volume fraction is less than the solid packing limit assumed to be 0.63 in FLUENT. Equation (2.21) is the modification of general solids pressure formulation in the presences of other phases, the first term on the right hand side of the equation represents kinetic term and the second is due to particle collisions. This equation is different for cases that have one solid phase, the bubbling bed comprising of one solid phase represented by equation (2.22) would be applicable. Solids pressure is an essential parameter for solving solids momentum and energy equation and its given by [48] as follows;

$$P_{s_i} = \alpha_{s_i} \rho_{s_i} \theta_{s_i} + \sum_{j=1, j\neq i}^{n} \frac{\left(d_{s_i} + d_{s_j}\right)^3}{4 d_{s_i}^3} g_{0,s_is_j} \rho_{s_i} \alpha_{s_i} \alpha_{s_j} \theta_{s_i} \left(1 + e_{s_is_j}\right) \tag{2.21}$$

$$P_s = \alpha_s \rho_s \theta_s + 2\rho_s (1 + e_{ss}) g_{0,s} {\alpha_s}^2 \alpha_s \theta_s \tag{2.22}$$

Solid-solid drag coefficient

This constitutive model is only applicable for the CFB bed as there are multiple solid phases. The exchange coefficient was solved according to [50] as follows;

$$\beta_{s_is_j} = \frac{3\left(1 + e_{s_is_j}\right)\left(\frac{\pi}{2} + C_{frs_is_j}\frac{\pi^2}{8}\right)\alpha_{s_i}\rho_s\alpha_{s_j}\rho_s\left(d_{s_i} + d_{s_j}\right)^2 g_{0,s_is_j}}{2\pi\rho_s\left(d_{s_i}^3 + d_{s_j}^3\right)} \left|\vec{v}_{s_i} - \vec{v}_{s_j}\right| \tag{2.23}$$

2.4.3 Turbulence model

The condition for the adsorption in bubbling bed is laminar flow due to the fluidizing velocity. However, the conditions for the CFB bed necessitate the use of high fluidizing velocity to circulate the solid phase, it's a common feature for CFB systems [51]. An equation that takes into consideration the effects of turbulent fluctuations velocities and scalar quantities is implemented using the widely reported standard *K*-epsilon (k-ε) dispersed turbulence model. The model comprises of kinetic energy and dissipation rate, as follows [52];

Turbulent kinetic energy:

$$\frac{\partial}{\partial t}(\alpha_g \rho_g k_g) + \nabla\left(\alpha_{g_q} \rho_g v_g k_g\right) = \alpha_g G_{k,g} + \nabla\left(\alpha_g \frac{\mu_{t,g}}{\sigma_k} k_g\right) - \alpha_g \rho_g \varepsilon_g + \alpha_g \rho_g \quad (2.24)$$

where k_g is the turbulent kinetic energy,$\mu_{t,g}$ turbulent viscosity of the gas phase and $G_{k,g}$ is the production of turbulent kinetic energy and σ_k is a model constant = 1.00.

The dissipation of turbulence energy:

$$\frac{\partial}{\partial t}(\alpha_g \rho_g \varepsilon_g) + \nabla\left(\alpha_{g_q} \rho_g v_g \varepsilon_g\right) = \nabla\left(\alpha_g \frac{\mu_{t,g}}{\sigma_\varepsilon} \varepsilon_g\right) - \alpha_g \frac{\varepsilon_g}{k_g}\left(C_{1\varepsilon} G_{k,g} - C_{2\varepsilon} \rho_g \varepsilon_g\right) + \alpha_g \rho_g \quad (2.25)$$

where ε_g is the dissipation of turbulence energy and σ_ε, $C_{1\varepsilon}$, & $C_{2\varepsilon}$ are model constants with values 1.30, 1.44 and 1.92 respectively.

2.4.4 Heat transfer

Heat transfer was only solved for the CFB system. In the CFB, the heat balance in the reactor was solved for the solid and gas phases by using the following energy conservation equation for both phases:

$$\frac{\partial}{\partial t}(\alpha_i \rho_i h_i) + \nabla \cdot (\alpha_i \rho_i u_i h_i) = \alpha_i \frac{\partial P_i}{\partial t} + \bar{\bar{\tau}}_i : \nabla u_i - \nabla \cdot q_i + S_i + \sum_{j=1}^{n} Q_{s_j g} \quad (2.26)$$

where Q refers to the volumetric rate of energy transfer and the subscript i used here refers to solid or gas and j=1 refers to the solid phases (catalysts). The volumetric rate of energy transfer between the gas and solid phases is given by:

$$Q_{s_j g} = h_{s_j g} A_{s_j}\left(T_{s_j} - T_g\right) \quad (2.27)$$

where A_s is the interfacial transfer area, T_s and T_g are the solid phases and gas temperatures respectively, and h_{sg} is the volumetric heat transfer coefficient given in terms of the Nusselt number as follows:

$$h_{s_j g} = \frac{k_{s_j} Nu_S}{d_{s_j}} \quad (2.28)$$

where k_s is the thermal conductivity of the solid phase and Nu_S is the Nusselt number given by Gunn correlation as follow [53]:

$$Nu_{S_j} = \left(7 - 10\alpha_{s_j} + 5\alpha_{s_j}^2\right)\left(1 + 0.7 Re_{s_j}^{0.2} Pr^{1/3}\right) + \left(1.33 - 2.4\alpha_{s_j} + 1.2\alpha_{s_j}^2\right) Re_{s_j}^{0.7} Pr^{1/3} \quad (2.29)$$

2.5 Reactor Geometry, Boundary Conditions and Solution Procedure for CFD Simulation

This section gives further insight on the geometries for the project which includes a bubbling and CFB beds for DME adsorption and steam reforming respectively incorporated in a DFB loop system as described in chapter 1. As a result of computational time the DFB system would be investigated separately. The solution procedure to achieve results together with the boundary conditions to define the inlets and outlets from the reactors are explained. The geometries were constructed using SOLIDWORKS, popular modelling CAD software compatible with ANSYS FLUENT. Designed domain were imported into ANSYS for meshing and FLUENT simulation, this similarly has been done by Sharma et al, [54]. The diameter and height for both beds are 3m and 15m respectively. The choice of this is size is made to be close to a commercially proven scale of a CFB reactor (e.g. PYROFLOW CFB system of Goodrich Co in Illinois U.S.A as reported in [4]).

2.5.1 Adsorption reactor (bubbling bed)

In the initial design for the project as described broadly in chapter 1, the fluidized bed suggested was a dual-circulating bed for the adsorption and steam reforming of DME. Preliminary results from an experimental work conducted in a separate Ph.D. project estimated that the residence time of the adsorbent in the fluidized bed was essential in ensuring that the DME is fully adsorbed into the solid [7]. This resulted in the re-evaluation of the fluidized bed design; bubbling bed for the adsorption process was thus considered as it increases residence time.

Geometry design for bubbling bed

Fig. 2.1 depicts the diagram for the bubbling bed. The proposed design is different from most reported bubbling beds that consisted of one outlet for the gas while the solid is retained in the bed. This system has two outlets one for the solid and the other for the fluidizing gas. The outlet for the solid adsorbent was proposed for the removal of adsorbent for the steam reforming process. The fluidizing gas enters from the bottom of the bed, it bubbles the solid already packed in the bed (static bed at 3m height) together with the incoming solid from the side of the bed. The solid adsorbent exits from the side bottom after undergoing chaotic mixing with the fluidizing gas while the gas leaves from the top exit. From the selected bed diameter, the fluidizing velocity was estimated using the industrial sponsor throughput. This velocity was investigated against solids elutriation from the top exit.

A preliminary design consideration on the freeboard, the Transport Disengaging Height (TDH) was calculated using empirical correlation from literature. TDH is the freeboard height beyond which the entrainment rate of solid particles does not change significantly[55]. Though the bed dimension was from an existing industrial scale fluidized bed, the TDH was estimated to understand the possibility of elutriation of solid particles from the bed. The empirical calculation was that of George and Grace [56], as seen in equation 2.30.

$$TDH = 18.2 d_{b_i} \tag{2.30}$$

where d_{b_i} is the bubble diameter estimated to be 0.41m/s (see chapter 4 for detail calculations).

The evaluation of the equation above gives the freeboard height of 7.5m. This suggests that above this height the entrainment of solid particles is significantly reduced, thereby reducing the elutriation of solids from the bubbling bed. This is an empirical estimation and due to the differences in the conditions for this study and for the correlation, the elutriation of solid particles was tested by running various simulations to ensure solid entrainment was avoided.

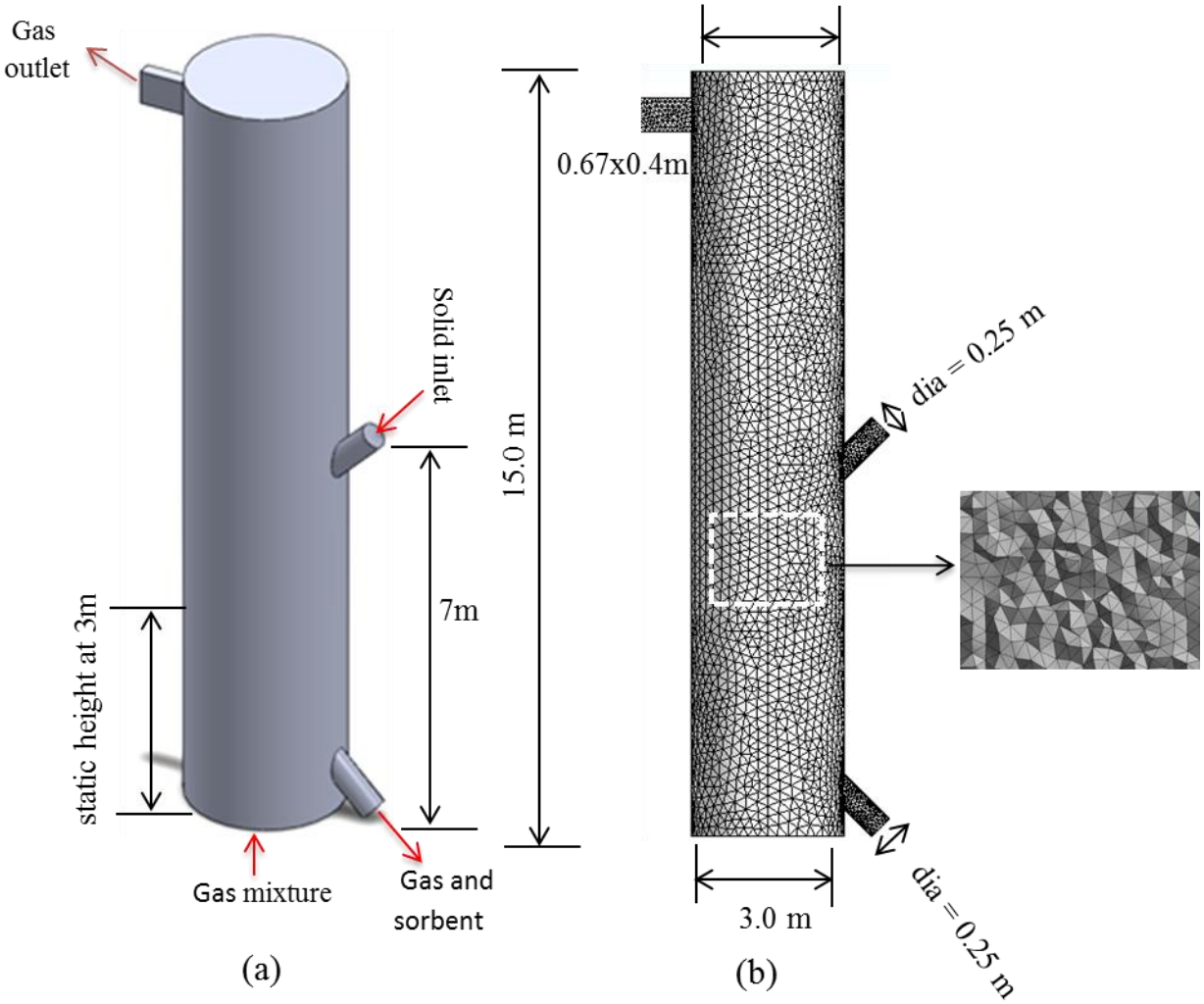

Fig. 2.1: Bubbling bed for adsorption process (a) diagram from SOLIDWORKS (b) diagram after meshing in ANSYS with a cross section plane showing elements/cells.

2.5.2 Steam reforming reactor (CFB)

In the steam reforming reactor, steam and DME in the presence of a catalyst undergoes catalytic reaction with the production of a hydrogen-rich gas. In the design of the unit from the already

discussed DFB system in chapter 1, the initial emphasis was on designing a reactor to validate kinetic DME-SR models in an established industrial scale reactor. Then depending on the conditions of the industrial specification, the DME-SR reactor could then be re-designed to facilitate the industrial sponsor DFB system.

Geometry design for CFB

Fig. 2.2 shows the geometry for the DME steam reforming process in CFB. The riser is equipped with three openings; at the bottom for introducing the fluidizing steam, at the lower part the wall through a 45^{o} inclined inlet for catalyst and DME feed and at the top part of the wall for the exit of the spent catalyst and product gases. Steam is used to produce hydrogen and other product gases. In the proposed concept, DME attached onto the solid adsorbent from the bubbling bed enters together with solid catalyst for the reactions to proceed.

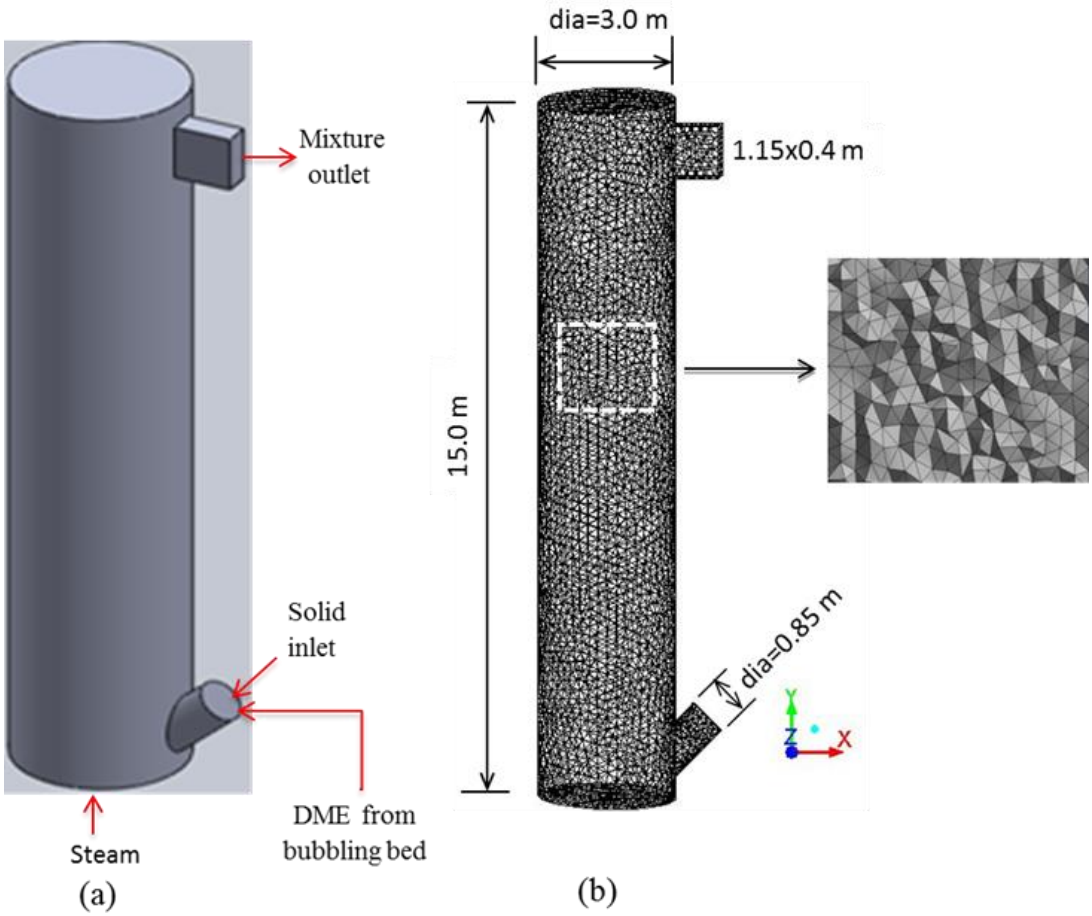

Fig. 2.2: CFB geometry (a) trimetric view and (b) mesh showing a section of elements.

2.5.3 Boundary conditions and solution procedure

The outlet of the reactors (CFB and bubbling bed) was set to "pressure outlet", which ensures the conservation of mass in an open boundary. The boundary for all the inlets into the reactors were set to mass flow except the bottom of the bubbling bed geometry which was set to velocity inlet.

In specifying the thermal boundary conditions, the reactor wall was treated as adiabatic, i.e. no heat flux. In the solution of the model equations, no-slip wall condition was assumed for the gas phase and a slip velocity and granular temperature was specified for the solid phases. The interaction of the solids with the wall was considered by using Johnson and Jackson [57] boundary condition given by the following equations;

$$u_{s_i,w} = -\frac{6\mu_{s_i}\alpha_{s_i,max}}{\sqrt{3\theta_{s_i}}\pi\varphi\rho_s\alpha_{s_i}g_{0,s_i}}\frac{\delta v_{s_iw}}{\delta n} \tag{2.31}$$

$$\theta_{s_i} = -\frac{k_{s_i}\theta_{s_i}}{\gamma_w}\frac{\delta\theta_{s_iw}}{\delta n} + \frac{\sqrt{3}\pi\varphi\rho_s\alpha_{s_i}v_{s_iw}^2 g_{0s_i}\theta_{s_i}^{\frac{3}{2}}}{6\alpha_{s,max}\gamma_w} \tag{2.32}$$

where e_{s_i} is the particle-wall restitution coefficient and φ is the specularity coefficient, which is the fraction of collision of particles that transfers significant amount of particle lateral momentum to the wall

Time-Step

A time-step is the time it takes for the CFD code to complete one iteration. A rule of thumb for determination of appropriate time step using equation (2.33) was used. The left hand side of the equation represents the time step, while the right hand side of the equation represents bed diameter divided by gas and solid velocities. The computation of right hand side was 0.01. This was the reason of selecting 0.001s time step for better accuracy as also reported in literature for stability and convergence [4,58].

$$\Delta t < {\Delta x}/{(u_g + u_s)} \tag{2.33}$$

For the solution procedure in the simulation, the domain was spatially discretized into a finite volume using first order upwind scheme. The various equations for the multiphase flow was coupled using phase couple SIMPLE algorithm which is under the pressure-velocity coupling scheme. In order to avoid divergence during simulation of reactive cases, the UDFs were implemented after some hydrodynamic iteration. Accuracy of results was ensured by ignoring the first 5 seconds of simulations and taking the time average results after system attained steady state. Table 2.3 is a list of some of the selected boundary and solution conditions selected for all the simulations for this work while Table 2.4 shows the operating conditions for the investigation. The selection of adsorbent MOL4A and its particle size was based on analysis of a separate PhD work [3,7]. The selection of the wall-particle and

restitution coefficient was taken according to previous work conducted by Makkawi et al [59] and the particle-particle restitution was according to work conducted by Benzarti et al [51].

Table 2.3: The parameters used in the model solution

Parameters	Parameters value
Drag model	Syamlal-O'Brien
Gas wall conditions	No Slip
Specularity coefficient, $\emptyset$ (-)	0.5
Wall-particle restitution coefficient, $e_{s,w}$ (-)	0.8
Particle-particle restitution coefficient, e_s (-)	0.9
Solution time step (s)	0.001
Maximum number of iterations (-)	20
Solution convergence criterion (-)	10^{-3}

Table 2.4: Operating conditions for the bubbling bed

Parameters	Operating condition
Gas superficial velocity	0.48 m s^{-1}
Temperature	25 ^{o}C
Adsorbent (Mol4A)	
Particle size	350 µm
Density	720 kg m^{-3}
Flowrate	20 kg s^{-1}
Gas mass fraction	
DME	1%
MeCl	99%
Pressure	1bar

2.6 Mesh

Meshing method employed was tetrahedral patch conforming which helps to divide the domain geometry into tetrahedral shaped cells, the edges and faces of the model were refined to enhance the solver calculations in these regions. The mesh quality was checked using skewness (see Table 2.5) and aspect ratio. Maximum skewness closer to one signifies there is much deviation from the ideal tetrahedral cell size while closer to zero signifies less deviation. Aspect ratio is the ratio of longest side of the element to the shortest side. It is recommended that maximum aspect ratio less than 40 is good for fluent simulation according to [41].

Table 2.5: Skewness guide from FLUENT[41]

0-0.25	0.25-0.50	0.5-0.80	0.80-0.95	0.95-0.98	0.98-1.00
Excellent	Very good	Good	Acceptable	Bad	Inacceptable

2.6.1 Mesh analysis for Bubbling and CFB bed

In the mesh analysis, the solid inlet and outlet were removed to study just the expansion of the solid at selected fluidizing velocities. For the investigation of other hydrodynamic features of the system the solid inlet and outlet were reinstalled to investigate gas-solid interactions.

Selected features in the hydrodynamics of the fluidized bed were examined against different mesh elements to investigate the impact mesh sizes have on the accuracy of the results from FLUENT. Mesh refinement enable the CFD codes to solve relevant equations in detail, mesh with more elements are usually considered. However due to computational time required, the study will enable appropriate selection of the mesh refinement that will not compromise accuracy while effectively reducing computational time.

Four different mesh sizes as listed in Table 2.7 were investigated with the same fluidizing velocity to check impact on results. The smaller the mesh size the higher the number of elements or cells in the computational domain. The element size was obtained by maintaining the maximum face size and maximum size in order to keep all the element sizes the same at the selected mesh sizes. Exception was the edges where FLUENT uses the span angle to evaluate the sizes of these regions. The parameters selected in the setting of the mesh are in Table 2.6.

Table 2.6: Some selected parameters for mesh

Physics preference	CFD
Solver preference	FLUENT
Advance size function	Curvature
Span angle centre	Fine
Relevance centre	Medium

The curvature selected for the advance size functions enables the creations of finer meshes around the edges of the domain which provides better results around these areas.

Table 2.7: different mesh properties for mesh analysis

Mesh	Elements	Nodes	Max. Skewness	Max. Aspect ratio	Mesh size (m)
1	117,000	22,375	0.81	9.34	0.2000
2	211,000	38,529	0.83	11.49	0.1650
3	400,000	71,693	0.83	10.02	0.1330
4	1,830,000	317,833	0.84	11.54	0.0800

There are some work that have been done with MFIX (Multiphase Flow with Interphase exchange) code that suggested that for a selected particle diameter, the mesh size should be about ten times the particle diameter [36,60]. Applying this rule of thumb to the geometry for a selected particle size of 350μm will require a mesh size of 0.0035m which is approximately mesh number 4 in Table 2.7 divided by 23. This grid size created mesh with millions of cells that the computer processor could not accommodate and hence crashed. This concludes that an industrial computer system will be required for such rule to apply for the geometry selected for this project.

Solid volume fraction distribution and the mean pressure along the axial bed height were two parameters investigated for the different meshes selected. This provides platform to analyse the impact of mesh refinements to hydrodynamics results, these are seen in Fig. 2.3 and Fig. 2.4 respectively. The bed was initially packed with solid to a height of 3m.

Fig. 2.3 shows that the finer mesh with 1,830,000 cells predicted lower bed expansion at about 5.70m with denser solid volume fraction at the bottom of the bed compared to the rest of the meshes selected for comparison. The next higher mesh is 400,000 cells which predicted solid expansion at around 6.40m, the remaining meshes 211,303 cells and 117,000cells predicted solid expansion at a height of 6.60m and 6.92m respectively. This means that the meshes with lower number of elements predicted solid volume fraction distribution at higher height along the bed while mesh with higher number of elements predicted lower. General rule of thumb adopted in the creation of mesh for a computational domain will recommend mesh 4 from Fig. 2.4 with highest number of elements for better accuracy of results. However, there is no experimental data to compare this to have a definitive conclusion. Observing the various meshes against predicted height of the solid volume fraction distribution, the difference between meshes with 400,000 cells, 211,303 cells and 117,000cells are not significant. However there is more profound difference when considering the mesh with 1,83,000cells.

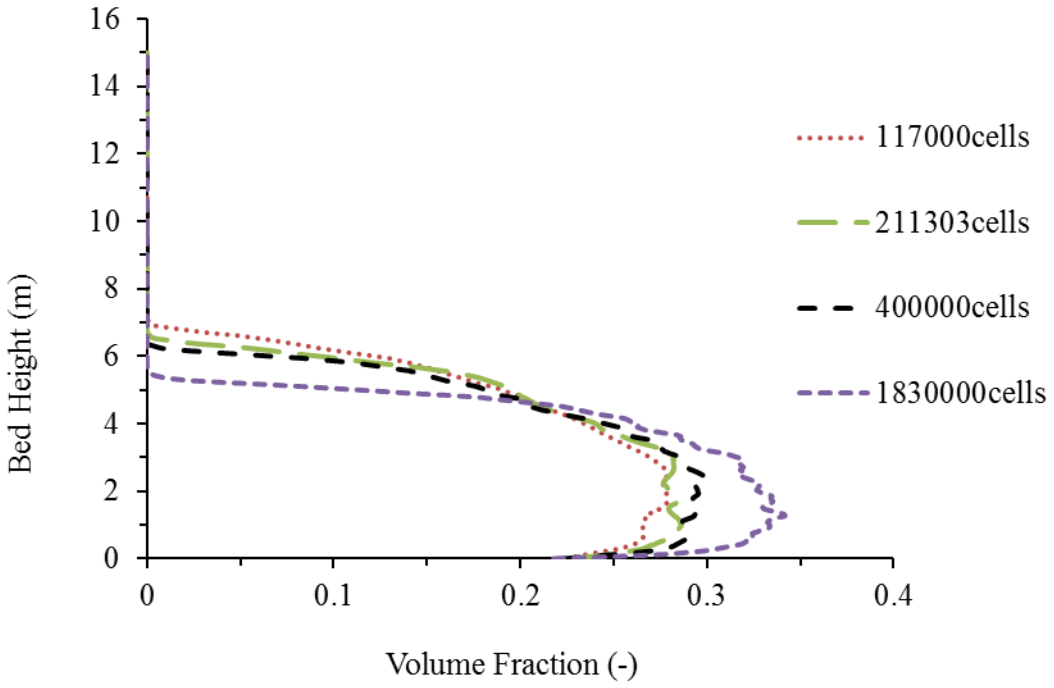

Fig. 2.3: Solid volume fraction distribution along the centre of the bed height for different meshes at simulation time of 40s, initial bed height (H_o) was 3m and fluidizing velocity at 0.48m/s.

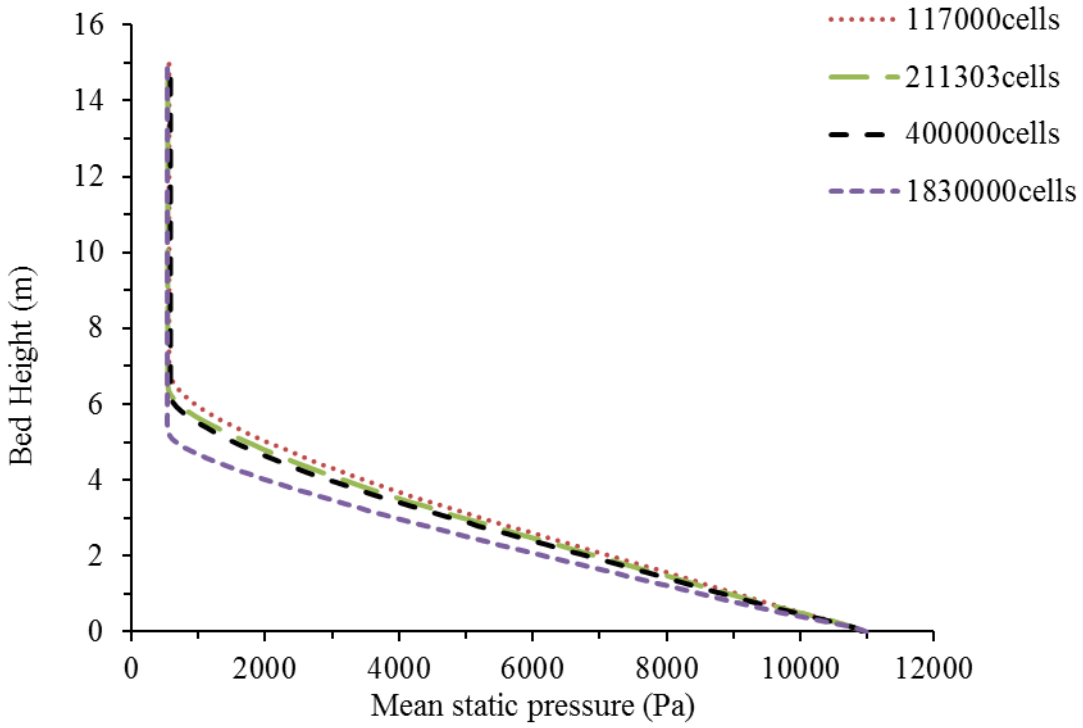

Fig. 2.4: Mean static pressure for the mixture along the centre of the bed at simulation time of 40s for different meshes.

Fig. 2.4 shows the mean static pressure of the mixture along the centre of the bed height. The pressure distribution of mesh with highest number of elements predicted lower bed expansion where there is presence of solids distribution compared to the mesh with lower cells.

Fig. 2.5 shows the time dependent of bed expansion at different simulation times; the bed appears to expand until around 40s. The difference between the expansion at 40s and 50s appear minimal and this justifies the utilisation of 40s simulation time for analysing the effects of the fluidising velocity to the maximum bed expansion. Considering the memory requirement for simulation it is always encouraged to work under shorter simulation time without compromising on the results outcome of the investigation. 30s showed slightly lower expansion in comparison with 40s and 50s. This means from 40s and above bed expansion becomes independent of the simulation time which suggests its attainment of steady state.

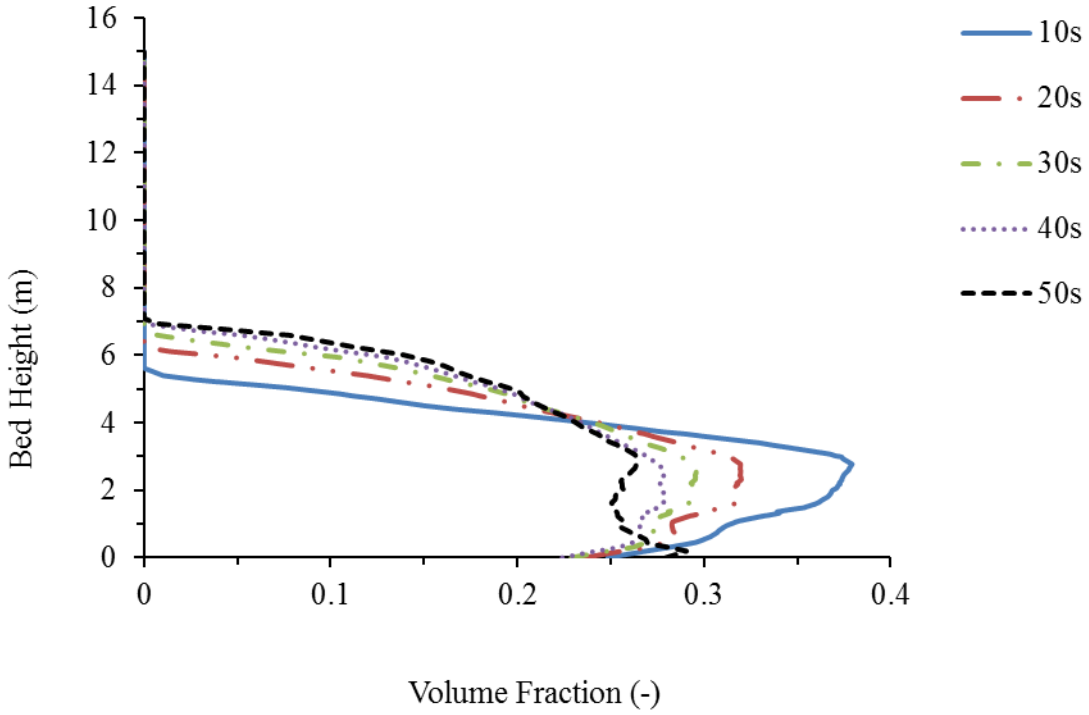

Fig. 2.5: Time average simulation showing effect of various simulation times to the bed expansion at fluidising velocity of 0.48m/s

From the observations, it will be easy to select the 1,830,000 cells as the mesh that will predict more accurate results. The mesh with 117,000cells was selected mainly based on the computational time and insignificant difference between the meshes. From Fig. 2.3 and Fig. 2.4, meshes with 400,000 cells and 211,303 cells were closely matched with 117,000cells for the cases investigated. It will be computationally unadvisable to select mesh with 400,000 cells or 211,303 cells in comparison with 117,000cells as the accuracy of the simulation results will not be significantly affected based on the

meshes investigated. Mesh closer to 1,830,000cells was considered but due to computational time required to run mesh with cells higher than 400,000cells was high, the idea was aborted.

2.7 Residence Time Distribution (RTD)

2.7.1 Introduction

The contact time between gases and solids is essential in the design and optimization of most reactors. A method that could provide details of such mixing in the reactor is the RTD, though it varies considerably with each reactor depending on the reactor design and conditions. In real reactors, flow patterns and conversions are usually difficult to estimate due to the complexity of the flow and chemical reactions involved in the reactor. Residence time distribution of the system facilitates the comprehension of these non-ideal scenarios that shows deviations from ideal reactors. Residence time in fluidized bed systems is complex due to the hydrodynamics and there is no generally accepted method established. Some have used plug-flow models; however in CFD some progress have being made.

In the analysis of an ideal reactor (for example an ideal plug flow reactor), it is usually assumed that materials leaving the reactor spend the same amount of time. This will be inaccurate when considering a real reactor where different atoms of the material entering and leaving the reactor spend different times. This behaviour prompts the utilization of a residence time distribution function in order to completely consider the reactor flow dynamics for reactor performance purpose. CFD has being applied in the determination of the RTD for gas and solid. The approach is similar to the experimental method. Some reports have successfully simulated RTD tracer method using CFD and achieved good agreements with experimental results [61,62]. Table 2.8 and Table 2.9 depict the operating conditions for bubbling and CFB beds for RTD preliminary studies.

Table 2.8: Operating conditions for the bubbling bed

Parameters	Operating condition
Gas velocity	0.48 m s^{-1}
Temperature	25 ^{o}C
Adsorbent (Mol4A)	
Particle size	350 µm
Density	720 kg m^{-3}
Flowrate	20 kg s^{-1}
Gas mass fraction	
DME	1%
MeCl	99%
Pressure	1bar

Table 2.9: The reactor operating conditions used in the simulation

Parameters	Operating condition
Steam	
Inlet temperature	300 °C
Flow rate	5.86 (kg/s)
DME	
Inlet temperature	300 °C
Flow rate	3.0 (kg/s)
Catalyst*	
particle diameter	150 μm (both catalyst)
Density	1300 kg/m3 (CuO/ZnO/Al2O3)
	720 kg/m3 (ZSM-5)
Mass flow rate	200 kg/s (100 kg/s each catalyst)
Reactor dimensions	
Diameter	3.0 m
Height	15.0 m

* *specifies as two separate solid materials: CuO/ZnO/Al_2O_3 and ZSM-5*

2.7.2 Plug flow model for bubbling and CFB beds

In this study, a plug flow model for the determination of the residence time of a reactor will be considered to compare it to the RTD studies. Only the particle residence times for the different beds examined were computed in this model. This model assumes that all particles possesses the same residence time i.e. spends similar amount of time all through the reactor; however this is for perfect plug flow or ideal plug flow. In real reactors, non-ideality is the norm which necessitates the consideration of optimum methods for determining mean residence time. The plug flow model is not accurate for fluidised beds; this is because of the assumptions of the plug flow model which neglects axial mixing. The mean residence time of particles in the plug-flow model is given as [63];

$$\bar{t_R} = \frac{W}{F_o} \tag{2.34}$$

where $\bar{t_R}$ mean residence time, W is the weight of the solid (kg) in the bed and F_o is the solid feed mass flowrate (kg/s)

2.7.3 Particle residence time bubbling bed

Equation (2.35) was amended to accommodate the maximum bed expansion and bed average volume fraction. Maximum bed expansion (see chapter 4) and mean solid volume fraction which was 0.22

obtained from FLUENT were used in determining the particle mean residence time for the solid in the bubbling bed. This was calculated as follows;

$$\bar{t_R} = \frac{W}{F_o} = \frac{\pi \times d^2 \times H_{max} \times \rho_s \times \varepsilon_s}{4 \times F_o} = \frac{\pi \times 3^2 \times 6.92 \times 0.22 \times 720}{4 \times 20} \quad (2.35)$$

$$= 387.4s$$

where H_{max} maximum bed expansion, ε_s average volume fraction of solid in bed, ρ_s molecular sieve 4A (MOL4A) density (kg/m^3), d is the bed diameter (m), F_o solid feed rate time (kg/s), d diameter of the bubbling bed.

2.7.4 Particle residence time CFB

For the selected case for the CFB bed, a plug flow model for the particle residence time was estimated as seen in equation (2.36).

$$\bar{t_R} = \frac{W}{F_o} = \frac{\pi \times d^2 \times H \times \rho_s \times \varepsilon_s}{4 \times F_o} = \frac{\pi \times 3^2 \times 15 \times 0.009 \times 720}{4 \times 100} \quad (2.36)$$

$$= 6.87s$$

where H bed height, ε_s average volume fraction of solid in bed, ρ_s zsm-5 density (kg/m^3), d is the bed diameter (m), F_o solid feed rate (kg/s), d diameter of the bubbling bed

2.7.5 RTD tracer methods bubbling and CFB beds

The typical behaviour of the mixing that occurs in a chemical reactor is captured in the RTD of most reactors. The RTD performed for continuous stirred tank reactors (CSTR) has a closer relationship to the RTD in fluidised beds as a result of the similarity in the intense and chaotic mixing observed in both reactors. Axial mixing is accounted in this method which makes it suitable for fluidized beds.

RTD is usually determined experimentally through the injection of a tracer, a chemically inert material from the inlet of the device at time t=0 and then the concentration of the tracer exiting the reactor measured as a function of time. There are two methods of injecting tracers namely pulse and step input.

Pulse input involves injecting the tracer into the feed stream inlet in a short a time as possible then the outlet concentration of the tracer monitored over time to derive a C-curve. In the simulation, the tracer was enabled for one iteration and then disabled. The concentration of the inserted tracer leaving from the outlet was then monitored [64].

The step input involves injecting a constant amount of tracer at the feed stream inlet continuously while the exit concentration is monitored until the same amount of feed is extracted from the effluent then the process is stopped [64]. In the simulation for this method, the tracer is enabled at the inlet then the outlet concentration of the tracer monitored. The tracers for this study were achieved by

creating a replica of the material (gas or solid) to be investigated in order to maintain the same characteristics. From preliminary simulation results both methods yielded similar results, which meant any of the method could be adopted depending on the difficulty of the simulation set-up.

2.7.5.1 Tracer RTD for solid distribution in bubbling bed

The residence time of the solid in the bubbling bed is essential in adsorbing DME from the gas mixture, longer contact time in the bubbling would increase the diffusion of the DME molecules to the adsorbent [7]. Emphasis was on the particle residence time and hence only this was considered in the RTD study.

The step method was used in the determination of the particle residence time distribution due to the multiple exits of the bed. For the simulations, the tracer which has the same properties as the solid or gas was injected into the selected case that had reached steady state. The species equation was then enabled and the tracer mass fraction was set to 1. An area weighted-average of the exit stream of the tracer was monitored which measures the exit concentration of the tracer until the exit concentration was equal to the inlet concentration. The curve obtained from this method is the non-dimensional cumulative distribution curve (F-curve) (see Fig. 2.6) which goes from 0 to 1, however due to computational time simulation was stopped after reaching 1200 simulation time, this took about a month. The initial concentration of the tracer at the inlet was 1.8 kmol/m^3. The F-curve is obtained by evaluating the F(t) using the equation (2.38), the concentration of the outlet which was a function with time was divided by the initial concentration of the tracer.

$$F(t) = \frac{C_t}{C_0} \tag{2.37}$$

where C_t is the concentration of the tracer exiting the bed and C_0 is the initial concentration

The mean residence time is derived as deduced from equation (2.38), see section 2.7.5.2 for further insight in the mean residence time evaluation The area under the curve of the evaluated function (1-F(t)) was estimated as the mean residence time of the solid in the bubbling bed which was ~600s. This value could have slightly increased if simulation was continued to reach a F(t) curve maximum of 1. This result is significantly higher than the plug-flow model which suggests a huge deviation from an ideal reactor estimation of residence time of the particle for the bubbling bed system. The increase will be attributed to consideration of the chaotic mixture which includes the axial mixing that is essential in fluidized bed systems.

$$t_m = \int_0^\infty tE(t)dt = \int_0^\infty \big(1 - F(t)\big)\, dt \tag{2.38}$$

Fig. 2.6 shows the normalised response to the tracer input into the system measured at the solid outlet of the bed. If the exit concentration reached the input amount then the maximum F(t) would be 1.

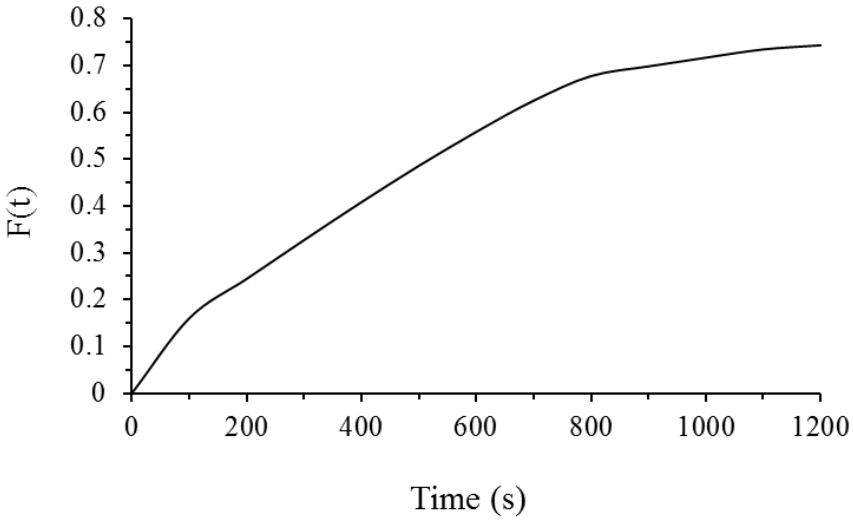

Fig. 2.6: Cumulative distribution curve, F (t)

Fig. 2.7 depicts the cumulative curve representing the fraction of the effluent leaving the bubbling bed for longer than the time t. Its area under the curve is the mean residence time of the particle.

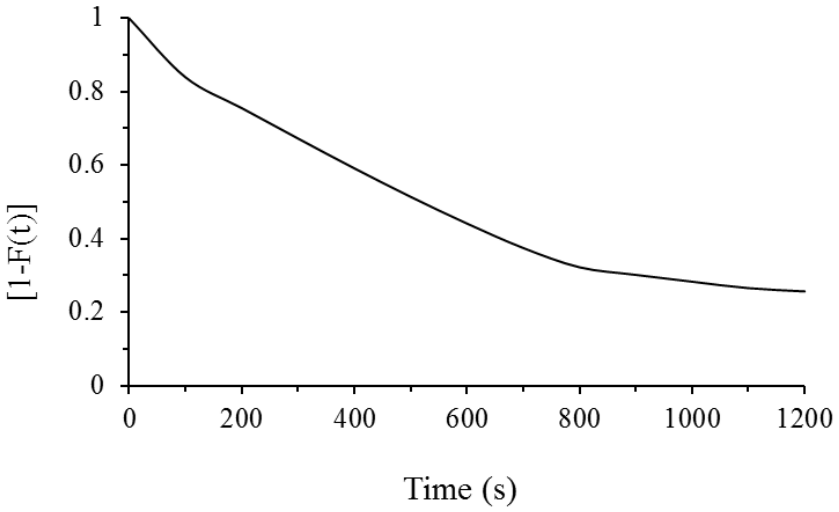

Fig. 2.7: Cumulative distribution curve for fraction of effluent in the bed longer than time t

2.7.5.2 Tracer RTD for gas and solid distribution in CFB Bed

Residence time in this section was achieved using pulse input method. For the simulations, the tracer which has the same properties as the solid or gas was injected into the selected case that had reached steady state. The species equation was then enabled and the tracer mass fraction was set to 1 at time t=0 for one time step and then disabled by setting it back to 0 for subsequent simulation times. An area weighted-average of the exit stream of the tracer was monitored which measures the exit concentration of the tracer. The tracer exit concentration produces a C-Curve which then needs to be correlated to a quantity called E (t). E (t) is a residence-time distribution function.

This function describes how much different particles or materials spend in the reactor; it is also regarded as the fraction of the tracer that has spent between t and t + dt inside the reactor. The integral of the E (t) eventually becomes 1 when all the materials have exited from the reactor. The inlet concentration of the tracer takes the form of a Dirac delta function and produces the relevant exit concentration of the tracer from the reactor. There are two important equations that are used for this method; these are equations (2.39) and (2.40).

$$E(t) = \frac{C(t)}{\int_0^\infty C(t)dt} \tag{2.39}$$

where E (t) is the fraction of the particles that spends between t and dt in the reactor, C (t) is the exit concentration of the tracer from FLUENT simulation and the denominator in equation (2.39) is the area under the curve of the plot between C (t) against time (t).

$$t_m = \int_0^\infty tE(t)dt = \frac{\int_0^\infty tE(t)dt}{\int_0^\infty E(t)dt} \tag{2.40}$$

where t_m is the mean residence time of the material which is the area under the integral in graphical method for the determination of t_m, when all the material leaves the reactor the integral of E (t) ($\int_0^\infty E(t)dt$) becomes 1and forms the basis for the derivation of the mean residence time.

Fig. 2.8 depicts the graph obtained for the estimation of the mean residence time of the feed gas into the CFB. The exit concentration curve appears not to arrive at 0 despite a reasonably long simulation time; this suggests stagnation of some fluid in the bed. From the exit concentration of the tracer, the E(t) curve was established which when multiplied by simulation time (t) produced the curve for the mean residence time. The area under the curve in Fig. 2.8 is the mean residence time and was estimated as 4.85s. However this is based on the selected case, if the fluidizing velocity was changed this apparently has significant effect on the residence time according to [65,66]. The authors' states that the increase in fluidizing velocity shortens the residence time of the gas in the reactor because the gas hold up is decreased. It was also discovered that the spread of the residence time distribution increases with increasing gas velocity. This means at lower gas hold up, the gas quickly attains majority of the bed because of rigorous displacement of the solids resulting from intense mixing as the gas velocity is increased.

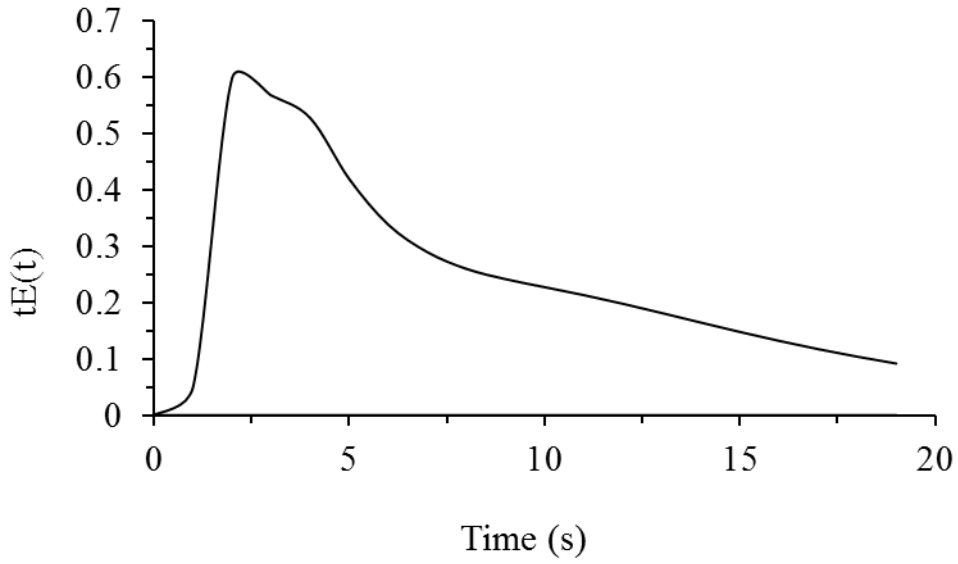

Fig. 2.8: The tE(t) curve used for the derivation of mean gas residence time.

Fig. 2.9 shows the E(t)t curve for the solid residence time of the CFB system. The mean residence time of the solid is derived as described previously for the gas RTD. The estimated mean residence time from the area under the curve in Fig. 2.9 is 5.13s. This is smaller than the computed value for the plug-flow model which could be attributed to hydrodynamics of the CFB particle distribution.

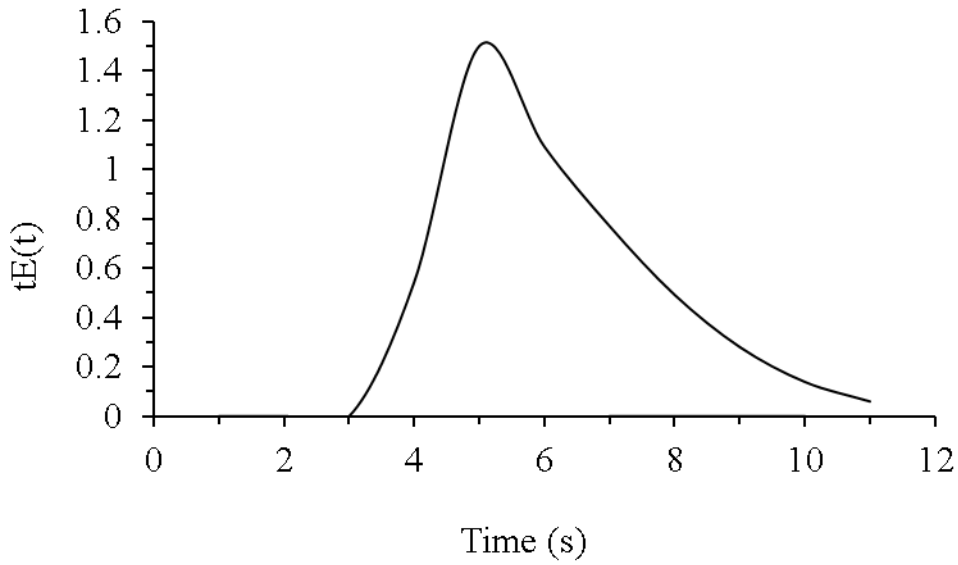

Fig. 2.9: The tE(t) curve used for the derivation of mean solid residence time.

The results for RTD studies for both the bubbling and CFB particle residence time in comparison to the plug-flow model suggests an ideal assumption will be inappropriate for estimating the behaviour of the gas and solid in fluidized bed systems. However, it must be noted that some fluidized bed system depending on the flow conditions such as space velocity and fluidizing velocity may potentially behave like plug flow according to Putten et al. [66]. The author proposed that solid flux had effect on the solid residence time contrary to the fluidizing gas velocity effect on residence time. It further

claimed that the RTD spread at higher solid flux transformed the CFB system behaviour to a plug flow system at shorter gas residence time due to smaller spreads. The reason is attributed to the hold-up which is extensively dependent on the gas velocity. Therefore at constant hold-up (constant gas velocity), increase in the solid flux reduces the residence time of the solids and also its ability to spread around the reactor. Considering the author's analysis it could also be suggested that the particle RTD of the CFB system somewhat behaved like a plug-flow model since the values are reasonably close. This observation is further supported by Andreux et al [61], who suggested that the solid residence time in CFB system tend towards plug-flow.

In the parametric analysis for the CFB system, only the gas phase RTD would be discussed in relation to the reactor performance. Emphasis was on the gas RTD mean residence time as it would provide significant insight in the flow patterns and optimization of reactor design. Solid RTD on the contrary would enable the characterisation of hotspots and identification of unreacted solids [67]. Some of these aspects of solid RTD function would be difficult to analyse with a CFD model in this study.

3. CHAPTER 3: KINETIC MODELLING FOR DME ADSORPTION AND STEAM REFORMING

3.1 Introduction

Chemical reactions are usually associated with the interactions involving different or similar phases in a system; these behaviours are represented using a kinetic model which describes the changes of the various species during the process. In this section, the kinetics considered for the adsorption and steam reforming of DME is presented. The adsorption kinetics has been derived, for the first, from experimental from an experimental work conducted by another member of this project as a separate PhD study, Lad and Makkawi [3,7]. The data analysis and kinetic model development was a joint collaboration with the experimental work conducted by a separate PhD [3]. The experimental analysis confirmed selective adsorption of using MOL4A. The steam reforming kinetics was selected from literatures and then modified to suit modelling purposes.

3.2 Literature Review

3.2.1 Gas adsorption

In gas-solid system, factors influencing adsorption could be categorically different depending on the form of adsorption and structure of the solid surface. Physical and chemical adsorptions are the two different forms that are observed in systems with the surface of the adsorbent been either heterogeneous or homogeneous. Microscopic views of solids show a complex structure that comprises not only exterior surfaces but also internal surfaces due to primary particle aggregation or intrinsic nature of the solid which forms pores. Pores are classified according to their diameter which are micropores with (diameter < 2nm), mesopores with (diameter between 2-50nm) and macroporous (diameter >50nm) [68]. Adsorbents may undergo certain treatments such as thermal heating and impregnation depending on adsorbent type to improve its functionality by increasing surface area or pores available on the surface [69].

Adsorbents are available in different shapes and sizes such as in granules, extruded pellets and formed spheres. Examples of adsorbent include such as silica gel, carbons and molecular sieves (zeolite). In the process of adsorption, the mass of a solid adsorbent exposed to the gas phase at pressure in a closed system increases while the pressure of the gas decreases; this depicts adsorption of gas by the solid. When the system reaches dynamic equilibrium, the mass of solid and corresponding pressure of the gas phase ceases to change. The adsorbate (amount of gas adsorbed by the solid) is determined experimentally by monitoring the increase of the solid weight using spring balance (Gravimetric) or the fall of gas pressure using pressure gauges (Volumetric) or monitoring changes in other parameters such as heat of adsorption [70].

Adsorption for most systems at equilibrium is described by isotherms which use functions connecting adsorbate with the equilibrium pressure and temperature with other parameters being constants. The amount of adsorbate depends on the nature of gas and its pressure, solid and system temperature. It is often referred as dimensionless parameter called relative pressure (P/P^o). This is defined as system pressure divided by vapour pressure of the gas below its critical temperature. Adsorption isotherms are categorised to 5 types according to [71]. The five isotherm curves and their distinctive characteristics are found in Fig. 3.1 and Table 3.1 respectively.

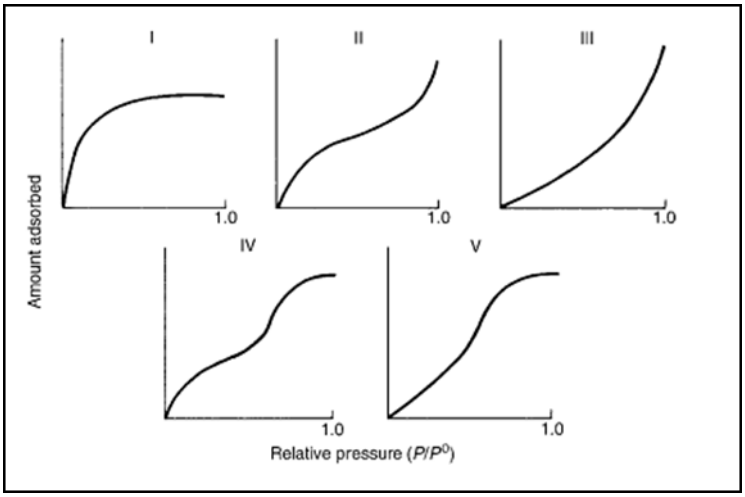

Fig. 3.1: Five types of the adsorption isotherms [72].

Table 3.1: Description of the five different types of adsorptive isotherms [72]

Isotherm Types	Properties
I	Adsorption is completed on a single monolayer on the solid surface. Adsorbent pore sizes are not bigger than the sizes of the adsorbate gases.
II	No limit on adsorption on the solid, multi layers formed due to continual adsorption of the adsorbate after completion of monolayer
III	Show continual increase in adsorption with increasing relative pressure
IV	Behaves like type II isotherm but however, adsorption halts close to where the relative pressure unifies
V	Behaves like type III isotherm at low relative pressure, however at higher relative pressure it reaches a saturation point

Equilibrium adsorption through correlations of isotherms is one of the main methods that has being used to explain the separation mechanism of adsorption, there are others which includes steric and kinetic effects [73]. Steric effects separate materials based on properties peculiar to molecular sieves i.e permits only selective size of a particular particle while kinetic mechanism separates through the

differences in diffusion rates of molecules in the mixture. There are many common isotherms models that are used in the description of single gas adsorption phenomenon, some of these equations are listed in Table 3.2.

- Freundlich model (equation (3.1)) has been applicable for both monolayer and multilayer adsorption, the latter is facilitated by the subjection of the model to a heterogeneous surfaces with uniform energy [74,75]. The model is derived empirically and hence its regarded as not a suitable representation of fundamental description of adsorption [76]. The Freundlich constant (K_f) is an empirical estimation which depends on environmental factors, ($^1/_n$) is the heterogeneity factor and ranges between 0 and 1, with values lower than 1 representing chemical reaction (more heterogeneous surface), values above unity is regarded as physical process and values at unity considered as linear adsorption [74].
- Langmuir isotherm model (equation (3.2)) is the most common model used to describe behaviours of adsorption due to its suitability to different systems, in the formulation of this empirical model, it assumes that adsorption occurs only in a monolayer [75]. In the derivation of the model, the assumptions made for the adhesion of molecules on available sites of the adsorbent includes (i) homogeneous adsorption site (ii) each adsorption site binds an individual molecule (iii) dynamic reversible equilibrium established in the time-frame of the experiment (iv) No interaction between molecules on the surface to alter their adsorption behaviour [77].
- The Toth model (equation (3.3)) is a modified Langmuir model that reduces the error between experimental data and predicted values from equilibrium data, its application its best suited for a multilayer adsorption similar to BET isotherms [78]. The model is applicable to varied systems as its describes adsorption at both low and high pressure limits [79].
- Sips model (equation (3.4)) was proposed to combine Langmuir and Freundlich isotherm models in one equation, the expression sufficiently exhibits a finite limit at relatively high pressure, its regarded that the model predicts accurate behaviour over large range of pressure compared to Langmuir and Freundlich, at low pressure limit it reduce to Henry's Law similar with Freundlich model [75].
- Dubinin-Astahkov model (equation (3.5)) has been applied for the description of adsorption in gas-solid and liquid-solid systems in microporous sorbents, it originated from Polanyi adsorption potential of micropore filling. Dubinin-Raduskevich (D-R) and Dubinin-Astakhov (D-A) are two postulation derived from Dubinin theory, D-R model assumes the m constant (degree of heterogeneity) as seen in Table 3.2 as two while D-A allocates different values depending on the type of catalyst involved. It has also been observed that the D-A model linearizes adsorption data more accurately at varied pressure range compared to D-R model [80]. D-A is suitable when the whole pressure range in the system is considered, at lower

pressure range it is suggested that Henry's law of linear behaviour is not obeyed, this is usually a concern as Henry's law is the foundation of gas adsorption [80,81]. It was recommended that the D-A be utilised for a system that considers the whole relative pressure range between 10^{-5} and 0.8 pa, if the system had only the low pressure range it does not represent the whole micropore filling [80].

Table 3.2: Selected adsorption isotherm models for single gas adsorption

Models	Formula		Reference
Freundlich	$q_e = K_f C_e^{\frac{1}{n}}$	(3.1)	[82]
Langmuir	$q_e = \frac{Q_o b C_e}{1 + b C_e}$	(3.2)	[83]
Tóth	$q_e = \frac{K_T C_e}{(a_T + C_e)^{1/t}}$	(3.3)	[84]
Sips	$q_e = \frac{K_S {C_e}^{\beta_s}}{1 + a_S {C_e}^{\beta_s}}$	(3.4)	[85]
Dubnin-Astakhov	$V = V_0 \exp\left(-\left[\frac{A}{\beta E^0}\right]^n\right)$	(3.5)	[86]

3.2.1.1 Thermodynamic considerations

The utilisation of the appropriate isotherm model is required to correctly predict the behaviour of adsorption in a system. The thermodynamic principles of low and high pressure behaviours is discussed to enable the application of the suitable isotherm model to analyse the experimental data [76]. During adsorption at low pressure, the gas pressure in the gas phase reduces, this reduction continues until it approaches zero. At this level, the isotherm model describing the relationship between the gas and solid phases are expected to behave linearly in analogous to Henry's Law ($q=K_HP$ with K_H Henry's constant). This means that adsorbate can then be estimated using Henry's Law. [87]. Some isotherm models theories of adsorbate contradict this, adsorbate is rather expressed in terms of maximum adsorption capacity which means that adsorbate can only saturate the monolayer only at infinitely high system pressure [76]. It is believed that this expression is in disagreement with Gibbs thermodynamic explanation of gas-solid adsorption. For example, Langmuir model which is limited to low pressures is expressed in terms of maximum adsorption capacity.

3.2.2 Rate kinetics for adsorption

This sub-section examines the literatures on gas adsorption through the medium of kinetic data. This aspect of the literature will provide information on the methods that have been envisaged for the integration of DME adsorption into FLUENT due to the complex nature of the assumed reaction between DME and MOL4A. Kinetic data is usually essential in establishing how effective an adsorption process occurs, it provide invaluable information on the expression of gas uptake by the

solid adsorbent with time through a model in the form of rate equation. These could be beneficial in the design for the adsorption process system.

Kinetics establishes if the reaction is rate determining step, governed by mass transfer or intraparticle diffusion. Some models assume the adsorption rate as the rate controlling step ignoring individual estimation of mass transfer and intraparticle diffusion, however, some models accounts for these other phenomenon [88–90]. It has been considered that adsorption rate could be treated in the same manner as chemical reaction rate [90].

There are several models available to describe the adsorption mechanism which includes pseudo-first order, pseudo-second order, intraparticle diffusion model and elovich model [91–95]. Pseudo-first order and pseudo-second order are the most popular models due to its simplicity and adsorption constant obtained through linear or non-linear regression of batch adsorption data. However these models neglects the diffusion and intraparticle transfer effects of adsorption but considers the global rate constant which incorporates the mass transfer and rate constant in a unified rate [91]. This negligence of diffusion and intraparticle diffusion into the solid pores for pseudo-first and pseudo-second rate equations are a drawback as adsorption is dependent on these mechanisms.

Pseudo-first order

This model was initially introduced by [96] to describe the kinetic adsorption process between liquid and solid phase, the liquid was oxalic and malonic acid while the solid was charcoal. Though it has been applied for gas-solid adsorption, the model is represented as seen below:

$$\frac{dq_t}{dt} = k_1(q_e - q_t) \tag{3.6}$$

where q_t (mol/kg) and q_e (mol/kg) are adsorption capacities at time (min) and at equilibrium respectively, k_1 (min-1) the pseudo-first order rate constant for the model. Integration of equation above under the boundary conditions t=0, $q_t = 0$; t = t , $q_t = q_t$ produces the following linear expression for pseudo-first order model [97];

$$\log(q_e - q_t) = \log q_e - \frac{k_1 t}{2.303} \tag{3.7}$$

From the linear format of the model, $\log(q_e - q_t)$ is plotted against t. the rate constant is derived from the gradient of the graph and the intercept the equilibrium amount adsorbed which is compared to experimental value to determine if the model was a good fit for the experimental work.

Pseudo-second order model

Like the pseudo-first order model, the pseudo-second order model can be represented as

$$\frac{dq_t}{dt} = k_2(q_e - q_t)^2 \tag{3.8}$$

where q_t (mol/kg) and q_e (mol/kg) are adsorption capacities at time (min) and at equilibrium respectively, k_1 (kg mol-1 min-1) the pseudo-second order rate constant for the model. Integration of equation above under the boundary conditions t=0, $q_t = 0$; t = t , $q_t = q_t$ produces the following linear expression for pseudo-first order model

$$\frac{t}{q_t} = \frac{t}{q_e} + \frac{1}{k_2 q_e^2} \tag{3.9}$$

The rate constant k_2 (kg mol-1 min-1) is derived from the intercept of the linear plot of t/qt against t, the inverse of the gradient determines the amount adsorbed at equilibrium which is compared to the experimental value and also utilised in the evaluation of the rate constant.

Intraparticle diffusion model

Adsorption from bulk fluid to available sites on the solid or adsorbent usually involves three steps. The first step involves mass transfer of the fluid to the film on the surface of the solid, the second step is the intraparticle diffusion (involves the diffusion of the gas molecules through the film to the solid surface), the third step is the adsorption of the gas molecules onto the active sites of the solid. This model considers the second step in the overall adsorption rate in a porous media. It is represented in the form below;

$$q_t = k_{int} t^{1/2} \tag{3.10}$$

where q_t (mol/kg) adsorption capacities at time (min), k_{int} is the intraparticle diffusion rate constant (mol kg^{-1}-$min^{1/2}$) and it's obtained from gradient of the plot of qt against $t^{0.5}$

Elovich model

This model is regarded as the kinetic law of chemisorption which was established by Zeldonwitsch, it is used to determine chemisorption kinetics of gasses adsorbed by heterogeneous solids [98]. It is equally treated as rate equation based on adsorption capacities. It is represented in the form below,

$$\frac{dq}{dt} = \alpha e^{-\beta q_t} \tag{3.11}$$

where q_t (mol/kg) adsorption capacities at time (min), α is the initial adsorption rate, a is the chemisorption activation energy. The rate above is integrated to transform it into a linear form as follows;

$$q_t = \frac{1}{\beta} \ln(\alpha\beta) + \frac{1}{\beta} \ln(t) \tag{3.12}$$

Parameters for the initial rate of adsorption and chemisorption activation energy are achieved from the plot of q_t against ln (t).

The pseudo-first and pseudo-second orders are the rate equations that are considered for the simulation purpose. The reason is based on the inability of FLUENT Eulerian model to demonstrate the

intraparticle diffusion to sorbent sites. Elovich model was eliminated because of absence of concentration variable in the equation to monitor the change in the DME flowing in the system.

3.2.3 DME steam reforming

There is an appreciable number of research papers on methane and methanol steam reforming processes, as briefly discussed here. However there is less focus on DME Steam Reforming (DME-SR), particularly in fluidized bed reactors. As far as the author's knowledge, there is not a single publication on experimental or computational modelling of the process in a circulating fluidized bed system. Owing to their superior heat transfer, intensive solid-gas mixing and the potential integration with catalyst regeneration within a closed loop Dual Fluidized Bed (DFB), it could be easily argued that the circulating fluidized bed could be one of the most important technologies for industrial scale hydrogen production.

Numerical investigations have shown the potential of the DFB in carrying out simultaneous reforming reaction, catalyst regeneration and carbon dioxide capture [99–101]. This has been demonstrated for hydrogen production by methane steam reforming where reforming reactions and carbon dioxide capture have been shown to take place in one reactor while the sorbent regeneration is assumed to take place in a second joint reactor, thus forming a continuous flow closed loop system. The DFB system has also been frequently reported as a promising technology for other large scale processes involving solid-gas interactions [4,102].

Experimental studies have also shown that a fluidized bed reactor has a 20% higher conversion efficiency in hydrogen production via catalytic steam reforming of methanol compared to fixed bed reactors [103]. This is mainly due to the advantages of having larger surface contact area, uniform temperature distribution and better control of the gas residence time.

The DME-SR reaction occurs in two main steps: DME hydrolysis and steam reforming of methanol, with the latter being produced from the first step [104–106]. It is this two steps reactions that necessities the use of a bifunctional catalyst to facilitate both reactions. However, depending on the catalyst used and the reaction parameters, some side reactions may occur which include the water-gas shift reaction (WGSR) and DME decomposition reaction [107]. The catalysts that have been frequently reported in DME-SR are alumina or zeolite acid catalyst in combination with metallic copper oxides [105,108–110]. The zeolite components are preferred choice as acid site for the hydrolysis of the DME because it promotes reaction at a lower temperature compared to the alumina [111]. It is understood that the alumina catalyst promotes the reverse WGSR while the zeolites acid site promotes the forward reaction. Hence, the zeolite help in increasing the hydrogen yield by converting the carbon monoxide formed during the process to hydrogen and carbon dioxide [1].

The metal based catalyst $CuO/ZnO/Al_2O_3$ has been commonly reported in methanol steam reforming studies [112–114]. The same metal catalyst, but with an added ZSM-5 zeolite catalyst, has been recently reported in an experimental study of DME-SR [115]. Such a bifunctional catalyst is suitable for achieving very high hydrogen yield with minimum carbon monoxide produced due to presence of WGSR.

Vicente et al [1] studied the effect of operating conditions on DME-SR in a laboratory scale isothermal automated reaction bubbling fluidized bed using $CuO/ZnO/Al_2O_3$+ZSM-5 catalyst . The range of conditions considered were temperature (225 ^oC -325 ^oC), pressure (1.2bar), steam/DME molar ratio (between 3 to 6), partial pressure of DME (between 0.08bar to 0.25bar) and space time up to 2.2 $g_{catalyst}$ h/g_{DME} DME-SR kinetics were not incorporated as it was an experimental study, it was discovered from results analysis that increase in temperature, steam to DME molar ratio, space time significantly increased the conversion and yield of hydrogen. Author reported catalyst deactivation was caused by coking on the copper based catalyst which could be remedied by operating below 325 ^oC.
Feng et al. [116] developed a one-dimensional isotherm plug flow model to model the kinetics for DME-SR and also conducted the experiment work in a fixed bed reactor with bifunctional catalyst $CuO/ZnO/Al_2O_3$+ZSM-5. Parametric analysis conducted for the experiment investigated the impact of steam to DME molar ratio, effect of temperature and effect of space velocity on the process. Results showed that increase in temperature and steam to DME molar ratio increased DME conversion and hydrogen yield while increase in space velocity. The PFR Model adopted for the determination of the kinetics agreed well with the experimental data.

There are different catalysts combinations and compositions that impact the steam reforming process and some works have being conducted to evaluate these. Though the catalyst selected for this project was based on the availability of kinetics on the acclaimed catalysts.
Zhang et al [117] investigated the effects of a novel anodised γ-Al_2O_3 monolithic acidic catalyst for the hydrolysis reaction part of the DME-SR reaction in comparison to the commercialised γ-Al_2O_3. It was observed that the novel catalyst enhanced the conversion of DME compared to commercial γ-Al_2O_3.

Zhang [118] investigated DME-SR in a fixed bed using a mechanical mixture containing HPA/Al_2O_3 acidic catalyst and Cu/SiO_2 metallic catalyst, 100% DME conversion was achieved at 290 ^oC. Takeishi [108] performed an extensive investigation for DME-SR using various catalysts prepared under different conditions. It was found that $Cu/Zn(9/1wt.\%)/Al_2O_3$ prepared by sol-gel method was admirable for the production of hydrogen with less CO content at temperature range between 300-350 ^oC, another catalyst prepared in similar method with excellent hydrogen production at lower temperature was $Cu/Pd(9/1\ wt.\%)/Al_2O_3$.

Hirunsit et al [119] investigated the effects of Cu-spinel-oxide based catalyst ($CuFe_2O_4$, $CuMn_2O_4$, on methanol steam reforming and stream reforming and compared the catalytic performance of the spinel with Cu /ZnO/Al_2O_3. In the DME-SR with γ-Al_2O_3 acid catalyst it was revealed that the Cu-spinel oxide based catalyst performed better than the Cu /ZnO/Al_2O_3, with $CuFe_2O_4$- Al_2O_3 exhibiting the highest conversion of DME and production of hydrogen.

Galivita et al [118] investigated a mechanically mixed HPA/Al_2O_3 acidic catalyst and Cu/SiO_2 metallic catalyst, it was conducted experimentally in a fixed bed reactor and results show achievement of near 100% DME conversion at 290 ^oC

3.3 Derivation of Experimental Data for Mono-Gas Adsorption

The derivation of the rate kinetics for the adsorption of DME onto Mol4A was experimentally determined in a packed bed system conducted on a separate project. The derivation was necessary as the assumed reaction between DME and MOL4A was complex and unavailable from open literature. Kinetic modelling of a process permits the discovery of sorption rate as well as the establishment of a rate expressions characteristic of possible reaction mechanism.

3.3.1 Experimental set-up and adsorption procedure

The experimental set up for analysing the adsorption process was conducted in a batch fixed bed column by [7], as seen in Fig. 3.2. There is currently no experimental work that has been conducted for the estimation of DME adsorption rate in fluidized bed system. The rate obtained from the batch system will be used for the fluidized bed system; hence, the rate derived from the set up will be multiplied by the solid volume fraction to account for the uneven solid distribution in the control volume (Eulerian form) in ANSYS FLUENT.

Adsorption study was conducted via the volumetric adsorption method which consists of five main parts namely gas flow meter, manifold region, digital pressure gauge and adsorption cell (See Fig. 3.2) [7]. The adsorption cell was constructed with 50µm fine mesh at the bottom to support the adsorbent in the cell. The meter connected to the manifold region controlled and measured the gas supplied to the system. A pressure gauge of high precision quality was installed in the manifold line to measure the pressure per second, two thermocouple measured the temperature in the manifold and adsorption cell. A vacuum pump was also installed to create a vacuum particularly before the experiments. The experiments were done in fume cupboard as seen in Fig. 3.2. More details on the experimental set-up and adsorption procedure can be found in [7].

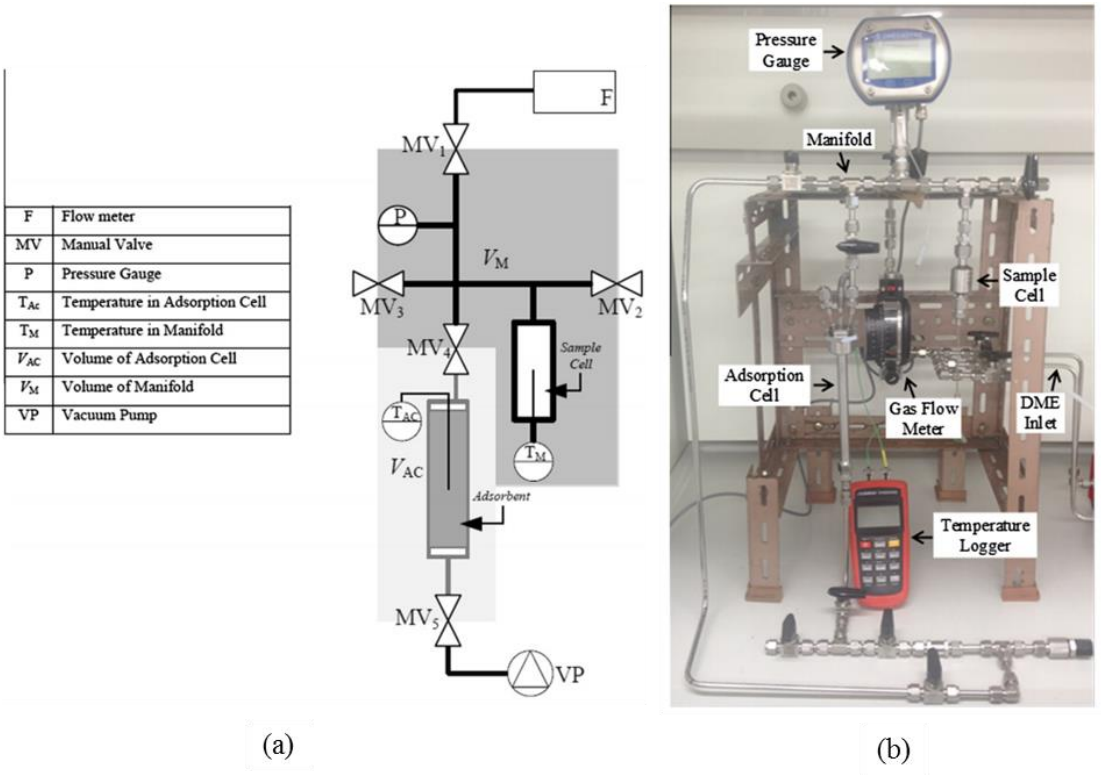

F	Flow meter
MV	Manual Valve
P	Pressure Gauge
T_{Ac}	Temperature in Adsorption Cell
T_M	Temperature in Manifold
V_{AC}	Volume of Adsorption Cell
V_M	Volume of Manifold
VP	Vacuum Pump

Fig. 3.2:(a) Schematic diagram of the manifold and adsorption cell (b) Picture of the adsorption system [7].

3.4 Determination of Rate Constant

From the data obtained from the experimental studies for different conditions of temperature and pressures, the moles of the DME gas adsorbed by Mol4A were analysed. This analysis was essential in order to determine the rate constants associated with pseudo-first and second order reaction.

In the analysis of the data, there were two sets of data that were recorded for the adsorption of DME on the solid adsorbent. The first experiment was based on starting at pressure of 4.0 atm until adoption reached equilibrium. The second set of data was individual runs for selected pressure obtained by successive increment of the pressure until approximately 3.5atm.

3.4.1 Pseudo-first order and Pseudo-second order for data at 4atm

This experimental data was achieved by starting the process at 4.0 atm and 20 ^{o}C condition and as the adsorption proceeded, there was slight reduction in the initial pressure. In Table 3.3, the amount adsorbed over a period of 30 minutes was computed at a given mass of adsorbent of 0.0025kg. From the experimental data, the amount adsorbed was estimated in moles of the gas DME to the mass of Mol4A adsorbent (Q). In FLUENT, the rate kinetics is expressed in a different format with concentration in kmol/m^3. This resulted in transforming the unit from experiment to accommodate FLUENT requirement which is in kmol m^{-3}. In the conversion, the amount of the gas DME adsorbed was re-evaluated by using equation (3.13) to obtain the acceptable unit of the gas concentration for

FLUENT. These converted values are C_{ads} in Table 3.3 and represents the amount of the gas DME adsorbed in the cell onto the solid.

Table 3.3: Pseudo-first order rate evaluation from experimental data

Time (min)	Q (mol kg^{-1})	C_{ads} (kmol m^{-3})	Ln (Q_e-Q) (mol kg^{-1})	Ln (C_e-C_{ads}) (kmol m^{-3})
0	0	0	-0.605	-1.743
5	0.246	0.079	-1.204	-2.342
10	0.281	0.090	-1.329	-2.467
15	0.380	0.122	-1.794	-2.932
20	0.438	0.140	-2.228	-3.366
25	0.466	0.149	-2.530	-3.668
30	*0.546 (*Q_e)	*0.175(*C_e)	-	-

**Initial Concentration of DME was 0.1765 kmol* m^{-3}

$$C\text{onc. DME (kmol m}^3) = \frac{\text{Q} \times \text{mass of the adsorbent (0.0025kg)}}{\text{cell void volume (m}^3) \times 1000} \quad (3.13)$$

From Table 3.3, it can be seen that as the pressure of the system gradually reduces over time, the amount of the gas adsorbed increased. Adsorption continued until attaining 30 minutes (~3 atm) were equilibrium was reached though further adsorption of the gas is possible, this also can be linked one of the characteristics of the Type II isotherm which suggests completion of monolayer to multilayer. This sort of adsorption is familiar with microporous solids with limited porosity which hinders further adsorption when its layers are completely full. Q_e and C_e are concentrations of the gas at equilibrium in mol/kg and kmol/m^3 respectively; these were used in the evaluation of the pseudo-first order and pseudo-second order rate to estimate the rate constants.

In the evaluation of the experimental data against pseudo-first order, the linear plot yielded the rate constant and the graphical equilibrium concentrations for the pseudo-first order. Table 3.4 shows the different parameters obtained from the graphical plot of the data.

Table 3.4: Data evaluated from the graphical plot of the experimental data for obtaining the rate constant for pseudo-first order and pseudo-second order rates

Parameters	Pseudo-first order	Units	Pseudo-second order	Units
C_e	0.163	kmol m^{-3}	0.186	kmol m^{-3}
k_1	0.003	s^{-1}	-	
k_2	-	-	0.016	m^3 $kmol^{-1}$ s^{-1}
R^2	0.983	-	0.900	-

Fig. 3.3 shows the graphical representation of the linear plot of the pseudo-first order for the determination of the rate constant, statistical measure of how the data are fitted to the regression line (R^2) was close to 1 which demonstrates good response to the variability of the data plotted. Table 3.4, shows the different parameters evaluated from the plot and the concentration of DME at equilibrium

obtained as the intercept in the graph was approximately 0.1632 kmol/m^3 which represent approximately 7.5% offset from experimental data. This further demonstrates the accuracy of the linear plot for the determination of the rate constant. The rate constant obtained from the slope of the graph was 0.003/s.

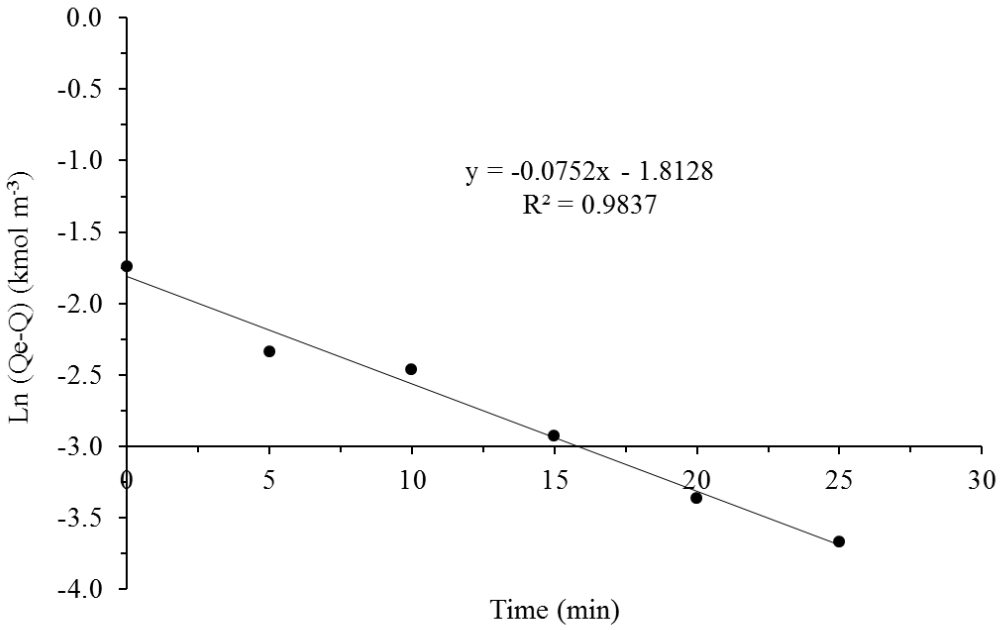

Fig. 3.3: Linear plot of the pseudo-first order rate for the determination of rate constant

Table 3.5 shows the evaluated data from the experiment plotted for the determination of the rate constant for the pseudo-second order, the linear form of the pseudo-second order was applied in the derivation of the plot data.

Table 3.5: Pseudo-second order rate evaluation from experimental data

Time (min)	Q (mol kg^{-1})	C_{ads} (kmol m^{-3})	t/Q (min mol kg^{-1})	t/Q (min kmol m^{-3})
0	0	0	0.00	0
5	0.246	0.079	20.33	63.417
10	0.281	0.09	35.57	110.970
15	0.380	0.122	39.52	123.289
20	0.438	0.140	45.64	142.408
25	0.466	0.149	53.62	167.281
30	*0.546 (*Q_e)	*0.175(*C_e)	54.95	171.456

**Initial Concentration of DME was 0.1765 kmol m^{-3}*

Fig. 3.4 shows the graphical representation of the linear plot of the pseudo-second order for the determination of the rate constant, statistical measure of how the data are fitted to the regression line (R^2) was close to 1 which demonstrates good response to the variability of the data plotted however it was lower compared to the value achieved for pseudo-first order.

Table 3.4, shows the different parameters evaluated from the plot and the concentration of DME at equilibrium obtained as the intercept in the graph was approximately 0.1858 kmol/m^3 which represents 5.3% offset from experimental data, this further demonstrates the accuracy of the linear plot for the data. The rate constant obtained from the slope of the graph was 0.0158 m^3 $kmol^{-1}$ s^{-1}

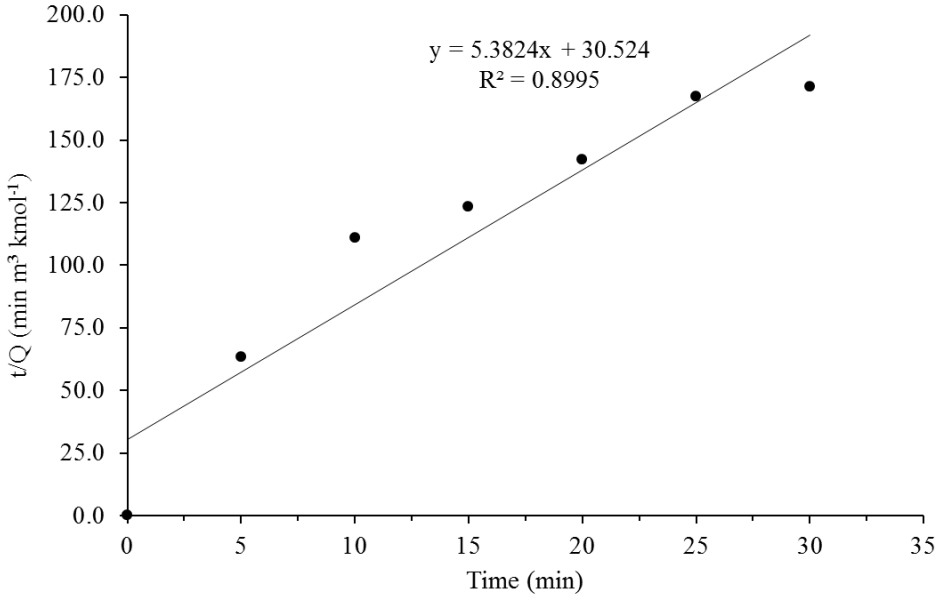

Fig. 3.4: Linear plot of the pseudo-second order rate for the determination of rate constant

Observing the two rates shows a close similarity in the representation of the frequency at which gas DME is adsorbed onto the solid adsorbent, however pseudo-first order due to its higher R^2 value which shows better fitting compared to the pseudo-second order rate for the experimental data was selected for the reaction rate for modelling purposes. This shows that the rate of DME adsorption onto Mol4A was a pseudo-first order rate.

3.4.2 Effect of pressure on rate constant

The second set of experimental study on the rate kinetics was conducted by increasing the pressure in the manifold every 15minutes. Using similar equations for the pseudo-first and pseudo-second orders as previously discussed, the rate constants were determined for each selected pressure. There are some impediments in this set of experimental data, the 15 minutes allotment for adsorption was insufficient for attainment of equilibrium for each pressure however, and the data was reasonably good enough to determine the effect of pressure on the rate constant.

Table 3.6: Rate parameters for both selected rate kinetics for determining rate constants at various pressures

	Pseudo-first order		Pseudo-second order	
Pressure (atm)	k_1 (s^{-1})	R^2	k_2 (kg mol^{-1} s^{-1})	R^2
0.5	0.018	0.890	0.445	0.996
1	0.025	0.977	0.807	0.999
1.5	0.018	0.897	0.783	0.999
2	0.013	0.496	0.819	0.999
2.5	0.014	0.595	0.646	0.999
3	0.015	0.656	0.599	0.999
3.5	0.027	0.646	0.784	1.000

Table 3.6depicts the various rate constants for corresponding pressure for both the pseudo-first and pseudo-second orders together with the R^2. Observing the R^2 for both rate equations, its obvious that pseudo-second order was better fitted to the experimental data compared to pseudo-first order, this suggests that the rate for the adsorption of DME onto Mol4A was a pseudo-second order rate. The rate constants obtained for both rate equations seems to fluctuate as the pressure was increased, though isotherm model suggests that increasing pressure increases the adsorption of the gas onto the solid. In this case studied the rate constant seems not to progressively increase. It could be assumed that the increase in adsorption during the increase in pressure is potentially through other mechanism such as mass diffusion and intraparticle diffusion which is not reflected in the adsorption rate. This aspect of adsorption is neglected in the rate equation [91].

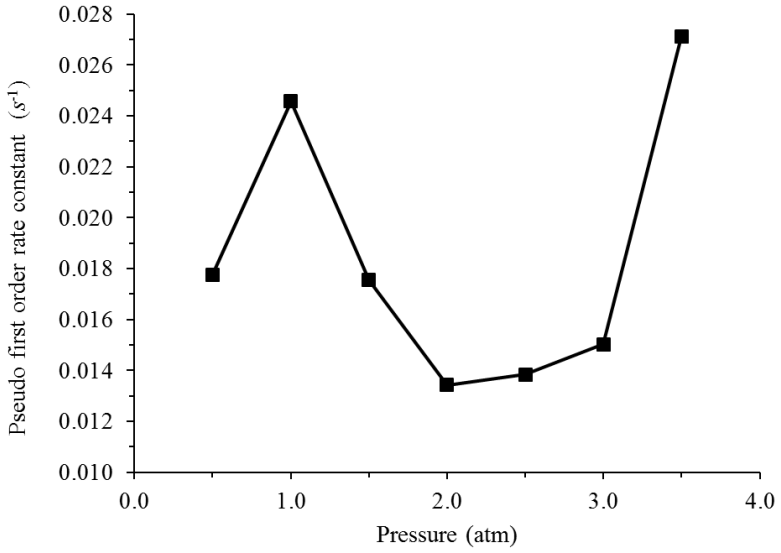

Fig. 3.5: Rate constants for pseudo-first order at different pressures.

Fig. 3.5 shows the graphical representation of the variation observed in the rate constants of DME adsorption onto Mol4A postulated by pseudo-first order rate equation. The low and high ends of the pressure data showed much impact on the rate mechanism compared to rest of the pressure data. Starting from 0.5 atm the rate of adsorption appears to rapidly increase until it reached 1atm where it decreased steadily to 2 atm and remained almost constant till 3atm then shoots up again until 3.5 atm. Between 1 atm and 3 atm it could be suggested that the rate remained unaffected by pressure. There is no clear explanation of this behaviour but rather it can be attributed to pseudo-first order unfittingly representing the data from the experiment and rate constants been unaffected by the change in pressure of the system.

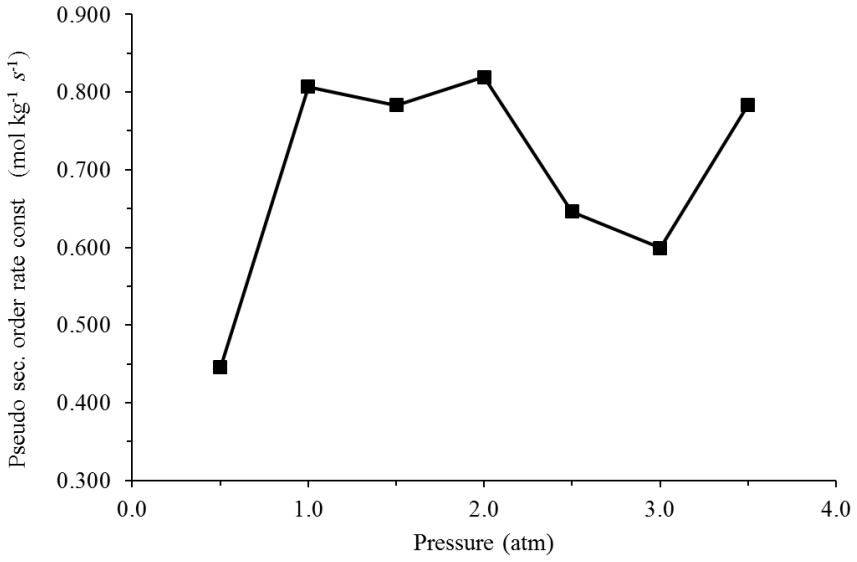

Fig. 3.6: Rate constants for pseudo-second order at different pressures.

Fig. 3.6 shows the effect of pressure on the adsorption of DME on Mol4A for pseudo-second order rate. Low pressure represented by 0.5 atm doubled the rate constant when the pressure was doubled; however the rate constant appears to remain constant or varied slightly from 1atm to 3atm while displaying fluctuating behaviour. Between 3 atm and 3.5 atm the rate increased considerably, these trend were similar to the pseudo-first order rate mechanism. Pseudo-second order fits the experimental data better due to high R2 values (Table 3.6). This demonstrate the applicability of this rate equation in describing the assumed reactive adsorption of DME gas on Mol4A, the effects of pressure remains negligible on the rate constant.

The conclusion drawn from this subsection is that pressure has negligible effect on the rate constants, as the analysed rate constants for each pressure suggested. This evidently, eliminates the utilisation of

this set of experimental data and recommends data from the 4 atm experiment for simulation of DME adsorption on Mol4A adsorbent.

3.5 Proposed Rate Equation for DME Adsorption

Lad and Makkawi [7] in the separate study in relation to this project suggested molecular sieves were more suitable for the process. Molecular sieves 4A (MOL4A) and 5A (MOL5A) were studied with both sorbents showing reasonable adsorption of the gas at a selected condition. MOL5A was observed to have higher adsorptive capacity due to its surface morphology which has a larger pore size compared to MOL4A [7]. Isotherm behaviour for the MOL4A exhibited trends typical to Type II isotherm associated with limited porosity which is characteristic for monolayer to multilayer adsorption, MOL5A displayed a Type I at pressures >1.0atm and III isotherm at lower pressure [7]. Subsequent work conducted in the mono gas adsorption for DME revealed that MOL4A was suitable for almost a complete removal of DME from the mixture. Though this was depending on various conditions in which the gas was subjected to such as pressure and amount of the gas in the system. This resulted in the selection of this type of molecular sieve for this project.

The characteristic complexity nature of the MOL4A makes it highly difficult to simulate in FLUENT Eulerian model as the tool is unable to simulate solid surface morphology, the data representing MOL4A were physical properties. The heat of adsorption or enthalpy obtained from experimental investigation of the adsorption of DME on MOL4A shows that the heats of adsorption was 25.8 kJmol^{-1}. This suggests physisorption binding energy in the attachment of the adsorbate on the sorbent surface instigated by a weak Van der Waals force [7]. However, despite the system being a physical process, an assumed reaction was envisaged for the attachment of the gas to the solid. This rate equation derived will be implemented into FLUENT in the same manner the reactive cases reported in literature were integrated into CFD. The stoichiometric equation involving DME and MOL4A was assumed to interact in this form as seen in equation (3.14).

$$CH_3OCH_{3(g)} + (0.8CaO \cdot 0.2Na_2O \cdot Al_2O_3 \cdot 2SiO_2 \cdot 5H_2O)_s = CH_3OCH_{3(ads)} + (0.8CaO \cdot 0.2Na_2O \cdot Al_2O_3 \cdot 2SiO_2 \cdot 5H_2O)_s \quad (3.14)$$

As there was no reaction in the process, the DME attached to the solid through the Van der Waals force is denoted by the (ads) meaning adsorbed or removed from the bulk DME concentration. There are two rate equations that have been proposed from the observation of the experimental data both based on the pseudo-first order with rate constant as derived from section 3.4.1, simulations will be conducted for both rate equations and results analysed.

The rate kinetics were multiplied by solid volume fraction to get the reaction rate in a control volume (arbitrary volume) which is the form required by FLUENT. There are two proposed rate expressions.

In the first rate expression as seen in equation (3.15), the equilibrium concentration at which adsorbed DME reaches saturation point or completes monolayer to multilayer adsorption was replaced with the DME bulk concentration. This is based on the assumption that at every time t, the amount of DME adsorbed will be in equilibrium with the bulk DME (unadsorbed). So instead of using the equilibrium concentration of DME at equilibrium time t (from Table 3.3), the equilibrium concentration in the bulk at time t is used.

$$\frac{dq_t}{dt} = r_{(ads)_1} = k_1(C_b - C_{ads})\varepsilon_s \tag{3.15}$$

where r_{ads} is rate of adsorption, k_1 rate constant, C_b bulk concentration of DME, C_{ads} concentration of DME on the solid Mol4A (the code was provided by ANSYS customer support) and ε_s solid volume fraction.

$$\frac{dq_t}{dt} = r_{(ads)_2} = k_1\left(C_{fe} - C_{ads}\right)\varepsilon_s \tag{3.16}$$

where C_{fe} is the equilibrium concentration of DME derived from Freundlich isotherm model

For the second rate expression (see Equation (3.16)), Freundlich equation was used in the determination of the adsorbed DME concentration at equilibrium, this enables the estimation of equilibrium concentration of DME at any time in the process regardless of the pressure of the system (0.5atm-3.5atm). [7] suggested that Freundlich model fitted well for the adsorption of DME on Mol4A from experimental analysis this was the reason of using the isotherm model. In the derivation of the Freundlich parameters the experimental data for the incremental pressure was used to enable analysing the behaviour of the gas adsorbed at varied pressure. The parameters were then computed by using MATLAB which assisted in providing parameters that best fits the mathematical Freundlich equation for the experimental data as seen in equation (3.17) [91,93];

$$q_e = KC^{1/n} \tag{3.17}$$

where q_e DME concentration adsorbed at equilibrium is, C is the bulk concentration of DME, K (adsorption capacity) and n (adsorption intensity) are Freundlich constants respectively.

From MATLAB, Freundlich parameters computed were K = 0.46 and n =1.99. n constant depicts the degree of nonlinearity between concentration of the solution. n = 1 means the adsorption is linear, n <1 means that adsorption is a chemical process and if n >1 means adsorption is physical process. Since the derived n for this study was 1.99, this suggest good adsorption and confirms the process was a physical process [120].

Table **3.7** shows the required data for the computation of the Freundlich parameters, the initial concentration of DME in the bulk (C_o) before adsorption by solid sorbent was estimated from the initial number of moles of the gas (n_o). The adsorbed DME at equilibrium expressed in moles of the gas per kg of the adsorbent was converted to kmol/m^3 for each pressure. According to the bulk phase mass balance in a batch adsorption process, the bulk concentration of DME (C_b) is obtained from equation (3.18) [91,95].

$$C_0 - C_b = C_{ads} \tag{3.18}$$

Table 3.7: Experimental data for the derivation of Freundlich constants in MATLAB

Pressure (atm)	n_o (moles)	C_o (kmol m^{-3})	C_{ads} (kmol m^{-3})	C_b (kmol m^{-3})
0.5	0.0007	0.024	0.0061	0.018
1.0	0.0012	0.043	0.0062	0.037
1.5	0.0018	0.064	0.0090	0.055
2.0	0.0024	0.084	0.0096	0.074
2.5	0.0029	0.104	0.0103	0.094
3.0	0.0036	0.126	0.0117	0.114
3.5	0.0041	0.147	0.0117	0.135

The Freundlich model is usually expressed in pressure for gas and in concentration for liquids. Though as FLUENT requires rate kinetics in concentration form, this was converted to suite the CFD model.

Table **3.7** further reveals that the system unattained full equilibrium within the 15 minutes allotted for the experiments. In the data from Table 3.3, the amount adsorbed at equilibrium saturation time was close to the initial concentration of DME gas at the start of the adsorption process. This was different from

Table **3.7**, though the data was used for the Freundlich constant as it best represented the behaviour of the gas adsorbed at different pressure.

3.6 DME-SR Kinetics Selected for this Study

This section will focus on the chemical kinetics for DME-SR process that will be applied for the conversion of adsorbed DME from the bubbling bed to hydrogen and other products. Understanding the kinetics of the catalytic behaviour of DME reforming is a necessary step in determining the conversion of DME reactant to potential products. Currently there is no established reaction mechanism kinetics for the DME steam reforming reaction to produce hydrogen nor reaction condition in which catalyst was neglected [116].

In the review of the literatures for the DME-SR process, the focus was on the two main constitutive reactions kinetics which has been reported in literatures. The proposed reactions and kinetics used in this study have been extracted from various literature sources reporting these two major reactions as well as the additional side reactions, since there is no overall rate kinetics for DME-SR. This includes a hydrolysis reaction converting the DME to methanol and a steam reforming reaction converting the methanol to hydrogen and carbon dioxide, as described below. In order to avoid ambiguous review on the kinetic study due to myriad catalysts available for methanol steam reforming and DME hydrolysis, this literature review will be limited to the most common catalyst reported for DME-SR kinetic which is the bifunctional catalyst $CuO/ZnO/Al_2O_3$-ZSM-5. The metallic copper based catalyst accelerates the reactions for methanol steam reforming and its side reactions while the acidic zeolite catalyst acts on the hydrolysis reaction. Following [112,121,122] and many others, it has been suggested that within the temperature range of 200 °C to 300 °C the copper based catalyst is less subjective to catalyst deactivation and coking whereas ZSM-5 is unaffected by such activity. However this temperature range have been suggested to be within 200 ^oC-350 ^oC [103,114].

The extensively accepted kinetics for the DME hydrolysis is the dehydration of methanol for formation of DME in terms of elementary steps proposed by [123,124], this has been applied by [115,116].

DME Hydrolysis

$$CH_3OCH_3 + H_2O \leftrightarrow 2CH_3OH \qquad \Delta H_r^o = +24.5\text{kJ/mol} \tag{3.19}$$

The second step in the DME steams reforming involves the reaction of the methanol produced from first step to generate carbon dioxide and hydrogen in the presence of copper based catalysts of the form $CuO/ZnO/Al_2O_3$.

Methanol steam reforming

$$CH_3OH + H_2O \rightarrow CO_2 + 3H_2 \qquad \Delta H_r^o = +49.1\text{kJ/mol} \tag{3.20}$$

It has been reported that without this catalyst only methanol is produced whereas with the catalyst, hydrogen and carbon dioxide were major products along with some portion of unreacted methanol and carbon monoxide [110]. The side reactions associated with the methanol reforming includes methnaol decomposition and water-gas shift reaction (WGSR) [112]. These rections are as follows:

Methanol decomposition

$$CH_3OH \rightarrow CO + 2H_2 \qquad \Delta H_r^o = +90\ \text{kJ/mol} \tag{3.21}$$

Water gas shift

$$CO + H_2O \leftrightarrow CO_2 + H_2 \qquad \Delta H_r^o = -41.17\ \text{kJ/mol} \tag{3.22}$$

DME hydrolysis kinetics

The DME hydrolysis rate equation as seen in equation (3.23) was extracted from [115,116], this was based on the reverse reaction elementary steps for methanol dehydration to DME. Feng et al [116] conducted experimental work using similar data from [123,124] due to slight differences in its bifunctional catalyst. They both assumed from their experimental work that the process consisted of four steps as seen in Table 3.8.

Table 3.8: DME formation from elementary steps [123,124]

Step	Elementary steps	Rate or equilibrium parameters
1	$MeOH + H^+ \rightleftharpoons MeOH_2^+$	$K_{pr,MeOH}$
2	$MeOH_2^+ \rightleftharpoons R_1^+ + H_2O$	$k'_{F,R_1^+}, k'_{C,R_1^+}$
3	$R_1^+ + MeOH_2^+ \rightleftharpoons DMO^+$	$k'_{F(DMO^+)}, k'_{C(DMO^+)}$
4	$DMO^+ \rightleftharpoons DME + H^+$	$\{K_{pr(DME)}\}^{-1}$

The net rate of reaction from the steps in Table 3.8 can be written as

$$r_{DME} = r_{DMO^+} = k'_{F,DMO^+} C_{R_1^+} P_{MeOH} - k'_{C,DMO^+} C_{DMO^-} \tag{3.23}$$

From the experimental data, the Protonation of $MeOH$ and DME concentrations from Table 3.8is seen as reaching pseudo-equilibrium such that equations (3.24), (3.25) and (3.26) were proposed.

$$C_{MeOH_2^+} = K_{pr,MeOH} p_{MeOH} C_{H^+} \tag{3.24}$$

where $K_{pr,MeOH}$ is the equilibrium constant for methanol protonation, p_{MeOH} is the partial pressure of methanol, C_{H^+} is the concentration of vacant site on the acidic catalyst

$$C_{DMO^+} = K_{pr(DME)} p_{DME} C_{H^+} \tag{3.25}$$

where $K_{pr(DME)}$ is the equilibrium constant for methanol protonation, p_{DME} is the partial pressure of DME

MeOH reaction with the surface of the zeolite catalyst produces a surface methoxy which then further reacts with MeOH to form DME. Concentration of the surface methoxy ($C_{R_1^+}$) is given in a relation to C_{H^+} in equation (3.26) in a pseudo-steady state balance.

$$C_{R_1^+} = \eta'_{R_1^+} C_{H^+} \tag{3.26}$$

Where $\eta'_{R_1^+}$ ratio of concentration of surface species *i* to that of acid site

$$\eta'_{R_1^+} = \frac{k'_{F,R_1^+} K_{pr,MeOH} p_{MeOH} + k'_{C(DMO^+)} K_{pr(DME)} p_{DME}}{k'_{C,R_1^+} p_{H_2O} + k'_{F(DMO^+)} p_{DME}} \tag{3.27}$$

Incorporating equations above the net rate of DME elementary steps can be re-written as

$$r_{DME} = C_{H^+}\left[\left(\frac{k'_{F,R_1^+}K_{pr,MeOH}p_{MeOH} + k'_{C(DMO^+)}K_{pr(DME)}p_{DME}}{k'_{C,R_1^+}p_{H_2O} + k'_{F(DMO^+)}p_{DME}}\right)k'_{F,DMO^+}P_{MeOH} - k'_{C,DMO^+}K_{pr(DME)}p_{DME}\right] \quad (3.28)$$

In the determination of the rate constants and equilibrium constants, [123] introduced a mean temperature (T_m) to reduce the correlation between pre-exponential factors and activation energies to perform reparametrization. Vacant site for the catalysts (C_{H^+}) was taken from Feng et al. [116].
From the normal Arrhenius form of the rate coefficient

$$k_i = A_i exp\left(\frac{-E}{RT}\right) \quad (3.29)$$

Re-parametrization changes the Arrhenius form to;

$$k_i = exp\left[\left(\ln A_i - \frac{E_i}{RT_m}\right) - \frac{E_i}{R}\left(\frac{1}{T} - \frac{1}{T_m}\right)\right] \quad (3.30)$$

A_i is the parameter for pre-exponential factor of elementary step, E_i activation energy of the reaction step the definition of the parameters of the kinetic model for rate and equilibrium constants can be seen in Table 3.9

Table 3.9: Parameters for rate and equilibrium constants [116]

Rate constants (r_i)	Definition
r_1	$\Delta S^o_{pr,MeOH}/_R - \Delta H^o_{pr,MeOH}/_{RT_m}$
r_2	$\Delta H^o_{pr,MeOH}/_R$
r_3	$\Delta S^o_{Hyd,R_1^+}/_R - \Delta H^o_{Hyd,R_1^+}/_{RT_m}$
r_4	$\Delta H^o_{Hyd,R_1^+}/_R$
r_5	$\ln A_{c,R_1^+} - E_{c,R_1^+}/_{RT_m}$
r_6	$E_{c,R_1^+}/_R$
r_7	$\ln A_{F,DME} - E_{F,DME}/_{RT_m}$
r_8	$E_{F,DME}/_R$
r_9	$\Delta S^o_{pr,DME}/_R - \Delta H^o_{pr,DME}/_{RT_m}$
r_{10}	$\Delta H^o_{pr,DME}/_{RT_m}$

The rate and equilibrium coefficients of each step were evaluated from [123,124], the mean temperature was estimated to be the average operating temperature from the experimental work in determining the elementary reaction steps for DME formation from dehydration of methanol.

Methanol steam reforming kinetics

For methanol steam reforming, there are various models that have been suggested from literatures based on $CuO/ZnO/Al_2O_3$ catalyst, some of the proposed models are mentioned in Table 3.10. Some selected rate have been expressed as Arrhenius rate as suggested by [121] but this was initially proposed by [125]. Other works that supported the Arrhenius proposed model includes [122,126]. For this work, the rate proposed by [112] was selected.

$$r_R = (1-\varepsilon)\rho_s k_R C_{CH_3OH} \tag{3.31}$$

$$k_R = C_R[A_1 + B_1 \ln \emptyset] exp\left(^{-E_R}/_{RT}\right) \tag{3.32}$$

where ρ_s is the density of catalyst ($CuO/ZnO/Al_2O_3$), k_R reforming rate and C_{CH_3OH} is the methanol concentration, C_R reforming rate constant (5.5), $\emptyset$ is the ratio of steam to methanol (1.1), A_1 and B_1 are Arrhenius constants.

Steam reforming decomposition

Decomposition reaction is one of the side reactions that could occur during steam reforming of methanol produced in the DME-SR process. The selected rate is from [112,127] where a semi-empirical model was formulated.

$$r_D = (1-\varepsilon)\rho_s k_D \tag{3.33}$$

where ρ_s is the density of catalyst ($CuO/ZnO/Al_2O_3$), k_D is the rate constant given as

$$k_D = C_D A_2 exp\left(^{-E_D}/_{RT}\right) \tag{3.34}$$

The values of the Arrhenius pre-exponential constant and activation energy for the methanol reforming and decomposition processes were taken from [113] and decomposition constant C_D from [127] as 5.5.

Water gas shift reaction kinetics

The water gas shift reaction was considered instead of the reverse water gas shift reaction according to [1] as the catalyst for the kinetics for the process utilised was $CuO/ZnO/Al_2O_3$. High temperature shift and low temperature shift water gas reactions are two available reaction types from literature with the LTWGSR favoured at temperatures between 150-300ºC on a CuO/ZnO catalyst while the HTWGSR favoured by iron chromium catalyst at 350-500ºC [128]. Based on the catalyst and condition of the

current study, the LTWGSR will be the assumed side reaction produced from MeOH reforming. The rate equation selected have been proposed by [115,127,128].

$$r_{WGS} = C_{WGS} k_{WGS} \left(p_{CO} p_{H_2O} - p_{CO} p_{H_2} / K_{eq} \right) \tag{3.35}$$

where C_{WGS} is a constant (11.2), k_{WGS} is the rate constant and K_{eq} equilibrium constant

$$K_{eq} = exp\left(\frac{4577.8}{T} - 4.33 \right) \tag{3.36}$$

$$k_{WGS} = 1.74 \times 10^{17} (1 - 0.1540\delta + 0.008\delta^2) T^{-8.5} exp\left(\frac{-35000}{RT} \right) \tag{3.37}$$

where δ is steam to CO molar ratio.

Table 3.10: Some selected rate kinetics for main and side reactions for DME-SR

Steps	Reactions	Rate equation	References
DME Hydrolysis	$CH_3OCH_3 + H_2O \leftrightarrow 2CH_3OH$	$r_{DME} = r_{DMO^+} = k'_{F,DMO^+} C_{R_1^+} P_{MeOH} - k'_{C,DMO^+} C_{DMO^-}$	[115,116]
MeOH-SR	$CH_3OH + H_2O \rightarrow CO_2 + 3H_2$	$r_R = \frac{k_R K^*_{CH_3O}\left(p_{CH_3OH}/p_{H_2}^{1/2}\right)\left(1-p_{H_2}^3 p_{CO_2}/K_R p_{CH_3OH} p_{H_2O}\right) C_{S_1}^T C_{S_{1a}}^T}{\left[1+K^*_{CH_3O}\left(p_{CH_3OH}/p_{H_2}^{1/2}\right)+K^*_{HCOO} p_{CO_2} p_{H_2}^{1/2}+K^*_{OH}\left(p_{H_2O}/p_{H_2}^{1/2}\right)\right]\left(1+K_H^{1/2} p_{H_2}^{1/2}\right)}$	[116]
		$r_R = (1-\varepsilon)\rho_s k_R C_{CH_3OH}$	[112,127]
		$r_R = k_1 C_{CH_3OH}^{0.4} C_{H_2O}^{0.4} exp\left(\frac{-E_a}{RT}\right) - k_{-1} C_{CO_2} C_{H_2} exp\left(\frac{-E_a}{RT}\right)$	[114]
		$r_R = \frac{\eta \rho_{cat} \delta (w+2h+2\delta)}{w} k_0 exp\left(\frac{-E_a}{RT}\right) \times (RT)^{0.09} C_A^{0.26} C_B^{0.03} C_C^{-0.2}$	[121]
		$r_R = k_0 exp\left(\frac{-105\times10^3}{RT}\right) \times P_{MeOH}^{0.26} P_{H_2O}^{0.03} P_{H_2}^{-0.2}$	[121]
MeOH decomposition	$CH_3OH \rightarrow CO + 2H_2$	$r_D = (1-\varepsilon)\rho_s k_D$	[112,127]
		$r_D = \frac{k_D K^*_{CH_3O}\left(p_{CH_3OH}/p_{H_2}^{1/2}\right)\left(1-p_{H_2}^2 p_{CO_2}/K_D p_{CH_3OH}\right) C_{S_2}^T C_{S_{2a}}^T}{\left[1+K^*_{CH_3O}\left(p_{CH_3OH}/p_{H_2}^{1/2}\right)+K^*_{OH}\left(p_{H_2O}/p_{H_2}^{1/2}\right)\right]\left(1+K_H^{1/2} p_{H_2}^{1/2}\right)}$	[116]
		$r_D = k_3 C_{CH_3OH}^{1.3} exp\left(\frac{-E_a}{RT}\right) - k_{-2} C_{CO} C_{H_2O} exp\left(\frac{-E_a}{RT}\right)$	[114]
Water gas shift	$CO + H_2O \rightarrow CO_2 + H_2$	$r_{WGS} = C_{WGS} k_{WGS}\left(p_{CO} p_{H_2O} - p_{CO} p_{H_2}/K_{eq}\right)$	[112,115]
		$r_W = \frac{k_W^* K^*_{OH}\left(p_{CO} p_{H_2O}/p_{H_2}^{1/2}\right)\left(1-p_{H_2} p_{CO_2}/K_W p_{CO} p_{H_2O}\right) C_{S_1}^{T^2}}{\left[1+K^*_{CH_3O}\left(p_{CH_3OH}/p_{H_2}^{1/2}\right)+K^*_{HCOO} p_{CO_2} p_{H_2}^{1/2} K^*_{OH}\left(p_{H_2O}/p_{H_2}^{1/2}\right)\right]^2}$	[116]
		$r_{WGS} = k_3 C_{CH_3OH}^{1.3} exp\left(\frac{-E_a}{RT}\right)$	[114]

Table 3.11: Selected rate kinetics for DME-SR simulation from literature

Steps	Reactions	Rate equations	Reference
DME hydrolysis	$CH_3OCH_3 + H_2O \leftrightarrow 2CH_3OH$	$r_{DME} = r_{DMO^+} = k'_{F,DMO^+} C_{R_1^+} P_{MeOH} - k'_{C,DMO^+} C_{DMO^-}$ Further details of this reaction and the definition of the symbols can be found in the given references)	[115,116,124]
MeOH-SR	$CH_3OH + H_2O \rightarrow CO_2 + 3H_2$	$r_R = (1-\varepsilon)\rho_s k_R C_{CH_3OH}$ where $k_R = = C_R[A_1 + B_1 \ln \emptyset]\exp\left(-E_R/RT\right)$ C_R=5.5 is the reforming rate constant, $\emptyset$ is the steam to methanol ratio, A_1 and B_1 are constants (=1..15 x 10^6 and 9.41x 10^5 $m^3s^{-1}kg^{-1}$ respectively)and E_R= -84100 $Jmol^{-1}$ is the activation energy	[112,113]
MeOH Decomposition	$CH_3OH \rightarrow CO + 2H_2$	$r_D = (1-\varepsilon)\rho_s k_D$ where $k_D = C_D A_2 \exp\left(-E_D/RT\right)$ C_D =5.5 is the decomposition rate constant, A_2 =7.09 x 10^7 mol s^{-1} kg^{-1} is a constants and E_D= -111200 J mol^{-1} is the activation energy	[112,113,129]
Water gas shift	$CO + H_2O \leftrightarrow CO_2 + H_2$	$r_{WGS} = C_{WGS} k_{WGS}\left(p_{CO}p_{H_2O} - p_{CO}p_{H_2}/K_{eq}\right)$ where $K_{eq} = \exp\left(\frac{4577.8}{T} - 4.33\right)$ $k_{WGS} = 1.74 \times 10^{17}(1 - 0.1540\delta + 0.008\delta^2)T^{-8.5}\exp\left(\frac{-35000}{RT}\right)$ C_{WGS}=11.2 is a constant and δ is steam to CO molar ratio	[128,129]

3.7 Implementation of the Kinetic Models in FLUENT

3.7.1 Adsorption model

The adsorption kinetics was implemented in FLUENT using an *in-house* UDF. The concentration of the adsorbed DME was coded as the concentration of the gas on the solid surface. Due to the form of the rate kinetics, the heterogeneous reaction rate in FLUENT was the platform for integrating the assumed chemical reaction together with the built UDF codes.

3.7.2 DME-SR models

The reactions considered for the DME-SR process, given in section 3.3.1, have been implemented in the main computational model using an *in-house* developed UDF. It is assumed that the two main reactions of DME hydrolysis and methanol steam reforming are initiated and accelerated by the bifunctional catalyst $CuO/ZnO/Al_2O_3$+ZSM-5 with the ZSM-5 group acting as the acid site for enhancing the hydrolysis step of the reaction. The catalyst was introduced to the model as two separate solid phases with the same size and mass flow rate but different densities. This procedure allowed the UDF to impose the effects of the acidic and metallic functions separately on the different reaction. All the reactions have been implemented as heterogeneous in order to take into consideration the presence of the catalysts and its spatial variations in concentration.

4. CHAPTER 4: DME ADSORPTION AND PARAMETRIC ANALYSIS

4.1 Introduction

The investigation of the DME removal from the gas mixture is analysed in this chapter by altering the operating conditions. A literature review on the fundamentals and current modelling approach on adsorption of gas is discussed to provide relevant insight on the phenomenon that occurs in the bubbling bed. From chapter 3, the two rate kinetics for the adsorption processes were derived based on an experimental data produced by another PhD study, as part of this overall project. The selected rates kinetics was then integrated as gas-solid heterogeneous reaction in the CFD commercial code, FLUENT. The hydrodynamic behaviour of the bubbling bed was examined against DME removal at different regions of the bed to correlate distribution and collision theories for solid interactions with gas phase and the walls of the bed. The analysis conducted in this chapter is based on the mono-gas adsorption (only DME in the system), this consideration resulted from significant observation of the mixture (DME + MeCl) when subjected to required experimental conditions with molecular sieve 4Å MOL4A as the solid adsorbent. It was seen that mainly DME was removed from the system close to 100% selective adsorption. This evidently prompted the assumption that only DME was in the system for the derivation of the rate kinetics.

4.2 Literature Review

This section of the review has subsections for hydrodynamic and work conducted through CFD to study adsorption behaviour in fluidized beds with emphasis on bubbling bed.

4.2.1 Literature review on bubbling beds hydrodynamics

The study of hydrodynamics is always an important aspect of the design of fluidized bed systems, there are various works that have been done in this area using computational fluid dynamics (CFD) to describe how most fluidized beds system behave.

Cloete et al [130] studied the general behaviour of 2D bubbling bed hydrodynamics using a two fluid flow model. It was observed that low static bed height (0.25m) and large particle sizes (350μm) under-predicted the bed expansion while small particles (150μm) and large static bed height (0.4m) over-predicted the bed expansion. It was assumed that the over-prediction was associated with the formation of slug-like bubbles while the under-prediction was due to slow rising bubbles. It was observed that a large discrepancy was seen between the solid axial velocity profiles from simulation and experiment which was suggested to be due to frictional stresses on the front and back walls which are excluded in a 2D simulation.

Mineto et al [131] investigated the influence of granular temperature in simulation of a gas-solid two fluid Eulerian-Eulerian model in a bubbling bed using an MFIX (Multiphase Flow with Interphase

exchange) code. Simulations were done using partial differentiation equation (PDE) and algebraic expression to implement the granular temperature through the kinetic theory of granular flow (KTGF) in order to analyse the differences between the two models. The two cases presented similar results which suggest that any of the two models could be used to describe the behaviour of gas-solid flow in bubbling beds however it was recommenced to use the PDE for more realistic results with the Jackson and Johnson wall boundary condition.

Taghiour et al [58] conducted an experimental and computational analysis of 2D bubbling bed hydrodynamics to study bed expansion, pressure drop and general flow characteristics using Eulerian model incorporated through KTGF. It was observed that the bed expansion flow patterns and pressure drop from simulation using Syamlal-O'Brien, Wen &Yu and Gidaspow drag models gave reasonable predictions compared to experimental results.

Guan et al [132] investigated the hydrodynamics of an interconnected fluidised bed comprising of a circulating and bubbling beds in a loop system using a 3D two-phase multiphase flow. It was observed that effect of drag model on the hydrodynamics for fluidized systems was significant, Syamlal-O'Brien and Gidaspow drag models both gave good predictions compared to the experimental results. In the bubbling bed, bubbles formed moves upward in the bed, its upward movements continues at increased superficial velocities and leads to the expansion of the bed height due to increased number of bubble and its sizes. Solids volume fraction appeared to be dilute in the centre region but higher in around the walls.

4.2.2 Literature review on CFD modelling of gas adsorption in fluidized bed

Adsorptions of species using a sorbent in a gas-solid system have been performed in numerous occasions by researchers notably in the area of flue gas purification. Most applications which have involved carbon dioxide specie removal from flue gases have been implemented into the CFD code FLUENT as an adsorption rate. A rate equation is often proposed for the removal of carbon monoxide. Several researchers [4,5,29,133] investigated the capture of carbon dioxide in fluidized bed system using a solid sorbent. The adsorption rates were incorporated as a heterogeneous reaction between carbon dioxide and the solids sorbent. In this section, literatures on the simulation of adsorption in fluidized bed systems will be covered, there is currently no published work or data on the modelling of DME adsorption, particularly in fluidized bed systems. The current study is thus unique in this regard.

Ryan et al. [29] focused on the application of multiphase CFD approach in the investigation of a 1kWe solid sorbent carbon capture reactor designed to predict the flow properties of the system. A comprehensive review on the utilisation of multiphase Eulerian-Eulerian and Eulerian-Lagrangian models for ANSYS FLUENT CFD tool and BARRACUDA (computational particle fluid dynamics) were equally conducted. For the purpose of this literature review, only the Eulerian-Eulerian multiphase model for ANSYS FLUENT will be analysed in detail. 1kWe reactor experimental setup is

a fluidized bed loop which consists of a riser section which extends to the to the bottom section of an internal circulating fluidised bed (ICFB) and a regenerator as seen in Fig. 4.1.

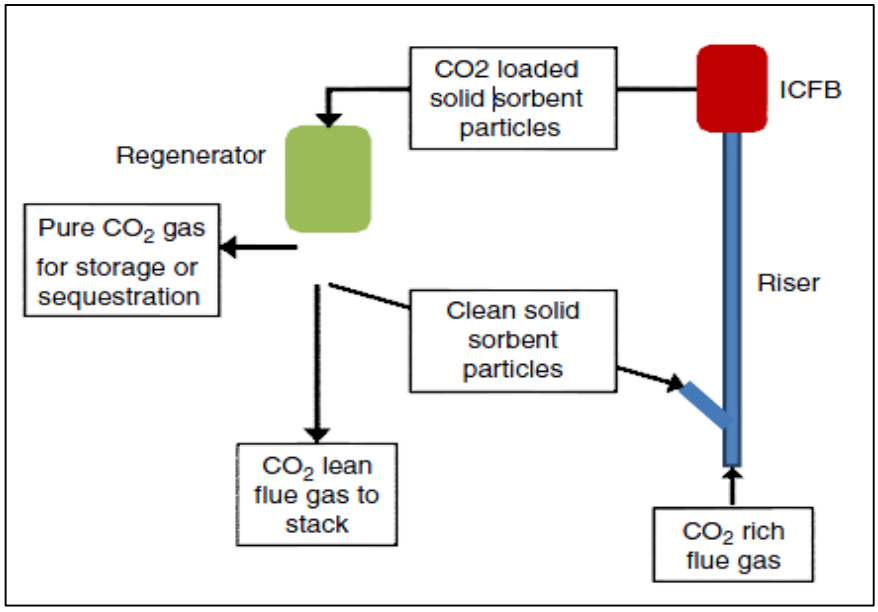

Fig. 4.1: kWe Sorbent carbon capture system extracted from Ryan et al, [29].

From Fig. 4.1, the flue gas mixture containing the CO_2 enters from the bottom of the riser while the desorbed solid sorbent enters through an angled section in the riser upstream of the flue gas inlet; adsorption of CO_2 starts from the riser and continues to the ICFB and continues in the loop system. The mixture exits the ICFB and enters the regenerator where CO_2 is removed by heating with steam, the cleaned solid particles then re-enter the riser. Simulation was only conducted for the riser section which was divided into sections to enable quicker computational time; section with more complexity were modelled in 3D (bottom of riser and ICFB) and less complex in 2D (upper riser section) to improve accuracy of the results, coupling between sections was achieved by using the average output from one section as the input in the next section.

The kinetic model was initially written in terms of site fractions but was converted to mass basis for coding purposes. CO_2 absorption was incorporated into FLUENT as a homogeneous reaction through a user defined function. The dry absorption model was only considered as seen in following equations;

$$R = -\alpha k\left([CO_2][R_2NH]^2 - \frac{1}{K}[R_2NCO_2^-][R_2NH_2^+]\right) \tag{4.1}$$

where α is the volume fraction, k is the forward rate constant and K is equilibrium constant

Forward rate constant:

$$k = AT_sT_gR_g exp\left(\frac{-\Delta H_f}{T_s}\right) \tag{4.2}$$

Equilibrium constant:

$$K = \frac{R_g T_g}{P_{ref}} \, exp\left(\frac{dSdH}{T_s}\right) \tag{4.3}$$

where A is Arrhenius constant, T_s is solid temperature, T_g is gas temperature, R_g is gas constant, P_{ref} is reference pressure.

The hydrodynamic study showed that a mixing zone was established around the angled entrance of the solid sorbent, the chaotic mixing of the solid distribution resulted in the high solid velocity around the region of about 10m/s, this was gradually reduced to 2.5-3.5m/s as the solid progressed to the along the full length of the riser. The solid volume fraction was dilute along the bed height with at around 5% with the bottom of the bed much denser.

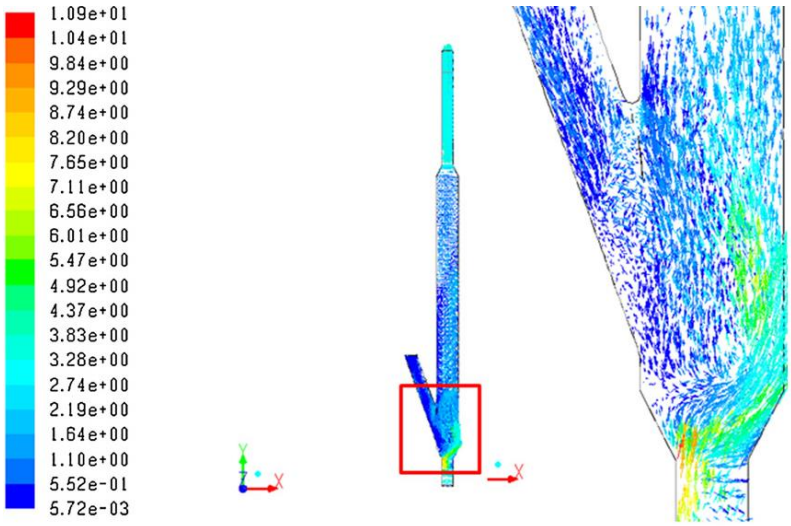

Fig. 4.2: Velocity vector showing the strong mixing zone around the solid inlet region of the lower 3D section of the riser [29].

The author in this review, Ryan et al [29], did not have a detail description of how CO_2 adsorption by the solid adsorbent removed the CO_2 from the flue gases using the Eulerian-Eulerian model. However, it was indicated that around the ICFB, the mass fraction of unreacted solid sorbent showed decreasing volume fraction from the bottom to the top as reaction occurs and that quantity of CO_2 in the gas phase at the upper section of the ICFB was less compared to the lower region which suggests that adsorption of the gas mainly occurred around the lower region with higher solid volume fraction. Due to difficulties (divergence) encountered in the simulation for Eulerian-Lagrangian multiphase model, it was concluded that more development is required for the model to efficiently simulate such system. Eulerian-Eulerian was more practicable to implement and solutions were achieved relatively quick.

Breault et al. [134] executed a sensitivity analysis on the work initially conducted by [29] as already mentioned in this section, the focus was on the lower mixing zone of the riser, where the bulk of CO_2

capture was observed. Simulation was performed with CFPD Barracuda code; the code implements the multiphase model as Eulerian-Lagrangian approach.

The CO_2 adsorption for the dry reaction step was selected with the kinetics adjusted for the heterogeneous volume-average reaction model method implementation in Barracuda software, the forward and backward reaction are given in equation (4.4) and (4.5) respectively.

$$R_{abs} = AT^b P^c exp\left(\frac{-E}{T} + E_0\right)\frac{1}{\alpha_s}\left(\frac{M_A}{V_{cell}}\right)^2 [CO_2] \tag{4.4}$$

$$R_{des} = AT^b P^c exp\left(\frac{-E}{T} + E_0\right)\frac{1}{\alpha_s}\left(\frac{M_B}{V_{cell}}\right)^2 [CO_2] \tag{4.5}$$

The chemical reaction was examined based on the effect of solid adsorbent and gas mass flowrates. It was observed that increasing the flow rate decreased CO_2 concentration exiting the bed which means more adsorption had occurred. This resulted in the increase of the solid holdup in the bed creating more sites for the absorption reaction which gradually reduced CO_2 concentration as reaction proceeded. Reducing the gas mass flowrate did not necessarily improve the CO_2 capture which wasn't expected as this increases the residence time in the bed; however, capture efficiency was increased at certain low gas mass flowrate. Increasing the gas mass flowrate again at some level increased the efficiency which suggests a suitable operating range was required to have an effective removal; efficiency.

Chalermsinsuwan et al. [4] utilised an experimentally determined sorption rate in the CFD investigation of CO_2 capture from a coal power fluidized bed system. The novel system (Fig. 4.3) proposed for the work was a sorption-regeneration CFB loop system, which is an extract from existing Pyro-flow CFB at Illinois USA for Goodrich. The solid sorbent which enters the riser at an angle from the downcomer interacts with the flue gases entering from the bottom of the riser, reaction occur as the two phases are in contact. Adsorbed CO_2 and steam gas from the flue gases leave the system from the grid in the regenerator zone, desorption is facilitated by a cooling system. Regenerated sorbents are then sent back to the riser.

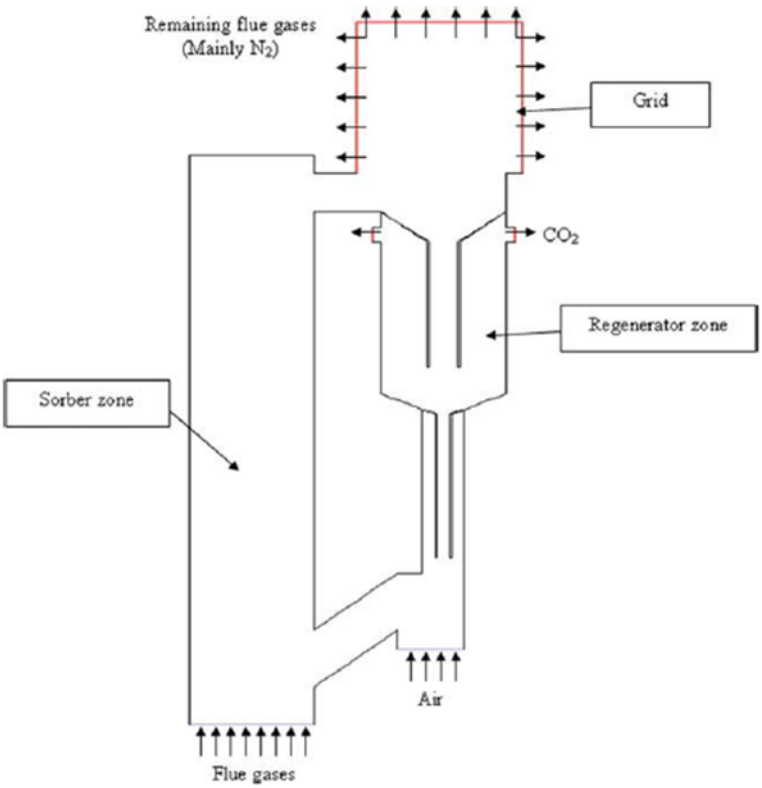

Fig. 4.3:Novel compact sorption-regenerated CFB system [4]

The adsorption of CO_2 by sorbent was integrated into fluent as a heterogeneous chemical reaction using a user defined function (UDF) code. The rate kinetics ignored the sorption of steam as it was considered negligible, the rate of desorption was unavailable, hence boundary condition for regenerated sorbent was set as introduction of fresh new solid sorbents. Equation (4.6) and (4.7) are the chemical and rate equations respectively.

$$K_2CO_3 + CO_2 + H_2O \Leftrightarrow 2KHCO_3 \tag{4.6}$$

$$r = -k_{reaction} C_{co_2} \varepsilon_s \tag{4.7}$$

where $k_{reaction}$ is the reaction rate constant, r is the sorption reaction rate, C_{co_2} is carbon dioxide concentration and ε_s is the solid volume fraction.

The hydrodynamics feature of the riser was typical for CFB, the solid volume fraction was found denser around the bottom and the walls compared to the centre. The gas and solid sorbent velocities investigation demonstrated that the velocity profiles of solid sorbent and gas had similar trends except that there was a slip velocity between the two phases due to differences in densities. Further comparison showed that axial velocity was much higher than the radial velocity in both phases this is due to the system flowing mainly in an axial direction.

In order to investigate the effect of chemical reaction to provide more CO_2 removal, some parameters were altered. The operating parameters changed were reactor length, solid sorbent density, solid sorbent diameter, and inlet gas velocity and reaction rate constant. During each alteration, the base cases which are the set operating parameters for all other were unaltered. The table below shows the different effects on CO_2 removal on the changes to operating parameters.

Table 4.1: Parametric analysis for CO_2 adsorption in the system by varying some parameters [4]

Operating parameter	CO_2 Weight on the Solid Sorbent (kg)	CO_2 Weight on the Flue Gas (kg)	CO_2 concentration (kmol/m^3)	CO_2 Removal Percentage (%)
Base case h= 15.0m, ρ_s= 1,530kg/m^3, d_p= 210µm, v_g =3m/s and $K_{reaction}$ = 1.95s^{-1}	19.68	8.78	1.88 x 10^{-3}	69.16
Effect of reactor length (h)	19.56	8.90	1.91 x 10^{-3}	68.71
h = 12.5m	20.09	8.37	1.79 x 10^{-3}	70.58
h = 17.5m				
Effect of sorbent density (ρ_s)				
ρ_s= 1730kg/m^3	19.73	8.73	1.87 x 10^{-3}	69.31
ρ_s= 1930 kg/m^3	20.11	8.35	1.79 x 10^{-3}	70.64
Effect of solid sorbent (d_p)				
d_p = 75 µm	17.10	11.36	2.43 x 10^{-3}	60.09
d_p= 520µm	19.91	8.55	1.83 x 10^{-3}	69.95
Effect of inlet gas (v_g)				
v_g =1m/s	28.41	0.05	1.24 x 10^{-3}	99.80
v_g = 5m/s	13.05	15.41	3.30 x 10^{-3}	45.85
Effect of reaction rate constant ($k_{reaction}$)	28.45	0.01	1.04 x 10^{-6}	99.98
$k_{reaction}$ = 19.50s^{-1}	28.46	0.00	1.72 x 10^{-26}	100.00
$k_{reaction}$ = 195.00s^{-1}				

From Table 4.1 inlet gas velocity and reaction rate constant were the two most influential operating parameters to the CO_2 removal. Inlet gas velocity determines the circulation of gas and solid phases in the axial and radial directions, reducing it increases the residence time of the fluid which consequently increases reaction time in the system. The increase in reaction rate constant was proportional to the radial dispersion coefficients (gas and solid), Sherwood number and also to the mass transfer coefficient. It implies that an increase in the radial dispersion, Sherwood number and mass transfer coefficient facilitate system mixing improvement which increases CO_2 removal. The effect of temperature was regarded as negligible as only a slightly increase was observed in the system. Computed mass transfer coefficient and Sherwood number were used to estimate the controlling rate at selected areas in the CFB system, it was observed that mass transfer was insignificant in the adsorption process.

Ayobi et al. [5] experimentally and numerically investigated the CO_2 adsorption from a flue gas using potassium carbonate as solid sorbent in a bubbling fluidized bed. An Eulerian two phase theory based

on the kinetic theory of granular flow was adopted in the simulation of the bubbling bed. The adsorption of CO_2 by the solid was experimentally conducted in a bubbling bed where gas and steam was bubbled through a potassium carbonate solid. The rate equation is an inevitable parameter in the chemical reaction model for the adsorption process, the carbonation reaction which is a non-catalytic heterogeneous reaction have limited and unestablished rate kinetics. The author selected proposed kinetics reflecting the presence of steam in the adsorption process for the simulation as seen in equation (4.8);

$$r = -k_{reaction} C_{co_2} C_{H_2O} \varepsilon_s \tag{4.8}$$

The hydrodynamic features of the bubbling bed from simulation were compared with experimental data in terms of the bed expansion and solid volume fraction distribution The chemical reaction analysis showed that along the bed height CO_2 adsorption reaction at the bottom of the bed was high due to higher concentrations of CO_2 and solid adsorbent; however reaction rate decreased towards the top and eventually terminated due to low volume fraction of the adsorbent. This means that interaction of CO_2 and the solid adsorbent, results in the removal of CO_2 (adsorption) from the flue gases, this process proceeds till it reaches a level in the bed that CO_2 concentration remains unchanged due to low level of solid volume fraction as seen in Fig. 4.4.

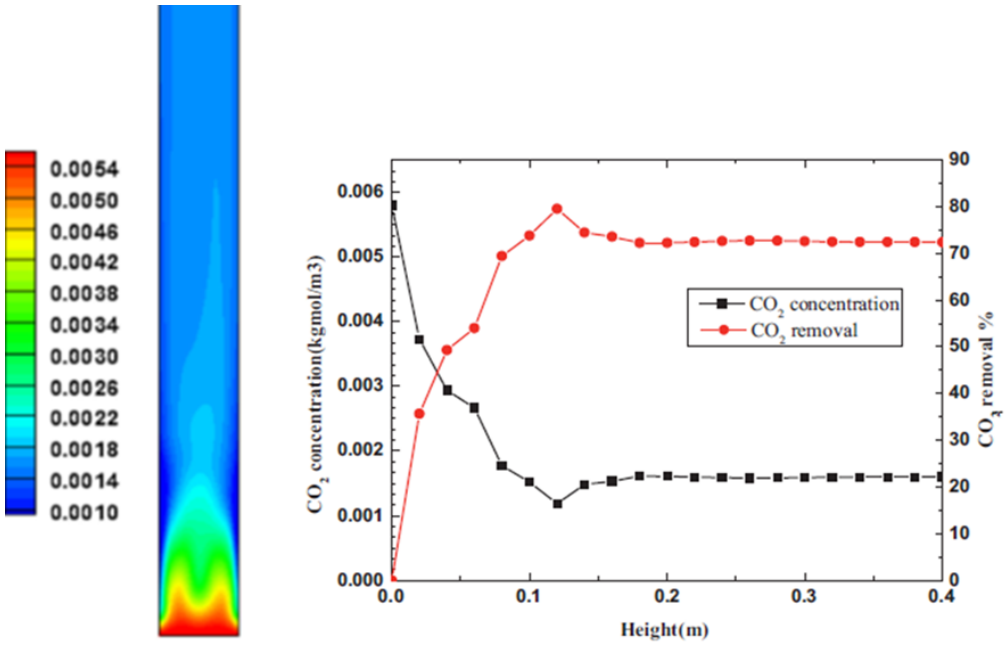

(a) (b)

Fig. 4.4: (a) Time-averaged CO_2 concentration (kmol/m^3) at condition of (u_g =0.71m/s and 15 %mole fraction of CO_2 and H_2O) along the bed height (b) Time and area-averaged CO_2 mass fractions and percent removal of CO_2 against the reactor height (u_g = 0.71 m/s and 15% mole fraction of CO_2 and H_2O) [5].

Fig. 4.4b is a reflection of the Fig. 4.4a in the aspect of the distribution of the solid adsorbent and adsorption of CO_2 from the flue gases. The adsorption process proceeded effectively from the start of the bed height to about 0.12m where it concentration of the gas became constant. The removal efficiency at the top of the bed was about 72.4% this was in agreement with an industrial scale CO_2 removal system.

Chang et al. [133] investigated the hydrodynamic and chemical reaction behaviour in fluidized bed (Fig. 4.5) for the adsorption of CO_2. An Eulerian model in FLUENT CFD tool was used in the implementation of the kinetic models for CO_2 adsorption, experimental work was conducted to compare flow characteristics and species concentrations from simulation.

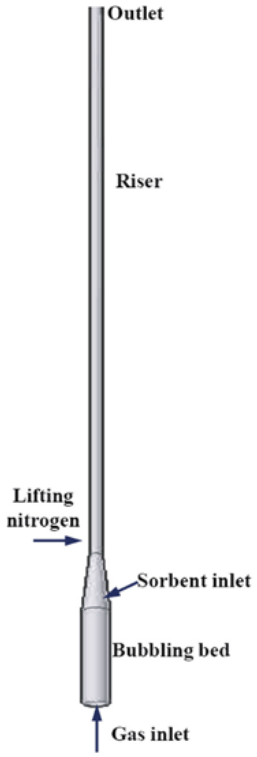

Fig. 4.5: Geometry of the fluidized bed system [133].

The kinetic model for the adsorption was similar to [29] but in this study the wet kinetics and reaction was considered, the catalyst was an amine specially prepared catalyst. If no moisture surrounds the solid sorbent, then the dry adsorption model is activated which reacts the gaseous CO_2 with two amine sites as seen in equation (4.9). However if moisture is present then an alternative reaction proceeds the reactions as seen in equation (4.10).

$$2R_2NH + CO_2 \rightleftharpoons R_2NCO_2^- + R_2NH_2^+ \tag{4.9}$$

$$R_2NH + CO_2 + H_2O \rightleftharpoons HCO_3^- + R_2NH_2^+ \tag{4.10}$$

The kinetics for the two reactions were implemented as a heterogeneous reactions, the kinetics can be seen in equation (4.11) and (4.12) for the dry and wet models respectively.

$$R_d = \frac{dC_{R_2NCO_2^-}}{dt} = \frac{A_d TP}{A_{m_o}} exp\left(-\frac{Ea_d}{RT}\right)\left(\frac{C_{CO_2}C_{R_2NH}}{RTP} - \frac{C_{R_2NH_2^+}C_{R_2NCO_2^-}}{exp\left(\frac{\Delta H_d - T\Delta S_d}{RT}\right)}\right) \tag{4.11}$$

$$R_w = \frac{dC_{HCO_3^-}}{dt} = \frac{A_w TP}{A_{m_o}} exp\left(-\frac{Ea_w}{RT}\right)\left(\frac{C_{CO_2}C_{R_2NH}C_{H_2O}}{RTP} - \frac{C_{R_2NH_2^+}C_{H_2O}}{exp\left(\frac{\Delta H_w - T\Delta S_w}{RT}\right)}\right) \tag{4.12}$$

Hydrodynamic study of the bed showed a good agreement with expected features in the flow characteristics in a fluidized bed design.

The reaction characteristics showed CO_2 concentration reduction along the axial direction of the riser as a result of lower solid sorbent volume fraction. When the gas enters the bed, a rapid reaction rate rapidly decreases the CO_2 content resulting from its consumption of the solid sorbent, this eventually reduces the solid sorbent available for further reactions. Though when fresh adsorbent enters from the side around the top of the bubbling bed (Fig. 4.5), there's low CO_2 concentration which only consumes small amount of the solid in which case the fresh sorbent only decreases slightly. In the simulation work the CO_2 removal efficiency was 78.6% for dry reaction and 86.7% for wet reaction while experimental were 84.4% and 90.6% respectively, this shows reasonable agreement.

Parametric analysis was conducted to investigate the behaviour of the adsorption model in the variation of certain parameters. It was observed that increasing the initial CO_2 content reduced the capture efficiency this is because the increase in the adsorption rate rarely removes the excess CO_2 hence leaving more of the gas in the riser outlet. Increasing the temperature of the system increased the CO_2 removal efficiency but however this is contrary to the thermodynamic equilibrium of adsorption as it's required to remain constant. Reducing superficial velocity increased the residence time in the bed and solid loading which are essential for reactive activities that improves adsorption, this effect increases the capture efficiency of the CO_2 gas. Increasing the sorbent while fluidizing velocity remains unchanged increases the loading of the solid in the bed this eventually provides greater platform for adsorption to occur which increases the CO_2 capture efficiency in the fluidized bed.

Marocco et al. [135] performed modelling of a Dry Sorbent Injection (DSI) method in the control of sulphur dioxide in a flue gas through the injection of a solid sorbent into the flue gases. The dry adsorption of SO_2 by sorbent (Ca (OH) $_2$) in an industrial plant system was simulated using FLUENT Eulerian-Lagrangian model to study removal efficiency. Other components in the flue gas were ignored for the simulation purposes.

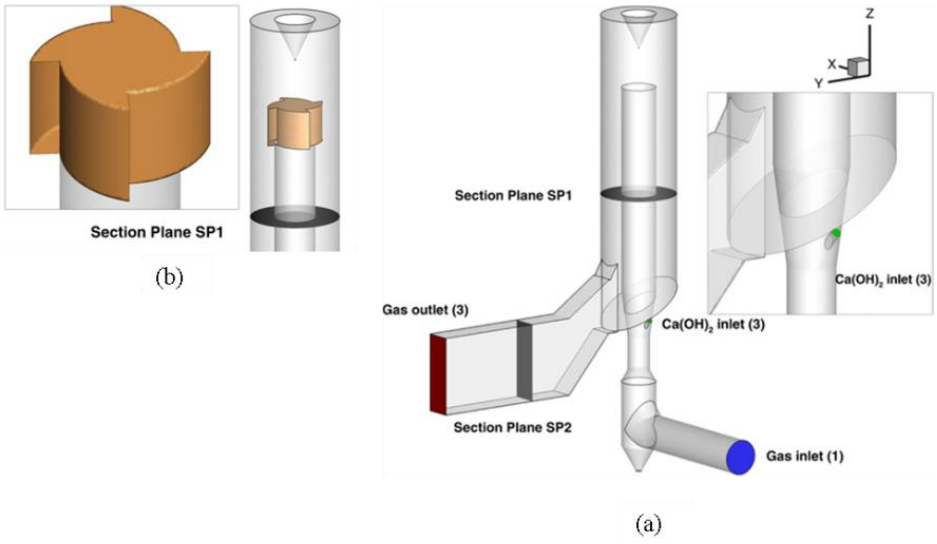

Fig. 4.6: (a) DSI plant simulated with section highlighted (b) adjusted design to improve mixing [135]

The kinetic model for the SO_2 adsorption with hydrated lime was derived from an experimental DSI pilot plant scale, previous kinetic models from a fixed bed yield unsatisfactory conversion and efficiency. The chemical adsorption reaction and rate kinetics selected for the simulation are seen in equation (4.13) and (4.14) respectively. The kinetic model was implemented in FLUENT as User Defined Function (UDF)

$$Ca(OH)_2 + SO_2 \rightarrow CaSO_3 \cdot \frac{1}{2}H_2O + \frac{1}{2}H_2O \tag{4.13}$$

$$\frac{dX}{dt} = K_1\left(\frac{BET}{12.9}\right) \cdot exp\left(-\frac{12.9K_{II}X}{\frac{RH}{100} \cdot BET \cdot Y_{SO_2}}\right) \tag{4.14}$$

In the analyses of the SO_2 adsorption, it was observed that the distribution of the sorbent was essential in the efficiency of the SO_2 removal, the initial design showed particle uneven distribution inside the geometry which resulted in low mixing efficiency. The gas-solid mixing was improved by adjusting the initial design as seen in Fig 5.7b; a more homogeneous distribution of the solid was observed which increases the removal efficiency in comparison with the initial design.

4.3 Results and Discussion

This section would give insight on the preliminary validation of the designed bubbling bed through comparison with trends in literatures. Based on the adsorption models presented in chapter 3, this section will also depict results from simulations conducted. This includes study of a base case and parametric analysis performed to further understand the DME adsorptive behaviour with molecular sieves 4A (MOL4A). The parameter varied in the simulation includes DME inlet mass fraction, MOL4A particle size, rate constant and DME fluidizing velocities.

4.3.1 Preliminary design validation for bubbling bed

In designing the bubbling bed system for adsorption of DME, no experimental work was conducted to perform any validations. For this reason the simulation work was conducted to compare trends in the bed with established literatures on the behaviour of fluidized bed systems.

4.3.1.1 Estimation of bubbling bed fluidizing velocity

The industrial sponsor had a specification on the throughput of the process. As the selected geometry for this project was based on already existing fluidized bed plant, the flow parameters were estimated from the specified throughput to fit the chosen diameter of the industrial large scale fluidized bed system. It was then necessary to estimate the required feed gas velocity entering the adsorber. It was specified that the industrial throughput consisted a maximum of 1wt% DME in the total feed gas into the bubbling bed according to the flow diagram in Fig. 4.7.

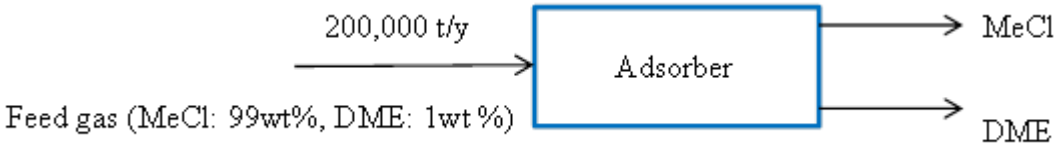

Fig. 4.7: Process flow diagram for throughput entering adsorber.

Assuming the plant would work for 8000 hours in a calendar year out of possible 8760 hours due to shutdowns and other circumstances, the throughput is converted to kg/s as follows;

$$\frac{200{,}000\ (t)\ x\ 1000\ (kg) x (hr)}{8000\ (hr)\ x\ 3600(s)\ x\ (t)} = 6.94\ {}^{kg}/_{s} \tag{4.15}$$

Assuming basis of per second, mass of gas mixture entering absorber;

$MeCl\ inlet\ = 0.99\ x\ 6.94 = 6.8706kg$

$DME\ inlet\ = 0.01\ x\ 6.94 = 0.0694kg$

Applying the ideal gas law equation with compressibility factor to account for non-ideal situation of the process at 1bar pressure and 25°C, the densities of the individual gas component in the mixture can be estimated and hence the total density of the gas mixture.

Gas law with compressibility factor assumed to be 1

$$PV = nZRT \tag{4.16}$$

where R is gas rate constant (8.3145 m^3Pa/K/mol), Z is compressibility factor (assumed as 1), T is temperature (298K), n number of moles for DME is (0.301474 moles) and for MeCl is (137.2713 moles).

Density of DME

$$\rho_{DME} = \frac{m\ x\ P}{n_{DME}\ RT} = 1.88\ {}^{kg}/_{m^3} \tag{4.17}$$

Density of MeCl

$$\rho_{MeCl} = \frac{m\ x\ P}{n_{MeCl}\ RT} = 2.07\ {}^{kg}/_{m^3} \tag{4.18}$$

Volume of DME

$$V_{DME} = \frac{n_{DME} RT}{P} = 0.29\ m^3 \tag{4.19}$$

Volume of MeCl

$$V_{MeCl} = \frac{n_{MeCl} RT}{P} = 3.36\ m^3 \tag{4.20}$$

Density of gas mixture

$$\rho_m = \frac{\left(\left(\rho_{DME}\ x\ V_{DME}\right) + \left(\rho_{MeCl}\ x\ V_{MeCl}\right)\right)}{V_{DME} + V_{MeCl}} = 2.05\ kg/m^3 \tag{4.21}$$

Having estimated the density of mixture at 25 °C and 1bar , the mass flowrate previously calculated can now be converted to volumetric flowrate in order to calculate the velocity inlet as follows;

Volumetric flowrate

$$\dot{V} = \frac{\dot{Q}}{\rho_m} = \frac{6.94}{2.05} = 3.39\ {}^{m^3}/_{s} \tag{4.22}$$

Area of feed inlet into the adsorber

$$A = \pi r^2 = \frac{\pi d^2}{4} = \frac{\pi\ x\ 3^2}{4} = 7.07 m^2 \tag{4.23}$$

Velocity of the feed gas into adsorber

$$v = \frac{\dot{V}}{A} = \frac{3.39}{7.07} = 0.48\ {}^{m}/_{s} \tag{4.24}$$

Viscosity of the mixture

The viscosity of the gas mixture was calculated using [136] correlations as a function of temperature at 298K as seen in the equation below.

$$n_{gas} = A + BT + CT^2 \tag{4.25}$$

where n_{gas} is the viscosity of gas μP (Micropoise), A, B and C are regression coefficients for chemical compounds and T is the temperature.

MeCl viscosity

$$n_{MeCl} = -1.3735 + 0.3863(298) - 4.87x10^{-5}(298^2) = 109.42\ \mu P \tag{4.26}$$

DME viscosity

$$n_{DME} = -4.276 + 0.3026(298) + 6.35x10^{-5} = 91.54\ \mu P \tag{4.27}$$

Table 4.2: Viscosity of the feed gas mixture from calculation

Components	μP	Kg/m/s
MeCl	109.42	1.09424E-05
DME	91.54	9.15403E-06
Mixture Average		1.00482E-05

4.3.1.2 Minimum fluidisation and bubbling velocities

Minimum fluidization velocity is the velocity at which packed solid in a fixed bed becomes suspended by the entering velocity of the fluid. There are different correlations available in literature to investigate the minimum fluidization velocity; often these correlations give different estimation due to inefficiencies or assumptions in the equations. Some of these equations and their resultant values are listed in Table 4.3. The condition selected for the evaluation of the minimum fluidization velocity was based on properties of the gas mixture (DME and MeCl) and molecular sieve 4A (MOL4A) properties. From Table 4.3, empirical correlations obtained from [137] and [138] were reasonably close to each other which would suggest that the appropriate minimum fluidization velocity for the condition selected for the hydrodynamics would be among these correlations. Grace [138] correlation is applicable for spherical and non-spherical particles within a wide range of particle properties, this makes it highly recommendable [139]. For this reason the minimum fluidization velocity was selected for the bubbling bed design.as 0.064m/s.

Table 4.3: Summary of Minimum Fluidisation Velocity Calculated

Reference	Equation	U_{mf} (m s^{-1})
[140]	$U_{mf} = \frac{\mu_g}{\rho_p d_p}\left[{C_1}^2 + C_2 A_r\right]^{0.5} - C_1$ $A_r = \frac{\rho_g {d_p}^3 (\rho_p - \rho_g) g}{{\mu_g}^2}$ $C_1 = 33.7$, $C_2 = 0.0408$	0.000179421
[141]	$U_{mf} = \frac{0.00081\, {d_p}^2 (\rho_p - \rho_g) g}{\mu_f}$	0.091
[137]	$U_{mf} = \left[0.0007 {(Re)_{mf}}^{-0.063}\right] \frac{g {d_p}^2 (\rho_p - \rho_f)}{\mu}$ $(Re)_{mf} = \sqrt{{C_1}^2 + C_2 A_r} - C_1$ $A_r = \frac{\rho_g {d_p}^3 (\rho_p - \rho_g) g}{{\mu_g}^2}$ $C_1 = 33.7$, $C_2 = 0.0408$	0.048
[138]	$U_{mf} = 0.00075 \frac{g {d_p}^2 (\rho_p - \rho_f)}{\mu}$	0.064

Note: The materials used to obtain U_{mf} in the table above were [solid density-720kg/m^3, gas density- 2.05kg/m^3, Gas viscosity- 0.000010048kg/m/s, solid diameter- 0.000350m, gravity- 9.8 m/s^2

The minimum bubbling velocity which is the velocity at which the first initial bubbles starts to appear was evaluated using equation (4.28) according to [142]. The correlation is applicable for group D particles and is proposed to be correct for $U_{mb} < U_{mf}$. Based on the selected Grace [138] correlation for minimum fluidization velocity, the minimum bubbling velocity was 0.037 m s^{-1} which agrees well with the proposed correlation.

$$\frac{U_{mb}}{U_{mf}} = \frac{4.125 \times 10^4 \mu^{0.9} {\rho_f}^{0.1}}{(\rho_p - \rho_f) g d_p} \tag{4.28}$$

4.3.1.3 Comparison of designed bubbling bed to literature (simulation)

In bubbling bed design as the fluidizing velocity of the fluid entering from the bottom of the bed counterbalances the terminal velocity of the packed solid in the fixed bed, the bed begins to form bubbles when the fluidizing velocity reaches the minimum bubbling velocity. The bubbling bed behaviour was compared to literature to investigate the design.

Bed expansion ratio which is the ratio of average expanded bed height to initial static bed height and bed fluctuation ratio which is the ratio of maximum to minimum expanded height within which the bed fluctuates were the parameters for comparison as seen in equation (4.29) and (4.30) respectively

[143]. The bed expansion ratio demonstrates the ability of the bed to expand. The establishment of this parameter for the bubbling bed for adsorption will reassure the accuracy of the bubbling bed design.

$$bed\ expansion\ ratio = \frac{H_{avg}}{H_s} = \frac{(H_{max} + H_{min})/2}{H_s} \tag{4.29}$$

where H_{max} is the maximum expanded bed height, H_{min} is minimum expanded bed height, H_s is the initial static bed height and H_{avg} is the average expanded bed height.

$$bed\ fluctuation\ ratio = \frac{H_{max}}{H_{min}} \tag{4.30}$$

The bubbling fluidised bed simulations were conducted by initially packing it to a height of 3m and the maximum bed expansion determined through correlations and simulation. The simulation for the minimum expanded bed height was obtained using the minimum fluidization velocity from empirical. The simulation for the maximum expanded bed height was conducted using velocities within the range of selected fluidizing velocities as seen in the Table 4.4.

From Table 4.4, the average bed expansion increased as the superficial velocity was increased; this is in agreement with most reported literatures [5,143], this validates the results obtained from this simulation work to accurately predict the flow hydrodynamics of the bubbling bed. This trend resulted because the drag force acting on the particles becomes larger due to the increasing superficial velocities. This in effect increases the particle-particle interaction of the dispersed phase in the system. Bed expansion and fluctuation ratios shows uniform increase when the fluidizing velocity is increased, this trend is equally similar with reported experimental work from literature.

Table 4.4: Bed expansion and fluctuation ratios estimation for some selected fluidizing velocities with initial static bed (Hs) at 3m

Superficial velocity (m/s)	Bed Height (m)			Bed expansion ratio	Bed fluctuation ratio
	H_{min}	H_{max}	H_{avg}		
0.4	3.23	5.80	4.52	1.51	1.80
0.48	3.23	6.92	5.08	1.69	2.14
0.6	3.23	8.86	6.05	2.02	2.74

4.3.1.4 Comparison of designed bubbling bed to literature (Empirical)

This section studies the comparison of bed expansion and fluctuation ratios from simulation results to empirical correlations. Ideally comparison with experimental work would have been preferred but due

to this aspect is beyond the scope of this project work, this study was done. The estimation of the maximum expansion height of the bed is taken from [63] as seen in equation below.

$$\frac{H_{max} - H_{mf}}{H_{mf}} = \frac{U - U_{mf}}{U_B} \tag{4.31}$$

where H_{max} is the maximum expanded height, H_{mf} is the initial static bed, U is the superficial velocity, U_{mf} is the minimum fluidised velocity and U_B is the bubbling rise velocity

The bubble rise velocity is initiated when the gas contacts the solids whereby some inertial downward force of the solid is countered by the gas resulting in the formation of the bubbles. The bubbles formed then travels upward within the bed at a velocity known as the bubble rise velocity. This velocity is essential in studying the hydrodynamics of the bed. Accurate determination of bubbling velocity will require an experimental investigation into the materials and conditions of the bubbling bed set up. For the purpose of this study a correlation given by [144] in equation (4.32) is used to evaluate bubble diameter. The knowledge of the bubble diameter was then used to calculate the bubbles rise velocity using [145] as seen in equation (4.35).

$$\frac{D_{BM} - D_B}{D_{BM} - D_{B0}} = exp\left(-\frac{0.3h}{D}\right) \tag{4.32}$$

where D_{BM} maximum bubble diameter, D_{B0} initial bubble diameter, h initial bed height and D diameter of the bubbling bed

$$D_{B0} = 0.00376\left(u_0 - u_{mf}\right)^2 \tag{4.33}$$

$$D_{BM} = 0.652\left[A_t\left(u_0 - u_{mf}\right)\right]^{2/5} \tag{4.34}$$

where A_t cross sectional area of the bed, u_o and u_{mf} fluidising and minimum fluidisation velocities respectively

$$U_{bo} = U - U_{mf} + 0.711(gD_b)^{0.5} \tag{4.35}$$

Table 4.5: Empirical correlation estimation of bed expansion and fluctuation ratio

Superficial velocity (m/s)	Bed Height (m)			Bed expansion ratio	Bed fluctuation ratio
	H_{min}	H_{max}	H_{avg}		
0.4	3.23	3.98	3.61	1.20	1.23
0.48	3.23	4.09	3.66	1.22	1.27
0.6	3.23	4.22	3.73	1.24	1.31

Table 4.5, shows that bed expansion and fluctuation ratios obtained from empirical derivation increased uniformly in agreement with simulation results in Table 4.1. There are however a significant differences in the corresponding maximum bed expansion, bed expansion and fluctuation ratios for the different superficial velocities investigated for the simulation and empirical estimations. These variations between simulation and empirical results is arguably due to the parameters obtained from Mori and Wen [144] for estimating bubble rise velocity and bubble diameter as their conditions were different from current project conditions. The conditions for the empirical correlation were (0.5cm/s <umf< 20cm/s, 0.006 <dp < 0.045cm, u_0 -Umf < 48 cm/s and D_t < 130cm).

The bed diameter, fluidising velocity and particle diameter for the proposed design are larger than the empirical conditions for Mori and Wen [144]. The larger bed expansion, which was observed from simulation can be justified as it is expected to achieve high expansion due to larger conditions according to [144].

4.3.1.5 Solid and gas distribution in the bubbling bed

In the simulation, kinetic energy from random particle motion also known as granular temperature model was enabled in FLUENT. Divergence was encountered when partial differentiation equation (PDE) solved constitutive equation for gas-solid interaction. However, the algebraic method worked effectively. It has been recommended to use this method for dense fluidized bed system [41]. The reason was because dense solid volume reaction reduced the collision of the particles; this consequently reduced the energy dissipated from the collision in the bubbling bed. It has being reported that the results from the two separate models are not significantly different as suggested by [131] in its investigation on the effect of PDE and algebraic equations on hydrodynamic results. This resulted in the selection of algebraic method; further boundary conditions can be seen in chapter 2. Table 5.6 depicts the operating conditions for a selected base case condition to conduct a preliminary hydrodynamic study.

Table 4.6: Bubbling bed hydrodynamic operating conditions

Parameters	Operating condition
Gas properties	
Inlet temperature	25 ^{o}C
Flow rate	6.92 (kg/s)
Velocity	0.48m/s
DME mass fraction	1wt%
MeCl mass fraction	99wt%
Catalyst	
Inlet temperature	25 ^{o}C
particle diameter	350 µm
Density	720 kg/m3 (MOL4A)
mass flow rate	20 kg/s
Reactor dimensions	
Diameter	3.0 m
Height	15.0 m

Fig. 4.8 shows the bubbling bed initially packed with solid at a height of 3m and the expansion of the bed by fluidizing the packed solid with 0.48m/s feed gas velocity. The superficial velocity exerted drag force on the solid, this force which exceeds the terminal velocity of the solid increases solid-solid interaction and the voids between the solid. Industrial sponsor specification suggested fluidising velocity for the process at 0.48m/s. Since the fluidization at this velocity expanded the bed to 6.92m, it was decided to construct the inlet of the solid at 7m of the bed height. This position of the inlet for the solid will avoid occurrence of reverse flow of the static solid moving upwards. This is possible due to the lower volume fraction observed around the maximum expansion area compared to the volume fraction of the solid entering at the 7m point of the bed height.

Fig. 4.9a and Fig. 4.9b shows how the solid entering the bed at higher volume fraction and velocity pushes the bubbling solid downwards hence avoiding reverse flow situation. This physical interaction in counter-current direction leads to swirl movements due to collision of particles which spirals around the area of maximum bed expansion before falling downwards.

In the case where the velocity is increased above 0.48m/s, as this might occur due to company's demand, simulation shows that reverse flow or elutriation will not occur. This accounts to the higher volume fraction of the solid entering the bed which will be higher compared the volume fraction of the fluidized static bed resulting from increase in the fluidizing velocity.

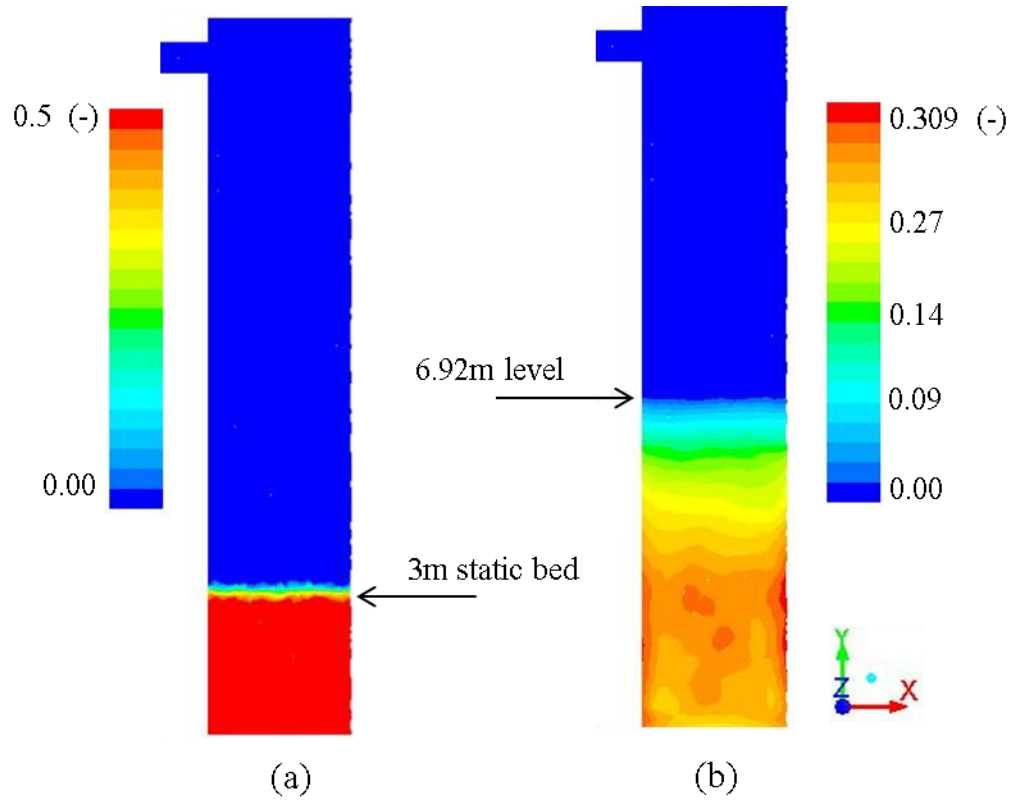

Fig. 4.8: Diagram showing initial static bed at height of 3m (a) and expanded bed at height at 6.92m (b) after 40s simulation time using 0.48m/s superficial velocity.

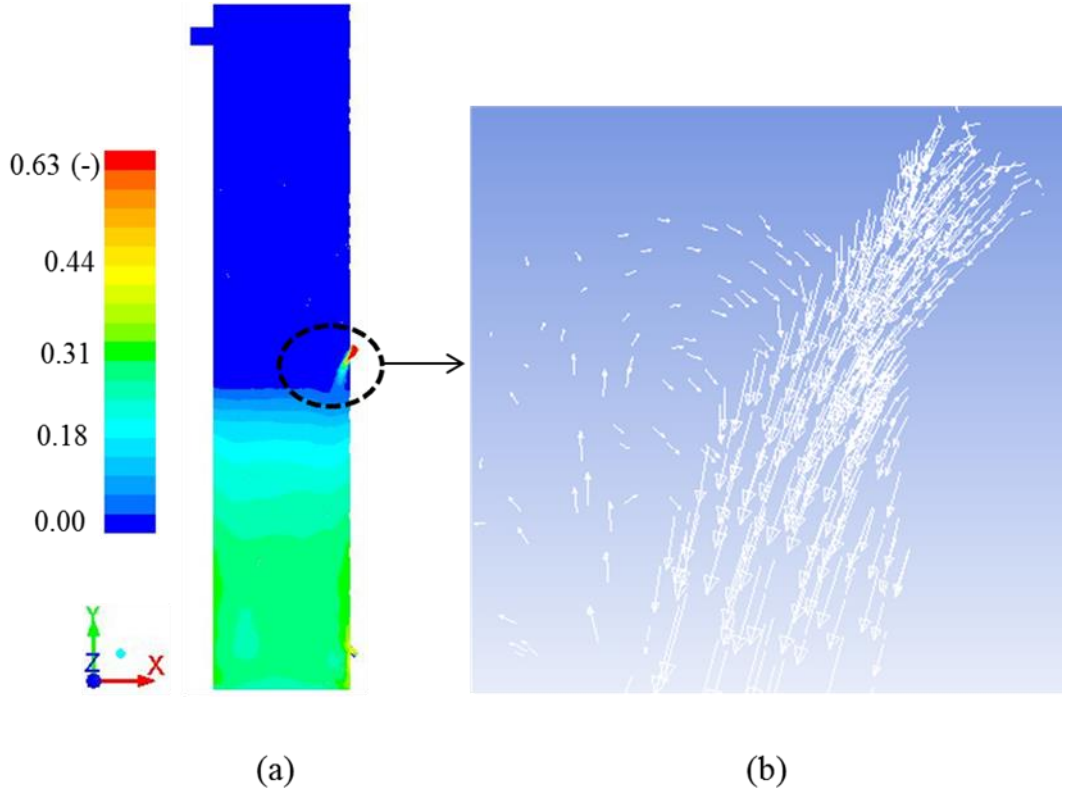

Fig. 4.9: Times averaged volume fraction of solid showing solid entrance (a) and velocity vector around the solid entrance showing movement of the solids (b) after 40s simulation time at 0.48m/s fluidising velocity.

Fig. 4.10 shows top and bottom part of the bubbling bed represented by the radial lines drawn across the bed diameter at bed height of 5m and 1m respectively. The bottom section of the bed has higher solid volume fraction compared to the top part due to downward recirculation of the fluidized static bed particles after reaching the maximum expandable height. During formation of bubbles there's a chaotic recirculation that is produced in the bed which causes reverse flow, this is a common feature with bubbling beds. It was also observed that the solid volume fraction are higher around the walls again due recirculation of the solids around these regions. These curves suggest that during adsorption, the bottom section particularly around the walls will provide better platforms for the adsorbing of DME by the solid adsorbent.

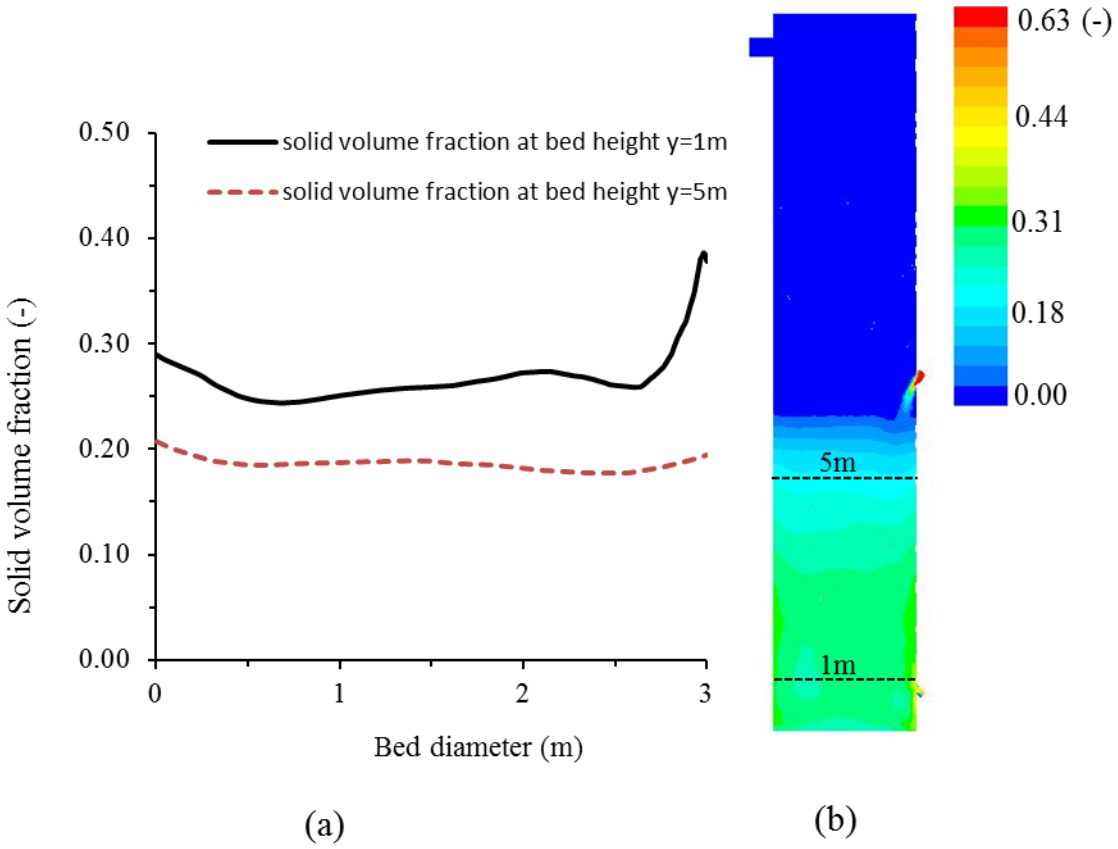

Fig. 4.10: Time average solid volume fraction along bed diameter taken at bed height 1m and 5m with (a) and the contour showing the time average solid volume fraction.

Fig. 4.11 shows the axial gas and solid velocity around in the bottom section of the bed, the downward or reverse flow of the solid and gas around the walls of the bed is seen in this section. This phenomenon is encouraged by the upward movement of the gas and solid in the middle of the bed which when maximum bed height is attained begin to fall backwards.

The symmetrical curves for the bed is a typical characteristic of fluidized bed system and the curves suggest that the bed flow dynamics is in agreement with the reports in the literature.

Fig. 4.12 shows the axial gas and solid velocity in the top part of the bed, the downward movement of the solids is more prominent in this section compared to the bottom section. This movement is

attributed to the bubbled static bed which reaches the maximum expandable bed height begins to fall backwards. The inlet solid which is close in this region and creates a chaotic spiral mixing in this region due to counter-current flow formed, this also contributes to the back mixing observed.

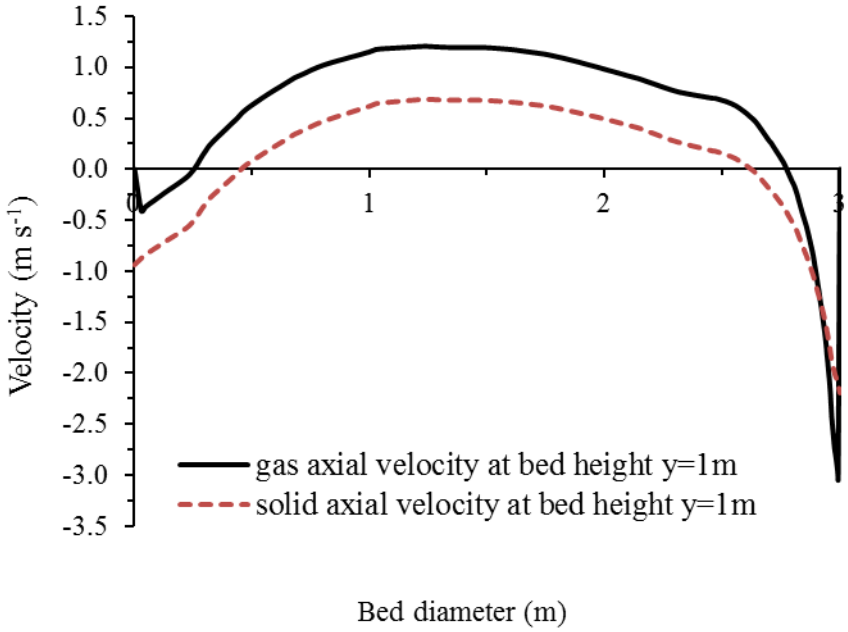

Fig. 4.11: Time average axial gas and solid velocities at bed height of 1m.

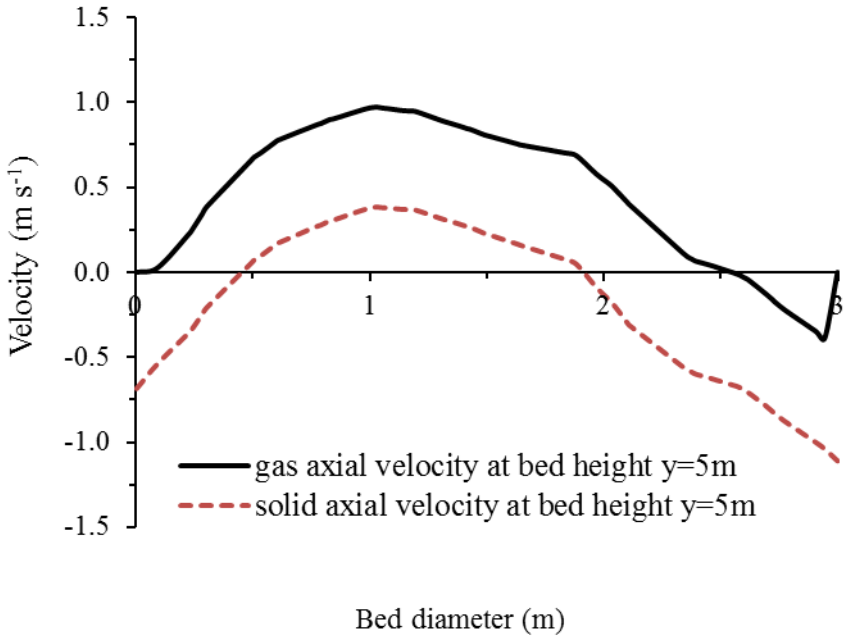

Fig. 4.12: Time average axial gas and solid velocity at be height of 5m.

In terms of adsorption, the back-mixing particularly around the walls would increase the residence time of the solid in the bubbling bed which is essential as this improves the amount of DME that gets

adsorbed by the solid. The observation in the gas-solid distribution agrees with the selected literatures discussed in the literature review section of this chapter.

4.3.2 Adsorption analysis of base case on the first rate kinetics

A base case of the first rate equation suggested from Chapter 3 was initially simulated and analysed to evaluate the behaviour of DME in the bubbling bed. Information obtained from this study will then undergo further parametric analysis to investigate the effects of condition variation to the process. In the set-up of the system, simulation was run for 10s before compiling the rate kinetics UDF to enable the attainment of near steady-state to avoid convergence issues. Consequently all the simulations results for the analysis of adsorption kinetics were extracted after 80s simulation time. The interaction of the DME gas and Mol4A would not have any effect on MeCl which is the other gas in the gas mixture entering in the bubbling as the rate kinetics was specifically derived for DME consumption in the bed.

Table 4.7, depicts the operating condition selected for the base case simulation, Chapter 3 has details for boundary condition and solution procedure selected for the simulations.

In the analysis of the experimental data from the separate study, DME was selectively adsorbed when the mass of adsorbent was restricted to certain amount. It was observed that mass of Mol4A lower than the expected mass in the bed, reduced DME selectivity. This evidently was considered in the simulation, estimation for mass flowrate to attain the maximum DME adsorbed at equilibrium was 20kg s^{-1} from the experimental data at 1 bar pressure. This is the reason for the MOL4A flowrate in Table 4.7. The inlet temperature into the bed was at 25 ^{o}C and there was no change in temperature observed during the simulation.

Table 4.7: Operating conditions for the base case

Parameters	Operating condition
Gas velocity	0.48 m s^{-1}
Temperature	25 ^{o}C
Adsorbent (MOL4A)	
Particle size	350 µm
Density	720 kg m^{-3}
Flowrate	20 kg s^{-1}
Rate constant (k)	0.003s^{-1}
Gas mass fraction (wt %)	
DME	1%
MeCl	99%
Pressure	1bar

Fig. 4.13 shows the concentration of DME along the bed height as reaction occurred, from the observation it's obvious that DME concentration profile decreased as a height increased. The lower section of the bed had a sharp variation in concentration compared to the upper section, this is attributed to the solid concentration around this region which is higher and promotes higher reaction. The initial sharp decrease was around 3m where the bed was initially packed and continued slowly till around 9m then remained almost constant because of absence of solid around this area, this is comparable to the observations in a bubbling bed by Ayobi [5].

The concentration of the gas leaving from the top outlet of bed was monitored and the percentage of the gas removed from the process was estimated. Fig. 4.13 also depicts the gradual increase of DME concentration removed from bottom of the bed to the upper part of the bed, beyond 9m level it appeared to stabilise with the concentration leaving at exit (around 14.25m) 5.62 x 10^{-5} kmol m^{-3} with removal percentage of ~88%. Chalermsinuswan [4] reported that in an industrial scale coal-fired power plant of the same geometry size as this study, the process of removing CO_2 with amine scrubbing method was ~70%. Though this is perhaps unsuitable comparison due to differences in adsorbent and gas involved, but if the adsorption removal in the scale of the fluidized bed was considered as a guideline it suggests that this study is comparable to what is expected in an industrial scale plant.

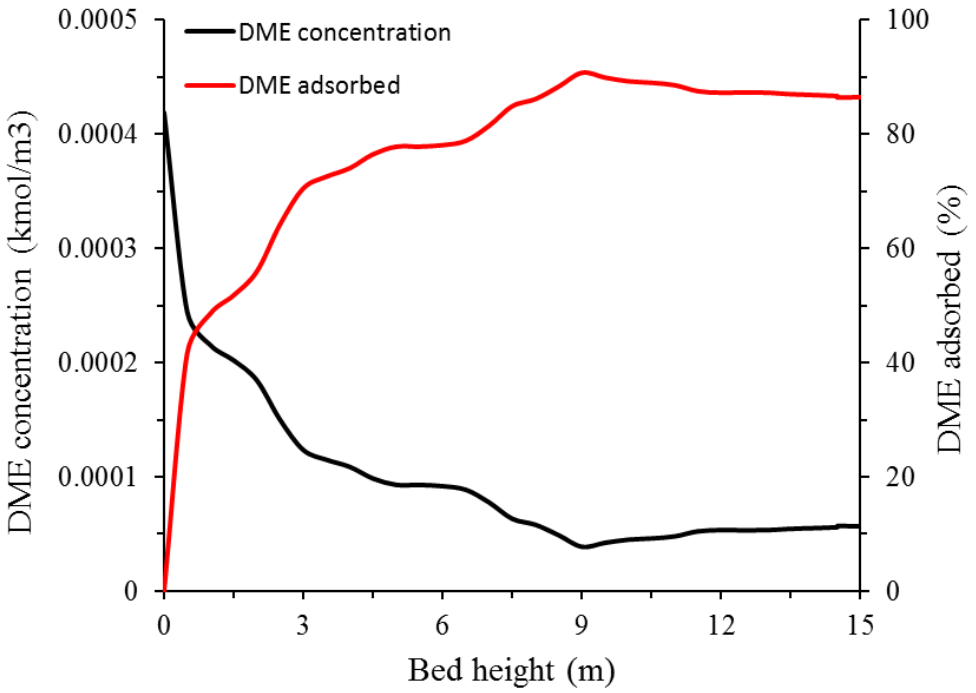

Fig. 4.13: Area-average distribution of DME concentration along the bed height and the percentage of DME removed from the process. Condition (MOL4A diameter =350µm, rate constant =0.003/s, DME mass fraction 1wt %, Temperature 25 ^{o}C, 1bar, velocity 0.48 m s^{-1}).

Fig. 4.14 depicts the contours achieved from the simulation for the analysis of DME adsorption, the MOL4A contour shows the dilute and dense regions of the bed with the bottom denser as expected compared to the upper region. This demonstrates that the diffusion of the DME gas towards the sorbent to initiate gas-solid interaction would be greater at the dense region of the bed. This increase in interactions creates more platform or surface for the adsorption of the gas and subsequently the reaction rate. The heterogeneous reaction rate contour shows the consumption of the gas as it enters the bottom of the bed and flows upward towards the exit. In the bottom of the bed, the reaction rate is higher which supports the analysis for the solid volume fraction. Reaction rate subsided towards the top of the bed and the region with no solid concentration had no or negligible reaction, this further shows the effect of multiplying the rate kinetics with the solid volume fraction in the controlled volume for FLUENT. The fast rate at the bottom reduces the concentration of the gas towards the top and hence exiting from the bed, this evidently is associated with the achievement of high removal percentage of the gas at the exit. The DME concentration contour further shows the visual decrement of the gas as it flows towards the exit from the bottom, the concentration of the gas is higher at the bottom as fresh DME gas continually enters the bed. The concentration then diminishes as it flows due to adsorption of the gas by MOL4A and the concentration at exit reflects the amount of the gas remaining after passing through the solid.

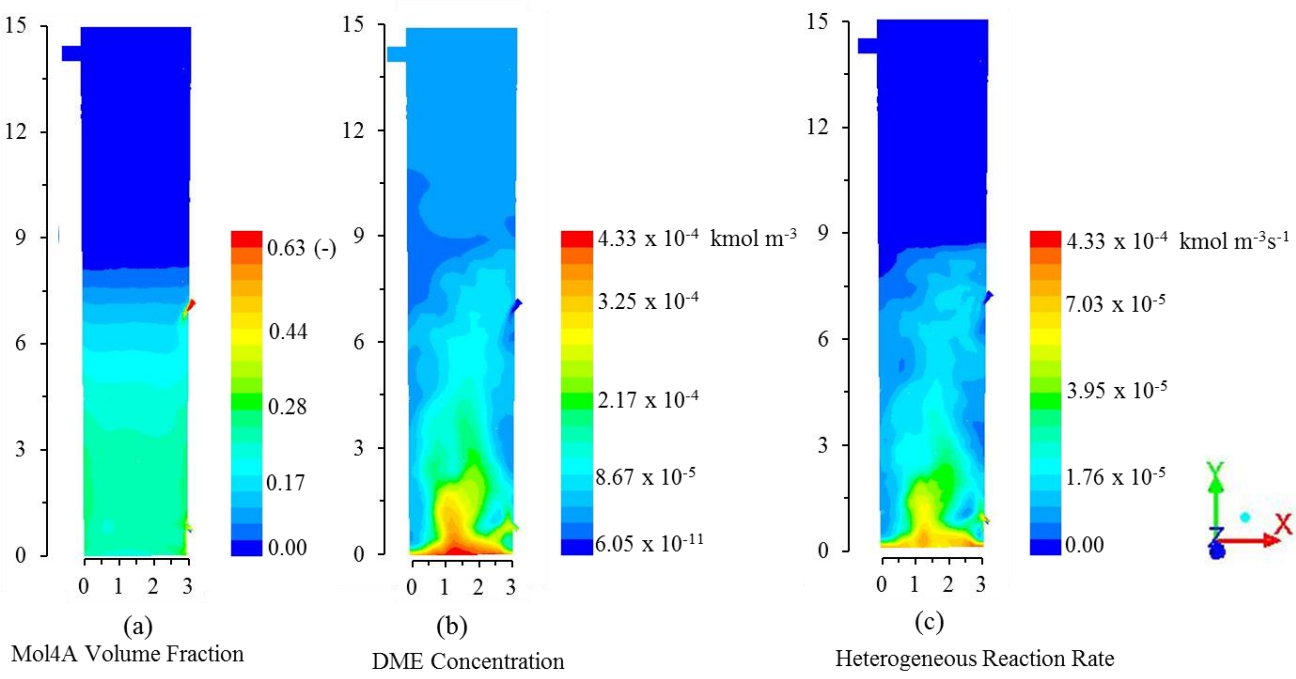

Fig. 4.14: Time-Average contours for the analysis of rate equation 1. Condition (MOL4A diameter =350µm, rate constant =0.003/s, DME mass fraction 1%, Temperature 25 ^{o}C, 1bar, velocity 0.48 m s^{-1}).

4.3.2.1 Amount of DME adsorbed (reaction rate 1)

The amount of the gas adsorbed was determined by computing the mass balance of the gas around the bed system. The rate of adsorption which replicates the rate of chemical reactions models the amount

consumed as the gas adsorbed by the solid. In the mass balance approach applied as illustrated in equation (4.36) for an open system

$$IN - OUT_{top} - OUT_{bottom} = mass\ adsorbed\ (consumed) \tag{4.36}$$

The summation of gas leaving from the top and bottom provides the overall unreacted gas or unconsumed gas in the system, however because the proposed idea is to design a system whereby all of the gas leaves from the same exit as the solid (bottom), the unreacted gas leaving from bottom will not be accounted for the performance of kinetic model. It will however be accounted for the overall performance of the fluidized bed. The obtained consumed gas is assumed to be leaving from the system while ignoring accumulations which is usually associated with bubbling bed systems. The reason for this assumption is because the stoichiometric equation for the reaction between the gas and MOL4A is not available due to the complexity of the adsorbent's compositions.

Table 4.8 illustrates the mass flowrate balance in the determination of the adsorbed DME gas leaving from the lower section of the bed with. The mass flowrates were averaged over simulation times from 60s to 80s though further simulation time could provide higher removal but the however computational time would be unjustifiable for such prolonged simulation. The percentage of the DME mass flowrate leaving from the top of the fluidized bed 12.29% while the amount adsorbed was 86.58%. The remaining amount of the gas could be assumed to exit the bottom side attached with the solid sorbent, this evidently postulate that the total amount adsorbed ~87.71%. However the adsorption rate performance in the fluidized bed would be 86.58% if the bottom DME amount was unaccounted.

Table 4.8: DME mass flowrate exiting fluidized bed system. Condition (MOL4A diameter =350µm, rate constant =0.003/s, DME mass fraction 1wt%, Temperature 25 ^{o}C, 1bar, velocity 0.48 m s^{-1})

		Inlet gas (kg s^{-1})	Exit$_{top}$ (kg s$^{-1)}$	Exit$_{bottom}$ (kg s^{-1})	Consumed (kg s^{-1})
DME	IN	0.0692	-	-	-
	OUT	-	0.0085	0.0008	0.0599

Fig. 4.15 depicts the exit concentration of DME gas leaving from the top of the fluidized bed against the simulation time. The concentration continuously reduced as simulation proceeded until it reached around 60s; this shows the attainment of a steady state in the system. The first 40s was ignored due to instability before reaching steady state. This is the reason the data were obtained from averaging results from 60s to 80s.

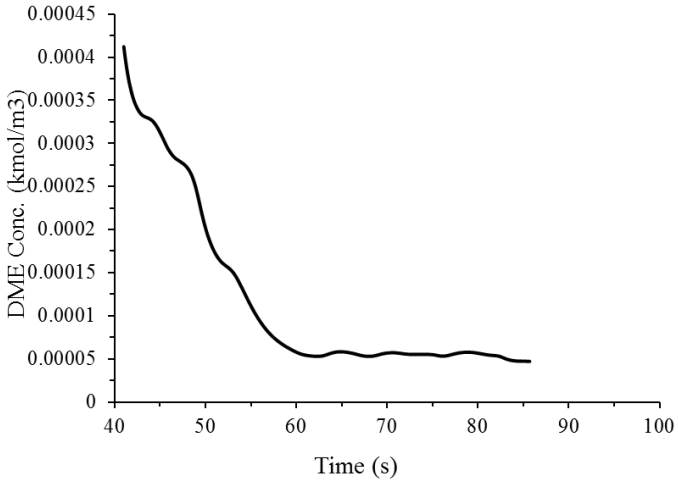

Fig. 4.15: Exit concentration from the top of the bed

4.3.3 Parametric analysis and discussion

In this section, the base case simulation conditions were subjected to parametric analysis to investigate the effect on the bubbling bed performance while maintaining the base case conditions. This provides insight on the improvement and optimization of the bubbling bed design. These analyses were conducted for first proposed rate expressions as discussed in chapter 3. A subsection would investigate the second proposed rate using the base case condition. The parameters considered are DME inlet mass fraction (concentration), DME fluidizing velocity, rate constant and MOL4A particle size. The mass fractions examined were 0.5wt% and 5wt% against the base case of 1wt%. The effect of the fluidizing investigated against 0.48 m/s base case were 0.4 m/s and 0.6 m/s. The effect of rate constant was conducted using 0.006 s^{-1} and 0.12 s^{-1} against 0.003 s^{-1} base case. The effect of MOL4A particle size on adsorption was checked by examining 200 μm and 500 μm against base case of 350 μm.

4.3.3.1 Effect of DME inlet mass fraction (concentration)

In this section the impact of inlet DME concentration was investigated in the bubbling bed while maintaining other conditions in the base case. The concentration was reduced to half of the required specification by the company and increased to 5wt% though this is beyond the design for this study; the investigation is to provide some understanding in the relation of the inlet concentration of the gas to the adsorption process. The experimental analysis of gas adsorption is usually measured in terms of pressure however in this simulation studies the boundary condition settings enables the introduction of the gas as mass fractions which is one of the benefits of CFD.

In literature, work conducted for adsorption on the effect of initial concentration of the adsorbate is centred mainly on liquid adsorption, as will be discussed. An experiment conducted for the adsorption of Chromium (IV) on ZeoliteNaX reported that the adsorption rate increased at increased initial concentration but subsided at certain level [94]. The increase was suggested to result from increased

driving force from increased abundance of the adsorbate which overcomes the mass transfer resistance to the pores of the solid. However, some researchers have shown that increasing the initial adsorbate concentration reduces the adsorption. A pseudo-first order rate was used in the analysis of the adsorption of Direct Red 80 dye from a solution by almond shells (adsorbent), it was reported that the adsorption of the dye decreased from 94 to 83.9% when the initial concentration was increased from 50 to 150mg/L at equilibrium [146]. Similar trend was observed by [88] who investigated the removal of phenol from a solution using luffa cylindrical fibre (adsorbent), it was suggested that the reduction of adsorption at higher phenol initial concentration could be due to saturation of the adsorption sites though the adsorption capacity was enhanced.

Fig. 4.16 depicts DME concentration and removal along the height of the bed. There is a negligible difference in the percentage of DME removed along the bed and towards the exit for inlet concentrations 0.5wt% and 1wt% mass fractions. This suggests that small increase in the inlet specification quantity for the gas has almost no impact on the rate of adsorption of the gas by the solid. Due to the small quantity of the gas between 0.5wt%-1wt%, the kinetic rate effectively removed the gas from the bed. The higher DME concentrations of 5wt% showed decrease in removal percentage notably around the lower section of the bed. The reason for this behaviour is suggested to be associated with the rate constant, which appears exclusively controlling the rate of adsorption of the gas on the solid though modelled as chemical reaction [90].

The increase in the quantity of the gas in the system could have promoted further adsorption rate, however, the increase in the adsorption rate is unable to compensate for the excess DME which causes rather an increase in the amount of unadsorbed gas leaving the system. This is in agreement with [133] numerical simulation investigation, but could be argued if the excess DME concentration could actually promote the adsorption rate. This is because, monolayer adsorption occurrence suggests that attaining saturation level at equilibrium hinders further DME adsorption regardless of the excess amount available for adsorption. This phenomenon is better examined in an experimental study where other means of adsorption kinetics such as intraparticle and diffusion rates are considered. However, this is a limitation in this project.

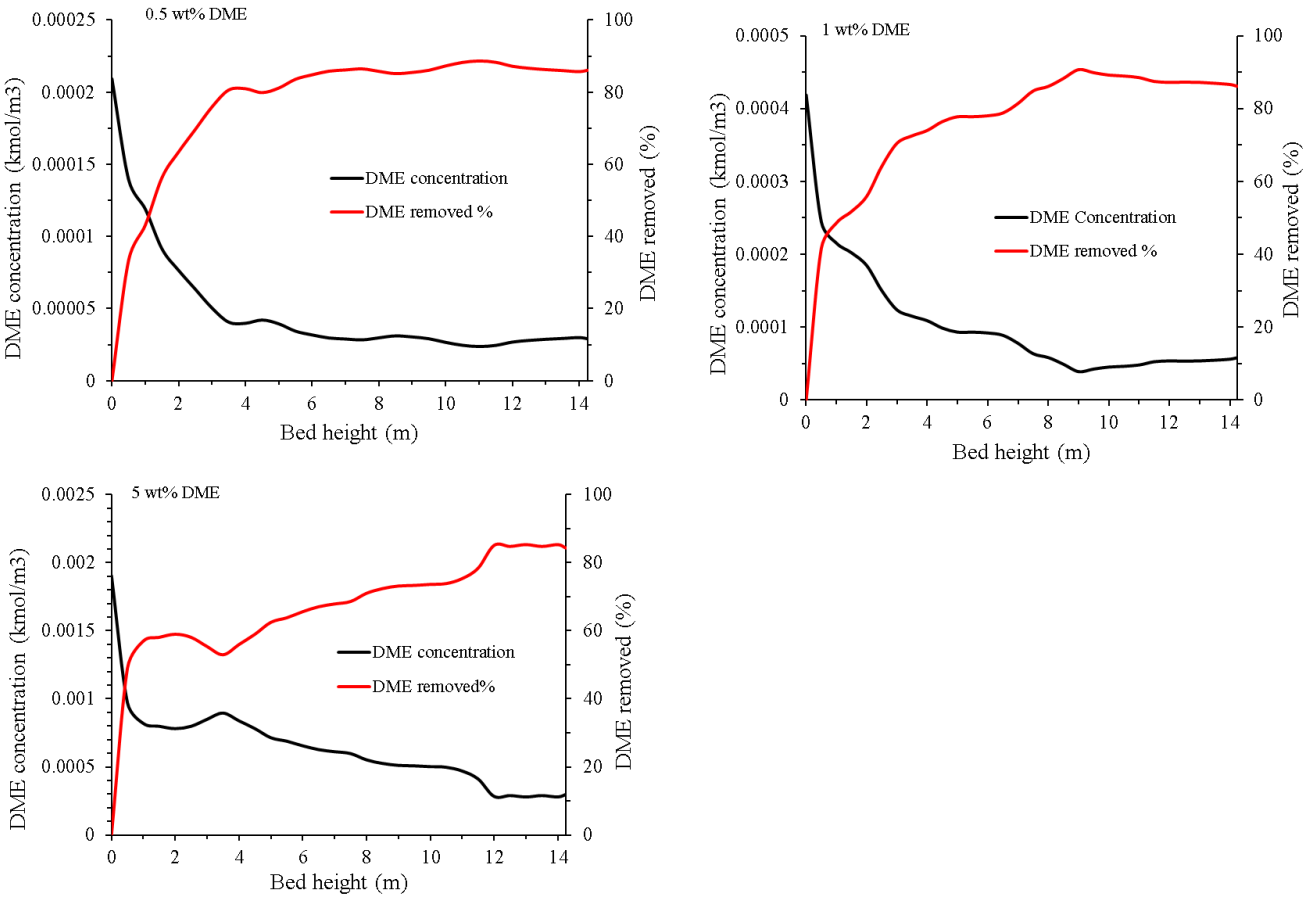

Fig. 4.16: Effect of DME mass fractions to the DME removal along the bed height. Condition (MOL4A diameter =350µm, rate constant =0.003/s, Temperature 25 ^{o}C, 1bar, velocity 0.48 m s^{-1}).

Fig. 4.17 depicts the effects that the initial DME concentration has on the gas removal from the top exit in the bubbling bed system. Negligible difference was seen between mass fractions between 0.5wt% and 1wt% arguably because of its low concentration amount, the rate constant was sufficient to effectively remove the gas from the system. Percentage of the gas removed from the top for 0.5wt% and 1wt% were ~86%. The percentage of the gas removed from the top reduced to 84.34% for inlet concentration of 5wt% initial concentration.

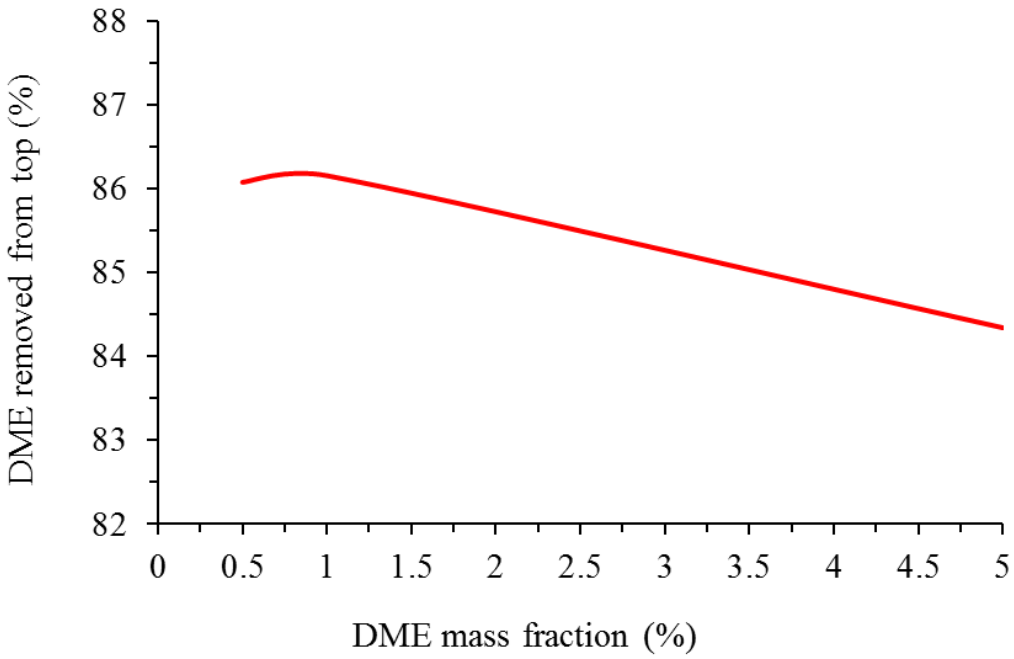

Fig. 4.17: DME removal percentage from the top exit of the bed at different DME mass fractions. Condition (MOL4A diameter =350µm, rate constant =0.003/s, Temperature 25 ^{o}C, 1bar, velocity 0.48 m s^{-1}).

Table 4.9 depicts the effect of the initial DME concentration on the mass balance around the bed. It shows that the DME leaving from the top of the bed with lower mass fractions were closely matched while the mass fraction at 5wt% increased to ~13.9%. DME adsorbed resulting from the lower mass fractions (0.5wt% and 1wt%) further illustrated that the amount of the gas adsorbed onto the solid were correspondingly close. This amount reduced as the gas concentration increased in the system, it was 84.33% for 5wt% mass fractions. This reduction in the amount adsorbed for the higher mass fractions further demonstrates that the rate of adsorption could not complement the excess DME concentration which consequently reduces the overall performance of the system. DME leaving from the bottom of the bed for the lower mass fractions again showed some similarities which was attributed to the quantity.

Table 4.9: Effect of initial mass fractions on time-averaged mass flowrate of the gas leaving bubbling bed. Condition (Rate constant =0.003/s, Temperature 25 ^{o}C, 1bar, velocity 0.48 m s^{-1}).

Mass Fraction (wt%)	DME exiting from top		DME exiting bottom		DME consumed (on MOL4A solid)	
	kg s^{-1}	%	kg s^{-1}	%	kg s-1	%
0.5	0.0044	12.75	0.0004	1.16	0.0298	86.08
1	0.0085	12.28	0.0008	1.14	0.0599	86.58
5	0.0479	13.93	0.0059	1.74	0.2907	84.33

Fig. 4.18 depicts the concentration distribution of DME at varying initial mass fractions; this clearly shows the effect of the excess concentration on the system. The concentration of the gas for the lower mass fractions (0.5wt% and 1wt%) appear to diminish as it approaches the top section of the fluidized bed system as the reaction proceeded to consume the gas entering the system. Higher mass fractions (5wt%) with abundant presence of the gas which the adsorption rate is unable to compensate, shows more distribution of the gas towards the top section due to more unreacted gas leaving the system.

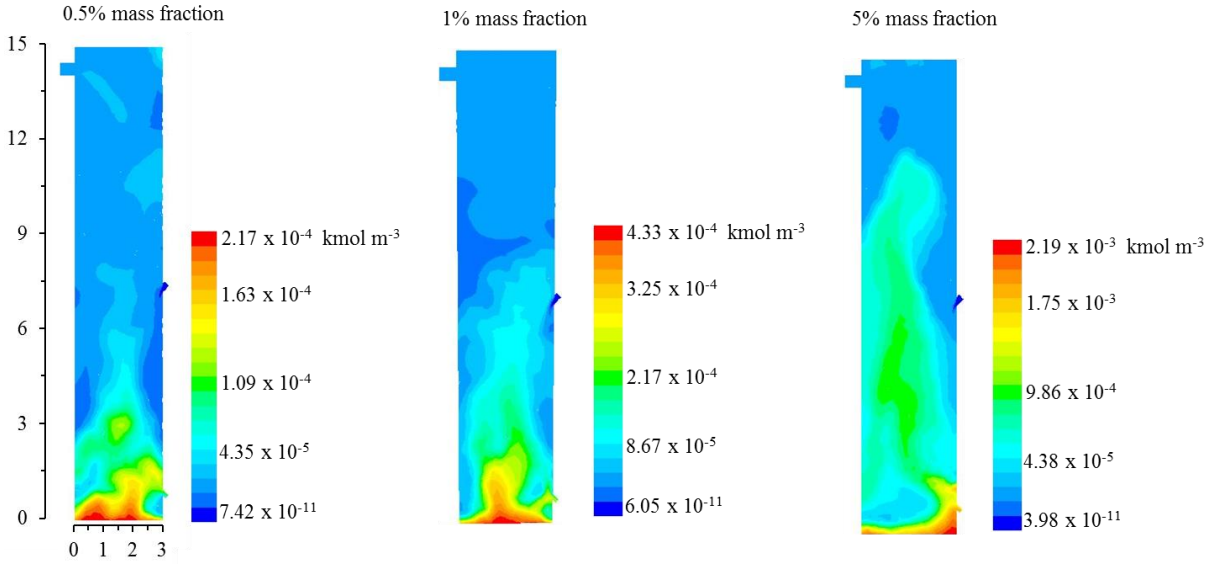

Fig. 4.18: DME concentration distribution contours along the height at different DME initial concentrations Condition (rate constant =0.003/s, Temperature 25 ^{o}C, 1bar, MOL4A diameter =350µm).

4.3.3.2 Effect of adsorbent particle diameter

The effect of the MOL4A particle size on the adsorption of DME gas in the fluidized bed system was analysed in this section. Solid particle size tends to increase the volume fraction of the solid in the system when increased and vice versa. In experimental investigations, adsorbent particles are analysed based on the surface morphology which considers the pore sizes of the solids. It has been reported in investigations involving liquid adsorption that smaller particle adsorbent sizes increases the uptake of

the adsorbate due to greater accessibility to pores and larger surface area. Another explanation attributes the increased adsorption to enhanced driving force of the reactive compounds [147,148]. A different author investigated the adsorption of solution and gaseous adsorbate, smaller particle sizes increased the adsorption of the liquid adsorbate while larger particle sizes increased the adsorption of the gaseous component, the adsorption of both components were attributed to the interaction with the pores and transport inside the porous particles [149].

The observation in Fig. 4.19 shows that the increase in particle sizes increased the rate of consumption of the gas. Noticeable increase was seen between 200µm and the base case of 350µm; however this was not the case for the particle size at 500µm in comparison which showed negligible increase. It appears that the impact of increasing the particle sizes has a diminishing point whereby further increase in the size shows negligible effect. The lower section of the bed in Fig. 4.19 for 500µm showed slightly higher removal efficiency compared to the base case though this efficiency was in proximity with the base case towards the top of the bed. This is attributed to the densely distributed solid volume fraction for 500µm at the lower region of the bed which increased the rate of adsorption in this region compared to the base case. This is in agreement with work conducted by [150] where the difference in CO_2 removal between 400µm and 500µm were very negligible compared to lower particle sizes. The trend observed from the modelling in this study agrees with the experimental study of [149] on the adsorption of gaseous adsorbate though the concept of adsorption in experimental method differ from simulation.

The modelling of the adsorption of DME gas in this study is limited, the adsorption of the gas into particle pores and intraparticle are neglected due to limitation of modelling tool (Eulerian-Eulerian) and rate kinetics selected (pseudo-first order). The Eulerian model treats the solid as a fluid in a control volume and neglects the surface properties (e.g pores) of the solid particles, though the other hydrodynamic features of the solid distribution is maintained. This means that effect of particle sizes as postulated in experimental studies will be different.

There are two postulations to explain the contradicting observation in regards to solid particle size effect on the adsorption of DME. Firstly, in CFD FLUENT code, the Eulerian multiphase phase flow calculates the dispersed phase volume fraction as the volume occupied by particles in a unit cell volume. The volume fraction of the solid thus calculated as the fraction of the solid volume divided by the total cell volume. The solid volume assumed as spherical is $4/24\pi d^3$. This is how the particle size (diameter) of the solid is taken into account. This suggests that increasing the particle diameter would increase the solid volume fraction and thus increasing DME removal. DME removal is improved because reaction rates increases due to increase in the solid concentration. Secondly, the pseudo-first order rate kinetics proposed for the adsorption of DME is in respect to DME concentration hence neglecting the effect of MOL4A particle size. This was suggested by Yu et al [6] for a first order rate.

This is coupled with the pseudo-first rate neglecting intraparticle diffusion. It could be argued that DME adsorption in this study is not directly affected by particle size but however indirectly through gas-solid behaviours. The trend achieved in this study was however in agreement with the works conducted by [4,150]. An argument that could be further investigated is regarding the work conducted by Fan et al [149], the author observed increased gas adsorption at increasing adsorbent particle size. This supports the trends seen in this study and for other authors whose work has been based on CFD simulation.

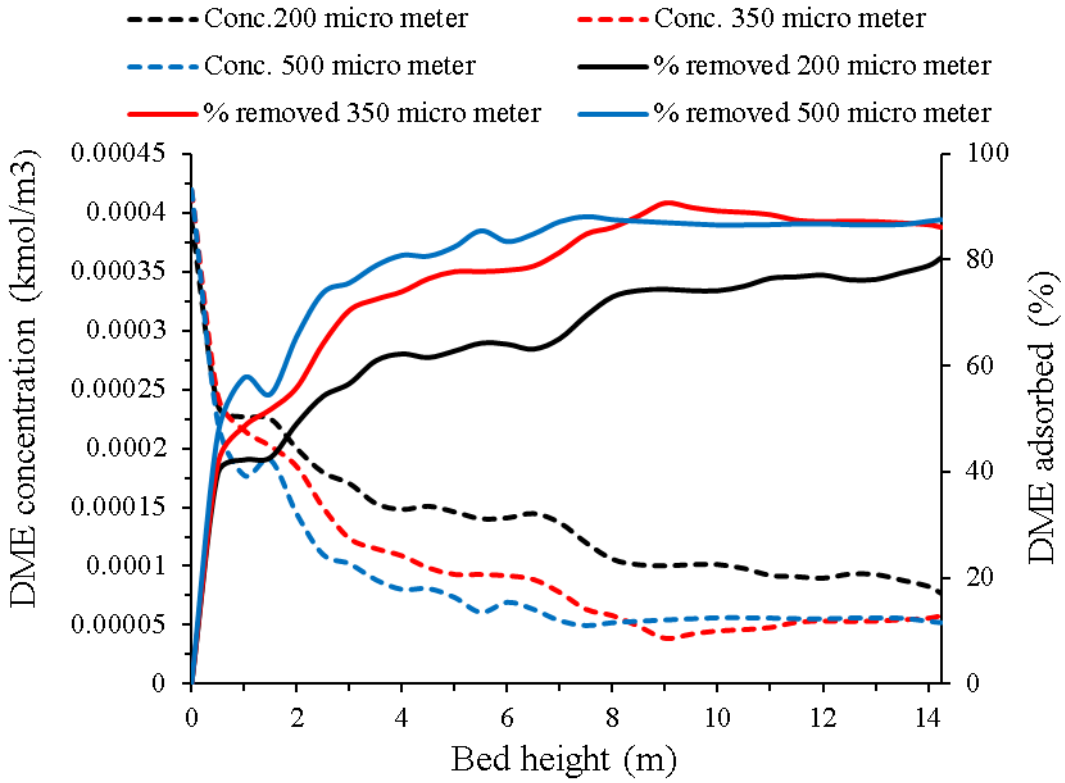

Fig. 4.19: Effect of particle diameter to area averaged DME concentration along the bed height and its percentage removal from the top outlet of the bed Condition (DME mass fraction 1wt%, Temperature 25 ^{o}C, 1bar).

Fig. 4.20 further illustrates the impact solid particle sizes have on adsorption of the unwanted gas entering the fluidized bed. Removal efficiency by investigating DME exiting from the top of the bed achieved approximately 80.43% and 86.85% at particle sizes of 200µm and 500µm respectively. Particle size at 500µm negligibly improved the removal by 0.28% compared to the base case particle size. The trend shows that lower particle sizes reduced the bed efficiency in adsorbing the gas while higher particle sizes improved bed efficiency when compared to the base case particle size of 350µm. The reasons are explained above and suggest that for optimum adsorption process a carefully selected adsorbent particle size will be required.

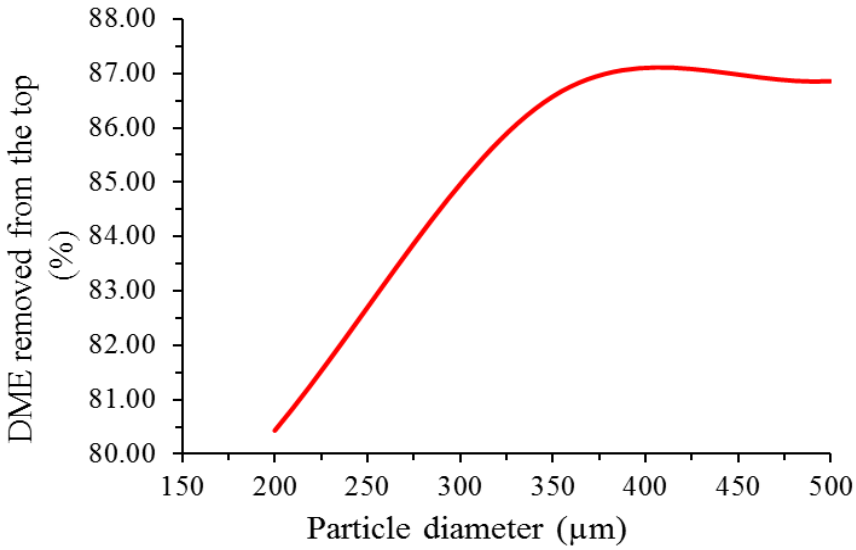

Fig. 4.20: DME removal percentage from the top exit of the bed at different fluidizing velocities Condition (rate constant =0.003/s, DME mass fraction 1wt%, Temperature 25 ^{o}C, 1bar).

Table 4.10 depicts the mass balance around the fluidized bed showing the adsorption efficiency in the removal of DME from the mixture gases. The table demonstrates the impact of solid particle sizes on the adsorption of the gas, lower particle size as described previously has 16.94% of its mass leaving from the top which is higher than the bigger particle sizes, and this further confirms that the amount of unadsorbed DME is higher for such particle sizes. The amount of the DME consumed or adsorbed equally increased as the particle sizes increased though it became negligible between 350µm and 500µm for the reasons explained above. Overall unadsorbed DME decreased from 18.86% for 200µm to 13.20% for 500µm. The overall fluidized bed performance shows that DME leaving from the bottom were 83.28%, 87.71% and 87.11% for 200µm, 350 µm and 500 µm respectively.

Table 4.10: Effect of solid particle size on time-averaged mass flowrate of the gas leaving bubbling bed. Condition (Rate constant =0.003/s, DME mass fraction 1wt%, Temperature 25 ^{o}C, 1bar)

Particle diameter (µm)	DME exiting from top		DME exiting bottom		DME consumed (on MOL4A solid)	
	kg s^{-1}	%	kg s^{-1}	%	kg s^{-1}	%
200	0.0116	16.72	0.0020	2.93	0.0556	80.35
350	0.0085	12.28	0.0008	1.14	0.0599	86.58
500	0.0084	12.09	0.0008	1.11	0.0600	86.80

Fig. 4.21 depicts the concentration contours of the different particles sizes investigated. The observation further illustrates the discussions above. The rate of reaction is increased as the solid particles were increased which resulted in the removal of DME. The contour shows slightly reduced

concentrations between 350µm and 500µm. This suggests that increase in solid concentration at higher particle sizes becomes negligible hence leading to negligible change in reaction rate.

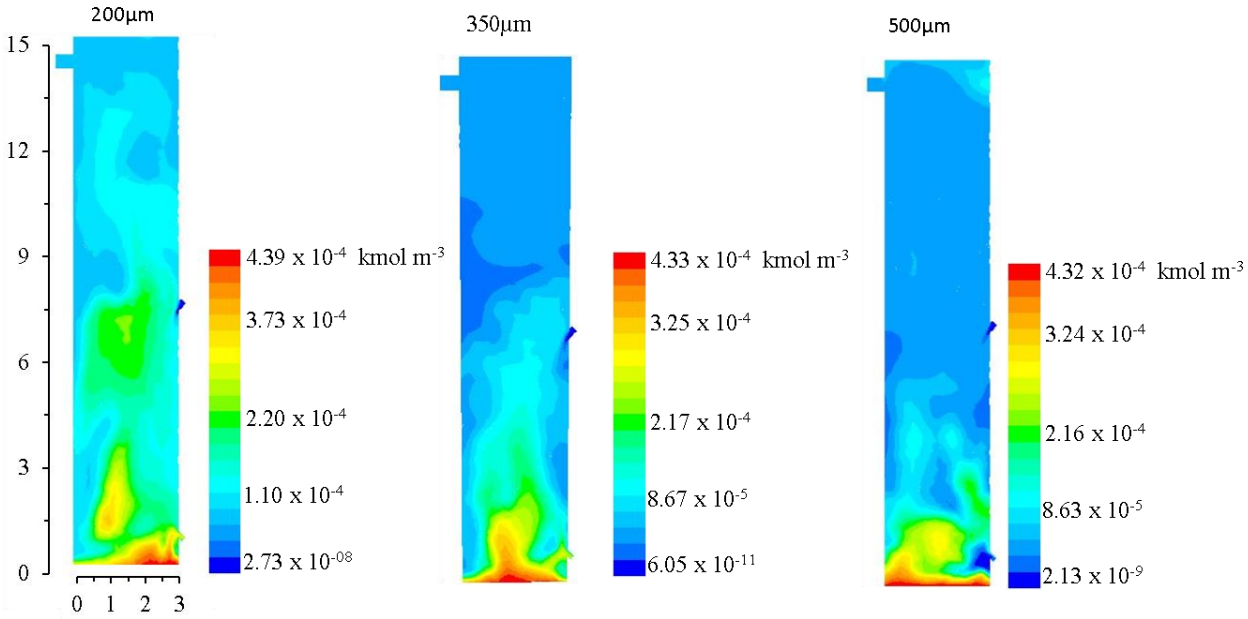

Fig. 4.21: Time-average contours for the analysis of solid particle sizes Condition (rate constant =0.003/s, DME mass fraction 1wt%, Temperature 25 ^{o}C, 1bar).

4.3.3.3 Effect of fluidizing velocity

The effect of the fluidizing velocity was investigated in this section by altering the base case velocity to 0.4m/s and 0.6m/s to observe the changes these would have on the system. These alterations were performed while maintaining other base case conditions as mentioned. The fluidizing velocity is an essential parameter that affects the hydrodynamic behaviour of the bed during operation. Generally in bubbling beds, increasing the fluidizing velocity reduces the gas residence time which limits the contact time with the solids; this increases the bed expansion due to increased bubble number and size [5]. Decreasing the gas velocity increases the gas residence time which increases the contact time with the solid while the bed expansion is reduced. The design of the bubbling bed in this study suggests that increasing the fluidizing velocity will increase the solid residence time in the system. This is because the solid exiting from the lower section of the bed will be hindered by higher flowing gas, while reduced gas fluidizing velocity would decrease solid residence time. The solid volume concentration distribution is increased when the fluidizing velocity of the gas is decreased and vice versa [18].

Fig. 4.22 depicts the concentration profiles for the different fluidizing velocities selected for this parametric analysis, it shows that lower fluidizing velocity effectively increased the amount of the gas consumed (adsorbed) in the system. The explanation of these trends is attributed to lower fluidizing gas increasing the gas residence time in the system. This results to the increase of interaction between the gas and solid. Higher fluidizing velocity reduces the gas residence time and hinders the level of interaction between the gas and the solid. This trend depicts that the gas contact time with the solid is

essential in the adsorption process compared to the solid residence time. This further illustrates that at higher velocities the solid volume fraction becomes sparsely distributed which increases the solid void fractions and effectively allow more gases to freely flow through the solid in the system. This hydrodynamics feature of the system becomes the contrary when the fluidizing velocity is reduced. Farag et al. [151] conducted modelling of polyethylene in an industrial scale fluidized bed (bubbling bed) with design similar with the current study and the author discovered that increasing the fluidizing velocity reduced ethylene conversion which is a reflection of the phenomenon observed in this study. However it should be acknowledged that selected low velocity should be sufficient to fluidize the bed otherwise there will be insufficient gas-solid contact; hence a reasonable range will be required. The removal efficiency increases from the bottom of the bed, while the DME concentration reduced for all the velocities investigated along the bed height. Further visual representation of the distribution of the gas along the bed height is seen in Fig. 4.24

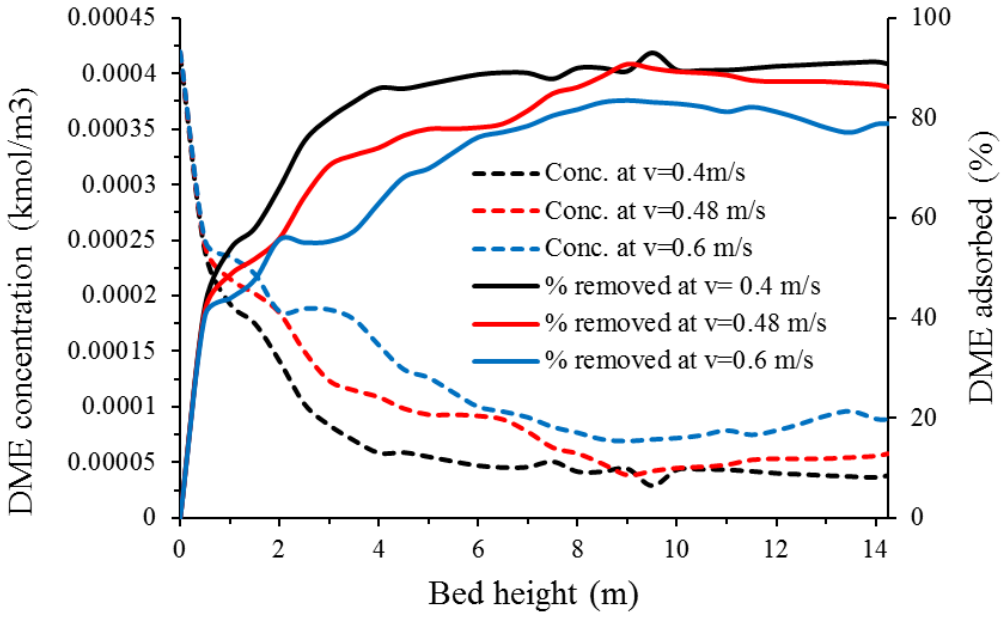

Fig. 4.22: Effect of fluidizing velocity to area averaged DME concentration along the bed height and its percentage removal from the top outlet of the bed Condition (MOL4A diameter =350µm, rate constant =0.003/s, DME mass fraction 1wt%, Temperature 25 ^{o}C, 1bar)

Fig. 4.23 illustrates the removal efficiency of DME from the top exit in the fluidized bed system. Fluidizing velocity at 0.4m/s increased the removal efficiency from the top of the fluidized bed to 90.13% from base case of 86.57%. The increase in the fluidizing velocity to 0.6m/s reduced the removal efficiency to 79.64%. It could be concluded that the increase in the fluidizing velocity is inversely proportional to the removal efficiency of the gas in the system.

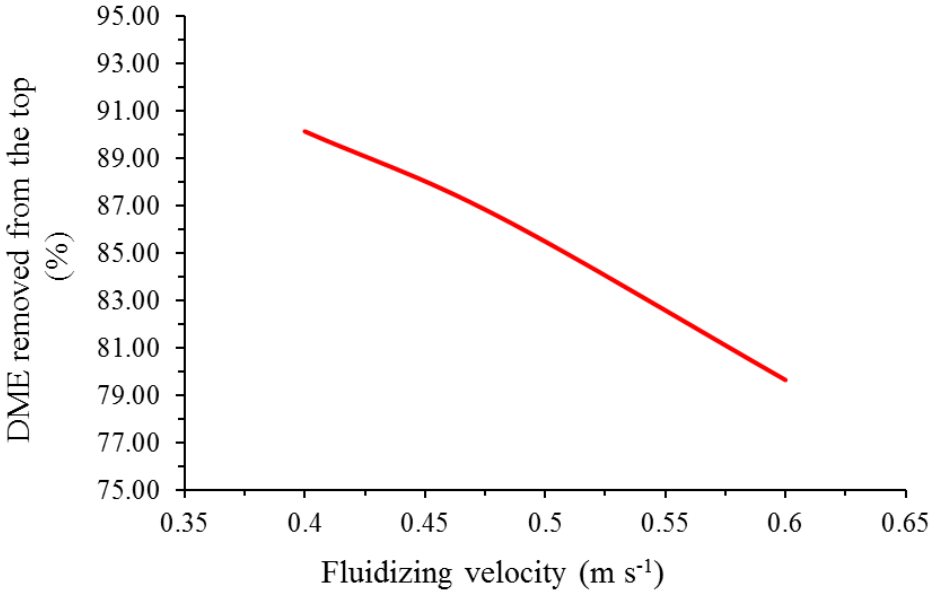

Fig. 4.23: DME removal percentage from the top exit of the bed at different fluidizing velocities Condition (MOL4A diameter =350µm, rate constant =0.003/s, DME mass fraction 1wt%, Temperature 25 ºC, 1bar)

Table 4.11 depicts the mass flow rates leaving the top and bottom section of the together with the estimation of the amount of the gas consumed (adsorbed) in the system. From the observation, lower velocity demonstrated lower mass flowrates leaving from the top as expected and the amount consumed equally increased to agree with the amount removed. 0.4m/s velocity with the lowest amount leaving from top had 90.09% of the gas consumed while the higher velocity at 0.6m/s reduced the amount adsorbed 79.62% from the base case value of 86.58%. In considering the overall removal performance of DME from the bottom of the system, the velocity at 0.4m/s would be 91.64% while 0.6m/s would be 81.22%. This result from the mass balances further confirms that the amount of the gas consumed is inversely proportional to the increase of fluidizing velocity.

Table 4.11: Effect of fluidizing velocity on time-averaged mass flowrate of the gas leaving bubbling bed. Condition (MOL4A diameter =350µm, rate constant =0.003/s, DME mass fraction 1wt%, Temperature 25 ºC, 1bar)

Fluidizing velocity (/s)	DME exiting from top		DME exiting bottom		DME consumed (on MOL4A solid)	
	kg s^{-1}	%	kg s^{-1}	%	kg s-1	%
0.4	0.0058	8.36	0.0010	1.55	0.0623	90.09
0.48	0.0085	12.28	0.0008	1.14	0.0599	86.58
0.6	0.0130	19.77	0.0011	1.60	0.0539	79.62

Fig. 4.24 depicts the DME concentration contours of different fluidizing velocities, these contours compliment the other observations in regards to the removal efficiency of the gas. 0.4m/s fluidizing

velocity case shows weakening DME concentration towards the top as reactions are enhanced due to the prolongment of the gas hold up in the system which resulted in the consumption of the gas, this evidently meant that the concentration of the gas leaving from the top was reduced in comparison to the base case which had a slightly higher velocity. The case with 0.6m/s showed higher concentration of the gas leaving from the top of the fluidized bed system due to expansion of the solid void fractions which limits the interaction of the gas and solid. The contours for the considered velocities further justifies the reactive and hydrodynamic behaviour of the interactions expected in the system according to literature [18].

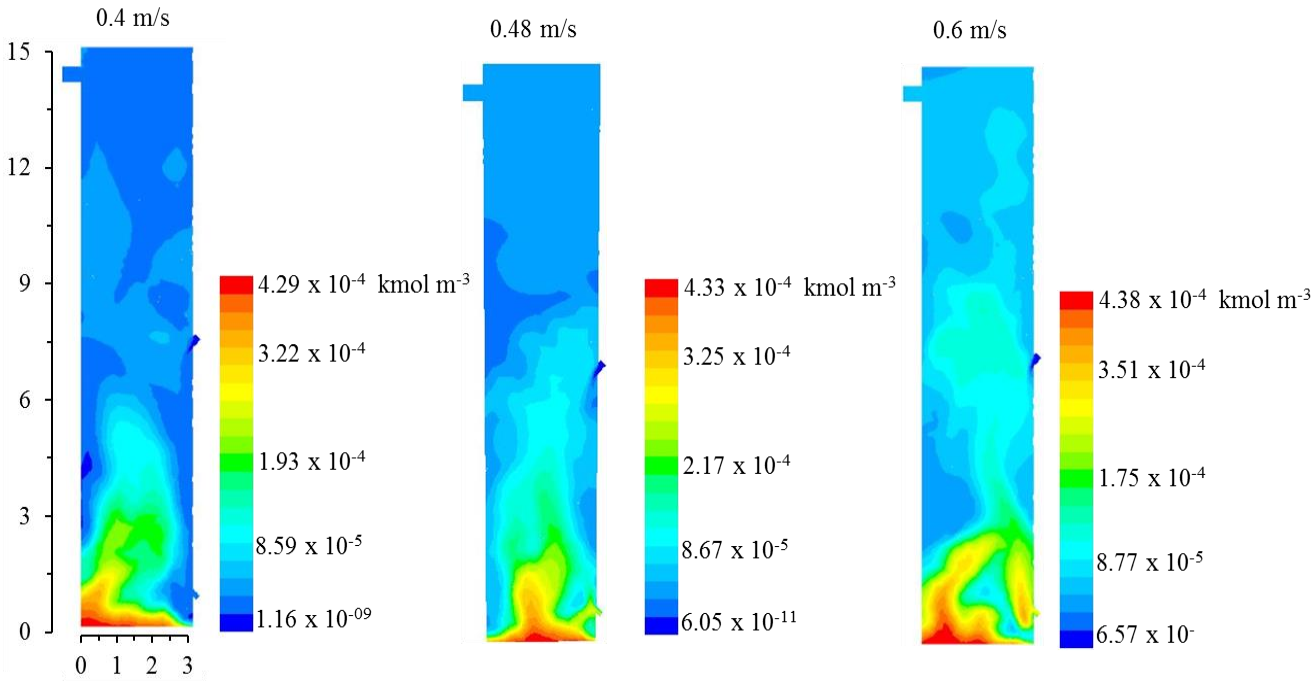

Fig. 4.24: Time-average contours for the analysis of fluidizing velocities Condition (MOL4A diameter =350µm, rate constant =0.003/s, DME mass fraction 1wt%, Temperature 25 ºC, 1bar).

4.3.3.4 Effect of reaction rate constant

The effect of rate constant on the adsorption process is analysed in this section, the adsorption rate constant is dependent on the adsorbent utilised in the adsorption of the gas, the modification or improvement of the adsorbent would enhance the rate constant achieved for the process. In this parametric analysis, it is assumed that these modifications have already been developed to increase the performance of the sorbent. DME adsorption was modelled by increasing the rate constants to 0.006/s and 0.012/s. There are numerous methods or means of enhancing the adsorbent performance through pre-treatments such as heating, reacting with chemicals and the methods of producing the adsorbents. For example Ahmadpour et al, [152] treated the adsorbent for removing strontium by subjecting the solid to a chemical reaction, this enhanced its adsorption capability by altering some ions on the solid surface which impacted the functional groups. The adsorbent used for this work was not treated and suggests that the performance can be improved if considerable treatments were conducted for the adsorbents.

Fig. 4.25 depicts the area-averaged DME concentration and removal along the bed height with other conditions remaining unaltered. It shows that DME removal improved as the rate constants were increased. The concentration of the gas along the bed height for decreased as the rate constants were increased this inevitably meant that the amount of the gas removed along the bed increased as in comparison to the base case. The trend was similar as the base case where the bottom of the bed with higher concentration of the gas exhibited lower removal efficiency but higher efficiency towards the upper section of the bed. DME concentration equally showed reduction in its concentration along the bed as the rate constant was increased as expected. These trends are in agreement with work conducted by [4,150] for the adsorption of CO_2 from a flue gas, the authors work projected an increase of adsorption and removal efficiency of the gas at increased rate constants.

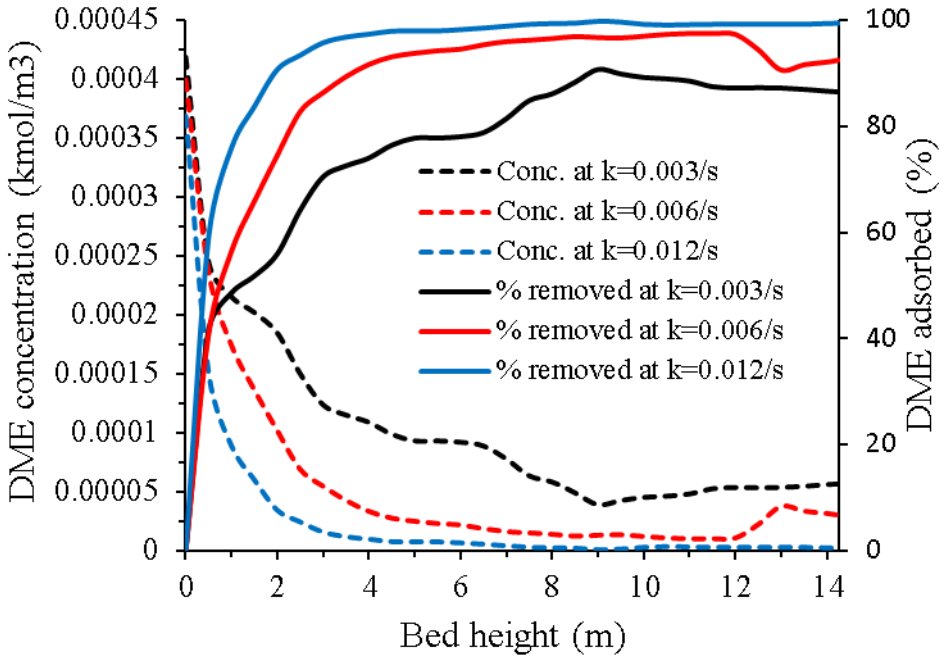

Fig. 4.25: Effect of increasing the rate constants to area-averaged DME concentration along the bed height and its percentage removal from the top outlet of the bed Condition (MOL4A diameter =350µm, DME mass fraction 1wt%, Temperature 25 ^{o}C, 1bar, velocity 0.48 m s^{-1})

Fig. 4.26 shows the DME removal efficiency at different rate constants from the top exit of the bed. The curve is in agreement with the observations in Fig. 4.27 on the DME concentration and removal distribution along the bed. The increase of the rate from its base case to 0.006/s increased DME removal to 95.42% from 86.57%. Further increase of the rate constant to 0.012/s improved the removal efficiency to 99.01%. The curve from the graph shows a steady increase which suggests that further increase of the rate constants resulting from improved or modified catalyst will continuously increase the removal efficiency in the fluidized bed system.

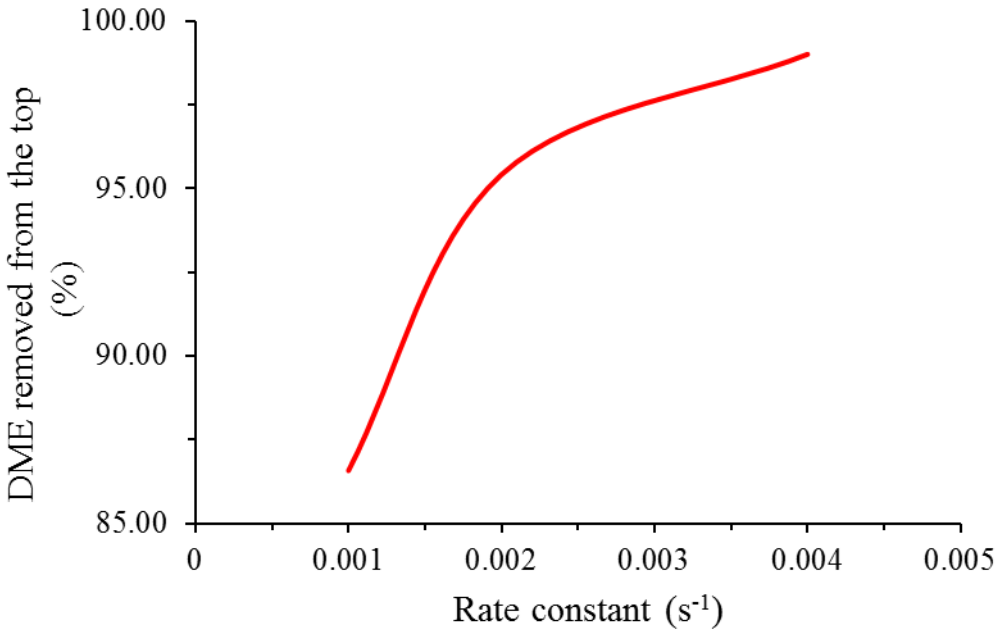

Fig. 4.26: DME removal at the top exit at different rate kinetics. Condition (MOL4A diameter =350µm, DME mass fraction 1wt%, Temperature 25 ^{o}C, 1bar, velocity 0.48 m s^{-1})

Fig. 4.27 depicts the contour for DME concentration distribution along the bed height at different rate constants. As expected, higher presence of the gas at lower rate constant was seen due to the less adsorption occurrence which meant less amount of the gas is removed from the fluidized bed system as unreacted gas. It further showed higher removal efficiency and lower distribution of the gas concentration in the fluidized beds system for increased rate constants from the base case. The concentration of the gas reduces as the rate constant was increased and contour for the rate constant at 0.012/s shows lower concentration of the unreacted gas in the system, this means that most of the gas had been adsorbed or prevented from leaving the system from the top exit. The observations suggest that at increased DME inlet concentration, higher rate constant would remove the gas effectively in contrary to the observation in section 4.3.3.1, where the rate of removal of the gas was reduced due to increased DME inlet concentration.

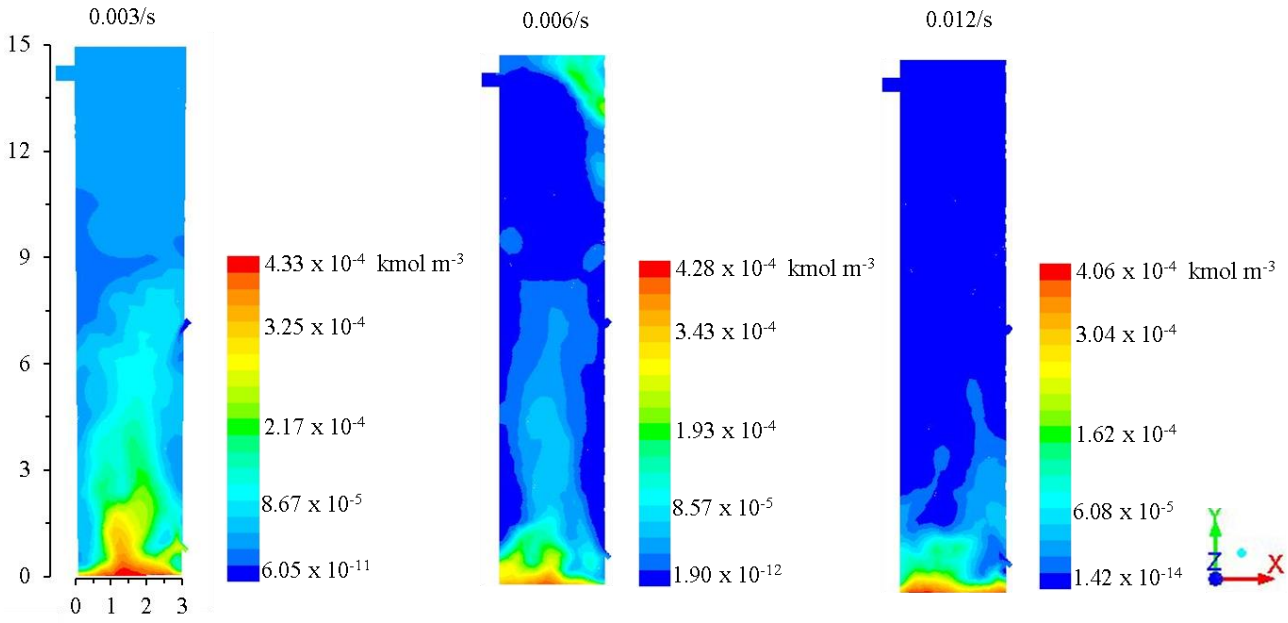

Fig. 4.27: DME concentration along the bed height at different rate constants. Condition (MOL4A diameter =350µm, DME mass fraction 1wt%, Temperature 25 ^{o}C, 1bar, velocity 0.48 m s^{-1}).

Table 4.12 shows the mass balance of the gas around the bubbling bed, it's evident that amount of DME leaving from the top exit decreased as the rate constants increased which shows more of the gas had been adsorbed or removed. The amount adsorbed equally showed an agreement as expected by increasing as the rate constant was increased. These observations further confirms that the improvement of the adsorbent to increase the rate constants will enhance the removal of DME from the gas mixture, this is consistent with the rate equation applied in the implementation of adsorption in the fluidized bed system.

Table 4.12: Effect of rate constant on time-averaged mass flowrate of DME leaving bubbling bed Condition (MOL4A diameter =350µm, DME mass fraction 1wt%, Temperature 25 ^{o}C, 1bar, velocity 0.48 m s^{-1})

Rate constant (/s)	DME exiting from top		DME exiting bottom		DME consumed (on MOL4A solid)	
	kg s^{-1}	%	kg s^{-1}	%	kg s-1	%
0.003	0.0085	12.28	0.0008	1.14	0.0599	86.58
0.006	0.0027	3.95	0.0005	0.65	0.0660	95.40
0.012	0.0004	0.61	0.0003	0.38	0.0685	99.01

4.3.4 Adsorption Analysis of Base Case for Second Rate Kinetics

The second rate proposed was investigated using similar conditions and FLUENT settings like the base case for the first rate equation. The purpose of the second rate equation is to examine the

application of Freundlich model in the determination of the equilibrium concentration for the pseudo-first order rate equation as discussed in Chapter 3 of this project. The results from the second rate equation will be compared to the first rate to examine the difference between the two rates. Knowledge from the comparison will facilitate the selection of appropriate model for future simulation studies for the adsorption of DME gas.

Fig. 4.28 depicts the DME concentration profile contour distribution along the fluidized bed height. DME concentration profile decreased as a height increased, the lower section of the bed had a sharp variation in concentration compared to the upper section. This is attributed to the solid concentration around this region which is higher and promotes higher reaction. The trends and distribution of DME concentration in this second proposed rate are very similar to the observation for first rate equation. DME concentration exiting the bed from the top at around bed height of 14.25m was 5.42 x 10^{-5} kmol m^{-3} with a removal percentage of ~87%. This suggests that the method applied in the derivation of the equilibrium concentration using Freundlich expression agreed well with the first proposed rate. The agreement between the two proposed rate equations evidently suggests that the assumptions as discussed in chapter 3 were reasonably appropriate. This further recommends the utilization of any of the two methods in the simulation of DME adsorption for future works. The Freundlich constants obtained using MATLAB for the second proposed rate, effectively makes the method more challenging. For this reason, first proposed rate equation, which was based on a simpler approximation would be recommended. However, this could be influenced by availability of data.

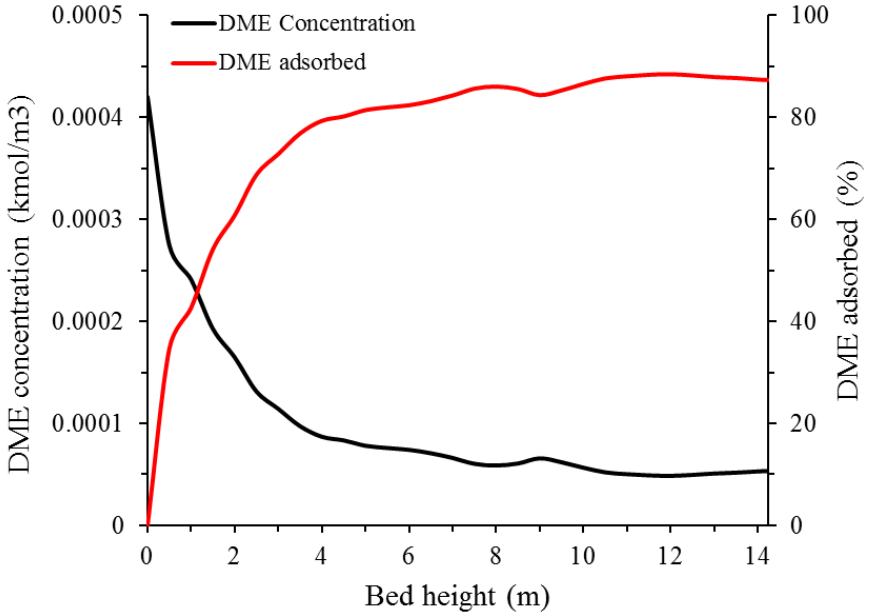

Fig. 4.28: Area-average distribution of DME concentration along the bed height and the percentage of DME removed from the process for rate equation 2. Condition (MOL4A diameter =350µm, rate constant =0.003/s, DME mass fraction 1wt%, Temperature 25 ^{o}C, 1bar, velocity 0.48 m s^{-1}).

Fig. 4.29 depicts the contour for the solid volume fraction, DME concentration and heterogeneous reaction rate for second proposed rate. The behaviour of the concentration suggests diminishing amount towards the upper section of the fluidized bed due to consumption of the gas instigated by the reaction rate. The bottom of the bed with more densely distributed solid volume fraction shows more reactive activity according to the heterogeneous reaction rate contour. The reaction is faster around these regions in the bed and results in the consumption of most DME gas entering the system. The reduction of unreacted gas which leaves towards the top depends on how effective the kinetics is as seen in the contour. The distributions observed in the bed are similar to the investigation for the first proposed rate. This further confirms the agreement between the two models that have been investigated for the adsorption of DME gas using pseudo-first order reaction kinetics.

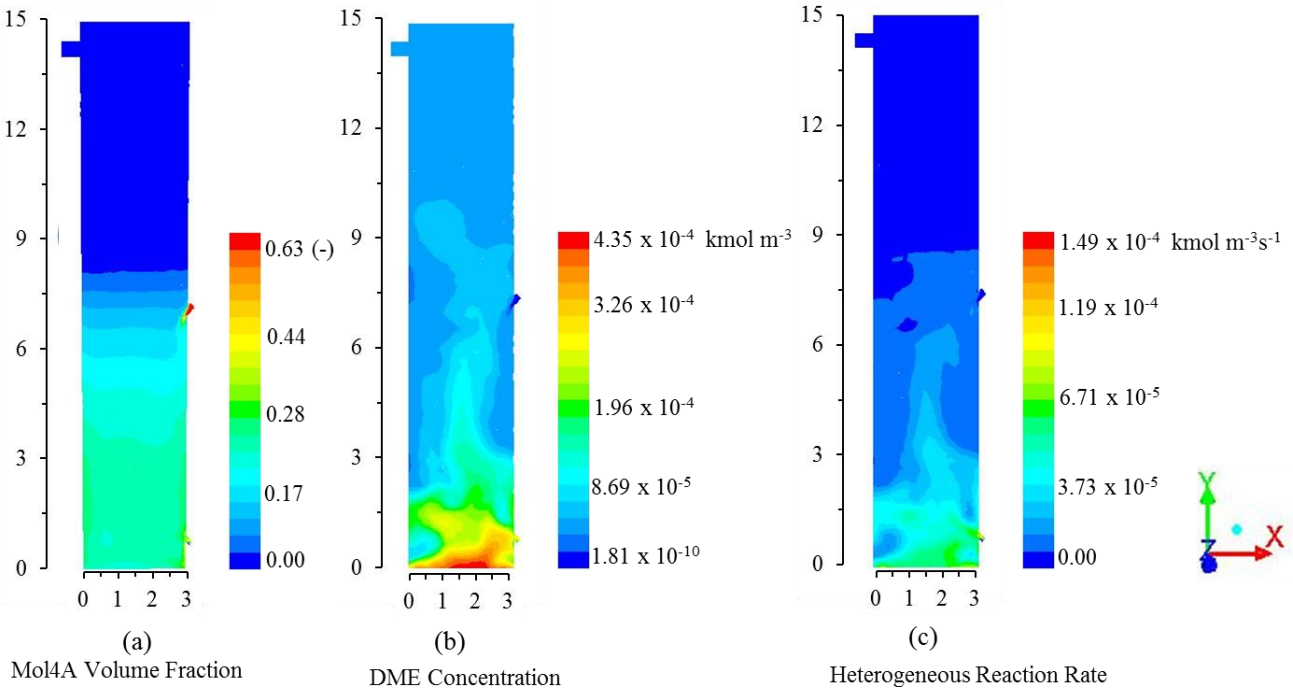

Fig. 4.29: Time-average contours for the analysis of rate equation 2. Condition (MOL4A diameter =350µm, rate constant =0.003/s, DME mass fraction 1wt%, Temperature 25 oC, 1bar, velocity 0.48 m s-1)

4.3.4.1 Amount of DME adsorbed by the solid reaction rate 2

Table 4.13, illustrates the mass flowrate balance in the determination of the adsorbed DME gas leaving from the lower section of the bed. The mass flowrates were averaged over simulation times from 60s to 80s as suggested by the steady state time of simulation (see Fig. 4.30). The percentage of the DME mass flowrate leaving from the top of the fluidized bed was 11.68% while the amount adsorbed was 87.07%. The remaining unconsumed gas leaving from the bottom section could be assumed to exit the bottom side attached with the solid sorbent, this evidently postulate that the total amount of DME gas adsorbed ~88.32% (overall bed performance). However the adsorption rate

performance in the fluidized bed would be 86.58% if the bottom DME amount was accounted as some level of ineffectiveness from the rate kinetics.

Table 4.13: DME mass flowrate exiting fluidized bed system rate equation 2. Condition (MOL4A diameter =350µm, rate constant =0.003/s, DME mass fraction 1wt%, Temperature 25 ^{o}C, 1bar, velocity 0.48 m s-1)

		Inlet gas (kg s^{-1})	$Exit_{top}$ (kg s^{-1})	$Exit_{bottom}$ (kg s^{-1})	Consumed (kg s^{-1})
DME	IN	0.0692	-	-	-
	OUT	-	0.0080	0.0009	0.0603

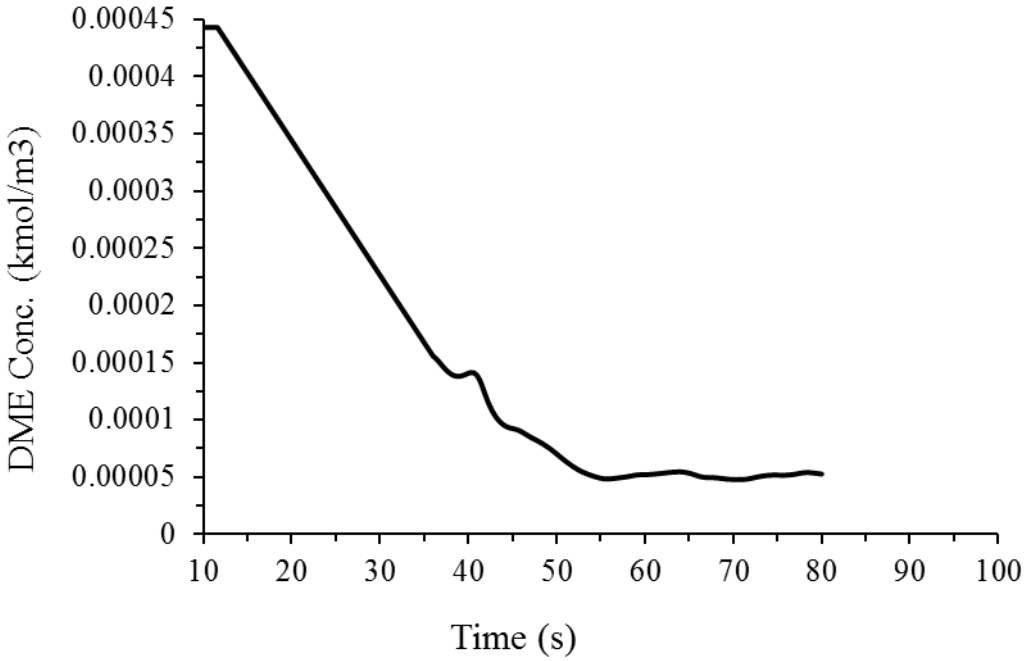

Fig. 4.30: Exit DME concentration from the top section of the bed over flow time

Parametric analysis to investigate the behaviour of second proposed rate was neglected in this study after reviewing the behaviour of its base case in comparison with the first proposed rate. The closeness of the two proposed rates suggests that the parametric analysis for rate equation 2 would be unnecessary as it will be very closely matched with the parametric analysis for rate equation 1. This was the reason the parametric analysis for the second proposed rate was aborted in this study.

5. CHAPTER 5: DME STEAM REFORMING AND PARAMETRIC ANALYSIS

5.1 Introduction

The continuous reliance on fossil fuel for energy supply has resulted in the establishment of energy regulations to limit pollution of the atmosphere. Hydrogen is one of the alternative sources of clean energy and has high potential applications, including the transportation sector and stationary power generation systems. It is a fuel that produces zero emission (carbon and particulate free) when burned in air. Most importantly, hydrogen has a higher energy content compared to other sources such as gasoline, ethanol, wood and natural gas. Traditionally, hydrogen is produced from fossil fuels by steam reforming of natural gas or heavy hydrocarbons; however recently, there is growing interest in hydrogen produced from other sources, such as biomass, methanol (MeOH) and Dimethyl Ether (DME). DME is particularly attractive for hydrogen production because it contains higher mass fraction of hydrogen (13 wt%) and the reforming process can be carried out at a lower temperature (200-350 ^{o}C), hence, less energy intensive compared to natural gas reforming for instance [153,154].

The idea of the proposed dual fluidized bed system for which the adsorbed DME from the bubbling bed is reformed by steam to produce hydrogen is established in this chapter. The simulation of DME-SR was initially proposed for an industrial scale Dual Fluidized Bed (DFB) system to justify the application to industrial sponsor. The operating conditions and parameters were assumed, the purpose was to get a working system that would show the potential of commercial implementation. The knowledge of the assumed system would then be applied to the industrial case.

The arrangement of the proposed DFB system and the particulate flow throughout the system is described schematically in Fig. 5.1. This system mainly consist of two coupled reactors; one for catalytic steam reforming of the DME and another for the thermal regeneration of the catalyst. The solid and gas mixture leaving both reactors are separated using two cyclones as part of the whole closed loop system. In this study, the focus is on the DME-SR reactor; hence the cyclones and regeneration reactor are outside the scope of the study. The steam reforming reactor is assumed to operate in a riser mode and has the dimensions of 3 m diameter and 15 m height. The choice of this is size is made to be close to a commercially proven scale of a CFB reactor (e.g. PYROFLOW CFB system of Goodrich Co in Illinois U.S.A as reported in [4]). The riser is equipped with three openings; at the bottom for introducing the fluidizing steam, at the lower part of the wall for catalyst and DME feeding and at the top part of the wall for the exit of the spent catalyst and product gases.

The selected reactions and kinetic models for DME-SR bed for this study was validated with a published experimental work conducted for a laboratory scale fluidized bed; there was no mention of any assigned or formulated kinetics for the reactions by the author. The experimental work was based on the reaction of the gases assisted with the selected catalyst while the products from the beds analysed. The analysed reactor performance and products compositions were then compared to a simulated case using similar reactor condition to literature with selected kinetics as discussed in chapter 3. The validated models and parametric analysis performed for an industrial DME-SR case provides a platform for the application of similar model to the proposed project.

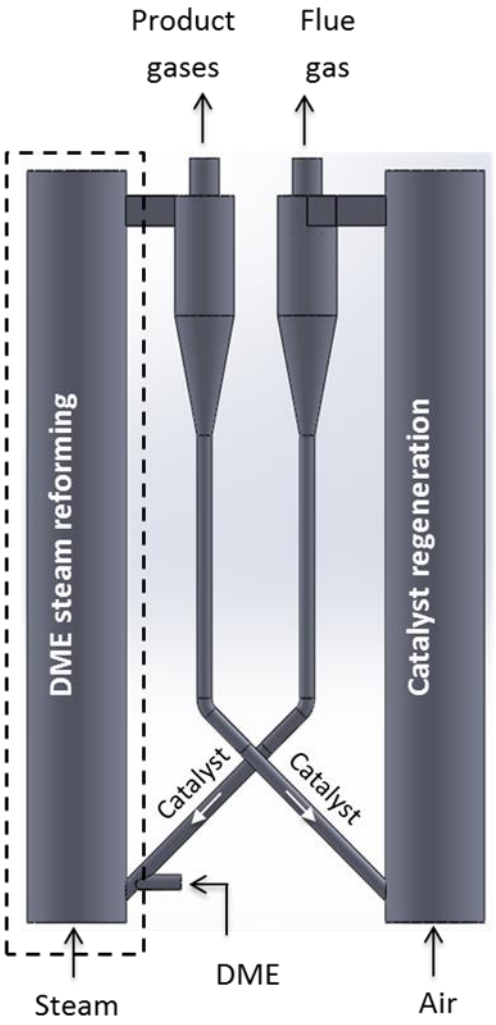

Fig. 5.1: Industrial proposed DFB system for DME-SR process to analysis the selected kinetics.

5.2 Literature Review on Circulating Fluidized Bed

This section will discuss the CFB hydrodynamic behaviour, this will provide platform to validate the design of the CFB for the DME-SR process. A subsection will examine some literature works on the CFD or numerical studies on DME-SR.

5.2.1 Literature review on CFB hydrodynamics

The study of hydrodynamics is an essential aspect of the design of CFB systems; there are various works that have been done in this area using computational fluid dynamics (CFD) to describe CFB behaviour.

Guan et al [132] investigated the hydrodynamics of an interconnected fluidised bed comprising of a circulating and bubbling beds in a loop system using a 3D two-phase multiphase flow. It was observed that effect of drag model on the hydrodynamics for fluidized systems was significant. The author proposed that both the Syamlal-O'Brien and Gidaspow drag models gave good predictions compared to the experimental results. For the CFB riser, it was observed that the solid volume fraction at the bottom part of the riser was denser compared to the upper part, however this was reversed when the superficial velocity was increased. The reverse was due to increase in the drag force resulting from the increase of the superficial velocity. Three distinctive areas were noticed for the CFB solid volume fraction distribution and solid velocities. These are the entrance region (solid entering the riser), bulk region (middle of the riser) and exit region (solid leaving the riser).

Zhang et al [155] studied the hydrodynamics of an industrial 150MWe scale CFB boiler in 3D model to analyse the pressure and solid volume fraction distribution around the loop. It was observed that the pressure gradient at the bottom of the bed was larger compared to the pressure towards the top of the furnace. The solids volume fraction was denser at the bottom of the bed and dilute around the top of the bed with the centre more dilute than the walls which was denser. It was also observed that the vertical solid velocity were mainly in the upward direction in the middle of the bed while downward around the walls which means solids were falling backwards (back-mixing).

Benzarti et al [51] explored the hydrodynamics character of gas-solid flow in a turbulent bed using 2D two fluid model implemented through KTGF in CFB on a Geldart B particle. Simulations were conducted for laminar and k-ε turbulence models, it was observed that k-ε flow behaviours were more in agreement with experimental results obtained compared to laminar flow model. Solid-solid interaction modelled through the restitution coefficient which represents the elasticity of the particles collision with each other was examined between inelastic (0) and fully elastic (1), it was observed that at lower restitution coefficient the dense region became more pronounced due to increment in the formation of bubbles while increasing the restitution made the dilute region more pronounced. Restitution coefficient of 0.9 was recommended as ideal case that agreed well with experimental work. Another condition checked was the effect of specularity coefficient which measures the fraction of collisions of solids that produces sufficient momentum that transfers solids to the walls. Specularity coefficient was examined between the range of 0 (smooth walls) and 1(rough walls), at zero there was no friction between the particles and wall which meant particles moved downwards when it contacts the wall of the bed hence making the bottom part of the bed more dense. Specularity coefficient at 1

reduces the downward movement of the solid when in contact with the walls due to existence of friction. It was observed that specularity coefficient closer to 1 agreed better with experimental works.

Verma et al [156] investigated the effects of system pressures on the hydrodynamics of a 3D fluidized bed system using a two fluid (gas-solid) model. The pressure range examined was between 1 to 32bar. It was observed that at lower pressures below 4 bars only small difference in porosity increase were witnessed were seen mainly in the centre while much larger difference in increase of porosity were observed at 4-32bars. It was also observed that at lower pressures substantial increase in bubble diameter is seen while at higher pressures a decrease in bubble diameter is seen.

Huilin et al [157] studied the hydrodynamic motions of particles in a gas bubbling bed system through KTGF with interest on the gas-particles and particle-particle interactions in the bed. The flow behaviour at 1.6ms^{-1} showed formation of non-periodic bubbles which led to the chaotic up and down movements that benefited particle recirculation in the bed. Particle velocities for different particle sizes were examined with, it was observed that initially before 10s both particles had upward movement in the middle and downward movement around the walls; however, by 10s non-homogeneity of the flow was more obvious with noticeable segregation within the bed. Larger particles settled at the bottom with the smaller particles moving upwards. The solid volume fraction of the particles at different fluidizing velocities shows that at lower superficial velocity, the smaller particles become accumulated around the upper part of the bed while at higher fluidizing velocity there was more homogeneity as both particles becomes more evenly distributed. The effects of fluidizing velocities on the particle sizes also showed that the bed height increased with decreasing mean particle diameter.

5.2.2 Literature review on DME-SR modelling

Limited studies on numerical simulation have being performed for the DME-SR process; it is believed that these modelling approaches would enable further insight in the optimization and development of the process.

Yan et al [115] investigated the steady state numerical model for DME steam reforming using FLUENT CFD to investigate the effect of better mass and heat transfer in a micro-reactor compared to a fixed bed. Micro-reactor DME conversion efficiency was between 70-97% compared to fixed bed 40-85% at the same temperature range of 240-280^{o}C. It was observed that increasing steam to DME molar ratio and reaction temperature increased DME conversion and hydrogen yield.

Li [107] performed a numerical study using STAR-CD software to investigate the fluid flow, heat transfer and chemical reactions during DME-SR in a fixed bed. The DME-SR kinetics was based on CuO-NiO/Al_2O_3/ZrO_2+ZSM-5 catalyst. The results have shown fast decrease of the temperature at the entrance region of the reactor because of the endothermic nature of the DME-SR reaction. The temperature however increased along the axial length of the bed to the exit. Li et al [158] further

analysed the parametric studies for the DME-SR using DME from exhaust gas into a porous catalytic bed (fixed bed) using Comsol CFD model. It was discovered from the results that DME conversion and hydrogen yield increased significantly when the DME to steam mass ratio was decreased. It was also observed that an increase in the exhaust DME gas into the fixed bed increased the DME conversion and hydrogen yield.

5.3 Results and Discussion

This section will give detail insight in the analysis of the CFB bed for DME-SR which encompasses hydrodynamic, base case and parametric analysis. It will also cover the validation of the selected kinetics.

5.3.1 Preliminary Hydrodynamic Features of the Designed CFB

For the purpose of the hydrodynamic study, a case with an assumed DME flowrate was used to investigate the hydrodynamic behaviour of the CFB. The two solids (ZSM-5 and $CuO/ZnO/Al_2O_3$) have physical property similarities and for this reason the hydrodynamics for one of the solids was used.

Table 5.1: The reactor operating conditions used in the simulation

Parameters	Operating condition
Steam	
Inlet temperature	300 ^oC
Flow rate	5.86 (kg/s)
DME	
Inlet temperature	300 ^oC
Flow rate	3.0 (kg/s)
Catalyst*	
particle diameter	150 μm (both catalyst)
Density	1300 kg/m3 (CuO/ZnO/Al2O3)
	720 kg/m3 (ZSM-5)
mass flow rate	200 kg/s (100 kg/s each catalyst)
Reactor dimensions	
Diameter	3.0 m
Height	15.0 m

* *specifies as two separate solid materials: $CuO/ZnO/Al_2O_3$ and ZSM-5*

5.3.1.1 Entrance and exit effects on solid volume fraction distributions

Fig. 5.2(a) shows the volume fraction of the solid along the centre of the bed. The bottom and the top of the bed show a characteristic asymmetrical feature of most CFB beds [159], this results from the entrance and exit effect of the solid. Fig. 5.2(b) shows where these effects are in the bed, solid entering at an angled inlet at higher velocity collides with the left wall which causes recirculation of the solid before moving into the core annular area. At the exit region, solids towards the top of the bed recirculate after contacting the top wall boundary, the right wall shows higher concentration of the solid due to the exit compared to the centre and left wall. The left and right wall regions have more distribution of solid volume fraction because of the friction between the wall and the core of the bed; however the bottom of the left wall had less due to the entrance effects on the solids. The core annular region has a more uniform symmetrical feature. These features observed are in agreement with literatures regarding CFB beds in industrial scale [132,155].

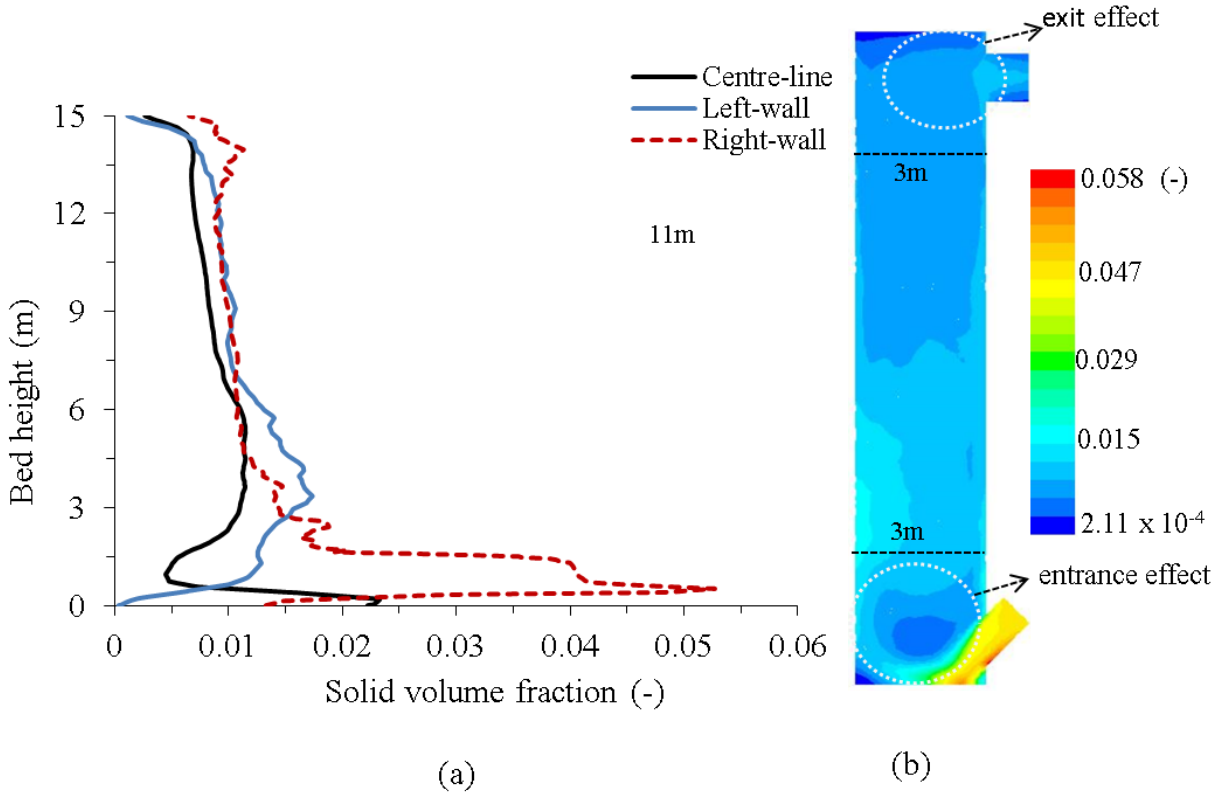

Fig. 5.2: Time average solid volume fraction along the centre of the bed (a) contour showing exit and entrance effects on the CFB bed.

Fig. 5.3 further illustrates how the solid is distributed around the bed, the bed is divided into the bottom and top represented by 3m and 11m respectively (see Fig. 5.2(b)). The bottom is asymmetrical due to the effects of the solid entrance while towards the top of the bed a more symmetrical feature of the solids which shows uniform distribution is prominent. The wall regions (left-wall and right-wall) along the bed height has higher volume fraction which results from the back mixing of solids. Fig. 5.3

also demonstrated that the upper part of the CFB bed was more dilute in comparison with the lower region. This has being attributed to particles falling backwards and is a common feature in CFB beds as discussed in the literature review section of this chapter.

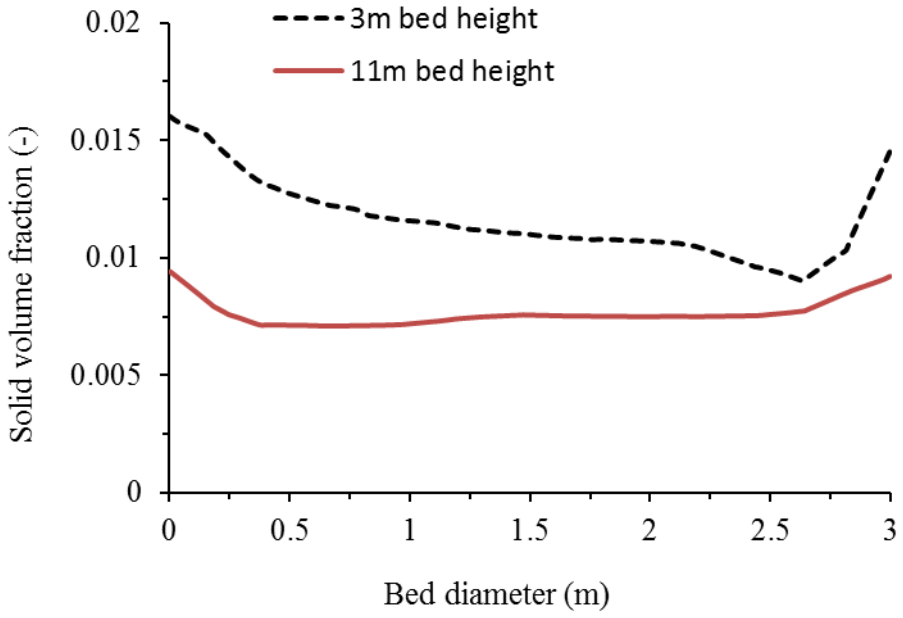

Fig. 5.3: Time average solid volume fraction along bed diameter taken at bed height =3m and 11m.

5.3.1.2 Gas and solid axial velocity profiles

Fig. 5.4 shows the contours and the curves of the axial velocities of the gas and solid phases for selected parts of the bed representing the top and bottom. The trend for the gas and solid velocities are similar however presence of slip velocity between the phases due to density difference is the reason of the gap between the phases. The lower section of the bed is more asymmetrical in shape compared to the top part which agrees well with the volume fraction distribution in Fig. 5.2. The negative axial velocities around the top and the walls agree well with the observation of for the solid volume fraction which showed back mixing and recirculation around the regions. The contour Fig. 5.4 (a) and Fig. 5.4(c) demonstrates the impact of the entrance and exit effects on the gas and solid velocity distribution. The left wall shows higher velocities resulting from the collision of the solid and gas towards that section of the bed resulting from the incoming solid from the side of the reactor.

In Fig 5.4, it appears that the average gas velocity decreases along the riser. The reason is attributed to the inlet effect in the lower section of the bed. This inlet effect created high velocities due to contact with the left, this consequently increased the velocities to the right wall. The preliminary hydrodynamic simulation was done within the lower range of conditions investigated.

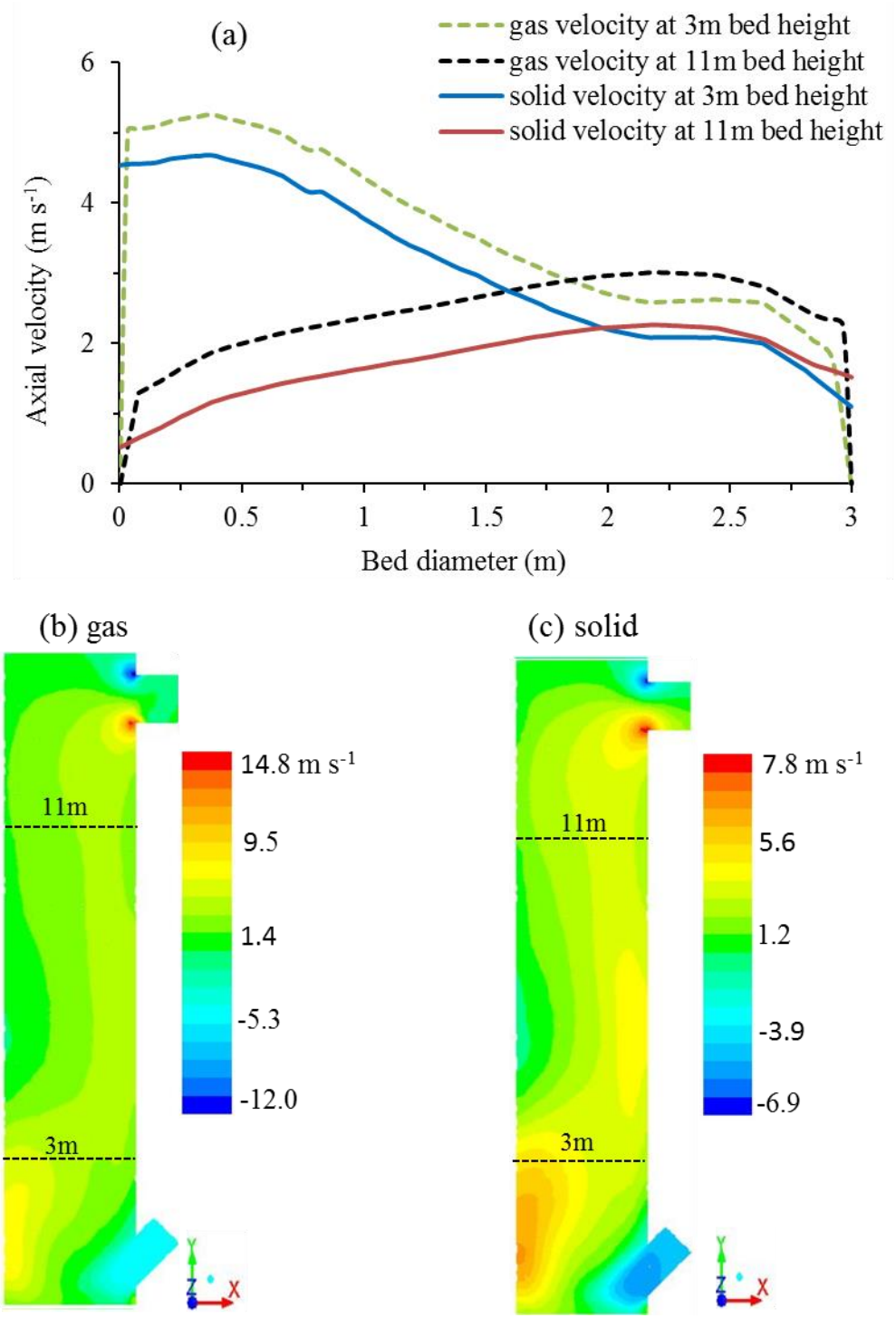

Fig. 5.4: (a) Time average gas and solid axial velocities at different bed heights representing bottom and top of the bed (b) Time average contour of the gas axial velocity (c) Time average contour for solid axial gas velocity.

5.3.2 Simulation of base case condition

An initial simulation was conducted at certain conditions to examine the selected kinetics for the study to provide a platform for validation of the models. The condition of the case was at temperature of 300 ^{o}C, Steam to DME molar ratio of 7.68 and 37104 mlg^{-1} h^{-1} space velocities. The steam to DME molar ratio was 7.68 to favour easier fluidization of the system due to the large scale nature of the bed, the remaining conditions can be seen in Table 5.1

Table 5.2: The reactor operating conditions used in the simulation for the base case

Parameters	Operating condition
Steam:	
Inlet temperature	300 ^{o}C
Flow rate	3.0 (kg/s)
DME:	
Inlet temperature	300 ^{o}C
Flow rate	9.0 (kg/s)
Catalyst*:	
Particle diameter	150 µm (both catalyst)
Density	1300 kg/m3 ($CuO/ZnO/Al_2O_3$)
	720 kg/m3 (ZSM-5)
Total mass flow rate	600 kg/s (300 kg/s each catalyst)
Calculated space velocity	37104 ml g_{cat}^{-1} h^{-1}
Reactor dimensions:	
Diameter	3.0 m
Height	15.0 m

* *specified as two separate solid materials: $CuO/ZnO/Al_2O_3$ and ZSM-5*

5.3.2.1 Validation procedure

In order to validate the model, comparison has been made with an experimental data reported by [1] for DME-SR in a simple bubbling fluidized bed of 0.022 m diameter with the bed material consisting of the same bifunctional catalyst considered in this study ($CuO/ZnO/Al_2O_3$+ZSM-5). In validating the proposed model, the exact experimental reactor geometry and operating condition used in the experiment has been applied in the simulation. These conditions are summarized in Table 5.3. The same simulation procedure described in Chapter 2 for the CFB case riser has been applied here. There was no given gas superficial velocities from the literature. However, the steam to DME molar ratio given was 3:1, the gas superficial velocity was then calculated using space velocity. Same modelling parameters for the bubbling bed were used.

Table 5.3: Operating condition for the validation simulation

Parameters	Operating condition
Steam to DME molar ratio	3:1
Space time ($W/F_{DME,0} = g_{catalyst}\ h/g_{DME}$)	0.2
DME partial pressure (bar)	0.16
DME inlet temperature (°C)	300
Steam inlet temperature (°C)	300
Catalyst particle diameter (µm)	150
Reactor diameter (m)	0.022

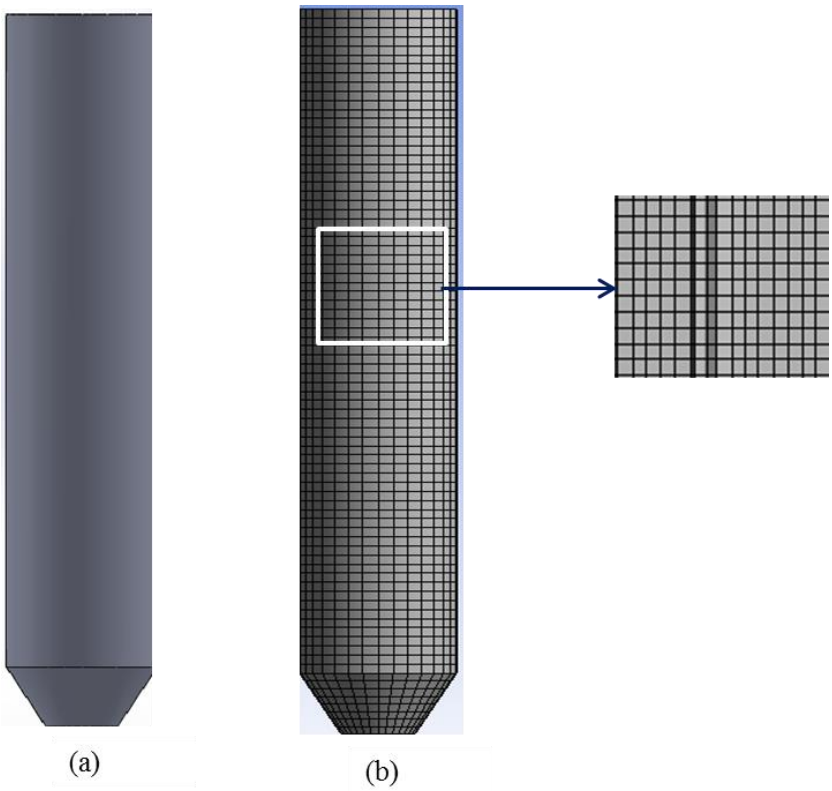

Fig. 5.5: Computational domain (a) and meshing (b) used for the simulation of the experimental work of Vicente et al [1].

The validation has been made by comparing the experiment measurements and predictions of the product gas composition, DME conversion (C_{DME}), MeOH conversion (C_{MeOH}), hydrogen yield (Y_{H_2}) and carbon dioxide selectivity (S_{CO_2}). Following [1,116], the DME conversion was given by:

$$C_{DME} = \frac{n_{DME,in} - n_{DME,out}}{n_{DME,in}} \times 100 \tag{5.1}$$

where $n_{DME,in}$ and $n_{DME,out}$ are the molar flowrate of the DME at the inlet and outlet of the reactor respectively. Similarly the methanol conversion (C_{MeOH}) was given by:

$$C_{MeOH} = \frac{n_{MeOH,prod} - n_{MeOH,out}}{n_{MeOH,prod}} \times 100 \quad (5.2)$$

where $n_{MeOH,prod}$ and $n_{MeOH,out}$ are the molar flow of methanol produced from the DME pyrolysis reaction and the unreacted methanol leaving with the product gas respectively. The former is assumed to be equal to the number of moles of DME consumed in the process. The percentage of hydrogen yield was given by:

$$Y_{H_2} = \frac{1}{6}\frac{n_{H_2}}{n_{DME,in}} \times 100\% \quad (5.3)$$

where the number 6 represent the stoichiometric coefficient of the hydrogen component produced in the reactions. The carbon dioxide selectivity was defined in terms of the molar flow ratio of carbon dioxide produced to the total moles of the carbon present in the product as follows:

$$S_{CO_2} = \frac{n_{CO2}}{n_{CO} + n_{CO_2}} \quad (5.4)$$

where n_{CO} and n_{CO_2} are the molar flowrate of carbon monoxide and carbon dioxide at the reactor outlet respectively.

5.3.2.2 Analysis of base case

This section presents first a validation of the proposed model by comparing the predictions with the reported experimental data produced by [1] using a bubbling fluidized bed. This is then followed by presentation of the predicted data and analysis of the CFB performance in terms of the flow hydrodynamics, gas residence time, temperature distribution and product gas composition for a selected operating condition.

5.3.2.2.1 Validation of the model

Fig. 5.6 shows a comparison between the model predictions and the experimental data. In Fig. 5.6(a), there is clear reasonable match between the two sets of data. In Fig. 5.6(b), the predicted mole fraction of hydrogen and DME are also in reasonable agreement with the experimental data, however the carbon monoxide, carbon dioxide and methanol are all over predicted. It is difficult to give precise reasons for such a discrepancy; however it has to be taken into consideration that the model assumes ideal conditions by neglecting the effects of catalyst deactivation. The experimental work of [1] has indicated possible catalyst deactivation by coke deposition on the metallic catalyst at temperatures above 275°C. According to [111,160] such a phenomena could have a complex effect on the equilibrium shift between the DME hydrolysis and methanol steam reforming. Another reason that may have contributed to this discripancy is the possible formation of small quantity of methane during the process. Some experimental studies have reported presence of small quantities of methane in the product gas, which is assumed to be generated from DME decomposition when a strong acidic function or high temperature is used [109,111,160]. In this study, such a reaction is neglected, and so did majority of the reported studies on DME catalytic steam reforming [104,161]. Finally, another

factor that is worth noting is the uncertainty about the side reactions during the DME-SR. A number of researchers have recommended more experimental work to reveal more details about the side reactions and its kinetics.

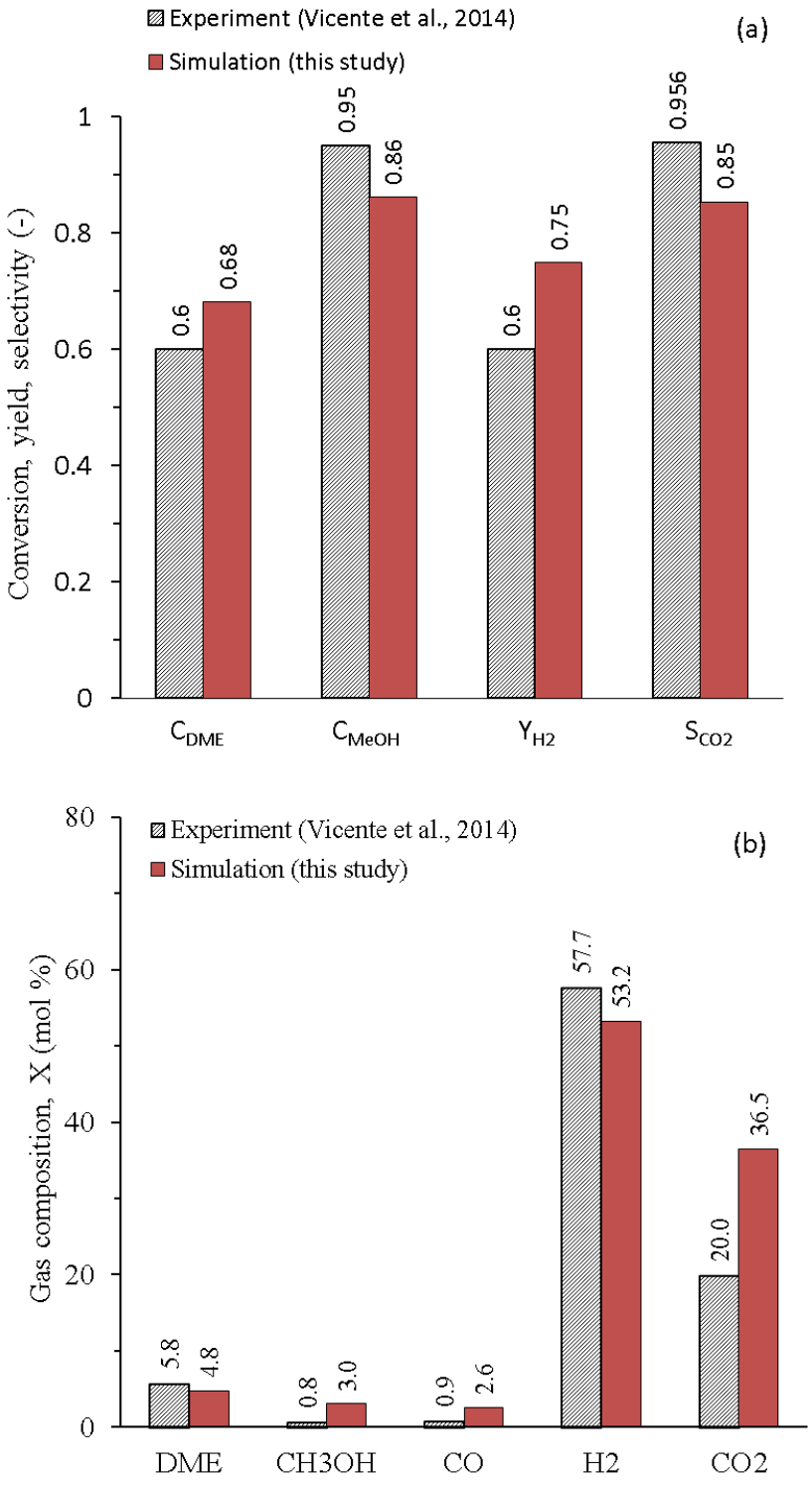

Fig. 5.6: Comparison between the predicted and experimental data (a) conversion, yield and selectivity (b) product gas composition (dry basis). Operating conditions: Inlet temperature=300 °C, space velocity=0.2 $g_{catalyst}$ h/g-DME, PDME =0.16 bar, steam to DME ratio.

5.3.2.2.2 Solid/gas distribution and velocities

It is desirable to have homogeneous flow patter and sufficient gas residence time inside the reactor in order to enhance the DME reforming reactions and increase the hydrogen yield. These can be analysed by looking at the solid volume concentration, which is a measure of the catalyst surface area available for reaction, and by estimating the average gas velocity, which is directly linked to the contact time or the gas residence time.

Fig. 5.7 shows the time-averaged contours of the solid volume fraction and vertical gas/solid velocities in a cross-section at the middle of the reactor. It should be mentioned that, the solid concentration and velocity presented here are for one selected solid phase because both catalysts, $CuO/ZnO/Al_2O_3$ and ZSM-5, have shown insignificant hydrodynamic differences due to their similarity in mass flow rate and minor differences in physical properties. Here, It is clear that the solid concentration is diluted and non-uniform (asymmetric). This non-uniformity is mainly due to the entrance effects (solid feeding from one side of the column). The extreme velocity spot near the exit is due to the sharp flow deflection at this region. It is important to note the back flow mixing and circulation of the gas and solid phases as indicated clearly by the negative or very low velocities in the upper left side and around the solid entrance at the bottom right in the velocities contour plots. Interestingly, these are the regions where the hydrogen concentration is highest, as will be demonstrated later.

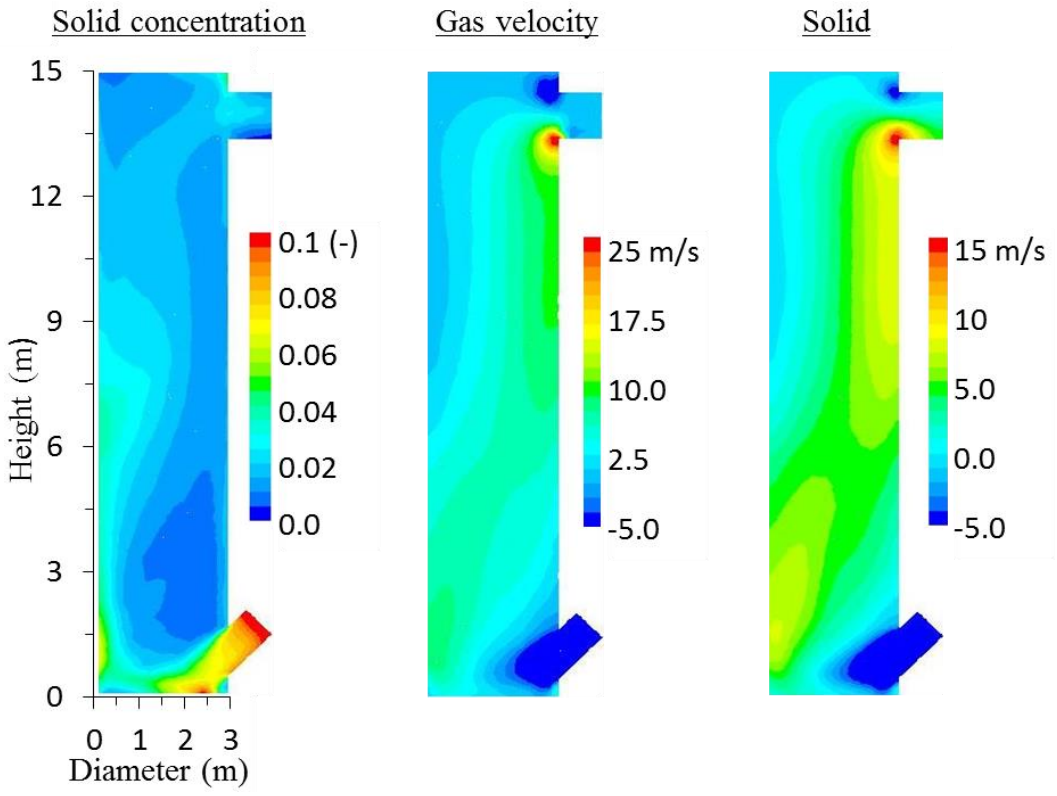

Fig. 5.7: Contour plots of the time-averaged solid (catalyst ZSM-5) volume fraction and vertical velocities of the solid and gas phases. The gas and solid velocities have been restricted to 25 m/s and 15 m/s respectively to allow better demonstration of the spatial distribution.

5.3.2.2.3 Gas residence time

The gas residence time is an important parameter defining the degree of contact between the gas and solid catalyst within the hot zone of the reactor. The information on the gas velocity, shown in Fig. 5.8, could be used for a first estimate of the gas residence time. Since there is clear evidence of considerable gas velocity variations and back mixing, as shown in Fig. 5.7, the gas velocity distribution and a mean gas velocity have to be calculated. For this purpose, an advanced numerical technique based on tracer method has been used. This is based on tracking an inert molecule of similar characteristics to the DME and steam mixture injected at the inlet of the reactor at time t =0 in a manner similar to pulse input [64].

The concentration of the tracer exiting the reactor was then monitored as a function of time to give a residence time distribution function $E(t)$ and a mean gas residence time was given by the area under the curve $E(t)$, as shown in Fig. 5.8 (more information about this method can be found in [64]). Using this method, the calculated mean gas residence time for the case considered here was 3.92s. Unfortunately, there is no experimental data on the recommended range of gas residence time for DME-SR in a CFB reactor, however, as a comparison, a study by [162] on methanol steam reforming in a micro-channel using copper–zinc catalyst has shown that a residence time of around 1.0 s is sufficient to achieve more than 80 % methanol conversion at the temperature of 350 ˚C. Clearly this much shorter time than what is used here because, unlike the methanol reforming. The complete reactions of DME-SR require additional time to accommodate for the first stage of the DME conversion to produce methanol. It is also recognized that the CFB reactor operates at a dilute suspension condition, thus requires more time for sufficient contact between the catalyst and gas.

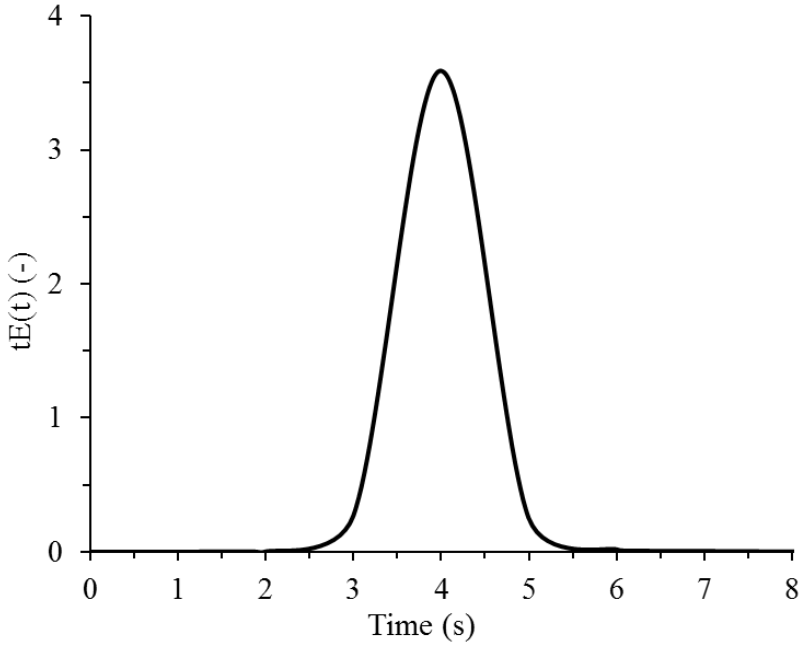

Fig. 5.8: The tE(t) curve used for the derivation of mean gas residence time.

5.3.2.2.4 Spatial distribution of temperature

The majority of the reported studies on DME and methanol steam reforming have been conducted on laboratory scale fixed bed reactors, with very little reference to the spatial variation of temperature, despite the well documented critical effect of the temperature on the reactor performance. The widely agreed range of temperatures for DME steam reforming using the catalyst considered in this study is within the range of 200-300 ^{o}C [115,116]. Though, Takeishi [108] recommended higher temperatures in the range of 300-350 ^{o}C in order to achieve excellent hydrogen production with less CO, however this was also reported to be dependent on the weight ratio between Cu and Zn in the $CuO/ZnO/Al_2O_3$ catalyst. The DME hydrolysis reaction is reported to be relatively slow and requires temperature higher than 200 ^{o}C, but it has to be noted that the metallic part of the bifunctional catalyst deactivates at temperatures higher than 325 ^{o}C as a result of coke deposition [1,105].

Fig. 5.9 shows the central-line time-averaged axial temperature profile of the gas and the contour plot in a cross-section at the middle of the reactor. In general, Fig. 5.9(a) show insignificant temperature variations along the reactor height, but there is a noticeable sharp temperature decrease in the lower part of the reactor between the bottom entrance and just above the catalyst entrance level, this is in agreement with Li et al. [107]. This is mainly due to the heat being consumed by the DME hydrolysis reaction, which is slightly endothermic. The observed temperature non-uniformity seen in the contour plot (Fig. 5.9(b)) is a reflection of the asymmetric flow structure and solid back mixing, as noted earlier. At the far top section of the reactor, the temperature increases and this could be attributed to the moderately exothermic water gas shift reaction (WGSR) associated with the increase in carbon monoxide formation in this region. This phenomenon is further confirmed by observing the spatial variation in the product gas composition inside the reactor, as will be discussed in the next section.

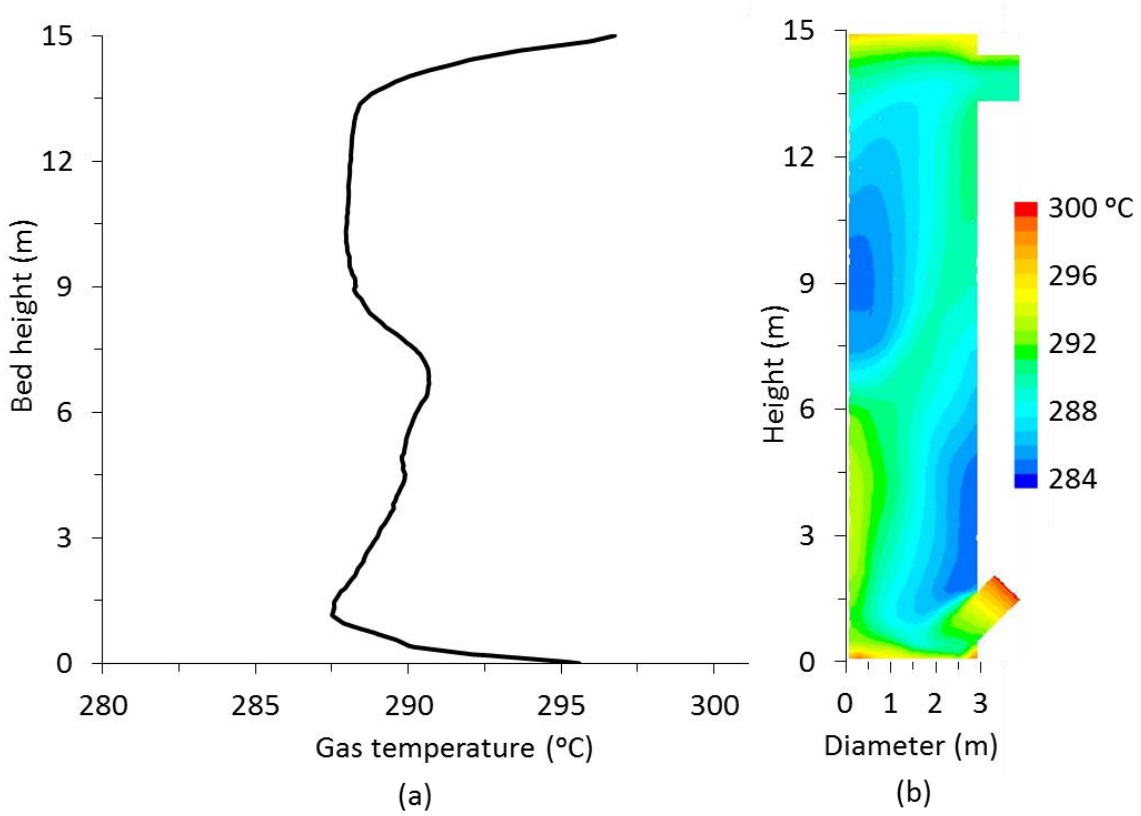

Fig. 5.9: Time-averaged gas temperature (a) centre-line axial profile and (b) cross-sectional contour plot.

5.3.2.2.5 Spatial distribution of gas species concentration

One of the great advantages in CFD modelling is that it predicts detailed microscopic data that may be difficult to measure experimentally, especially when considering large scale processing unit. Fig. 5.11 shows the spatial variation in concentration of the gas species inside the reactor after reaching a steady state condition. As expected, both of the reactants (DME and steam) appear with high concentrations at the entrance and then get consumed as they rise towards the top. The hydrogen and the carbon dioxide both appear with high quantities at the top, but with higher concentrations in a small region near the entrance. The information provided in Fig. 5.11 has been particularly useful in understanding the sequence of reactions as summarized below:

- The DME is rapidly consumed at a very short entrance length to form methanol. This behaviour matches well the observed sharp drop in temperature in the entrance region, as noted earlier, due to the endothermic nature of the DME hydrolysis reaction.
- The methanol, formed from the DME hydrolysis, is rapidly reformed to produce hydrogen and carbon monoxide within the entrance region. This reaction also contributes to the sharp drop of temperature in this region, as noted earlier.
- There is evidence of methanol decomposition at the entrance region indicated by the presence of appreciable quantity of carbon monoxide in this region.

- The highest hydrogen and carbon dioxide concentrations are found in a small region within the entrance zone, however these are also well spread and with high concentrations at the top of the reactor.
- Because most of the methanol is consumed at the lower part of the reactor, the increased concentration of the carbon monoxide appearing at the top can only be a result of the WGSR. This hypothesis is supported by the sharp increase in temperature at the far top of the reactor as shown earlier in Fig. 5.9(a) (WGSR is slightly exothermic).

Based on the above observations, a proposed map of reactions zones is shown in Fig. 5.10. In reality, it is not expected to see clear cut boundaries and the transition from one zone to another are most probably gradual and overlapping.

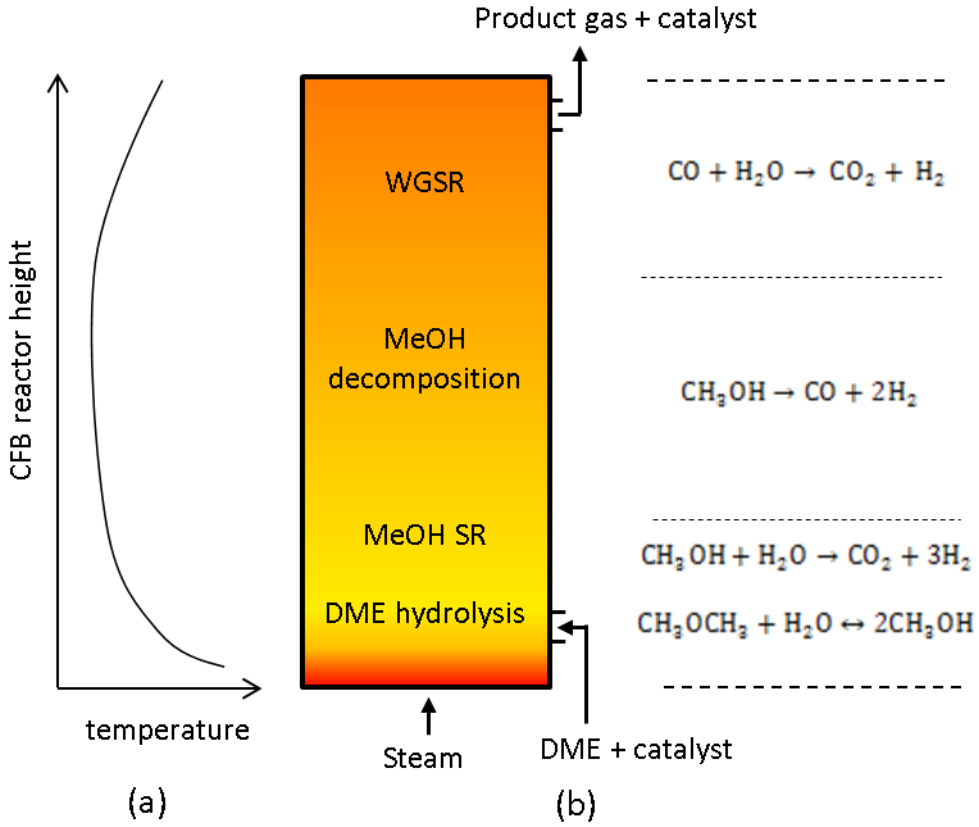

Fig. 5.10: The proposed DME-SR reaction zones and the corresponding temperature profile in the CFB reactor.

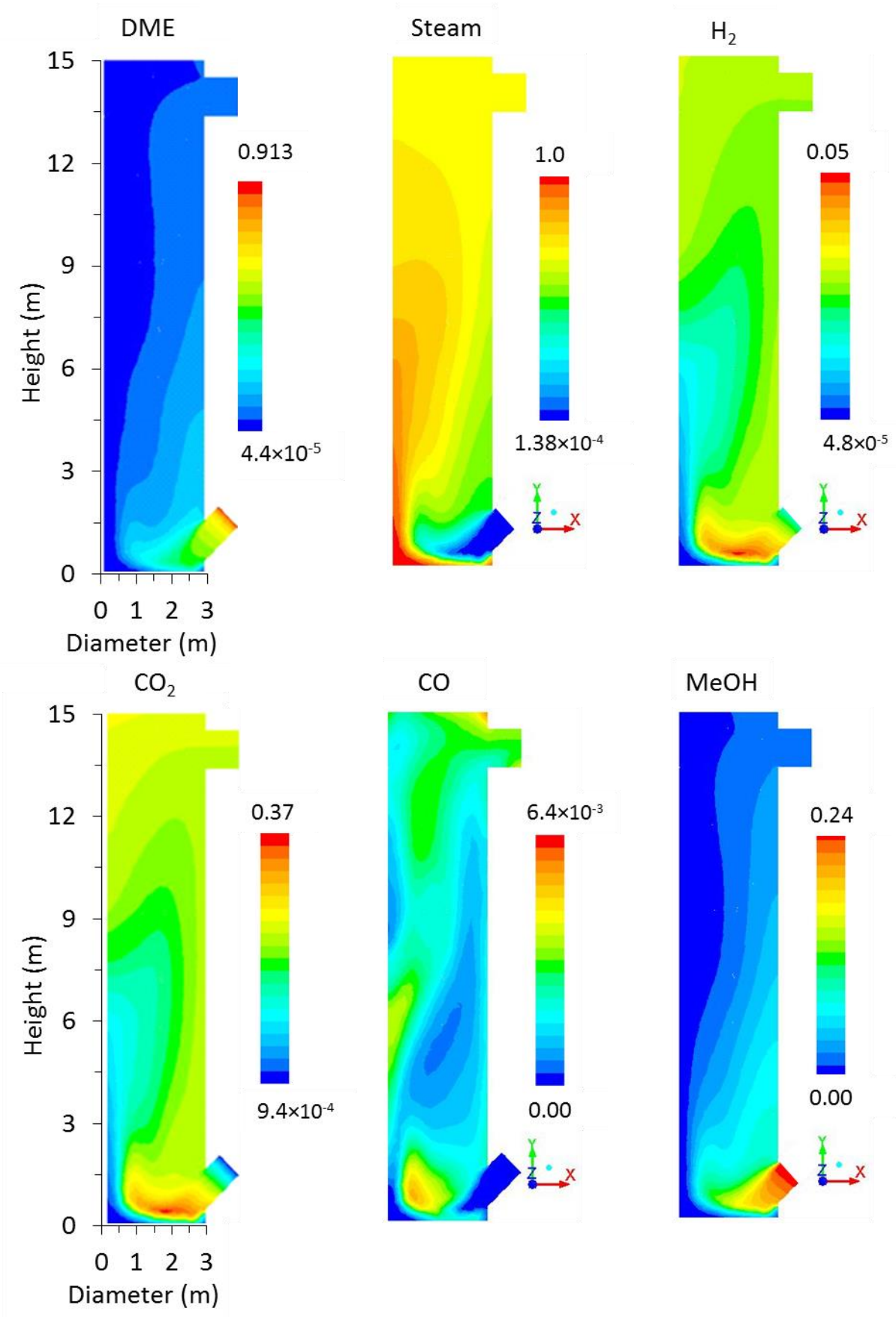

Fig. 5.11: The spatial variations of the gas species concentrations in mass fraction

5.3.2.2.6 Product gas composition

Fig. 5.12 shows the molar compositions of the product gas on dry basis at the outlet of the CFB reactor. The product gas mainly consists of hydrogen and carbon monoxide, representing a total of 95%, with the remaining 5% consisting of unreacted DME and MeOH in addition to carbon monoxide. Using this data, the calculated hydrogen yield and DME conversion were found to be 59% and 87% respectively. This is higher than the 85% DME conversion obtained experimentally by [115] in a fixed bed operating at 280 ^{o}C. Owing to the experimental work of [107,116], equilibrium conversion of DME at 200 ^{o}C is around 15% if only ZSM-5 catalyst was used. This low conversion was attributed to DME hydrolysis equilibrium limitation; hence it is plausible to conclude that the high DME conversion predicted here is a result of the significant contribution of the temperature and/or the metal part of the bifunctional catalyst ($CuO/ZnO/Al_2O_3$), almost increasing the hydrolysis reaction rate by a factor of 4. The carbon dioxide concentration in the product gas is the second highest with the calculated selectivity of 97.3%. This comes at the expense of the carbon monoxide concentration, which is consumed by the forward WGSR.

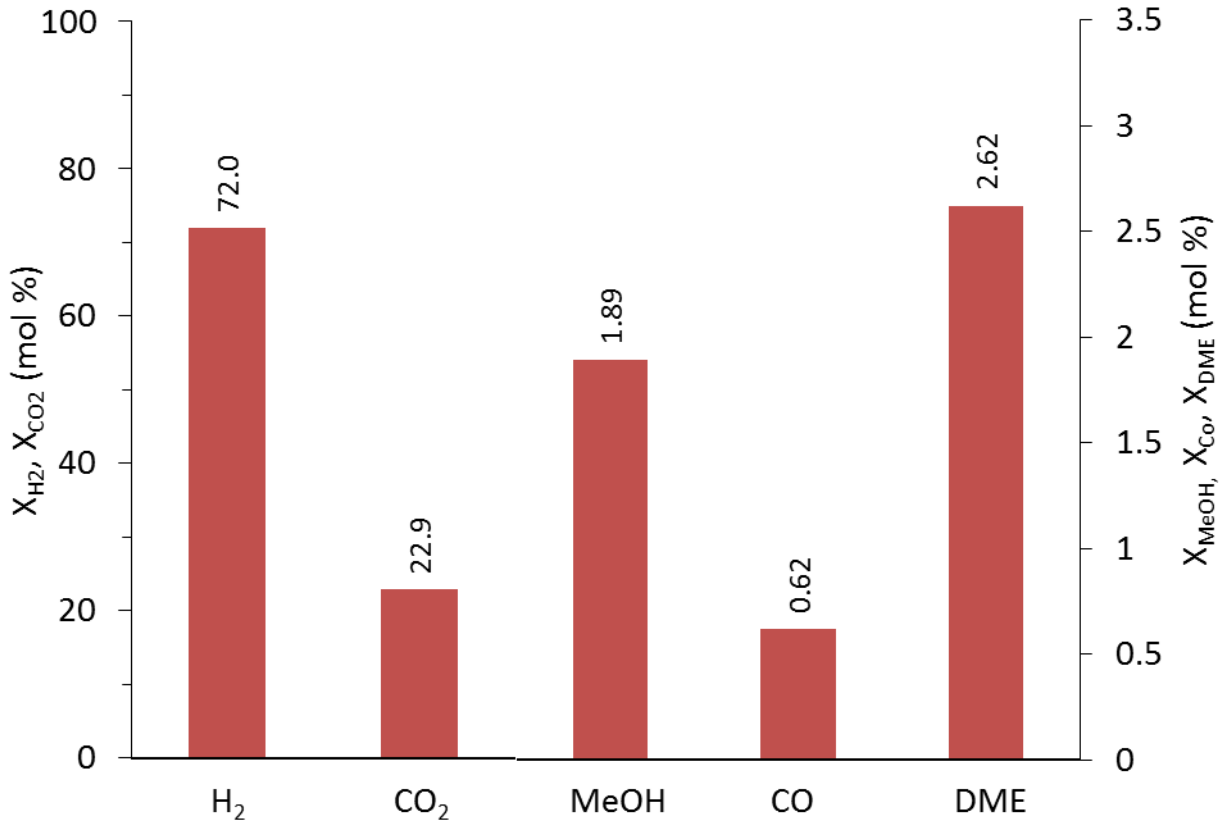

Fig. 5.12: The product gas composition at exit of the reactor in mole percentage (dry basis). Note that the left y-axis represent the hydrogen and carbon monoxide and the right axis represent the MeOH, DME and carbon dioxide.

5.3.3 Parametric Analysis of DME-SR

In this analysis, improvement and optimisation of the reactor performance was investigated through parametric analysis by modifying the temperature, steam to DME ratio, space velocity and residence time. In each case, comparison has been made against the performance at the base case condition. The choice of the range of parameters considered has been based on the reported literature on DME SR.

The reactor temperature was varied through changing the temperature of the inlets. The DME, steam and catalyst were all introduced at the same temperatures within the range of 200 °C-350 °C. The effect of steam to DME mass flow ratio was studied while maintaining the space velocity and the temperature of the inlets constant at 37104 $mlg^{-1}h^{-1}$ and 300 °C respectively. The effect of space velocity was studied by maintaining fluidizing gas flowrate while adjusting the solid feeding rate to attain a space velocity within the range of 37104 and 15394 $ml.gcat^{-1}.h^{-1}$. The gas residence time was varied by changing the reactor height while maintaining all of the operating conditions same as the base case. The heights investigated were 10 m and 20 m against the base case height of 15 m. Table 5.4 gives a summary of the range of all parameters used.

Table 5.4: A summary of Parameters amended in the parametric analysis of DME-SR and reactor performance

Parameters	DME Con (%)	YH_2 (%)	SCO_2 (%)
Bed height (m)			
10	78.18	49.58	98.56
15	87.10	59.33	97.50
20	88.45	65.05	96.93
Temperature (°C)			
200	46.56	10.75	100.00
250	67.08	34.81	100.00
300	87.14	59.22	97.50
350	98.80	100.00	91.16
Steam to DME molar ratio (-)			
4:1	68.47	39.59	100.00
5:1	73.38	44.85	99.98
6:1	77.46	49.29	99.68
7.68:1	87.14	59.22	97.50
Space velocity (mlg^{-1} h^{-1})			
15394	99.65	87.00	91.56
19846	94.10	71.26	92.63
37104	87.10	59.33	97.50

Base case

5.3.3.1 Effect of reactor bed height

The impact of reactor's length to the reactor performance was investigated by altering the base case height while maintaining other operating conditions. The height investigated was 10m and 20m against the base case height of 15m. This evaluation would effectively provide insight on effect of residence time on the reactor design which will be discussed later in this section.

Fig. 5.13 depicts the effect of changing the reactor height in relation to the performance of the reactor with other base case condition remaining unaltered. Reactor performance analysis showed that at the reactor height of 10m, DME conversion achieved was 78.2%. Hydrogen yield was 49.6% while the CO_2 selectivity was 98.6%. Increasing the height to 15m produced considerably increase in DME conversion and hydrogen yield to 87.1% and 59.2% respectively while CO_2 selectivity reduced slightly to 97.5%. Increasing the reactor height to 20m resulted in an insignificant change in DME conversion and increase in hydrogen yield to 88.9% and 65.1% respectively.

The results demonstrate that an optimum bed height would improve the reactor's performance. DME conversion and hydrogen yield at reactor height of 15m suggests that this is an effective bed height for the DME-SR. Further increment in the bed height would evidently yield improved conversions but in consideration of capital cost for the construction of a reactor of such height, 15m height would be recommended. This recommendation is because the difference in reactor's performance between 15m height to 20m was insignificant compared to the difference between 10m and 15m reactor's height.

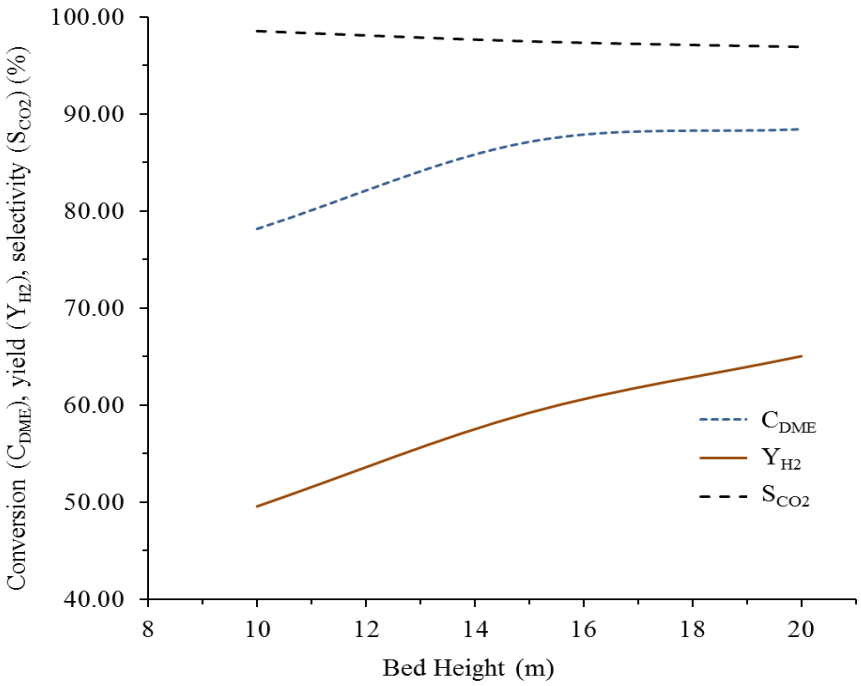

Fig. 5.13: Effect of bed height on DME conversion (C_{DME}), hydrogen yield (Y_{H2}) and carbon dioxide selectivity (S_{CO2}). Operating conditions: steam to DME molar ratio = 7.68 space velocity=37104 ml/g-cat/h, temperature 300 ^{o}C.

Fig. 5.14 depicts the effect of reactor's height on the product gas composition. The difference in hydrogen gas and unreacted DME between reactor height at 10m and 15m is very evident. This shows that selecting a reactor height of 10m would be inefficient as the gas contacts would be limited hence hindering chemical reactions. These results agree with the increased hydrogen yield and DME conversion as explained in Fig. 5.13. Unreacted methanol also showed significant decrease as the height was increased to 20m height, this explains that more methanol reaction was favoured.

The change between reactor height at 15m and 20m is also evident in Fig. 5.13. There was only slight increase in the gas compositions which justifies the insignificant DME conversion and hydrogen yield discussed previously on this parametric analysis. Carbon dioxide remained almost unaltered due to the condition selected for this parametric analysis. The equilibrium shift associated with carbon dioxide reactions in the DME-SR is explained using Le Chatelier's principle in subsequent section in this chapter.

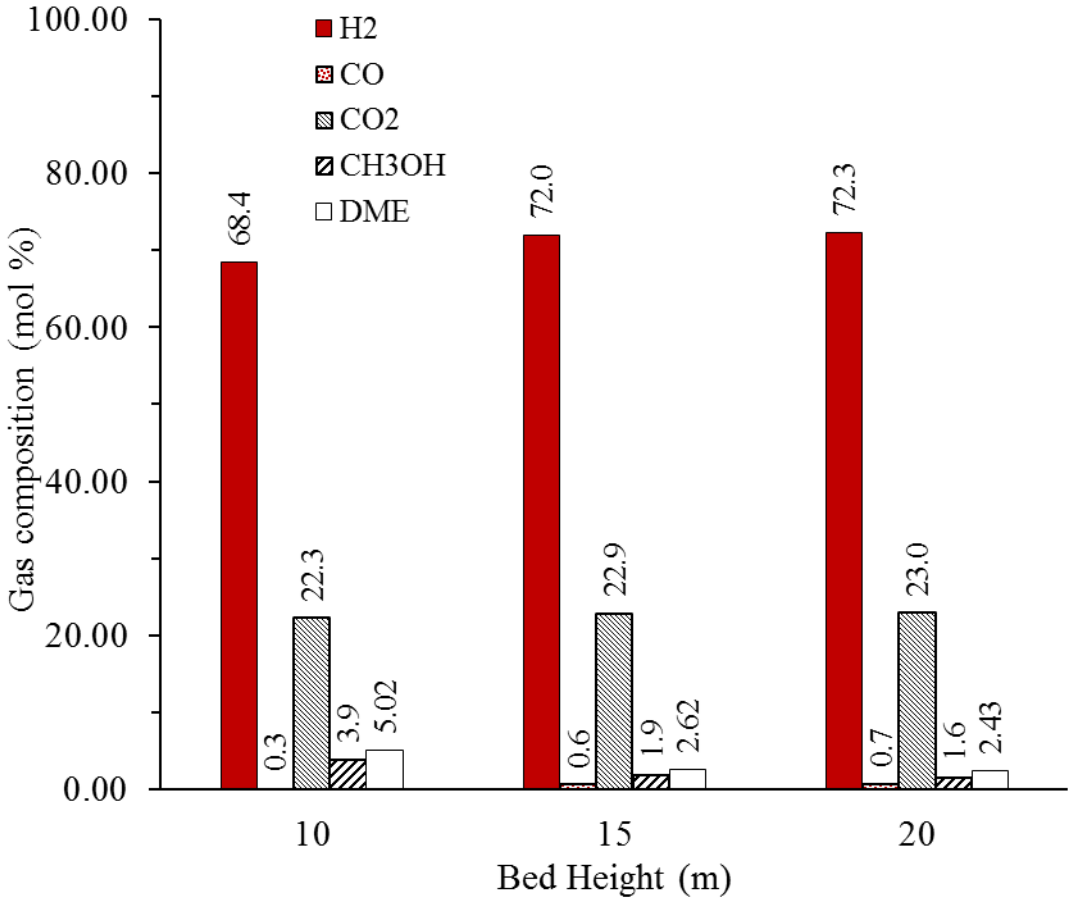

Fig. 5.14: Effect of reactor height on the product gas composition. Operating conditions: steam to DME molar ratio 7.68 and Space velocity 37104 $mlg^{-1}h^{-1}$, temperature 300 ^{o}C.

5.3.3.2 Effect of temperature

This section discusses the variations in the DME and methanol conversions, hydrogen yield and carbon dioxide selectivity as function of the reactor temperature. Temperature range selected for the parametric analysis was between 200 ^{o}C and 350 ^{o}C. The hydrolysis reaction in converting DME to methanol is regarded as the rate limiting step in the DME-SR process as it's a slow step. Thermodynamic consideration suggests that despite subjecting the reaction to high temperatures in the range of 350 ^{o}C to 500 ^{o}C, the attainment of high DME conversion would still be difficult [105]. High DME conversions would be achieved if the overall DME-SR reaction was considered. This is as a results of the methanol steam reforming shifting the hydrolysis reaction forward due to the complex reversible nature of the hydrolysis reaction [105].

It has been recommended to operate the DME-SR lower than 300 ^{o}C due to Cu based catalyst deactivation [105,111,160,163]. However, in the analysis of a catalyst composite (Cu based + ZSM-5) in the overall DME-SR, it was discovered that the increase in temperature increases the DME conversion in the system [163,164]. This suggests that the temperature effect on the composite in terms of deactivation could be considerably less when compared to the copper catalysts, though the Cu based catalyst was reported to be $CuFe_2O_4$. The cause of catalyst deactivation as a result of coking

from experimental work is still not clearly defined or accepted by the public. The work conducted by Takeishi [108] suggested that higher hydrogen yield was produced at temperatures between 300 ºC - 350 ºC without mentioning catalyst deactivation using the same $CuO/ZnO/Al_2O_3$ metallic catalyst. This stimulated the simulation of this work to consider the temperature range.

The simulation work would only effectively describe certain degree of catalytic activity for DME-SR due to the limitation of the Eulerian-Eulerian model which treats the solid and gas phase as interpenetrating continua. The effect of the temperature on the catalyst deactivation as reported in experimental literatures would be ignored due to limitation of the CFD tool.

Fig. 5.15 depicts the performance of the reactor when subjected to different temperatures while maintaining the space velocity and steam to DME ratio as the base case condition. The result suggests that the DME hydrolysis reaction, which is slightly endothermic, would shift towards the right hence producing more MeOH for subsequent reactions in the process. As earlier stated incorporation of methanol steam reforming reaction promotes the DME conversion due to the complexity in the reverse thermodynamic equilibrium condition of the overall reaction and as a result a higher DME conversion was achieved as the temperature in the system increased. The higher DME conversion consequently increased hydrogen yield as demonstrated here, this results from higher hydrogen produced from the methanol steam reforming, methanol decomposition and forward shift of WGSR reactions as the temperature increased.

According to Le Chatelier's principle, the hydrogen produced from forward shift of WGSR depends on the temperature; at lower temperature below 300 ºC the forward shift was favoured hence higher CO conversion to produce hydrogen. Whereas at temperatures from 300 ºC to 350 ºC the backward shift is favoured which reduces the CO conversion in the system [128,165] The equilibrium limitation of the WGSR means at lower temperature, CO conversion is higher and at higher temperature it reduces, this will be further analysed when the product gas compositions would be discussed. CO_2 selectivity which reflects the amount of CO_2 in the system according to Fig. 5.15 shows that it reduces from 100% as the temperature increased in the system. The decrease is attributed to the WGSR, CO_2 production is mainly from methanol steam reforming reaction and WGSR with the latter favoured at lower temperature below 300 ºC. This is evident in Fig. 5.15 where the decrease of CO_2 selectivity was observed to appear around 300 ºC; this consequently means CO becomes more prominent in the system.

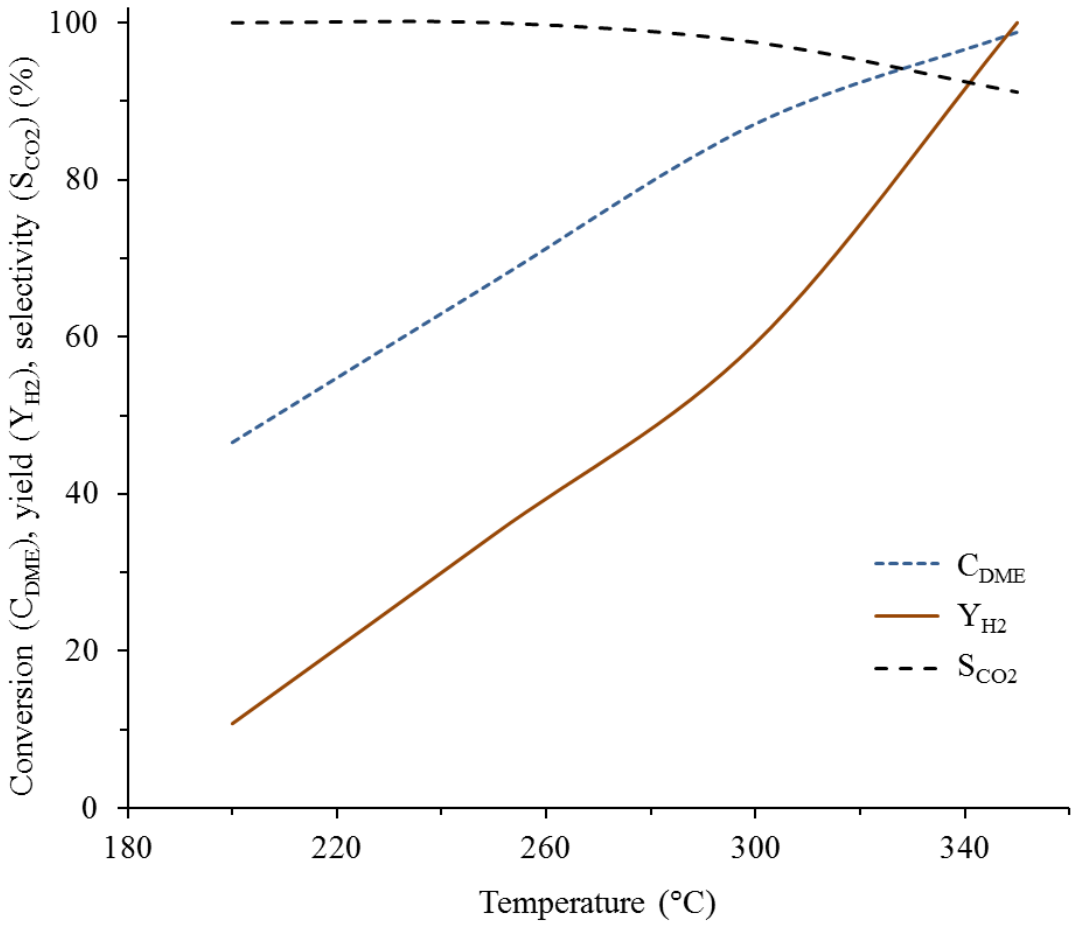

Fig. 5.15; Effect of temperature on DME conversion (C_{DME}), hydrogen yield (Y_{H2}) and carbon dioxide selectivity (S_{CO2}). Operating conditions: steam to DME molar ratio = 7.68 space velocity=37104 ml/g-cat/h.

Fig. 5.16 depicts the effect of temperature on the product gas compositions. It's evident that the hydrogen concentration in the product gas increases with increasing temperature for reasons explained earlier. It appears there's a significant change in hydrogen yield between 200 °C and 250 °C and shows that achievement of equilibrium at this lower temperature was implausible. The hydrogen yield increment after 250 °C slightly reduced, this suggests that the DME-SR process was close to attaining equilibrium in this spectrum of temperature. The higher conversions observed as the temperature increased reflected on the quantity of unreacted DME and methanol concentrations in the product gas, where both decrease to very low values of 0.27 mol% and 0.46 mol% respectively at 350 °C. In confirmation to the equilibrium dependant of the WGSR, the amounts of CO concentrations in the product gas at lower temperatures below 300 °C were reportedly negligible. Though as the CO conversion decreased at higher temperatures CO gas appeared in the product stream. The amount of CO_2 at 200 °C was small in comparison to higher temperature as a result of abundant unreacted MeOH in the system which hindered production of CO_2. MeOH quantity significantly reduced as the

temperature of the system increased demonstrating the endothermic nature of the DME-SR which promotes the conversions at higher temperature.

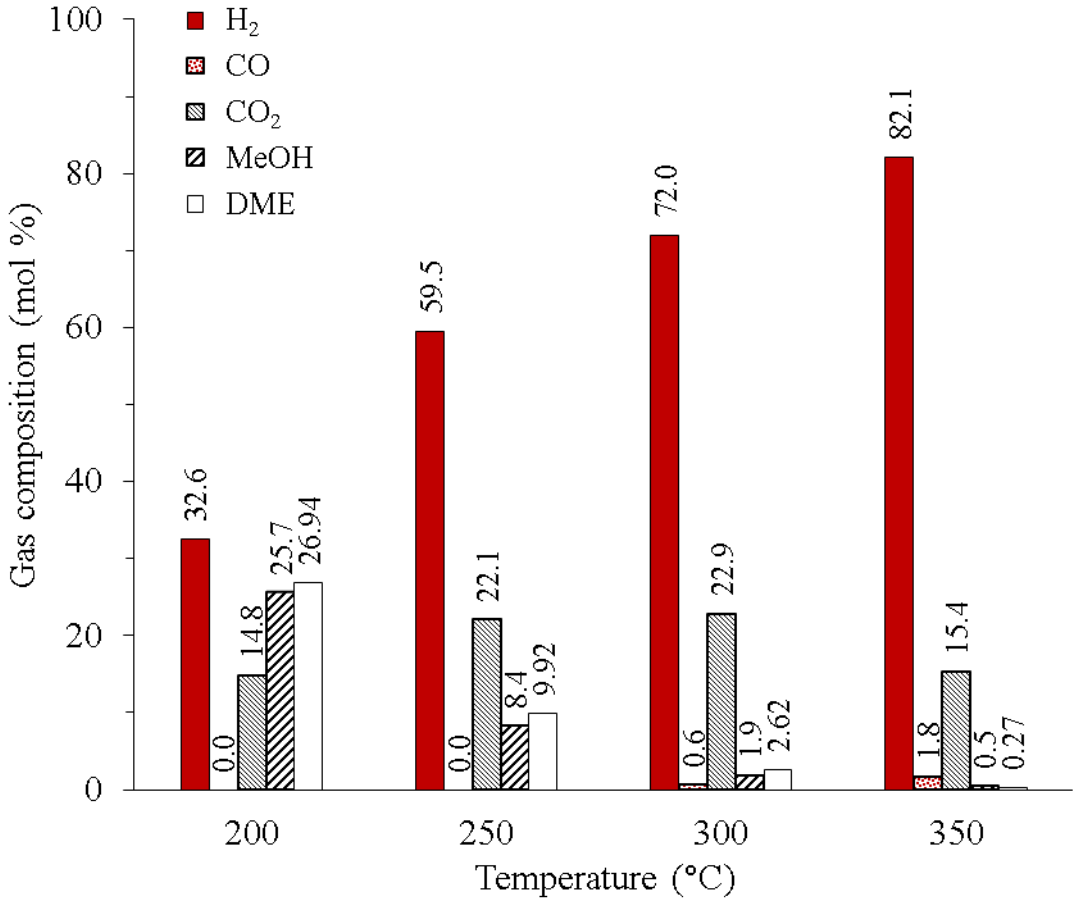

Fig. 5.16: Effect of the temperature on the product gas composition. Operating conditions: steam to DME molar ratio 7.68 and Space velocity 37104 $mlg^{-1}h^{-1}$.

Fig. 5.17 depicts the comparison of the effect of temperature on DME conversion and hydrogen yield in the current study against reported literatures for DME-SR in laboratory scale fixed bed and micro reactor. The comparison is arguably not the appropriate methodology to validate or compare DME-SR process in large scale fluidized bed system for this study against laboratory fixed bed or micro-reactor systems from literature. However, it is rather to demonstrate that the trends observed in the parametric analysis for this simulation work is comparable to those from literatures. DME conversions and hydrogen yield in the fixed bed and micro-reactor revealed that increasing the temperature enhanced the bed performance due to the endothermic reactiveness of DME-SR. Both of the selected literatures showed conversions reaching 100% at around 300 ^{o}C, though considerations of other parameters such as space velocity and steam to DME molar ratios would affect the conversions and yield as will be discussed later. These trends from literatures agrees well with the observed features in this study which suggests that the selected DME-SR kinetics simulations was effective in the production of hydrogen in the large scale fluidized bed system.

The question regarding the performance of fluidized bed system to fixed bed systems can be explained using the gas residence time as a cursor. It was observed that lower residence time favoured higher DME conversion and hydrogen yield (see Section 5.3.4). This suggests that CFB bed which is associated with lower residence time compared to fixed beds due to fluidization of the dispersed phase would provide improved reactor performance.

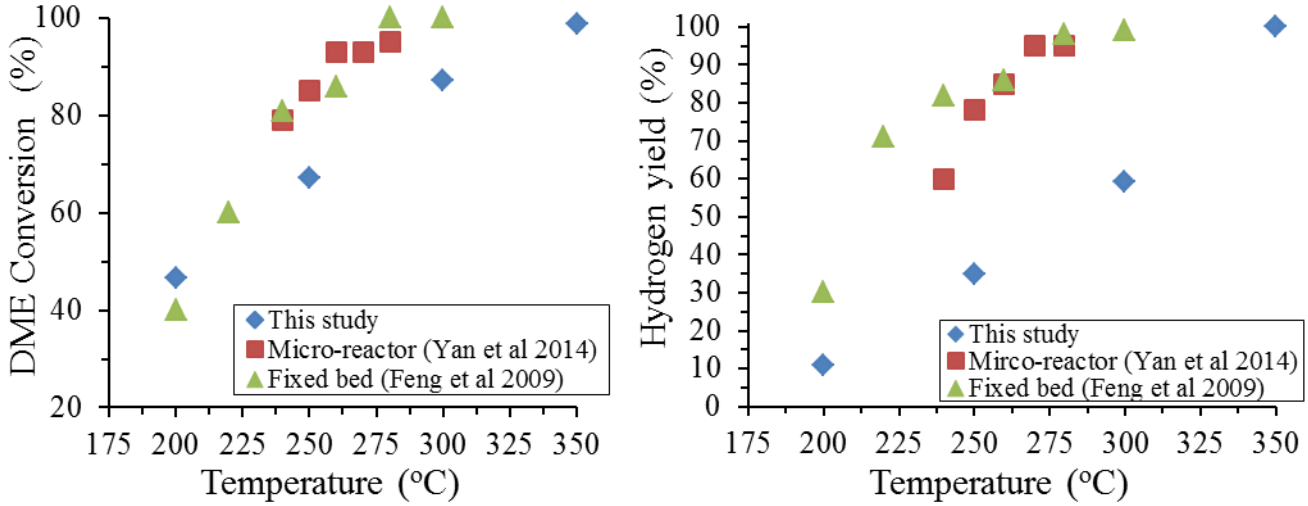

Fig. 5.17: Comparison of the effect of temperature on DME conversion and hydrogen yield from current study to literature (Yan et al., 2014 [115] condition: space velocity 3600 mlg-1 h-1, H_2O/DME =5), (Feng et al 2009 [116] condition: space velocity 2461 ml g-1 h-1, H_2O/DME =3.5).

5.3.3.3 Effect of steam to DME molar ratio

Fig.5.18 depicts effects of the steam to DME molar ratio (nH_2O/nDME) to DME conversion, hydrogen yield and CO_2 selectivity in the fluidized bed system. The effect was studied while maintaining the space velocity and temperature constant at 37104 $mlg^{-1}h^{-1}$ and 300 °C respectively. The nH_2O/nDME molar ratio is essential in the production of hydrogen in the system; the stoichiometric equation shows that the minimum molar ratio should be 3, it has been reported that steam to DME molar ratio higher than 3 is recommended for DME-SR [1,115,116]. Thermodynamically, the minimum molar ratio at equilibrium produces low hydrogen yield and DME conversion, this is the reason for operating above nH_2O/nDME=3. Considering the large scale fluidized bed for this study and the recommendations from literatures, the molar ratio for the parametric analysis was selected between 4 and 7.68 to facilitate the fluidization of the dispersed phase. The choice of 7.68 was made to achieve a steam to DME mass ratio of 3.

Fig. 5.18 shows that the hydrogen yield and the DME conversion both consistently increase with increasing steam to DME ratio, though the margin of percentage increase between each ratio is somewhat marginal. For example, between molar ratios of 4 &5 and 5&6 , the percentage increase for DME conversion were 7.2% and 5.6% while for hydrogen yield were 13.3% and 9.9%. This shows

that increasing steam to DME molar ratio would not significantly increase the performances of the reactor; a suitable range would be required to provide effective effect on the production of hydrogen while reducing the impact of energy cost on the process. It has been reported that the increase of steam at higher $nH_2O/nDME$ attenuates the coking effect on the catalyst in the process [1,166]. CFD tool for this study evidently would not distinguish this impact of the excess steam on the process due to limitations. However the literature suggestion further justifies the benefits of fluidized bed systems over fixed bed system as attenuation of coke by steam would be more efficient in fluidized bed due to uniform catalyst activity [1].

The increase of DME and hydrogen conversion and yield respectively confirms that increasing the molar ratio favours the forward shifts of the WGSR as the excess steam increases the conversion of the CO to hydrogen and CO_2. The increase in conversion of DME equally signifies increase in MeOH conversion which produces more CO in the system and depending on the reaction rate of the WGSR unreacted CO could remain in the system despite the presence of excess steam; this will be further illustrated later in the gas compositions.

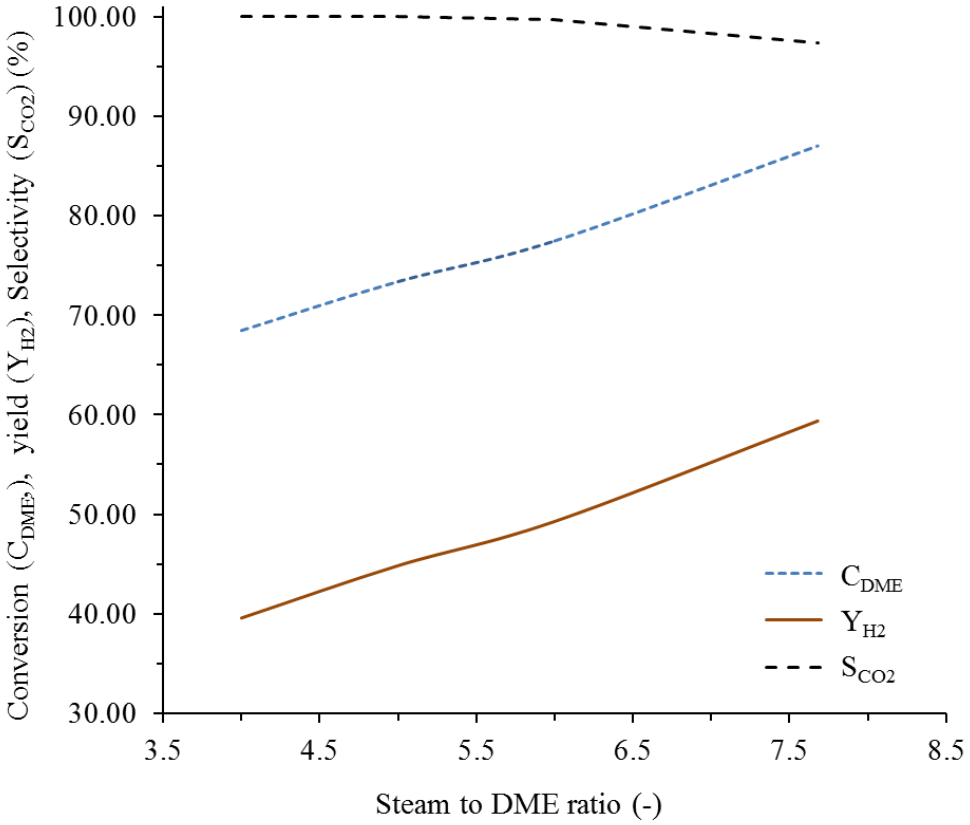

Fig. 5.18: Effect of steam to DME molar ratio on the DME conversion (C_{DME}), Hydrogen yield (YH2) and carbon dioxide selectivity (SCO2). Operating condition: temperature= 300 ^oC, Space velocity=37104 $mlg^{-1}h^{-1}$.

Fig. 5.19 shows the effect of increasing the steam to DME molar ratio on the product compositions, evidently this consequently increased hydrogen yield considerably. Reduction of unreacted DME and methanol exiting from the compositions reflects the improved conversion of DME in the process. CO_2 the product steam remained unaltered as the steam to DME molar ratio was increased. This is an unusual occurrence as the excess steam would favour the forward shift of the WGSR which increases the CO conversion meaning more CO_2 produced, the only explanation would be to suggest that the CO conversion was insufficient. This postulation could also explain the increment of the CO content in the gas composition at increasing nH_2O/nDME, steam to DME molar ratio of 7.68 shows that CO content was 0.62 mol% while 0.00% at nH_2O/nDME=4. The enhancement of the fluidized bed performance by increasing the steam to DME molar ratio beyond nH_2O/nDME =6 could be regarded as an ineffective approach as the margins of improvement appears minimal. Furthermore, it is also recognized that increasing the steam in the system implies increased energy input, which is undesirable and could prove costly for the plant. This then proposes a steam to DME molar ratio of 5 as a suitable choice for DME-SR process.

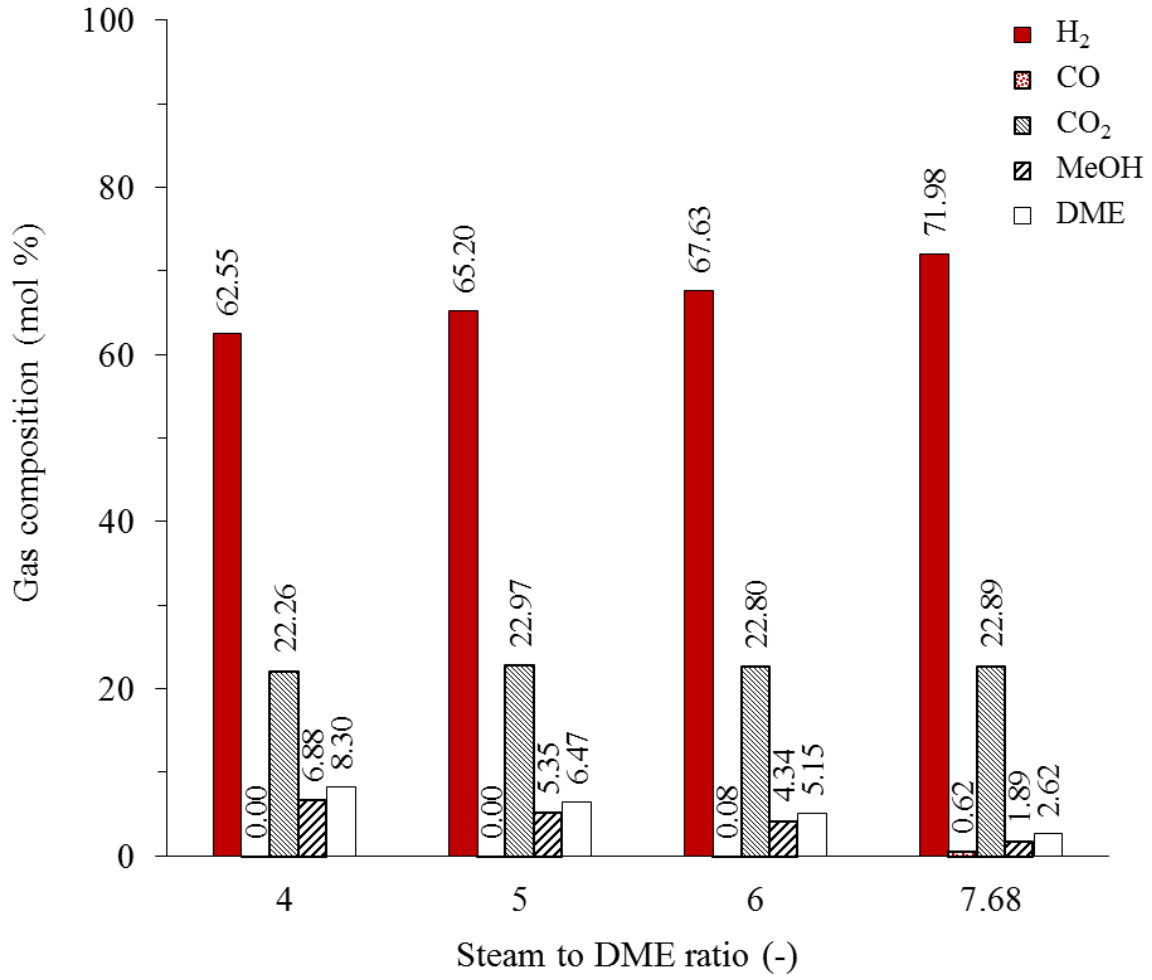

Fig. 5.19: Effect of the steam to DME ratio on the product gas composition (dry basis). Operating conditions: temperature= 300 ^oC, space velocity= 37104 $mlg^{-1}h^{-1}$.

Fig.5.20 illustrates the comparison of the effect of $nH_2O/nDME$ on DME conversion and hydrogen yield in the current study against reported literatures for DME-SR in laboratory scale fixed bed and micro reactor. DME conversion and hydrogen yield for both the fixed bed and micro-reactor demonstrated improved bed efficiencies as the $nH_2O/nDME$ were increased The percentage increase in the DME conversion and hydrogen yield for the micro-reactor superseded those of the fixed bed reactor. The percentage increase for this study was more of a reflection of the fixed bed results. Nevertheless the trends which are the main criterion for the comparison of these works from literature agreed well with the results achieved in this study. This reaffirms that this parametric analysis on the molar ratios effectively described the performance of the large scale fluidized bed for the production of hydrogen using the selected kinetics from literatures.

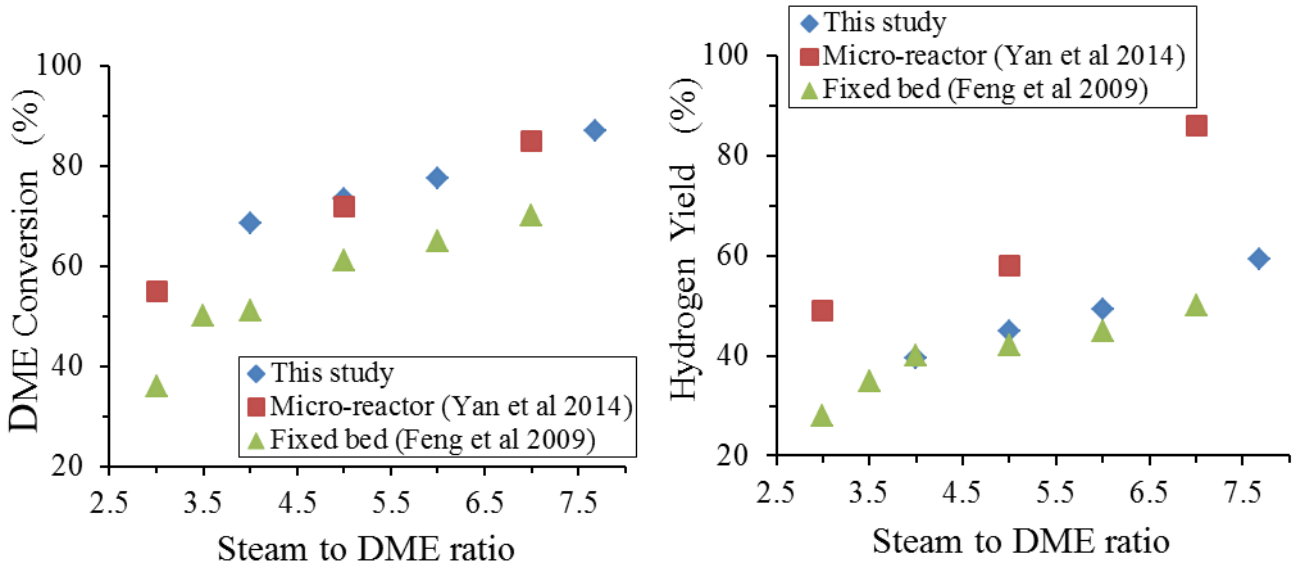

Fig. 5.20: Comparison of the effect of Steam to DME molar ratio on DME conversion and hydrogen yield from current study to literature (Yan et al., 2014 [115] condition: space velocity 3600 mlg^{-1} h^{-1}, temperature 240 ^oC), (Feng et al 2009 [116] condition: space velocity 4922 ml g^{-1} h^{-1}, temperature 240 ^oC).

5.3.3.4 Effect of space velocity

Fig.5.21 depicts effects of the space velocity on DME conversion, hydrogen yield and CO_2 selectivity in the fluidized bed system. The effect of space velocity was studied while maintaining the $nH_2O/nDME$ and temperature constant at 7.68 and 300 °C respectively.

The effects of the catalyst mass on the DME-SR were tested by the variation of the space velocity which is considered as an alternative method of checking the efficiency of the reactor; the space velocity was altered between 15394 ml g^{-1} h^{-1} and 37104 mlg^{-1} h^{-1}. The space velocity is expressed as a weight hourly space velocity (WHSV). The space velocity was achieved by increasing/decreasing the mass of the catalyst while maintaining the reactants flowrates into the reactor. Increasing the catalyst mass flowrate into the reactor decreases the space velocity and vice versa.

Fig. 5.21 shows that increasing the space velocity reduced the DME conversion and hydrogen yield; however the opposite was the case for CO_2 selectivity which slightly increased, (DME conversion decreased to 87% with hydrogen yield at 59% and CO_2 selectivity at 98% when the space velocity was reduced to 37104 mlg^{-1} h^{-1}). This demonstrates that decreasing the solid load in the fluidized bed via the mass flowrate reduced platforms for the endothermic reactions. This evidently decreased DME conversion and hydrogen yield, this further suggests that the reaction rate for DME hydrolysis and methanol steam reforming reduces hence limiting the production of CO from the methanol decomposition reaction. The forward shift of WGSR is favoured due to limited amount of CO in the process which then promotes the production of CO_2 gas at increased space velocity.

In Fig.5.21, reduced space velocity which was initiated by increasing the catalyst flowrate into the bed while the DME gas flowrate into the reactor remained unaltered, showed improved reactor performance. This purportedly increased the area for catalytic reactions hence increasing the DME conversion and hydrogen yield (DME conversion increased to 100% with hydrogen yield at 87% and CO_2 selectivity at 93% when the space velocity was reduced to 15394 ml g^{-1} h^{-1}). The CO_2 selectivity decreased in this spectrum of space velocity as a consequence of abundant CO production from the decomposition reaction as the DME conversion is increased. The CO conversion was insufficient to completely convert the gas to CO_2 and hydrogen hence favouring reverse shift.

This equilibrium behaviour of the WGSR could be alternatively be described using Le Chatelier's principle, in one of its assumptions it proposed that system in equilibrium will adjust if the concentration of the product or reactant was increased. This suggests that as the DME conversion was increased, the production of CO_2 from methanol steam reforming increased and hence shifted the WGSR to the left, this resulted in the production of CO and the reduction of CO_2 selectivity. The higher hydrogen yield achieved despite the reverse-WGSR proofs that the methanol reforming reaction produced abundant hydrogen and CO_2 due to the increased DME conversion. Observing Fig.5.21, it could be suggested that to achieve 100% DME conversion with high hydrogen yield at lower temperature, a low space velocity will be favourable. However it was be noted that increasing the catalyst flowrate while maintaining the reactant fluid to increase the space velocity would change the bed hydrodynamics and might lead to non-circulation. Hence, a certain range of space velocity will be required for effective performance.

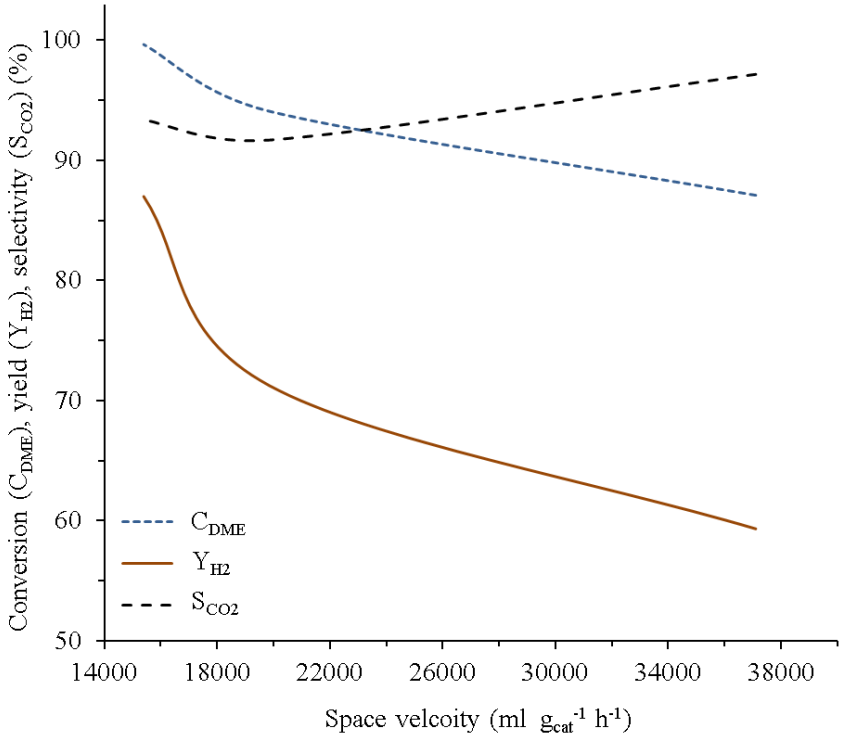

Fig. 5.21: Effect of space velocity on DME conversion, carbon dioxide selectivity (S_{CO2}) and Hydrogen yield (Y_{H2}). Operating conditions: temperature= 300 ^{o}C and steam to DME molar ratio =7.68.

Fig.5.22 shows the effect of the space velocity on the product gas composition, it's obvious to see the increase of the DME conversion, hydrogen yield and the reduction of CO_2 selectivity at reduced space velocity. The hydrogen yield at 15394 mlg^{-1} h^{-1} was equivalent to the yield obtained by increasing the temperature of the system to 350 ^{o}C in Fig. 5.16. This demonstrates the impact of the space velocity on the performance of the fluidized bed system in providing an efficient DME-SR process for the production of hydrogen. The decrease in CO_2 selectivity is reflected in Fig.5.22 whereby the amount of CO significantly increased from 0.6 mole% to 2.1 mole% (250% increase) to confirm that the reverse WGSR was supposedly favoured as explained using Le Chatelier's principle. Unreacted DME and methanol significantly reduced as the space velocity was decreased confirming the increase in DME conversion due to the increased reaction occurring as the catalyst mass in the bed was increased.

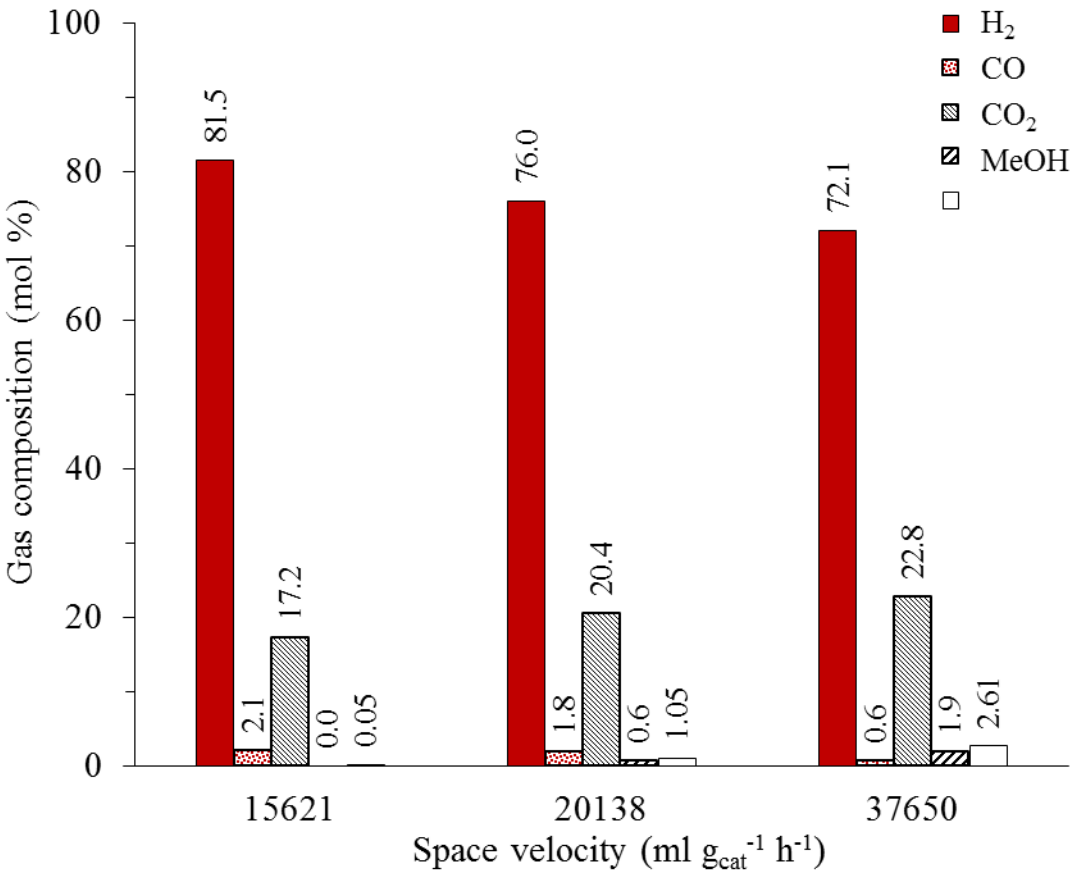

Fig. 5.22: Effect of space velocity on the product gas composition (dry basis). Operating conditions: temperature= 300 oC and steam to DME ratio=7.68.

Comparing the effect of space velocity on DME conversion and hydrogen yield in this study against reported literature, only Feng et al. [116] conducted relative investigation of the space velocity using similar units in a fixed bed system. Feng et al [116] DME conversion and hydrogen yield increased as the space velocity decreased, it was reported that at 1180 mlg^{-1} h^{-1}, 100% DME conversion and hydrogen yield were achieved whereas increasing the space velocity to 9000 mlg^{-1} h^{-1} reduced the DME conversion and hydrogen yield to 50% each. This was also reflected in the CO_2 selectivity at the extreme low and high space velocities, CO_2 reported at 1180 mlg^{-1} h^{-1} was 95% while at 9000 mlg^{-1} h^{-1} was 98%. This suggests that higher space velocity encouraged forward shift of the WGSR while lower space velocity favoured backward shift as explained earlier. The trends observed in the literature for Feng et al. [116] agreed well with the current study.

5.3.4 Residence time distributions (RTD)

In the analysis of the reactor, gas RTD studies were considered for the DME-SR process as discussed in chapter 2. The impact or behaviour of the gas mean residence time evaluated from the RTD study provides insight on the performance of the reactor at different conditions. The results from the analysis could be utilised in the prediction of future yield from the reactor using DME-SR kinetics. This aspect is beyond the scope of this project but provides results for further investigations.

Two parameters were explored in the investigation of the mean residence time; these are the reactor height and the steam to DME molar ratios.

5.3.4.1 Effect of reactor height on RTD

As earlier discussed in the previous section on the effect of reactor height on the DME-SR performance in CFB, the reactor height investigated were at 10m, 15m and 20m. RTD to evaluate the mean residence time at each reactor height was conducted as illustrated in chapter 2. The mean residence time estimated was 2.4s at 10m, 3.9s at 15m and 5.1s at 20m, Fig. 5.8 shows the mean residence time for reactor at 15m height while Fig. 5.23 for 10m and 20m reactor height. The mean residence time distribution at the varied height suggests that increasing the residence time improves reactor performance till about 3.9s where further increase have insignificant impact on the reactor performance. This suggestion is evident from Fig. 5.13 and Fig. 5.14.

The increase in residence time ensures that the gas undergoes comprehensive reaction which resulted in the increase of DME conversion and hydrogen yield. CO_2 selectivity decreased slightly due to the effect of reverse WGSR. The trend depicted by the mean residence time through changing the reactor height is useful in designing or optimizing the reactor to a suitable specification. The geometry selected for this project was an existing industrial operational reactor which suggests the reason a height of 15m was chosen.

The parametric analysis for reactor height change suggests that mean gas residence time of 3.9s would be effective for the gas phase chemical reactions to produce the relevant product gas composition. Longer gas mean residence time is unflavoured due to reverse reactive nature of the gas chemical reactions involving the hydrolysis and water gas shift reaction (see chapter 3). The reverse activities of the fluidizing fluid reduce the effectiveness of the product gas productions.

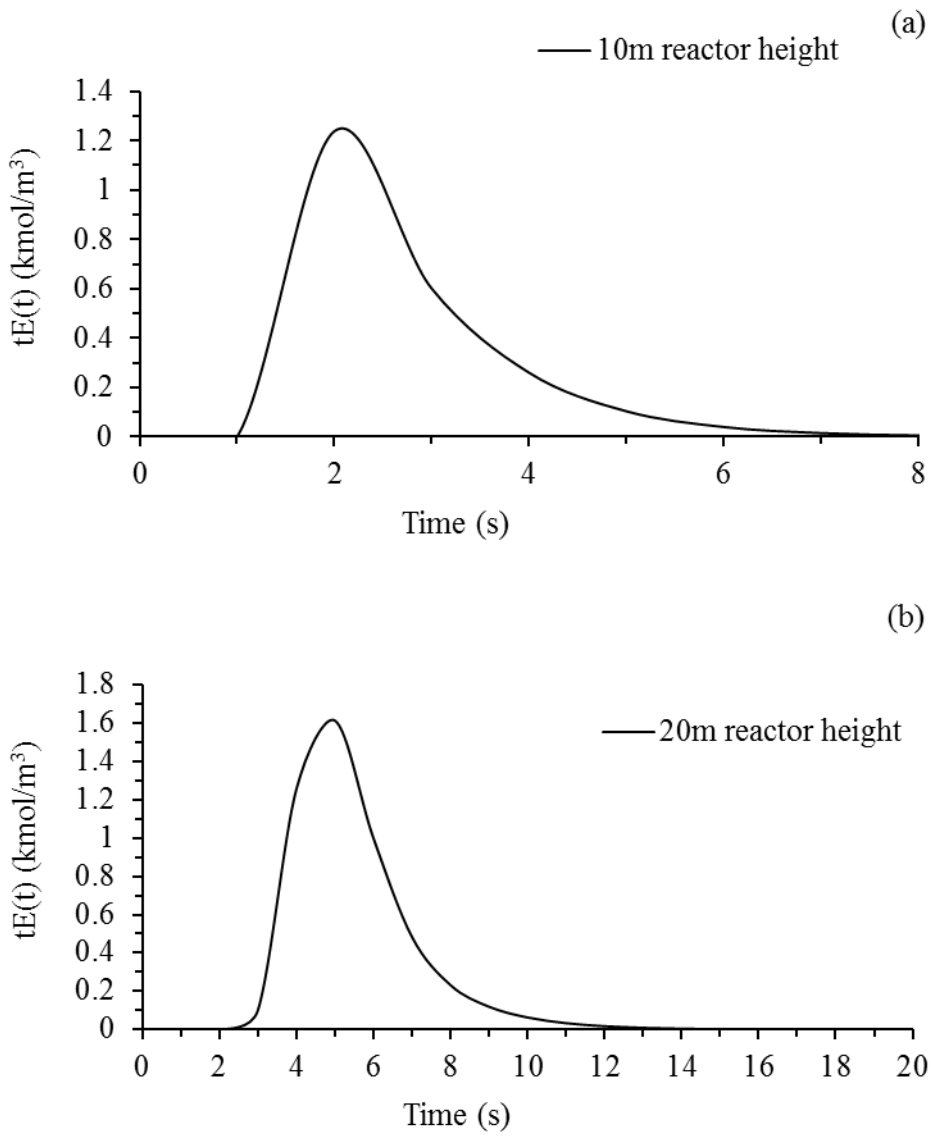

Fig. 5.23: The tE(t) curve used for the derivation of mean gas residence time for reactor at 10m and 20m height respectively.

5.3.4.2 Effect of steam to DME molar ratio on RTD

In the parametric analysis of the steam to DME molar ratio, it was explained that other conditions remained unaltered while the fluidizing fluid was adjusted. The adjustment of the steam to DME molar ratio changes the fluidizing velocity of the inlet gas (steam and DME) which directly relates to the time the gas spends in the reactor (residence time). The mean residence time was estimated for each steam to DME molar ratio to analyse how it affects the reactor performance.

Table 5.5 depicts the reactor performance at various mean gas residence time when subjected to different steam to DME molar ratio. It's obvious that the lower gas residence time favoured higher DME conversion and hydrogen yield. Due to these higher conversions, the water gas reverse shift reaction is favoured thereby producing more CO, this is the reason for the reduction of CO_2 selectivity at lower gas residence time.

The reduction of the gas residence time resulting from increase in fluidizing velocity (steam to molar ratio) reduced the magnitude of reverse activities in the chemical reactions. This evidently improved the performance of the conversions in the reactor as seen in Table 5.5. The corresponding graphs from simulations in deriving mean residence time is seen in Fig. 5.24 while that for the base case in Fig. 5.8. It could be suggested that a mean gas residence time window of operation is necessary for effective reactor performance. This was concluded from analysing results from the mean residence time from reactor height change and steam to DME molar ratio. A range of mean residence time within 3.9s would be suitable considering the operating condition. This is because mean residence time lower or higher than this window is rather ineffective in the reactor operation.

Table 5.5: Mean residence time behaviour for different steam to DME molar ratio

Parameters	τ(s)	C_{DME} (%)	Y_{H2} (%)	S_{CO2} (%)
H_2O/DME /(-)				
4	6.6	68.06	39.90	100.00
5	5.6	73.38	44.85	99.98
6	4.8	77.46	49.29	99.68
7.68	3.9	87.14	59.22	97.50

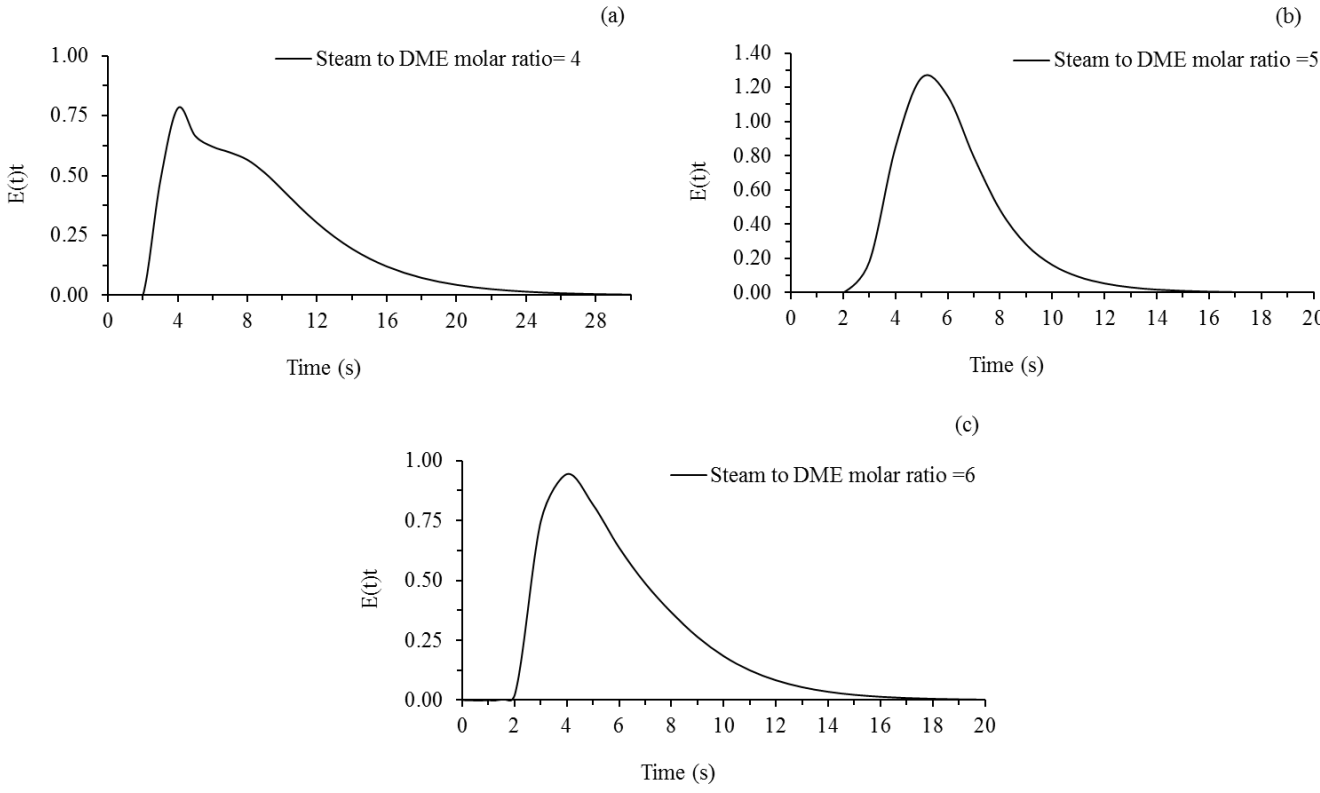

Fig. 5.24: The tE(t) curve used for the derivation of mean gas residence time for reactor at steam to DME molar ratio of 4, 5 and 6.

6 CHAPTER 6: INDUSTRIAL SPONSOR DFB RE-DESIGN

6.1 Introduction

The proposal to the sponsoring company was to investigate the removal of undesired gas and the utilisation of this gas in the production of hydrogen-rich gas as a clean fuel. This resulted in the design of adsorptive and reforming systems to facilitate the envisaged processes. In order to represent a realistic case, the designs and simulations were for an industrial case and based on the sponsor recommended operating conditions. The schematic DFB diagram for the coupled adsorption and steam reforming processes was given in chapter 1.

This chapter will discuss the potential improvement of the current simulated industrial CFB system in terms of the design. The DFB loop system incorporating the adsorptive and reforming processes was not simulated due to computational time and complexity of the design. For this reason, the results from the base case DME adsorption simulations were coupled into the DME-SR case created for the sponsoring company. The results from the sponsor's case simulation would then provide indication of the amount of hydrogen together with other product gases produced from the amount of DME adsorbed in the adsorptive system.

6.2 DME-SR CFB Re-Designed Side Inlets

In order to further enhance the mixing and uniformity of the materials inside the CFB, a new design was considered as seen in Fig. 6.1(b), with two side solid inlets around the lower section of the bed instead of the original design with one side inlet as seen in Fig. 6.1(a). The feed into the CFB for the new design were split into equal quantity on each side inlets of the bed. Though the new design is different from the conceptual design for the DME-SR system, the analysis of the results will demonstrate the impact of the reactor design to the performance of the kinetics for DME-SR for hydrogen-rich gas production. DME-SR base case operating conditions for the original design as discussed in chapter 5 was applied in this investigation.

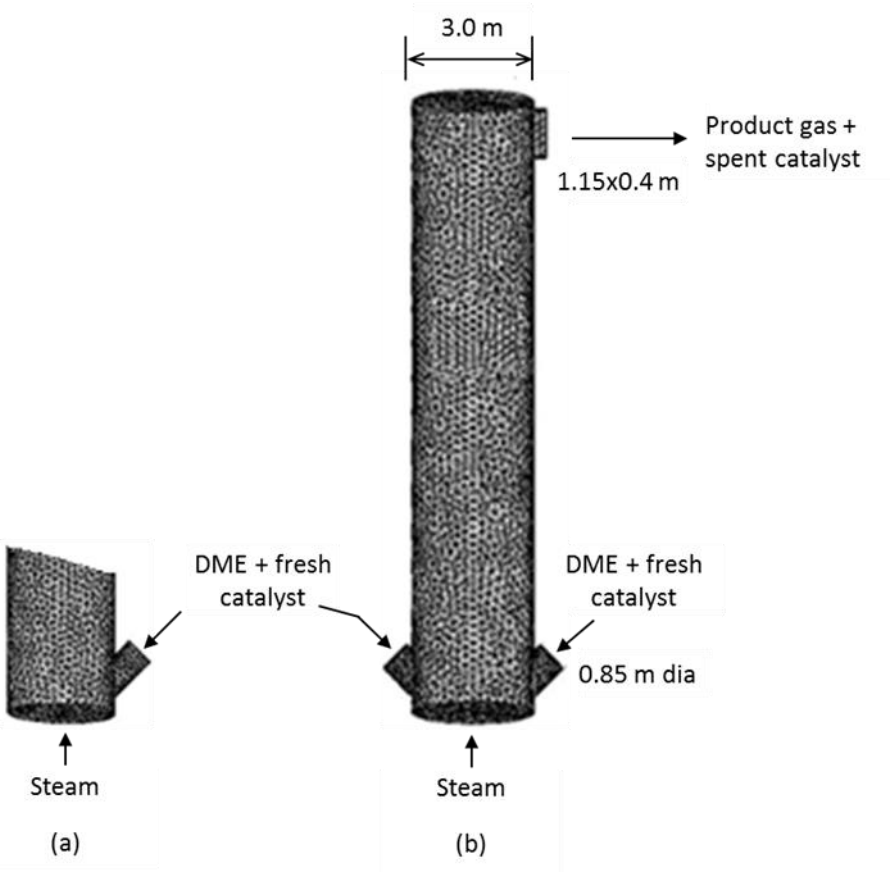

Fig. 6.1: The computational domain and meshing (a) Original CFB riser geometry (b) Redesigned geometry for present hydrodynamic study

6.1.1 Results and discussion of new design

This section presents the effect of changing the reactor design on the hydrodynamics and thermochemical performances for the CFB.

6.1.1.1 Hydrodynamic performance of new design

The analysis of the original CFB simulation showed an uneven distribution of the gas-solid materials in the hydrodynamics study. This suggested that the interactions were affected which inevitably impacted the conversions in the reactor. In this study a slightly changed geometry around the inlet zone was introduced to examine the entrance effect on the reactor performance by evenly distributing DME and catalyst inlets mass flow rates on each side of the reactor instead on just one side as seen in Fig. 6.1(a).

6.1.1.2 Solid/gas distribution and velocities

Fig. 6.2 depicts the characteristic flow observed in the new designed CFB to enhance the mixing in the bed. The flow pattern in the lower section of the bed around the solid and gas inlets has some resemblance to Annular Fluidized Bed (AFB) in terms of the mixing in this region [167]. Gas and solid entering from the two side inlets collide as they encounter in the middle of the lower section creating a chaotic spiral movement in this region. The gas-solid mixture moving upwards from the

middle of the lower section appears to deflect towards the right and left walls and spirals back to the middle section, the gas and solid flows at higher velocities around the walls. The middle section of the bed exhibits higher solid volume fraction due to reverse flow from the left and right walls. Furthermore, solid volume fraction in Fig. 6.2 illustrates this behaviour of the gas-solid flow pattern in the bed. The gas and solid velocities contours in Fig. 6.2 illustrates the upward and downward movements in the middle section of the bed with areas around the walls showing positive velocities which indicates upward flow while the middle section shows negative velocities demonstrating reverse flows. There is limited knowledge of this sort of flow pattern which has been suggested to be an AFB, though it is known for exhibiting better mixing due to the chaotic movements of the gas and solid [167,168].

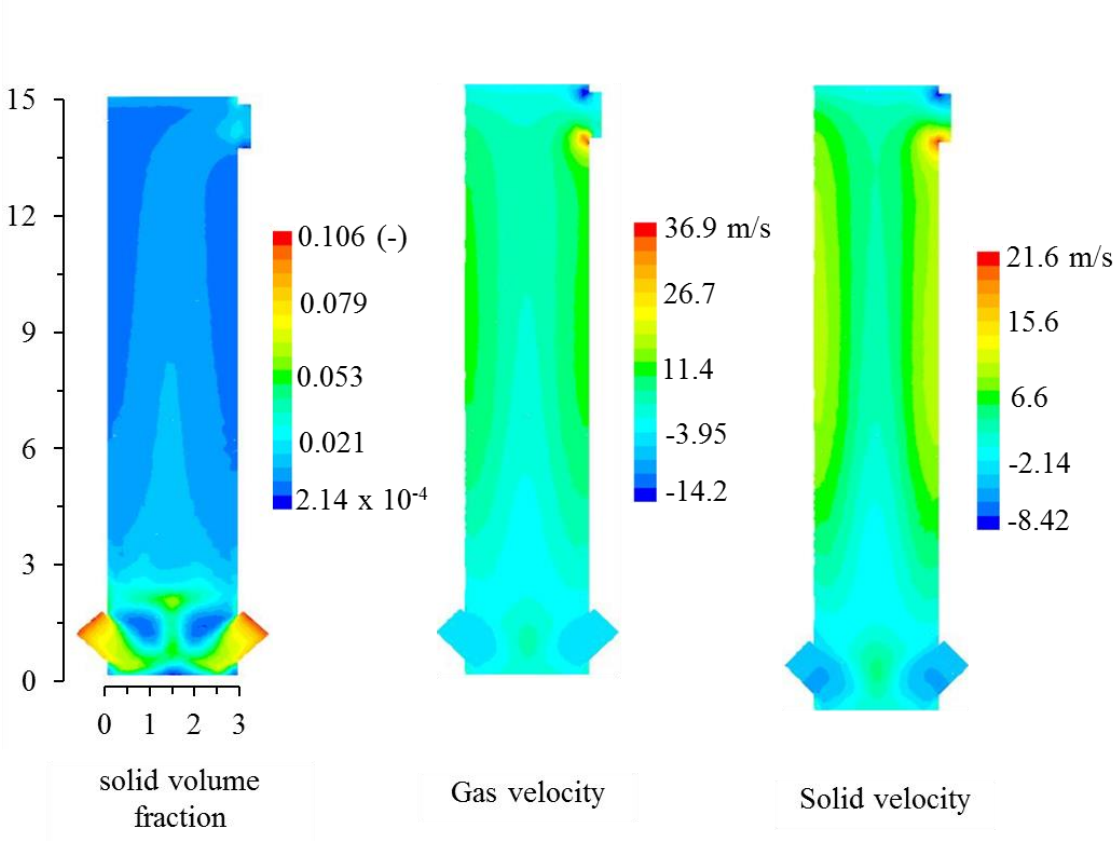

Fig. 6.2: Time averaged contours of the new designed CFB.

Fig. 6.3 depicts the velocity vectors of the gas phase in the lower section of the new CFB design demonstrating the areas of the bed described above, that suggested resemblance of AFB system. The Jet-like shape that's formed due to the collision of the two side inlets aided by the fluidizing velocities is peculiar to AFB systems [167,168] and spouted bed [169]. The jet-like gas vectors (very high velocities ~11m/s) around the region both side inlet feed collides move upward and cause the deflection of most of the gas towards the left and right walls, though some of the gas moves upward in the middle section. Some of the high velocities noticed around the walls spirals down into the middle section while the majority of the flow moves upwards to the top section of the bed before exiting. This

flow behaviour would suggest increased mixing in the new design which would benefit the reactor performance due to increased contact between the gas and solid catalyst for reaction purposes.

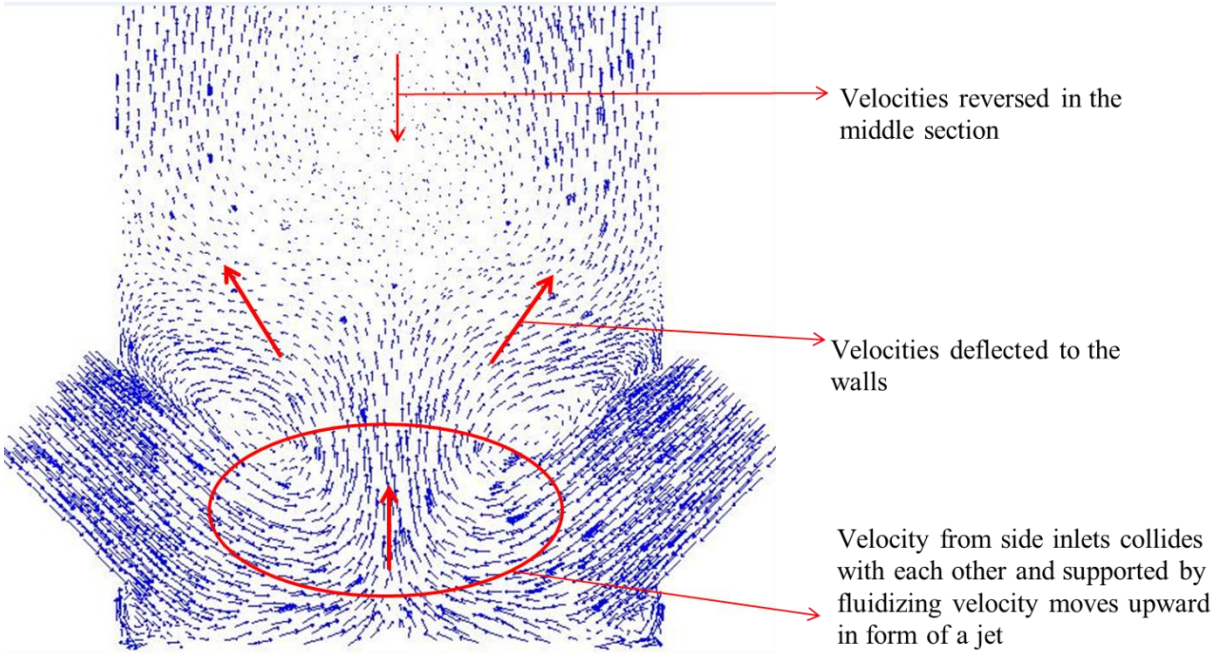

Fig. 6.3: Gas velocity vector showing the gas and solid distribution in the lower section of the bed.

Further details on the effect of modifying the reactor inlet is shown in Fig. 6.4 in terms of the contours and vectors of the solid (catalyst) velocity. The introduction of the solid from two axially opposite directions appear to create two vortices that disrupt the flow pattern in the lower region. This distribution in the entrance region lead to the transforming of the classic core-annular flow into a flow pattern similar to the upper part of a spouted bed, as noted earlier. Some of the solid appears to deflect towards the wall to fall under intense upward gas drag force, hence attaining high particle velocity in this region. Shah et al. [170], demonstrated through CFD modelling and experiment that a dense core and high solid velocity at the wall of a CFB riser was formed for this type of entrance. This is similar to the predictions here, it is a phenomenon related to the entrance effect, i.e. re-arrangement of the solid and gas feeding. It is worth noting that, there is little knowledge on the effect of dual solid feeding on CFB riser hydrodynamics, and perhaps, the CFD approach is the best option for such investigation, especially for a large scale system as considered here.

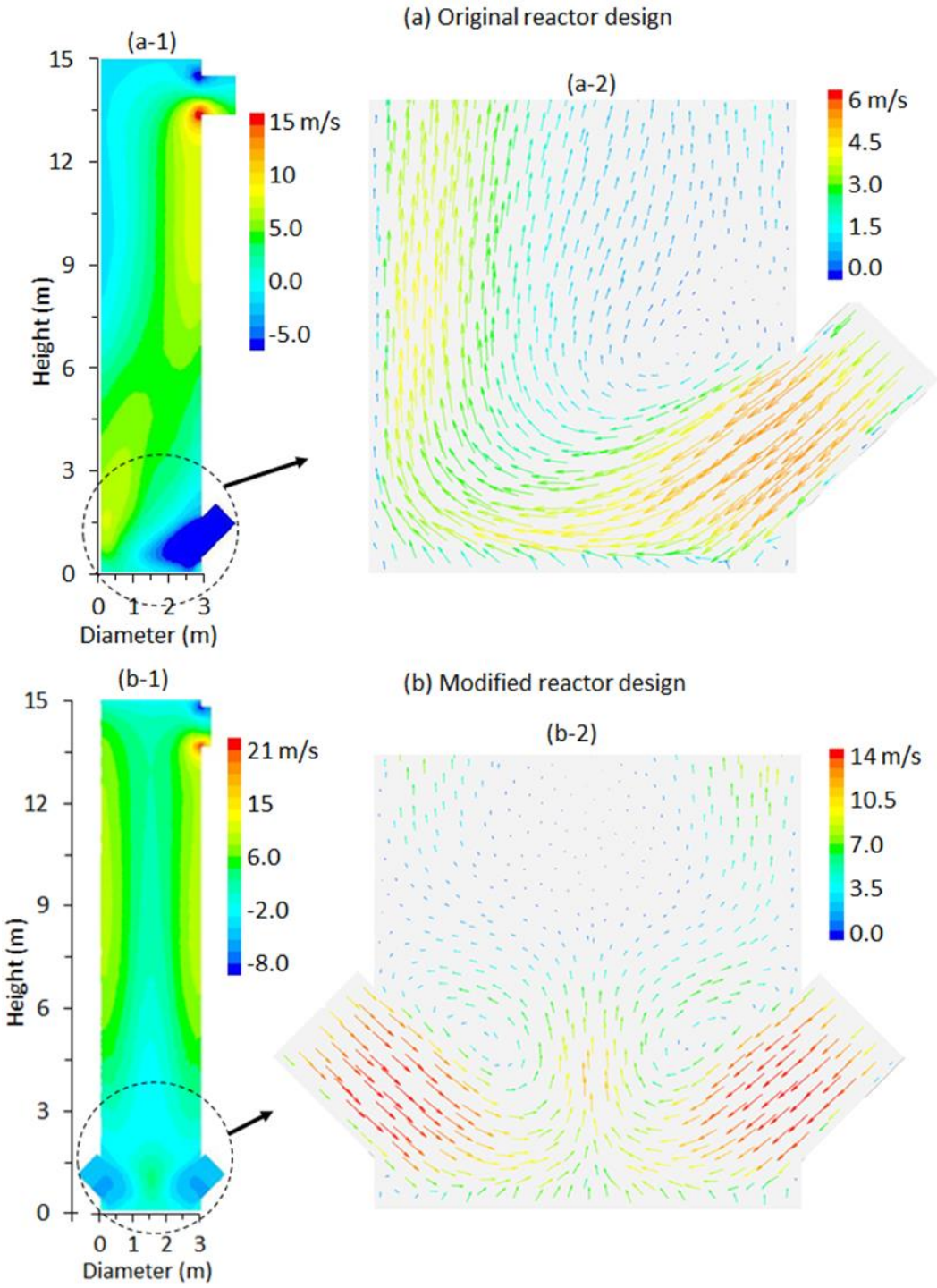

Fig. 6.4: Time averaged contours (a-1 and b-1) and vectors (a-2 and b-2) of solid velocity in the CFB reactor (a) original design with one side feeding point (b) modified design with two sides feeding. Operating conditions: inlet temperature= 300 °C, space velocity= 37104 ml $gcat^{-1}$ h^{-1}, steam to DME molar ratio= 7.68

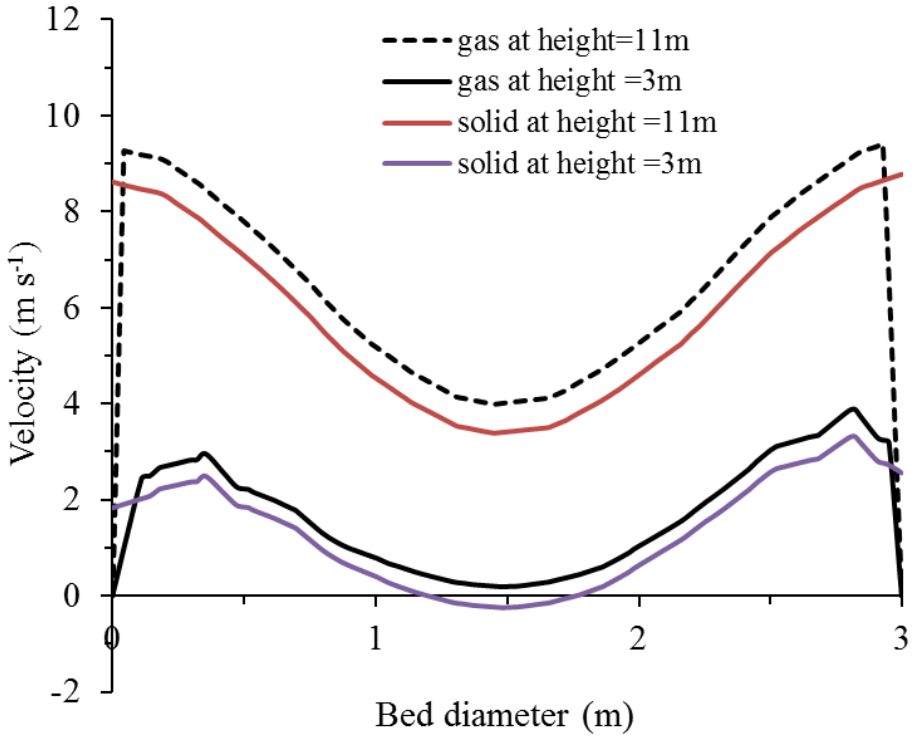

Fig. 6.5: Time averaged gas and solid axial velocities at different bed height representing bottom and upper section of the CFB.

Fig. 6.5 depicts the hydrodynamic feature of the gas and solid velocities around the lower (3m) and upper section (11m) of the new design. This feature is different from the usual features expected for a CFB. The difference is attributed to the unusual hydrodynamic feature of the annular fluidized bed which has limited information in the literature. The gas and solid velocities shows that the left and right walls possess higher velocities while the middle section with the reverse flow has lower velocities.

6.1.1.3 Thermochemical performance of the new design

Fig. 6.6 depicts the comparison between the base case and the new design reactor performance; it is obvious that there is a slight improvement in the reactor performance in the new design in terms of the DME conversion and hydrogen yield. The improvements are attributed to the better mixing that describes the hydrodynamic feature of the new design. The increase in DME conversion effectively meant the amount of CO produced would increase due to the reverse shift WGSR reaction; this explains the decrease in the CO_2 selectivity in the new design. The hydrogen yield also increased due to the higher conversion achieved with the DME gas.

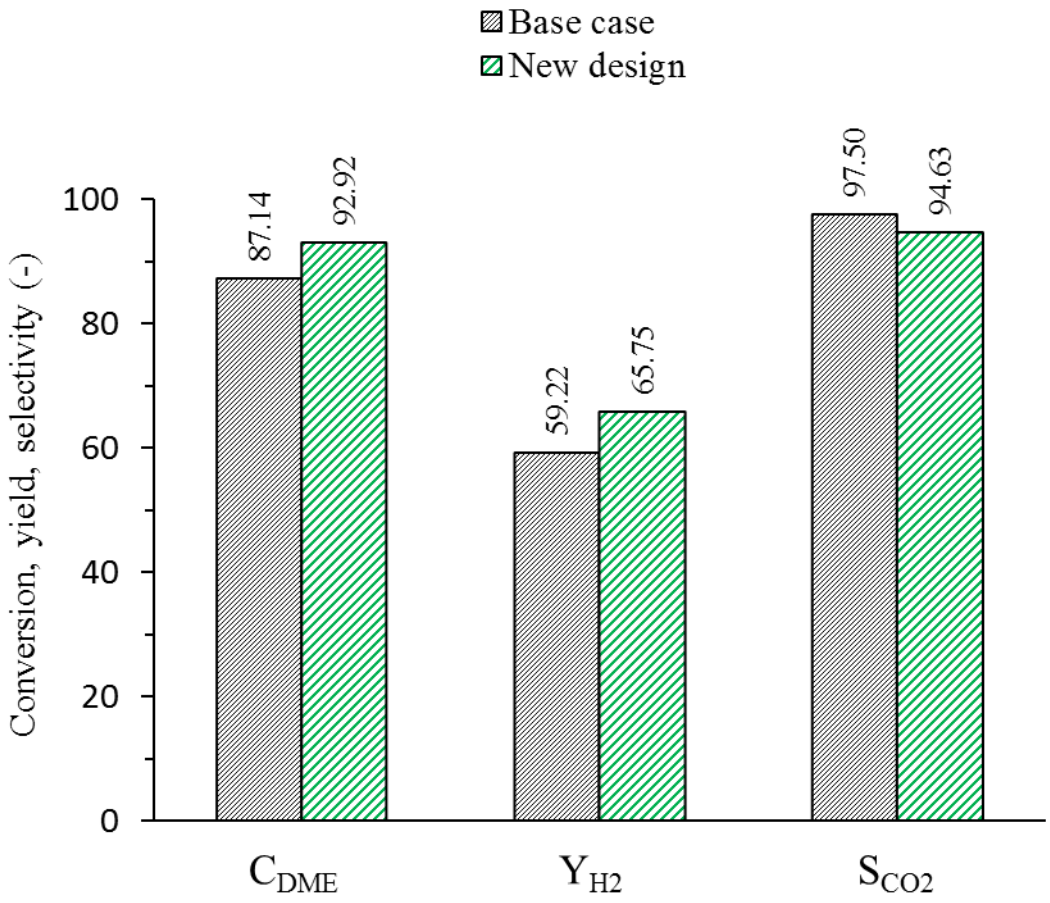

Fig. 6.6: Comparison DME conversion, hydrogen yield and CO2 selectivity for the base case DME-SR to the new design

Fig. 6.7 shows the product gas composition comparison between the base case and new design. As expected more hydrogen and CO compositions exited from the product stream. This is attributed to the increased DME conversion. The reduction of unreacted DME in the new design demonstrates that the hydrolysis reaction shifted to the right, this resulted to the improved conversions in the reactor. There was negligible effect on CO_2 product gas composition despite the increased conversions. It could be suggested that increased DME hydrolysis reaction was sufficient to produce CO_2 despite impact of reverse WGSR.

The enhanced conversions achieved in the new design demonstrate the effects of attaining substantial level of good mixing in the fluidized bed system and recommends that changing reactor geometry would have an impact on the performance. As the knowledge of the hydrodynamic and other features of the new design is limited and beyond the scope of this project, it provides a good argument for further investigation and validations to accurately predict the behaviours in the bed.

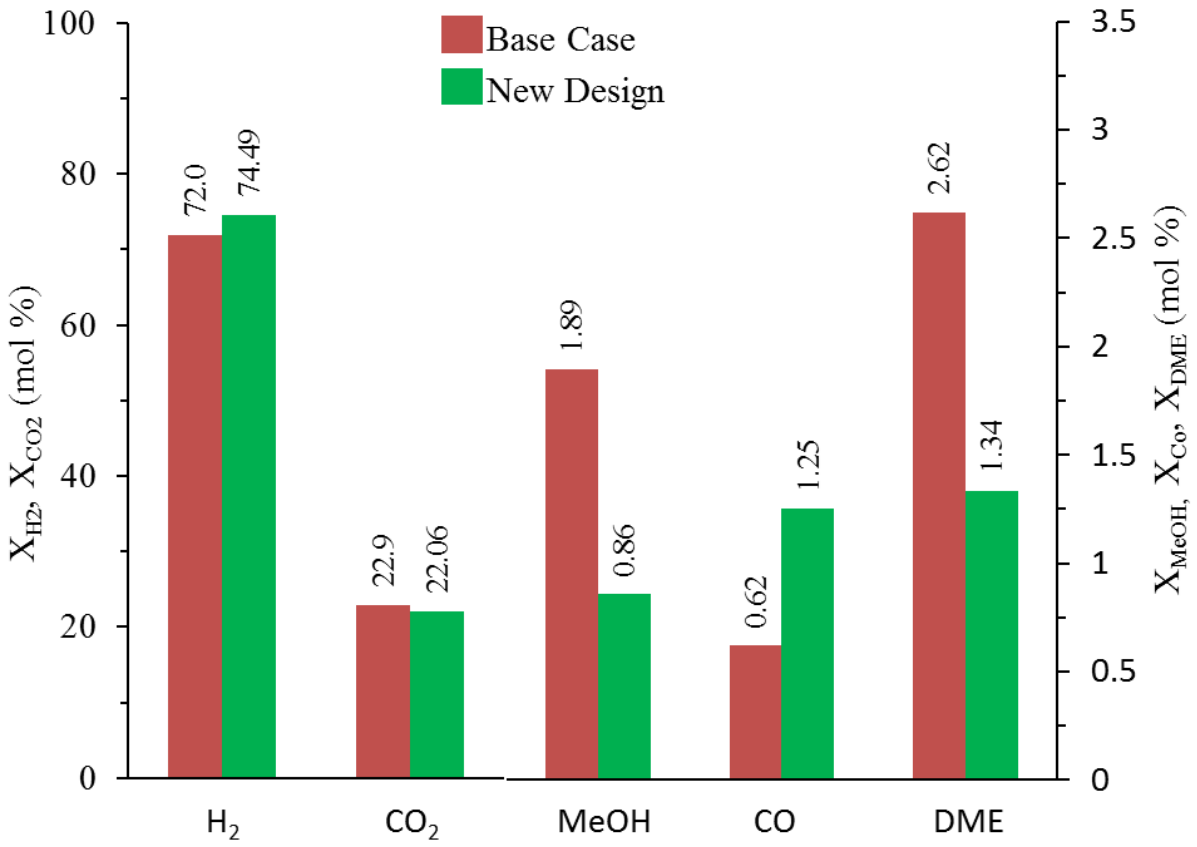

Fig. 6.7: Comparison of base case product gas composition to the new design

6.3 Industrial Sponsor Simulation

In this section, the integrated system with the coupling of adsorption and steam reforming beds were envisaged. The mass of the DME adsorbed in the base case in chapter 4 was coupled in the steam reforming system. The purpose of this section is to produce a preliminary estimation of the amount of hydrogen gas that would be produced if 1wt% DME gas was fed into bubbling bed system. The results from the DME adsorption in the bubbling bed were then coupled into the DME-SR section to complete the DFB loop. The amount of DME adsorbed for the DME-SR section was much smaller than the amount assumed for validation of the industrial existing CFB system. This resulted in the down scaling of the DME-SR for the sponsoring company to facilitate circulation. The fluidizing steam and DME mass flow rate for the DME-SR was equally adjusted to maintain a steam to DME molar ratio of 5 which was suggested as the appropriate feed ratio. The operating conditions can be seen in Table 6.1.

The amount of MOL4A (type of zeolite catalyst that acted as the adsorbent for the adsorption of DME in the bubbling bed) that adsorbed DME gas for the base case simulation was approximately 0.09kg/s; this was added to the ZSM-5 catalyst to achieve the appropriate space velocity in the system. The MOL4A and ZSM-5 were modelled to have similar properties. This is one area that would need

further research as the catalysts detailed behaviour could not be examined using FLUENT Eulerian model for this project.

6.3.1 Geometry re-design

The dimension of the reactor for the validation of the industrial CFB system was scaled down to allow fluidization in the system. The assumed conditions for the steam reforming of DME in the large scale CFB was much greater than the industrial conditions. This resulted in the scaling down of the reactor used for the large scale to fit the industrial conditions. The scaling down was done by using a non-dimensional analysis recommended by Glicksman [15]. The dimensionless quantity was (Height/Diameter = D/H) also called the aspect ratio. The aspect ratio is significant in the flow hydrodynamics (solid mixing) of the reactor and because the system is based on computational simulation, other scaling parameters were neglected as the Navier-stokes equation employed in the calculations of Eulerian-Eulerian model would adjust the system. In selecting the operating condition, steam to DME molar ratio of 5 was preferred based on the parametric analysis discussed in chapter 5. The aspect ratio was applied to maintain similar hydrodynamic features as discussed for the designed CFB bed in chapter 5. This will be verified through the analysis of the reactor performance as it will be expected to replicate the parametric analysis conducted for steam to DME molar ratio of 5.

The dimension of the DME-SR adopted from an industrial existing power plant was divided by the scaling factor (5) to scale down the original design in order to facilitate industrial sponsor case. The resultant diameter was investigated for its fluidization aspects by analysing the velocity through the diameter. The simulation operating and reactor condition can be seen in Table 6.1.

Table 6.1: The reactor operating conditions used in the simulation for the company case

Parameters	Operating condition
Steam:	
Inlet temperature	300 ^{o}C
Flow rate	0.119 (kg/s)
DME:	
Inlet temperature	300 ^{o}C
Flow rate	0.061 (kg/s)
Catalyst*:	
Particle diameter	150 µm (both catalyst)
Density	1300 kg/m3 ($CuO/ZnO/Al_2O_3$)
	720 kg/m3 (ZSM-5)
Total mass flow rate	10 kg/s (5 kg/s each catalyst)
Calculated space velocity	31000 ml g_{cat}^{-1} h^{-1}

Reactor dimensions:	
Aspect Ratio (H/D)	5
Diameter	0.6 m
Height	3.0 m

* *specified as two separate solid materials: $CuO/ZnO/Al_2O_3$ and ZSM-5*

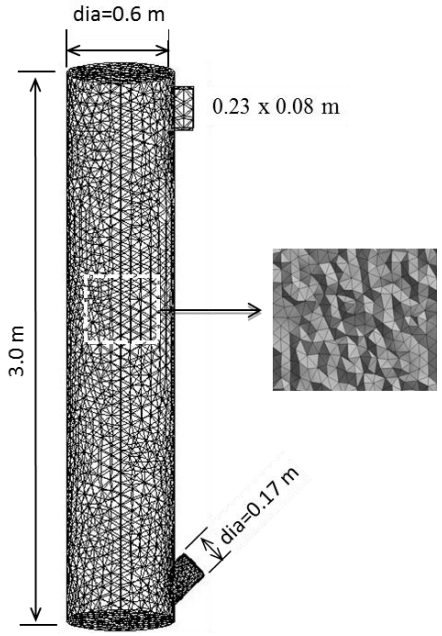

Fig. 6.8: Computational domain meshed for the company's fluidized bed with a section plane showing elements

The scaled down geometry as seen in Fig. 6.8 was meshed accordingly as described in chapter 2 and the mesh analysis was conducted. The appropriate reasonable suggested mesh number of cells was 40,000cells after comparison with 105,000 cells and 17,000 cells using the system's mean static pressure as investigative parameter (demonstrated in chapter 2).

6.3.2 Conversions and gas compositions

Fig. 6.9 depicts the DME conversion, hydrogen yield carbon dioxide selectivity in the system. As expected the hydrogen yield and DME conversion were closely matched with the parametric analysis conducted for the Steam/DME molar ratio 5, though CO_2 selectivity showed that more CO was produced. This could suggest that the system favoured the reverse WGSR or the conversion of CO to CO_2 and hydrogen was insufficient. The reason for the slight differences is attributed to the slight reduction of the space velocity for the company case compared to the space velocity for the parametric study for the Steam/DME molar ratio of 5. It was difficult to maintain the same space velocity after several trials. This reduction favoured reverse WGSR as seen in the parametric study for space velocity. It also favoured higher DME conversion and hydrogen yield and explains the differences

between the results to the steam to molar ratio of 5. This result further expresses the significant of the space velocity on the reactor performance as discussed in chapter 5. Efforts were made to maintain the space velocity

These results show that the scaling factor applied to reduce the dimensions from the industrial plant CFB system was effective. It further suggests that the discussion mentioned in the parametric analysis for the steam to DME molar ratio of 5 (discussed in chapter 5) would be applicable for this industrial sponsor case. This also suggests that the impact of the residence time as analysed for the industrial plant case in chapter 5 would be similar for the industrial sponsor case.

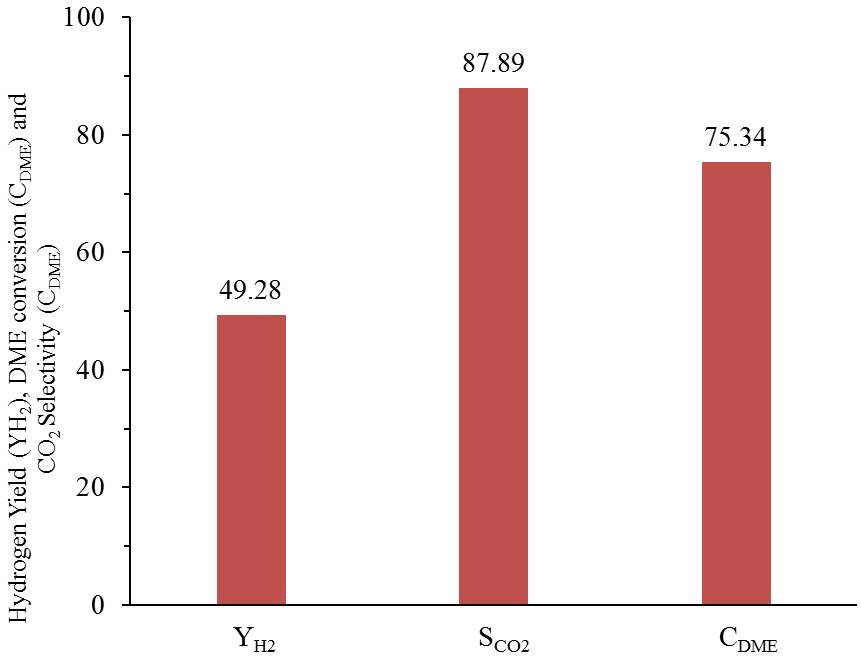

Fig. 6.9: DME conversion (C_{DME}), hydrogen yield (Y_{H2}) and CO_2 selectivity (S_{CO2}) in the company case system. Operating condition: steam to DME molar ratio 5 and Space velocity 31000 $mlg^{-1}h^{-1}$, Temperature =300 ^oC

Fig. 6.10 depicts the gas composition leaving from the outlet of the fluidized bed on dry basis; the trends were as expected closely related to the gas compositions for the Steam/DME molar ratio of 5 except for slight differences were discussed above. This further justifies the scaling down approach for the fluidized bed system as expected performance was observed. We refer to chapter 5 for further discussion on the gas compositions.

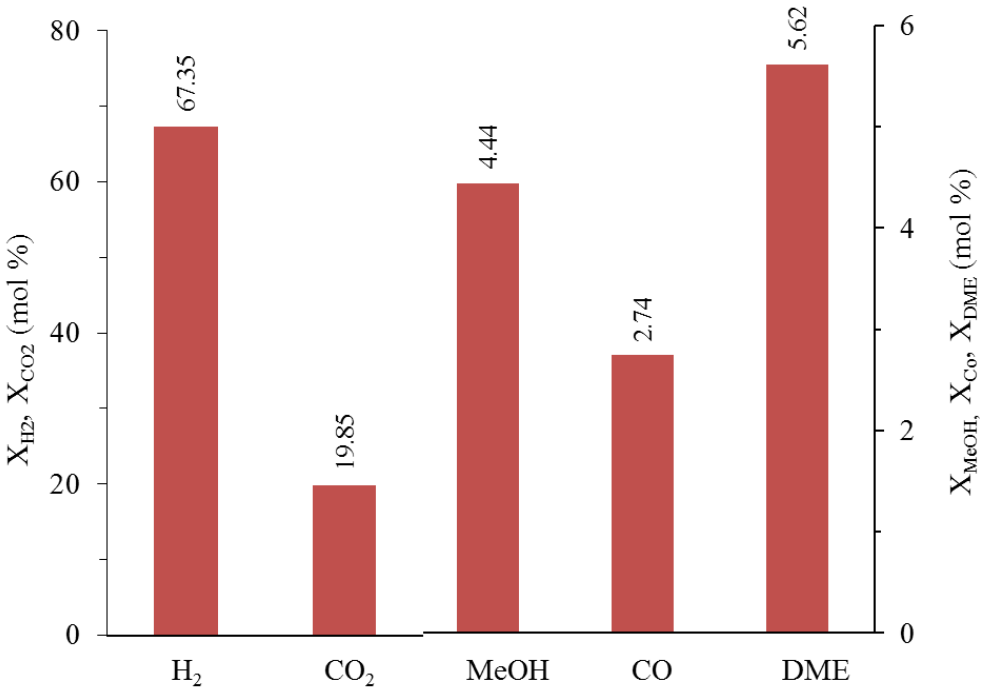

Fig. 6.10: Gas compositions of the exit from the company case system on (dry basis) in mole percentage. Operating condition: steam to DME molar ratio 5 and Space velocity 31000 $mlg^{-1}h^{-1}$, Temperature =300 ^{o}C.

6.3.3 Hydrogen produced based on 1wt% DME feed

In the proposed DFB system the DME adsorbed from the bubbling bed was coupled into the industrial sponsor DME-SR CFB case where hydrogen was produced. From the company's specification 1wt% of DME is the maximum amount of the gas that can be removed. Based on this condition the data for 1wt% DME adsorption was integrated into DME-SR to produce hydrogen.

Table 6.2 shows the amount of product gases from the industrial sponsor case based on the removal of 88% of DME from the adsorptive system. The total mass of DME entering the system is estimated as 1992.8t/y based on the company's throughput. From the analysis of the adsorptive system based on the kinetics derived from experimental data as discussed in chapter 3, 1747.9t/y of DME was adsorbed. This DME which is 88% of the maximum amount of DME in the adsorptive system by the catalyst produced 224.4 t/y of hydrogen with CO_2 and CO among other valuable products at 1454.4 t/y and 127.9 t/y respectively.

Table 6.2: Amount of product gases produced based on the removal of 88% of the maximum 1wt% DME in the process stream of 200,000t/y

Mass flowrate	kg/s	kg/h	kg/yr.	t/y
Hydrogen	0.007791	28.1	224373.7	224.4
CO_2	0.050515	181.9	1454823.8	1454.8
CO	0.004442	16.0	127916.0	127.9

6.3.4 Preliminary rough capital cost

This section briefly endorses potential establishment of the proposed dual system by giving a quick estimate of the cost of the project. The application of the designed bubbling and CFB beds is practical and has been developed commercially for other processes. A rapid preliminary capital cost (includes all equipment, materials, labour, civil installation, commissioning and control room) estimation for the dual system was produced using the step counting methods by Timms, IChemE (1998) [171], a more updated equation was applied instead [172]. Though the method is for gas phase system, this estimation is just a rough calculation. The step counting method is a simple and quick means of calculating the capital cost of project by counting the number of process units in the project. Considering the proposed dual system the number that will be accounted for the calculation will be 1 as the throughput is only through the bubbling bed system. Equation below shows the calculation.

$$C = 10560\ N\ Q^{0.615} \tag{6.1}$$

where C is the capital cost in £, N is the number process units and Q is the throughput (200,000t/y)

Estimation of the fixed cost was approximately £19,222,000; this value is usually adjusted with a ±30% error for the actual cost.

7 CHAPTER 7: ACHIEVEMENTS, CONCLUSIONS AND RECOMMENDATION

7.1 Introduction

This section of the thesis provides succinct conclusions on the different work of the thesis together with recommendations for future work. The application of CFD in the modelling of DME-SR for hydrogen production in a large scale fluidized bed system has never been performed; this study accomplished this breakthrough by implementing kinetic models from literatures which were validated with experimental data. The DME adsorption modelling was performed adopting methods previously reported in the literature for the removal of CO_2 from flue gas in fluidized bed system. The CFD models successfully provided detailed information which allowed drawing conclusions for future industrial implementation and process optimization. This confirms the benefits of CFD in the analysis of challenging processes without setting up a pilot plant, an expensive alternative.

7.2 Summary of achievements

This section provides a summary of the achievements accomplished with respect to industrial sponsor set targets and the overall academic objectives of the PhD study. This includes achievements in the areas of DME adsorption and steam reforming of the gas in large scale fluidized bed.

7.2.1 Achievements against industrial sponsor

The project targets set by the industrial sponsor together with accomplishment from this project are listed in Table 7.1.

Table 7.1: Industrial sponsor objectives for the project and the corresponding assessment from the project

Industrial sponsor Objectives	Project accomplishment
Removes at least 99% of (DME) from a feed stock of methyl chloride	Studies shows over 88% of DME is removed though this depended on conditions
Produces no toxic by-products that require transportation	No toxic by-products produced
Has low capital cost and size	Preliminary capital cost within acceptable range (see section 7.3.5)
Introduces no new compounds into the process	No new compound was introduced
Produces low levels of CO_2 not more than 2 tonnes/tonne DME removed	CO_2 produced was 0.8 tonnes/tonne of DME removed
Allows for recovering and re-using the DME	Yes the process allows re-processing of DME
Facilitate processing of 200,000 tonnes/year of MeCl feed	Yes the design was based on a 200,000 t/y capacity

7.2.2 Overall academic achievements

Computational models suitable for the design of a large scale process were successfully built for the DME adsorption and steam reforming. The CFD models were computationally effective given the size considered; it also permitted optimization of the reactor as well as identifying the residence time by applying two complementary methods. The derivation and implementation of the rate kinetics for DME adsorption in fluidized bed was performed for the first time. The implementation of the rate kinetics for DME steam reforming in circulating fluidized bed was performed for the first time. The analysis of the various investigations in this project strongly supported the novel proposed closed loop DFB system for combined separation and steam reforming process. The subsequent sections will further provide insight on the achievement.

7.2.2.1 DME adsorption

The modelling of DME in fluidized bed was performed for the first time in this project and highlights the novelty of the investigation. The fluidized bed size selected was of an industrial scale to match the industrial flow conditions set by the project industrial sponsor. The kinetics for the adsorption of DME using MOL4A was not available in the open literature and posed a challenging task at the early stage of the project. Experimental work conducted by a separate PhD project, with the same research group, provided data for the prediction of the rate equation for DME adsorption using the pseudo-first order kinetics mechanism from literature. The analysis of the adsorption of the gas showed that 88% of the DME was adsorbed in the base case simulation. The information from the base case was utilised as feed for the DME-SR to complete the dual system for the industrial case. The proportion of DME removed over a year was estimated as 1750t/y compared to a potential maximum of 2000t/y based on the adsorption of 1wt% DME feed into the bubbling bed system in the base case simulation.

7.2.2.2 DME-SR

This is the first time the DME steam reforming process has been implemented in a large scale fluidized bed reactor through simulation. The simulation results produced description of the spatial and chemical reaction behaviour in a CFB system for a DME-SR process for the first time. The validation of the models demonstrated the selected kinetics agreed reasonably with the experimental data which justified the application of the kinetics in the modelling of the DME-SR for the CFB industrial scale system. In the analysis of the company's case which considers the dual loop system, the data produced from the bubbling bed adsorption system was used as input in the steam reforming reactions in the CFB. Considering DME from the bubbling bed base case 224.4t/y of hydrogen was produced from 1750t/y of the gas. The remaining of the feed gas yielded CO_2 was 1458.4t/y and CO was 127.9t/y. In the event of utilising the hydrogen separately via selling to fuel cells companies it could be applied in the production of electricity, vehicles, airplanes etc. If the hydrogen produced was to be sold for fuel cell then conditions could be altered to favour reduction of CO in the system as this is regarded as one of the major impurities in fuel cells.

7.3 Conclusions

The conclusions for this thesis are sub-divided into various sections to properly narrate the conclusions drawn in each part of the thesis.

7.3.1 Developed CFD models for reactors

This chapter provided insight in the application of CFD in fluidized bed systems and also in other areas of engineering works. Eulerian-Eulerian multiphase CFD systems have being reported in numerous literatures as the preferred method for fluidized bed simulations, though Eulerian-Lagrangian predicts simulations with better accuracy. The computational time for tracking particles individually makes solving various computational equations undesirably long. This was the reason of eliminating the Eulerian-Lagrangian for this project.

Drag models which are essential parameters in fluidized bed system were investigated by analysing Syamlal-O'Brien and Gidaspow drag models. These models have been quoted in literature to predict satisfactory and in some cases accurate results with experimental data. Syamlal-O'Brien was however preferred for this project due to literature reviews on fluidized bed systems.

Mesh analysis study is a significant aspect of domain development for FLUENT simulation as it influences the accuracy of the results. The mesh refinement study showed that adopting the rule of thumb for mesh generation created millions of cells that consequently hindered the system performances. Mesh refinement study was conducted by investigating bed expansion and pressure distribution along the bed height. This resulted in the selection of mesh with 117,000cells for both the CFB and bubbling bed simulations because it provided accurate results while maintaining effective computational time.

Residence time which is an important aspect in the design and optimization of reactors were computed initially by the plug-flow method and then by an RTD pulse and step input methods. Results showed differences between plug-flow and RTD methods.

The CFD codes developed appear to provide effective analysis of the preliminary simulations which included residence time using the two different methods.

7.3.2 Kinetic models for DME-SR adsorption and DME-SR

Theoretical models and kinetics for the adsorption of DME on the adsorbent used in this study (MOL4A) has not been reported in literature. Therefore, one of the most important achievements in this project is the formulation of such model and kinetic. The proposed model is the pseudo-first order rate using data from an experimental work. Pseudo-first order was the selected rate kinetics as the linear plots suggested that it predicted the experimental data more accurately compared to the pseudo-second order. Further analysis of experimental data suggested that the effect of pressure changes to rate kinetics was negligibly and consequently the data for 4.5atm with a complete adsorption analysis

was used in the derivation of rate kinetics. The catalyst ($CuO/ZnO/Al_2O_3$+ZSM-5) was the impelling cause in the selection of the kinetics for the DME-SR. It was discovered that other catalysts from the literature would potentially improve conversions and yield existed. However there was limited information regarding the kinetics for such catalysts and hence eliminated the investigations of these catalysts kinetics in this project.

7.3.3 DME adsorption and parametric analysis

The simulations of DME adsorption on MOL4A was conducted assuming chemical reactions between the two components. This approach of using adsorption reaction rate was reported in notable literatures on adsorption of CO_2 from flue gases. The designed bubbling bed for the process was validated by estimation of bed expansion and fluctuation ratio from simulation and empirical computation. These were then compared to literatures. Bubbling bed hydrodynamics agreed well with literatures which validates the flow behaviour for the designed beds for the adsorption process.

In the parametric analysis it was observed that increasing rate constants increased the rate of adsorption which is expected if the adsorbent undergoes further treatments for improved performance. The impact of increasing fluidizing velocity reduced adsorption of DME due to reduction in the gas residence time which appears to have much effect compared to the solid residence time. Reducing adsorbent particle size decreased the adsorption of the gas, though this is contrary to experimental observations in literatures this effect is attributed to the CFD model and the pseudo-first order neglecting effect of particle size. The observation from the CFD simulation was however in agreement with the trends seen in other CFD analysis on the adsorbent particle size on adsorption. The effect of DME inlet mass fraction (DME inlet concentration) showed that the increase in the gas initial concentration decreased the amount of DME removed. It was suggested that the increase in DME mass fraction inlet could have potentially increased the overall adsorption rate. However, it was further suggested that the increase in adsorption rate, could have been insufficient to compensate for the excess DME. This argument is supported by the somewhat increase in the amount of unadsorbed gas leaving the system thus reducing the amount of DME adsorbed.

Both rate equations proposed had very similar trend and justified the application of any of the method in the process. The parameters that affected the adsorption of DME the most was the rate constant and the fluidizing velocity which suggests that for improved adsorption of the gas enhanced catalyst and lower fluidizing velocities would be encouraged.

The proposed CFD model has shown good predictions capability, hence can be used in the future as a tool for industrial scale development of DME adsorption or for any other gases, if the rate of adsorption data is available.

7.3.4 DME steam reforming and parametric analysis

CFB hydrodynamics agreed well with literatures which validates the flow behaviour for the designed beds for DME-SR process. The hydrodynamics also demonstrated impact of the entrance and exit effects on the flow around the bed which has being reported in literatures. There is very limited work on the simulation of DME-SR in the literatures; this thesis proposed the first simulation of DME-SR in large scale fluidized bed system.

The DME-SR base case simulation provided an insight in the development and validation of the process kinetics. The validation of the kinetics with an experimental bubbling bed demonstrated the effectiveness of the selected kinetics in the analysis of hydrogen production from DME in an industrial scale fluidized bed systems. In this work, the analysis of the spatial distribution of the species concentration in the CFB proposed four zones in the bed. The lower section were DME hydrolysis reaction was prominent, above the lower section is predominantly methanol steam reforming process. The middle section of the bed is dominated by the methanol decomposition reaction while the top demonstrated presence of WGSR.

The parametric analysis conducted for DME-SR in this project produced trends that agreed well with published works on laboratory fixed and micro-reactors. Analysis on the reactor below and above the base height of 15m showed that decreasing the height to 10m decreased DME conversion and hydrogen yield while increasing height to 20m showed insignificant change. The results further suggested that an optimum reactor height of 15m was effective for reactor performance, this arguably could be the reason the existing industrial plant adopted this dimension.

Increasing the temperature showed significant improvement in the DME conversion and hydrogen yield. Though it has been suggested to operate below 300 ^{o}C by some literatures due to the metallic catalyst deactivation, some literatures have proposed improved hydrogen yield achieved at above 300 ^{o}C with similar catalyst.

The increase of Steam/DME molar ratio showed considerable increase in the DME conversion and hydrogen yield. It was recommended that the appropriate steam/DME molar ratio of 5 should be adopted because of the energy impact of steam. Also from the simulations analysis, the effect of increasing the Steam/DME molar ratio above 5 was less significant.

The increase in the space velocity showed decrease in the DME conversion and hydrogen yield, this meant lower space velocity encouraged improved performance.

The gas residence time is an effective parameter that could predict future yield and optimise the reactor design. It was observed that significant improved reactor performance was achieved in increasing the residence time of the gas from 2.4s at 10m to 3.9s at 15m. The impact of the mean gas residence time above 3.9s on the reactor performance was insignificant; this suggested an “operating window” around 3.9s. At 20m reactor height, residence time of 5.1s was achieved. It was suggested

that if the gas spends more time in the reactor then the reverse nature of some of the chemical reactions would make product gas production unfavourable. This was supported by the analysis of the steam/DME molar ratio was analysed. It was discovered that there was significant reactor performance improvement when the residence time is reduced; this was evident in the performance of steam to DME molar ratio at 4 and 7.68.

The conclusion from the parametric analysis of the various simulations suggests effective operating conditions with 300 ^{o}C temperatures and Steam/DME molar ratio of 5. The space velocity specification will depend on the size and the type of fluidized bed system regime. The CFD model validated and analysed DME-SR process in this study notwithstanding the limited knowledge in this area of technology and kinetics. This was a substantial achievement and will evidently enable further research of CFD modelling of DME-SR in fluidized bed systems.

7.3.5 Industrial sponsor case

The DME-SR reactor was subjected to alteration to investigate the impact of component mixing on reactor performance. The change considered was creating two side inlets and fragmented the feed into the sides equally. The flow hydrodynamics demonstrated behaviour unusual to CFB system, it was suggested that an annular fluidized bed resemblance was achieved. This was due to the pattern of chaotic mixing observed in the reactor with a prominent jet-like form at the bottom of the bed. The comparison between new design to the base case DME-SR showed slight reactor improvement. This suggested that improved mixing in the reactor was essential for future reactor optimisation. The new design was not selected for proceeding analysis for the project due to insignificant improvement and indistinct hydrodynamic behaviour.

The completion of the DFB loop system involved coupling results from the DME adsorption from bubbling bed to a DME-SR reactor. As the quantity of DME adsorbed from the industrial sponsor specification (0.061kg/s) was much smaller than the validation operating conditions, the geometry was re-adjusted. The scaling down was achieved by adopting aspect ratio method by Glickman's scaling law; this resulted in the industrial plant CFB dimension reduced by 5. The operating condition selected were the recommendations from parametric analysis. The DME conversion and hydrogen yield were close to condition selected from parametric analysis. The analysis showed that 224.4 tonnes/year of hydrogen was produced based on adsorption of 88% of 1wt% DME feed into the bubbling bed. Other notable product gases included 1454.8toones/year of CO_2 and 127.9tonnes/year of CO.

Preliminary capital cost for the project showed the potential of future establishment of the proposed DFB system. Further discussion with industrial sponsor representative suggested that the cost was within an acceptable range. This was as a result of comparing the preliminary capital cost for this study to previous executed projects in the company.

7.4 Recommendation

7.4.1 DME adsorption in bubbling bed

Parametric analysis of the adsorption of the gas using FLUENT showed some weaknesses in the Eulerian model selected for the project. The impact of particle sizes was a good example of the limitation of the model, a more detailed understanding of the behaviour of the adsorbent particle characteristics would be probably much accomplished in Eulerian-Lagrangian model for two phase flow. The industrial scale size of the proposed system would mean large computational time that would probably require an industrial performance computers. The rate kinetics derived from the application of experimental data from a fixed bed system in the bubbling bed showed good agreement with the trends reported in literature. However, an experimental work using a laboratory scale fluidized bed system would be encouraged to validate the kinetic models. The ideal of the dual loop allows adsorbent with the adsorbate subjected by steam in the DME-SR reactor; the catalyst for the DME-SR coincidently was a zeolite catalyst with different method of preparation and possibly behaviours under certain conditions like pressure or temperature. Ideally this is one area that would require more investigation and research particularly as DME-SR catalyst could be changed to a non-zeolite acidic catalyst.

7.4.2 DME-SR in CFB

In the DME-SR simulation, the selected catalyst for the kinetics in the literature was observed not to exceptional produce the best DME conversion or hydrogen yield. It was reported that other catalysts provided better performance in comparison to CuO/ZnO/Al2O3+ZSM-5. This means that more investigations or research would be needed to achieve higher reactor performance in terms of the catalyst selected to provide the kinetics of the reactions in the system. The reactor re-designed showed some improvements in the mixing achieved in the bed which resulted in slightly enhanced conversions and yield in the bed. Though an unusual bed hydrodynamic behaviour was observed it demonstrated that further research can be done in the area of the fluidized bed design to facilitate better performance.

REFERENCE

[1] J. Vicente, J. Eren, L. Oar-arteta, M. Olazar, J. Bilbao, A.G. Gayubo, E ff ect of Operating Conditions on Dimethyl Ether Steam Reforming in a Fluidized Bed Reactor with a CuO- ZnO-Al2 O3 and Desilicated ZSM-5 Zeolite Bifunctional Catalyst, Industrial & Engineering Chemistry Research. 53 (2014) 3462–3471.

[2] W. Song, D. Tondeur, L. Luo, J. Li, VOC adsorption in circulating gas fluidized bed, Adsorption. 11 (2005) 853–858. doi:10.1007/s10450-005-6035-z.

[3] J. Lad, Methyl chloride purification for the silicone industry, Aston University, 2015.

[4] B. Chalermsinsuwan, P. Piumsomboon, D. Gidaspow, A Computational Fluid Dynamics Design of a Carbon Dioxide Sorption Circulating Fluidized Bed, AIChE Journal. 56 (2010) 2805–2824. doi:10.1002/aic.12213.

[5] M. Ayobi, S. Shahhosseini, Y. Behjat, Computational and experimental investigation of CO2 capture in gas-solid bubbling fluidized bed, Journal of the Taiwan Institute of Chemical Engineers. 45 (2014) 421–430. doi:10.1016/j.jtice.2013.06.009.

[6] G. Yu, L. Zhao, J. Chen, T. Hu, B. Dai, D. Liu, et al., Numerical Studies for the CO 2 Capture Process in a Fluidized-Bed Absorber, Energy & Fuels. 28 (2014) 4705–4713. doi:10.1021/ef5007963.

[7] J.B. Lad, Y.T. Makkawi, Adsorption of dimethyl ether (DME) on zeolite molecular sieves, Chemical Engineering Journal. 256 (2014) 335–346. doi:10.1016/j.cej.2014.07.001.

[8] Atkins Peter and de Paula Julio, ELEMENTS OF PHYSICAL CHEMISTRY, 4th ed., OXFORD UNIVERSITY PRESS, London, 2005.

[9] J.D. Holladay, J. Hu, D.L. King, Y. Wang, An overview of hydrogen production technologies, Catalysis Today. 139 (2009) 244–260. doi:10.1016/j.cattod.2008.08.039.

[10] Nigel Sammes, ed., Fuel Cell Technology: Reaching Towards Commercialization, 1st ed., Springer, London, 2006.

[11] T.L. LeValley, A.R. Richard, M. Fan, The progress in water gas shift and steam reforming hydrogen production technologies – A review, International Journal of Hydrogen Energy. 39 (2014) 16983–17000. doi:10.1016/j.ijhydene.2014.08.041.

[12] R. Chaubey, S. Sahu, O.O. James, S. Maity, A review on development of industrial processes and emerging techniques for production of hydrogen from renewable and sustainable sources, Renewable and Sustainable Energy Reviews. 23 (2013) 443–462. doi:10.1016/j.rser.2013.02.019.

[13] D.J. Wilhelm, D.R. Simbeck, a. D. Karp, R.L. Dickenson, Syngas production for gas-to-liquids applications: Technologies, issues and outlook, Fuel Processing Technology. 71 (2001) 139–148. doi:10.1016/S0378-3820(01)00140-0.

[14] C. Si, J. Wu, Y. Wang, Y. Zhang, X. Shang, Drying of Low-Rank Coals: A Review of Fluidized Bed Technologies, Drying Technology. 33 (2015) 277–287. doi:10.1080/07373937.2014.952382.

[15] M. Rüdisüli, T.J. Schildhauer, S.M. a Biollaz, J.R. Van Ommen, Scale-up of bubbling fluidized bed reactors - A review, Powder Technology. 217 (2012) 21–38. doi:10.1016/j.powtec.2011.10.004.

[16] F. Systems, HANDBOOK of FLUIDIZfiTION and FLUID-PARTICLE SYSTEMS edited by Wen-Ching Yang, 2003.

[17] J. Werther, E.-U. Hartge, S. Heinrich, Fluidized-Bed Reactors - Status and Some Development Perspectives, Chemie Ingenieur Technik. 86 (2014) 2022–2038. doi:10.1002/cite.201400117.

[18] P. Basu, Combustion and gasification in fluidized beds, Taylor& Francis Group, Oxford, 2006.

[19] S.C. Tsinontides, R. Jackson, The mechanics of gas fluidized beds with an interval of stable fluidization, Journal of Fluid Mechanics. 255 (1993) 237. doi:10.1017/S0022112093002472.

[20] V. Vinod Kumar, V.R. Raghavan, Developments in fluidized bed technology A review, 2011 National Postgraduate Conference - Energy and Sustainability: Exploring the Innovative Minds, NPC 2011. (2011). doi:10.1109/NatPC.2011.6136395.

[21] A. Mahecha-Botero, J.R. Grace, S.S.E.H. Elnashaie, C.J. Lim, Advances in Modeling of Fluidized-Bed Catalytic Reactors: a Comprehensive Review, Chemical Engineering Communications. 196 (2009) 1375–1405. doi:10.1080/00986440902938709.

[22] M. Rhodes, Introduction to Particle Technology: Second Edition, 2008. doi:10.1002/9780470727102.

[23] D. Kunii, O. Levenspiel, Fluidization Engineering, 2nd ed., Butterworth-Heinemann, Boston, 1991.

[24] N. Chhanwal, a. Tank, K.S.M.S. Raghavarao, C. Anandharamakrishnan, Computational Fluid Dynamics (CFD) Modeling for Bread Baking Process-A Review, Food and Bioprocess Technology. 5 (2012) 1157–1172. doi:10.1007/s11947-012-0804-y.

[25] B. Xia, D.-W. Sun, Applications of computational fluid dynamics (cfd) in the food industry: a review, Computers and Electronics in Agriculture. 34 (2002) 5–24. doi:10.1016/S0168-1699(01)00177-6.

[26] H.K. Versteeg, W. Malalasekera, An introduction to computational fluid dynamics: the finite volume method, Fluid Flow Handbook. McGraw-Hill …. (2007). http://www.mie.utoronto.ca/labs/mussl/cfd20.pdf\nhttp://books.google.com/books?hl=en&lr=&id=RvBZ-UMpGzIC&oi=fnd&pg=PP12&dq=An+Introduction+to+Computational+Fluid+Dynamics+-+The+Finite+Volume+Method&ots=u1vXu9CjGd&sig=hliwjbhQnS5p48PHdFs-NsFQnfU\nhttp://bo.

[27] B. Andersson, C. Engineering, R. Andersson, C. Uni-, E. Hightech, E.D. Resources, et al., Computational Fluid Dynamics for Engineers, 1st ed., Cambridge University Press, Cambridge, 2012.

[28] T.J. Jamaleddine, M.B. Ray, Application of Computational Fluid Dynamics for Simulation of Drying Processes: A Review, Drying Technology. 28 (2010) 120–154. doi:10.1080/07373930903517458.

[29] E.M. Ryan, D. DeCroix, R. Breault, W. Xu, E.D. Huckaby, K. Saha, et al., Multi-phase CFD modeling of solid sorbent carbon capture system, Powder Technology. 242 (2013) 117–134. doi:10.1016/j.powtec.2013.01.009.

[30] M.J.H. Khan, M. a. Hussain, Z. Mansourpour, N. Mostoufi, N.M. Ghasem, E.C. Abdullah, CFD simulation of fluidized bed reactors for polyolefin production – A review, Journal of Industrial and Engineering Chemistry. 20 (2014) 3919–3946. doi:10.1016/j.jiec.2014.01.044.

[31] M. Syamlal, T.. O'Brien, The derivation of aa drag coefficient formula from velocity-voidage correlations, AIChE Symp. Series. (1987).

[32] D. Gidaspow, R. Bezburuah, J. Ding, Hydrodynamics of circulating fluidized beds, kinetic theory approach, in: Fluidization VII, Proceedings of the 7th Engineering Foundation Conference on Fluidization, 1992: pp. 75–82.

[33] O. Šikula, J. Mohelníková, J. Plášek, Thermal analysis of light pipes for insulated flat roofs, Energy and Buildings. 85 (2014) 436–444. doi:10.1016/j.enbuild.2014.09.044.

[34] S. Bose, M. Banerjee, Effect of non-Newtonian characteristics of blood on magnetic particle capture in occluded blood vessel, Journal of Magnetism and Magnetic Materials. 374 (2015) 611–623. doi:10.1016/j.jmmm.2014.09.012.

[35] W. Li, K. Yu, B. Liu, X. Yuan, Computational fluid dynamics simulation of hydrodynamics and chemical reaction in a CFB downer, Powder Technology. 269 (2015) 425–436. doi:10.1016/j.powtec.2014.09.026.

[36] C. Loha, H. Chattopadhyay, P.K. Chatterjee, Assessment of drag models in simulating bubbling fluidized bed hydrodynamics, Chemical Engineering Science. 75 (2012) 400–407. doi:10.1016/j.ces.2012.03.044.

[37] S. Shah, K. Myöhänen, S. Kallio, T. Hyppänen, CFD simulations of gas–solid flow in an industrial-scale circulating fluidized bed furnace using subgrid-scale drag models, Particuology. 18 (2015) 66–75. doi:10.1016/j.partic.2014.05.008.

[38] Y. Behjat, S. Shahhosseini, S.H. Hashemabadi, CFD modeling of hydrodynamic and heat transfer in fluidized bed reactors, International Communications in Heat and Mass Transfer. 35 (2008) 357–368. doi:10.1016/j.icheatmasstransfer.2007.09.011.

[39] E. Esmaili, N. Mahinpey, Adjustment of drag coefficient correlations in three dimensional CFD simulation of gas-solid bubbling fluidized bed, Advances in Engineering Software. 42 (2011) 375–386. doi:10.1016/j.advengsoft.2011.03.005.

[40] F. Vejahati, N. Mahinpey, N. Ellis, M.B. Nikoo, CFD simulation of gas-solid bubbling fluidized bed: A new method for adjusting drag law, Canadian Journal of Chemical Engineering. 87 (2009) 19–30. doi:10.1002/cjce.20139.

[41] ANSYS Inc, ANSYS Fluent Theory Guide, 15317 (2013) 724–746. https://support.ansys.com/AnsysCustomerPortal/en_us/Knowledge+Resources/Online+Docum

entation/Previous+Releases/15.0/Fluid+Dynamics/ANSYS+Fluent/Fluent+Theory+Guide?doc_link=/prod_docu/15.0/html/flu_th/flu_th.html.

[42] F. Hernández-Jiménez, S. Sánchez-Delgado, a. Gómez-García, a. Acosta-Iborra, Comparison between two-fluid model simulations and particle image analysis & velocimetry (PIV) results for a two-dimensional gas-solid fluidized bed, Chemical Engineering Science. 66 (2011) 3753–3772. doi:10.1016/j.ces.2011.04.026.

[43] M. Syamlal, and, T.. O'Brien, Computer simulation of bubbles in a fluidized bed, AIChE Symp. Series. 85 (1989) 22–31.

[44] S. Benzarti, H. Mhiri, H. Bournot, Drag models for Simulation Gas-Solid Flow in the Bubbling Fluidized Bed of FCC Particles, Waset.Org. 61 (2012) 1138–1143. http://waset.org/journals/waset/v61/v61-210.pdf.

[45] S. Zimmermann, F. Taghipour, CFD modeling of the hydrodynamics and reaction kinetics of FCC fluidized-bed reactors, Industrial and Engineering Chemistry Research. 44 (2005) 9818–9827. doi:10.1021/ie050490+.

[46] K. Papadikis, S. Gu, a. Fivga, a. V. Bridgwater, Numerical comparison of the drag models of granular flows applied to the fast pyrolysis of biomass, Energy and Fuels. 24 (2010) 2133–2145. doi:10.1021/ef901497b.

[47] M. Syamlal, W. Rogers, T. O'Brien, MFIX documentation: Volume 1, Theory Guide. National Technical Information Service, Springfield, VA, 1993. doi:METC-9411004, NTIS/DE9400087.

[48] C.K.K. Lun, S.B. Savage, D.J. Jeffrey, N. Chepurniy, Kinetic theories for granular flow: inelastic particles in Couette flow and slightly inelastic particles in a general flowfield, Journal of Fluid Mechanics. 140 (1984) 223. doi:10.1017/S0022112084000586.

[49] R.F. Fedors, R.F. Landel, An Empirical method of estimating the void fraction in mixtures of uniform particles of different size, Powder Technology. 23 (1979) 225–231. doi:10.1016/0032-5910(79)87011-4.

[50] M. Syamlal, Particle-Particle Drag Term in a Multiparticle Model of Fluidization, National Technical Information Service. (1987). doi:MC/21353-2373, NTIS/DE87006500.

[51] S. Benzarti, H. Mhiri, H. Bournot, R. Occelli, Numerical simulation of turbulent fluidized bed with Geldart B particles, Advanced Powder Technology. 25 (2014) 1737–1747. doi:10.1016/j.apt.2014.06.024.

[52] B. Launder, D. Spalding, Lectures in mathematical models of turbulence, 1st ed., Academic Press, London, 1972.

[53] D.J. Gunn, Transfer of heat or mass to particles in fixed and fluidised beds, International Journal of Heat and Mass Transfer. 21 (1978) 467–476. doi:10.1016/0017-9310(78)90080-7.

[54] R. B. Sharma, CFD Simulation for Flow over Passenger Car Using Tail Plates \nfor Aerodynamic Drag Reduction, IOSR Journal of Mechanical and Civil Engineering (IOSR-JMCE). 7 (2013) 28–35. http://www.iosrjournals.org/iosr-jmce/papers/vol7-issue5/F0752835.pdf?id=2310.

[55] A. Cahyadi, A.H. Neumayer, C.M. Hrenya, R. a. Cocco, J.W. Chew, Comparative study of Transport Disengaging Height (TDH) correlations in gas-solid fluidization, Powder Technology. 275 (2015) 220–238. doi:10.1016/j.powtec.2015.02.010.

[56] S.. George, J.. Grace, Entrainment of particles from aggregative fluidized beds, AIChE Symp. Series. (1978) 67–74.

[57] P.C. Johnson, R. Jackson, Friction akollisional constitutive relations for granular materials, with application to plane shearing, Journal of Fluid Mechanics. 176 (1987) 67–93.

[58] F. Taghipour, N. Ellis, C. Wong, Experimental and computational study of gas–solid fluidized bed hydrodynamics, Chemical Engineering Science. 60 (2005) 6857–6867. doi:10.1016/j.ces.2005.05.044.

[59] Y.T. Makkawi, P.C. Wright, R. Ocone, The effect of friction and inter-particle cohesive forces on the hydrodynamics of gas-solid flow: A comparative analysis of theoretical predictions and experiments, Powder Technology. 163 (2006) 69–79. doi:10.1016/j.powtec.2006.01.020.

[60] S.J. Gelderbloom, D. Gidaspow, R.W. Lyczkowski, CFD Simulations of Bubbling / Collapsing Fluidized Beds for Three Geldart Groups, AIChE Journal. 49 (2003) 844–858. doi:10.1002/aic.690490405.

[61] R. Andreux, G. Petit, M. Hemati, O. Simonin, Hydrodynamic and solid residence time distribution in a circulating fluidized bed: Experimental and 3D computational study, Chemical Engineering and Processing: Process Intensification. 47 (2008) 463–473. doi:10.1016/j.cep.2007.01.023.

[62] M. Simcik, M.C. Ruzicka, a. Mota, J. a. Teixeira, Smart RTD for multiphase flow systems, Chemical Engineering Research and Design. 90 (2012) 1739–1749. doi:10.1016/j.cherd.2012.03.014.

[63] W.-C. Yang, Bubbling Fluidized Bed, in: W.-C. Yang (Ed.), Handbook of Fluidization and Fluid-Particle Sytems, Marcel Dekker, Inc, Philadelphia, 2003: pp. 63–114.

[64] H. Fogler, Scott, Elements of Chemical Reaction Engineering, 4th ed., Pearson Education, Inc, New Jersey, 2006.

[65] R.J. Dry, C.C. White, Gas residence-time characteristics in a high-velocity circulating fluidised bed of FCC catalyst, Powder Technology. 58 (1989) 17–23. doi:10.1016/0032-5910(89)80003-8.

[66] I.C. van Putten, M. van Sint Annaland, G. Weickert, Fluidization behavior in a circulating slugging fluidized bed reactor. Part I: Residence time and residence time distribution of polyethylene solids, Chemical Engineering Science. 62 (2007) 2522–2534. doi:10.1016/j.ces.2005.10.025.

[67] U. Lackermeier, J. Werther, Flow phenomena in the exit zone of a circulating fluidized bed, 2002. doi:10.1016/S0255-2701(02)00008-9.

[68] D.. Ruthven, S. Farooq, K.. Knaebel, Pressure Swing Adsorption, John Wiley & Sons Inc, New York, 1997.

[69] A. Bhatnagar, W. Hogland, M. Marques, M. Sillanpää, An overview of the modification methods of activated carbon for its water treatment applications, Chemical Engineering Journal. 219 (2013) 499–511. doi:10.1016/j.cej.2012.12.038.

[70] V. Bolis, Fundamentals in Adsorption at the Solid-Gas Interface. Concepts and Thermodynamics, in: A. Auroux (Ed.), Calorimetry and Thermal Methods in Catalysis, Springer, New York, 2013: pp. 3–45.

[71] S. Brunauer, P.H. Emmett, E. Teller, Adsorption of Gases in Multimolecular Layers, Journal of the American Chemical Society. 60 (1938) 309–319. doi:citeulike-article-id:4074706\rdoi: 10.1021/ja01269a023.

[72] W.J. Thomas, B. Crittenden, Adsorption Technology and Design, Elsevier, Oxford, 1998.

[73] R. Yang, Gas Separation by Adsorption Process, Imperial College Press, London, 1997.

[74] F. Gimbert, N. Morin-Crini, F. Renault, P.M. Badot, G. Crini, Adsorption isotherm models for dye removal by cationized starch-based material in a single component system: Error analysis, Journal of Hazardous Materials. 157 (2008) 34–46. doi:10.1016/j.jhazmat.2007.12.072.

[75] K.Y. Foo, B.H. Hameed, Insights into the modeling of adsorption isotherm systems, Chemical Engineering Journal. 156 (2010) 2–10. doi:10.1016/j.cej.2009.09.013.

[76] A. Ladshaw, S. Yiacoumi, C. Tsouris, D. DePaoli, Generalized gas–solid adsorption modeling: Single-component equilibria, Fluid Phase Equilibria. 388 (2015) 169–181. doi:10.1016/j.fluid.2015.01.003.

[77] R. a. Latour, The langmuir isotherm: A commonly applied but misleading approach for the analysis of protein adsorption behavior, Journal of Biomedical Materials Research Part A. 103 (2015) 949–958. doi:10.1002/jbm.a.35235.

[78] O. Hamdaoui, E. Naffrechoux, Modeling of adsorption isotherms of phenol and chlorophenols onto granular activated carbon. Part II. Models with more than two parameters, Journal of Hazardous Materials. 147 (2007) 401–411. doi:10.1016/j.jhazmat.2007.01.023.

[79] K.V. Kumar, M.M. de Castro, M. Martinez-Escandell, M. Molina-Sabio, F. Rodriguez-Reinoso, A site energy distribution function from Toth isotherm for adsorption of gases on heterogeneous surfaces., Physical Chemistry Chemical Physics : PCCP. 13 (2011) 5753–5759. doi:10.1039/c0cp00902d.

[80] R. Ghosal, D.M. Smith, Micropore characterization using the Dubinin-Astakhov equation to analyze high pressure CO2 (273 K) adsorption data, Journal of Porous Materials. 3 (1996) 247–255. doi:10.1007/BF01137914.

[81] M. Pera-Titus, On an isotherm thermodynamically consistent in Henry's region for describing gas adsorption in microporous materials, Journal of Colloid and Interface Science. 345 (2010) 410–416. doi:10.1016/j.jcis.2010.01.027.

[82] H.M.. Freundlich, Over the Adsorption in Solution, Journal of Physical Chemistry. 57 (1906).

[83] I. Langmuir, The Constitution and Fundamental Properties of Solids and Liquids, Journal of AmericaN Chemistry Society. 11 (1916) 2221–2295.

[84] J. Toth, State Equations of the Solid Gas Interface Layer, Acta Chimica Academiae Scientiarum Hungaricae. 69 (1971) 311–317.

[85] R. Sips, Combined Form of Langmuir and Freundlich Equations, Journal of Chemical Physics. 16 (1948) 490–495.

[86] M.. Dubinin, V.. Astakhov, Development of the Concepts of Volume Filling of Micropores in the Adsorption of Gases and Vapors by Microporous Adsorbents, Russian Chemical Bulletin. 20 (1971) 3–7.

[87] O. Talu, A.. Myers, Rigorous thermodynamic treatment of gas adsorption, AiChE Journal. 34 (1988) 1887–1893. doi:10.1002/aic.690341114.

[88] O. Abdelwahab, N.K. Amin, Adsorption of phenol from aqueous solutions by Luffa cylindrica fibers: Kinetics, isotherm and thermodynamic studies, The Egyptian Journal of Aquatic Research. 39 (2013) 215–223. doi:10.1016/j.ejar.2013.12.011.

[89] M.T. Ghaneian, G. Ghanizadeh, M.T.H. Alizadeh, M.H. Ehrampoush, F.M. Said, Equilibrium and kinetics of phosphorous adsorption onto bone charcoal from aqueous solution, Environmental Technology. 35 (2013) 882–890. doi:10.1080/09593330.2013.854838.

[90] R. Ocampo-Perez, R. Leyva-Ramos, J. Mendoza-Barron, R.M. Guerrero-Coronado, Adsorption rate of phenol from aqueous solution onto organobentonite: Surface diffusion and kinetic models, Journal of Colloid and Interface Science. 364 (2011) 195–204. doi:10.1016/j.jcis.2011.08.032.

[91] C. Yao, T. Chen, A new simplified method for estimating film mass transfer and surface diffusion coefficients from batch adsorption kinetic data, Chemical Engineering Journal. 265 (2015) 93–99. doi:10.1016/j.cej.2014.12.005.

[92] H. Qiu, L. Lv, B. Pan, Q. Zhang, W. Zhang, Q. Zhang, Critical review in adsorption kinetic models, Journal of Zhejiang University SCIENCE A. 10 (2009) 716–724. doi:10.1631/jzus.A0820524.

[93] M. Delavar, A. Asghar Ghoreyshi, M. Jahanshahi, S. Khalili, N. Nabian, Equilibria and kinetics of natural gas adsorption on multi-walled carbon nanotube material, RSC Advances. 2 (2012) 4490. doi:10.1039/c2ra01095j.

[94] P.K. Pandey, S.K. Sharma, S.S. Sambi, Kinetics and equilibrium study of chromium adsorption on zeoliteNaX, International Journal of Environmental Science & Technology. 7 (2010) 395–404. doi:10.1007/BF03326149.

[95] D. Robati, Pseudo-second-order kinetic equations for modeling adsorption systems for removal of lead ions using multi-walled carbon nanotube, Journal of Nanostructure in Chemistry. 3 (2013) 55. doi:10.1186/2193-8865-3-55.

[96] S. Lagergren, Zur theorie der sogenannten adsorption geloester stoffe,Kungliga Svenska Vetenskapsakad, Handl. 24 (1898) 1–39.

[97] K.V. Kumar, Linear and non-linear regression analysis for the sorption kinetics of methylene blue onto activated carbon, Journal of Hazardous Materials. 137 (2006) 1538–1544. doi:10.1016/j.jhazmat.2006.04.036.

[98] Y.S. Ho, Review of second-order models for adsorption systems, Journal of Hazardous Materials. 136 (2006) 681–689. doi:10.1016/j.jhazmat.2005.12.043.

[99] Y. Wang, Z. Chao, H. a. Jakobsen, 3D Simulation of bubbling fluidized bed reactors for sorption enhanced steam methane reforming processes, Journal of Natural Gas Science and Engineering. 2 (2010) 105–113. doi:10.1016/j.jngse.2010.04.004.

[100] Y. Wang, Z. Chao, D. Chen, H. a. Jakobsen, SE-SMR process performance in CFB reactors: Simulation of the CO2 adsorption/desorption processes with CaO based sorbents, International Journal of Greenhouse Gas Control. 5 (2011) 489–497. doi:10.1016/j.ijggc.2010.09.001.

[101] J. Wang, Y. Wang, H. a. Jakobsen, The modeling of circulating fluidized bed reactors for SE-SMR process and sorbent regeneration, Chemical Engineering Science. 108 (2014) 57–65. doi:10.1016/j.ces.2013.12.012.

[102] A. Larsson, M. Seemann, D. Neves, H. Thunman, Evaluation of performance of industrial-scale dual fluidized bed gasifiers using the chalmers 2-4-MWth gasifier, Energy and Fuels. 27 (2013) 6665–6680. doi:10.1021/ef400981j.

[103] Y. Shi, X. Du, L. Yang, Y. Sun, Y. Yang, Experiments on hydrogen production from methanol steam reforming in fluidized bed reactor, International Journal of Hydrogen Energy. 38 (2013) 13974–13981. doi:10.1016/j.ijhydene.2013.08.073.

[104] M. Yang, Y. Men, S. Li, G. Chen, Hydrogen production by steam reforming of dimethyl ether over ZnO–Al2O3 bi-functional catalyst, International Journal of Hydrogen Energy. 37 (2012) 8360–8369. doi:10.1016/j.ijhydene.2012.02.070.

[105] T. Kawabata, H. Matsuoka, T. Shishido, D. Li, Y. Tian, T. Sano, et al., Steam reforming of dimethyl ether over ZSM-5 coupled with Cu/ZnO/Al2O3 catalyst prepared by homogeneous precipitation, Applied Catalysis A: General. 308 (2006) 82–90. doi:10.1016/j.apcata.2006.04.032.

[106] J. Ereña, J. Vicente, A.T. Aguayo, M. Olazar, J. Bilbao, A.G. Gayubo, Kinetic behaviour of catalysts with different CuO-ZnO-Al2O3 metallic function compositions in DME steam reforming in a fluidized bed, Applied Catalysis B: Environmental. 142-143 (2013) 315–322. doi:10.1016/j.apcatb.2013.05.034.

[107] C. Li, Y. Wang, P. Fan, Numerical analysis and experimental study of hydrogen production from dimethyl ether steam reforming, Science China Chemistry. 55 (2012) 1982–1987. doi:10.1007/s11426-012-4603-0.

[108] K. Takeishi, Steam reforming of dimethyl ether, Applied Catalysis A: General. 260 (2004) 111–117. doi:10.1016/j.apcata.2003.10.006.

[109] K. Faungnawakij, Y. Tanaka, N. Shimoda, T. Fukunaga, R. Kikuchi, K. Eguchi, Hydrogen production from dimethyl ether steam reforming over composite catalysts of copper ferrite spinel and alumina, Applied Catalysis B: Environmental. 74 (2007) 144–151. doi:10.1016/j.apcatb.2007.02.010.

[110] D. Feng, Y. Zuo, D. Wang, J. Wang, Steam Reforming of Dimethyl Ether over Coupled ZSM-5 and Cu-Zn-Based Catalysts, Chinese Journal of Catalysis. 30 (2009) 223–229. doi:10.1016/S1872-2067(08)60098-4.

[111] A.G. Gayubo, J. Vicente, J. Ereña, L. Oar-Arteta, M.J. Azkoiti, M. Olazar, et al., Causes of deactivation of bifunctional catalysts made up of CuO-ZnO-Al 2O3 and desilicated HZSM-5 zeolite in DME steam reforming, Applied Catalysis A: General. 483 (2014) 76–84. doi:10.1016/j.apcata.2014.06.031.

[112] J.S. Suh, M.T. Lee, R. Greif, C.P. Grigoropoulos, A study of steam methanol reforming in a microreactor, Journal of Power Sources. 173 (2007) 458–466. doi:10.1016/j.jpowsour.2007.04.038.

[113] J.. Amphlett, K.A.. Creber, J.. Davies, R.. Mann, B.. Peppley, D.. Stokes, Hydrogen Production by Steam Reforming of Methanol for Polymer Electrolyte Fuel Cells, International Journal of Hydrogen Energy. 19 (1994) 131–137.

[114] P. Nehe, S. Kumar, Methanol reformation for hydrogen production from a single channel with cavities, International Journal of Hydrogen Energy. 38 (2013) 13216–13229. doi:10.1016/j.ijhydene.2013.07.119.

[115] C.-F. Yan, W. Ye, C.-Q. Guo, S.-L. Huang, W.-B. Li, W.-M. Luo, Numerical simulation and experimental study of hydrogen production from dimethyl ether steam reforming in a micro-reactor, International Journal of Hydrogen Energy. 39 (2014) 18642–18649. doi:http://dx.doi.org/10.1016/j.ijhydene.2014.02.133.

[116] D. Feng, Y. Wang, D. Wang, J. Wang, Steam reforming of dimethyl ether over CuO-ZnO-Al2O3-ZrO2 + ZSM-5: A kinetic study, Chemical Engineering Journal. 146 (2009) 477–485. doi:10.1016/j.cej.2008.11.005.

[117] Q. Zhang, F. Fan, G. Xu, D. Ye, W. Wang, Z. Zhu, Steam reforming of dimethyl ether over a novel anodic y-Al2O3 supported copper bi-functional catalyst, International Journal of Hydrogen Energy. 38 (2013) 10305–10314. doi:10.1016/j.ijhydene.2013.06.006.

[118] V. V Galvita, G.L. Semin, V.D. Belyaev, T.M. Yurieva, V. a Sobyanin, Production of hydrogen from dimethyl ether, Applied Catalysis a-General. 216 (2001) 85–90. doi:10.1016/S0926-860X(01)00540-3.

[119] P. Hirunsit, K. Faungnawakij, Cu − Cr , Cu − Mn , and Cu − Fe Spinel-Oxide-Type Catalysts for Reforming of Oxygenated Hydrocarbons, Journal of Physical Chemistry. 117 (2013) 23757–23765.

[120] M.B. Desta, Batch sorption experiments: Langmuir and freundlich isotherm studies for the adsorption of textile metal ions onto teff straw (eragrostis tef) agricultural waste, Journal of Thermodynamics. 1 (2013) 1–6. doi:10.1155/2013/375830.

[121] Y. Kawamura, N. Ogura, A. Igarashi, Hydrogen Production by Methanol Steam Reforming Using Microreactor, Journal of the Japan Petroleum Institute. 56 (2013) 288–297.

[122] J.K. Lee, J.B. Ko, D.H. Kim, Methanol steam reforming over Cu/ZnO/Al2O3 catalyst: Kinetics and effectiveness factor, Applied Catalysis A: General. 278 (2004) 25–35. doi:10.1016/j.apcata.2004.09.022.

[123] T.-Y.Y. Park, G.F. Froment, Kinetic modeling of the methanol to olefins process. 1. Model formulation, Industrial and Engineering Chemistry Research. 40 (2001) 4172–4186. doi:10.1021/ie0008530.

[124] T.-Y. Park, G.F. Froment, Kinetic Modeling of the Methanol to Olefins Process. 2. Experimental Results, Model Discrimination, and Parameter Estimation, Industrial & Engineering Chemistry Research. 40 (2001) 4187–4196. doi:10.1021/ie000854s.

[125] C.J. Jiang, D.L. Trimm, M.S. Wainwright, N.W. Cant, Kinetic study of steam reforming of methanol over copper-based catalysts, Applied Catalysis A: General. 93 (1993) 245–255. doi:10.1016/0926-860X(93)85197-W.

[126] H. Purnama, T. Ressler, R.E. Jentoft, H. Soerijanto, R. Schlögl, R. Schomäcker, CO formation/selectivity for steam reforming of methanol with a commercial CuO/ZnO/Al2O3 catalyst, Applied Catalysis A: General. 259 (2004) 83–94. doi:10.1016/j.apcata.2003.09.013.

[127] R. Chein, Y.-C. Chen, J.N. Chung, Numerical study of methanol–steam reforming and methanol–air catalytic combustion in annulus reactors for hydrogen production, Applied Energy. 102 (2013) 1022–1034. doi:10.1016/j.apenergy.2012.06.010.

[128] W. Chen, M. Lin, T. Jiang, M. Chen, Modeling and simulation of hydrogen generation from high-temperature and low-temperature water gas shift reactions, International Journal of Hydrogen Energy. 33 (2008) 6644–6656. doi:10.1016/j.ijhydene.2008.08.039.

[129] R. Chein, Y.C. Chen, J.N. Chung, Numerical study of methanol-steam reforming and methanol-air catalytic combustion in annulus reactors for hydrogen production, Applied Energy. 102 (2013) 1022–1034. doi:10.1016/j.apenergy.2012.06.010.

[130] S. Cloete, A. Zaabout, S.T. Johansen, M. van Sint Annaland, F. Gallucci, S. Amini, The generality of the standard 2D TFM approach in predicting bubbling fluidized bed hydrodynamics, Powder Technology. 235 (2013) 735–746. doi:10.1016/j.powtec.2012.11.041.

[131] A.T. Mineto, M.P.D.S. Braun, H.A. Navarro, L. Cabezas-Gómez, Influence of the Granular Temperature in the Numerical Simulation of Gas-Solid Flow in a Bubbling Fluidized Bed, Chemical Engineering Communications. 201 (2014) 1003–1020. doi:10.1080/00986445.2013.794138.

[132] Y. Guan, J. Chang, K. Zhang, B. Wang, Q. Sun, Three-dimensional CFD simulation of hydrodynamics in an interconnected fluidized bed for chemical looping combustion, Powder Technology. 268 (2014) 316–328. doi:10.1016/j.powtec.2014.08.046.

[133] J. Chang, K. Zhang, Y. Yang, B. Wang, Q. Sun, Computational investigation of solid sorbent carbon dioxide capture in a fluidized bed reactor, Powder Technology. 275 (2015) 94–104. doi:10.1016/j.powtec.2015.01.067.

[134] R.W. Breault, E.D. Huckaby, Parametric behavior of a CO2 capture process: CFD simulation of solid-sorbent CO2 absorption in a riser reactor, Applied Energy. 112 (2013) 224–234. doi:10.1016/j.apenergy.2013.06.008.

[135] L. Marocco, A. Mora, CFD modeling of the Dry-Sorbent-Injection process for flue gas desulfurization using hydrated lime, Separation and Purification Technology. 108 (2013) 205–214. doi:10.1016/j.seppur.2013.02.012.

[136] C. Yaws, Yaw's Handbook of Thermodynamic and Physical Properties of Chemical Compounds, Knovel, 2003.

[137] M. Leva, Fluidization, McGraw-Hill, New York, 1959.

[138] J. Grace, Fluidized-bed Hydrodynamics, in: G. Hetsroni (Ed.), Handbook of Multiphase Systems, Hemisphere, Washington, 1982: pp. 8–5 – 8–64.

[139] R.. Johnson, The Handbook of Fluid Dynamics, CRC Press LLC, Florida, 1998.

[140] A. Ergudenler, A.. Ghaly, F. Hamdullahpur, A.. Al-Taweel, Mathematical Modelling of a Fluidized bed Straw Gasifier: Part II-Model Sensitivity, Energy Sources. 19 (1997) 1085–1098. doi:10.1080/00908319708908909.

[141] P. Rowe, Drag forces in a hydraulic model of a fluidized bed, part II, Transactions of the Institution of Chemical Engineers. (1961) 175–180.

[142] D. Geldart, A. Abrahamsen, Homogeneous Fluidization of fine powders using various gases and pressures, Powder Technology. 19 (1978) 133–136.

[143] A. Sahoo, Bed expansion and fluctuation in cylindrical gas solid fluidized beds with stirred promoters, Advanced Powder Technology. 22 (2011) 753–760. doi:10.1016/j.apt.2010.10.019.

[144] S. Mori, C.. Wen, Estimation of bubble diameter in fluidized beds, AIChE. 21 (1975) 109–115.

[145] J.. Davidson, D. Harrison, Fluidized Particles, Cambridge University Press, Cambridge, 1963.

[146] F. Doulati Ardejani, K. Badii, N.Y. Limaee, S.Z. Shafaei, a. R. Mirhabibi, Adsorption of Direct Red 80 dye from aqueous solution onto almond shells: Effect of pH, initial concentration and shell type, Journal of Hazardous Materials. 151 (2008) 730–737. doi:10.1016/j.jhazmat.2007.06.048.

[147] R.H. Krishna, a V.V.S. Swamy, INVESTIGATION ON THE EFFECT OF PARTICLE SIZE AND ADSORPTION KINETICS FOR THE REMOVAL OF Cr (VI) FROM THE AQUEOUS SOLUTIONS USING LOW COST, Eur.Chem.Bull. 1 (2012) 258–262.

[148] Y.C. Wong, Y.S. Szeto, W.H. Cheung, G. McKay, Effect of temperature, particle size and percentage deacetylation on the adsorption of acid dyes on chitosan, Adsorption. 14 (2008) 11–20. doi:10.1007/s10450-007-9041-5.

[149] X. Fan, J. Zhou, T. Wang, J. Zheng, X. Li, Opposite particle size effects on the adsorption kinetics of ZIF-8 for gaseous and solution adsorbates, RSC Adv. 5 (2015) 58595–58599. doi:10.1039/C5RA09981A.

[150] G. Yu, L. Zhao, J. Chen, T. Hu, B. Dai, D. Liu, et al., Numerical studies for the CO2 capture process in a fluidized-bed absorber, Energy and Fuels. 28 (2014) 4705–4713. doi:10.1021/ef5007963.

[151] H. Farag, M. Ossman, M. Mansour, Y. Farid, Modeling of fluidized bed reactor for ethylene polymerization: effect of parameters on the single-pass ethylene conversion, International Journal of Industrial Chemistry. 4 (2013) 20. doi:10.1186/2228-5547-4-20.

[152] a. Ahmadpour, M. Zabihi, M. Tahmasbi, T.R. Bastami, Effect of adsorbents and chemical treatments on the removal of strontium from aqueous solutions, Journal of Hazardous Materials. 182 (2010) 552–556. doi:10.1016/j.jhazmat.2010.06.067.

[153] X.E. Verykios, Catalytic dry reforming of natural gas for the production of chemicals and hydrogen, International Journal of Hydrogen Energy. 28 (2003) 1045–1063. doi:10.1016/S0360-3199(02)00215-X.

[154] S.. Pamela, K.. Margaret, ., Life Cycle Assessment of Hydrogen Production via Natural Gas Steam Reforming, Technical Report (NREL/TP-570-27637), National Renewable Energy Laboratory. (2001).

[155] N. Zhang, B. Lu, W. Wang, J. Li, 3D CFD simulation of hydrodynamics of a 150MWe circulating fluidized bed boiler, Chemical Engineering Journal. 162 (2010) 821–828. doi:10.1016/j.cej.2010.06.033.

[156] V. Verma, J.T. Padding, N.G. Deen, J.A.M.H. Kuipers, Numerical Investigation on the E ff ect of Pressure on Fluidization in a 3D Fluidized Bed, (2014).

[157] L. Huilin, H. Yurong, D. Gidaspow, Hydrodynamic modelling of binary mixture in a gas bubbling fluidized bed using the kinetic theory of granular flow, Chemical Engineering Science. 58 (2003) 1197–1205. doi:10.1016/S0009-2509(02)00635-8.

[158] C. Li, Y. Gao, C. Wu, Modeling and simulation of hydrogen production from dimethyl ether steam reforming using exhaust gas, International Journal of Energy Research. 39 (2015) 1272–1280.

[159] A. Yan, J.H. Pärssinen, J.X. Zhu, Flow properties in the entrance and exit regions of a high-flux circulating fluidized bed riser, Powder Technology. 131 (2003) 256–263. doi:10.1016/S0032-5910(02)00348-0.

[160] B. Gayubo, G. Ana, B. Vicente, Effect of Operating Conditions on Dimethyl Ether Steam Reforming in a Fluidized Bed Reactor with a CuO–ZnO–Al 2 O 3 and Desilicated ZSM-5 Zeolite Bifunctional Catalyst, Industrial & Engineering Chemistry Research. 53 (2014) 3462–3471. doi:10.1021/ie402509c.

[161] T. a. Semelsberger, R.L. Borup, H.L. Greene, Dimethyl ether (DME) as an alternative fuel, Journal of Power Sources. 156 (2006) 497–511. doi:10.1016/j.jpowsour.2005.05.082.

[162] V. V. Kuznetsov, O. V. Vitovsky, Hydrogen production by methanol steam reforming in an annular microchannel on a Cu-ZnO catalyst, Journal of Engineering Thermophysics. 17 (2008) 191–195. doi:10.1134/S1810232808030041.

[163] K. Faungnawakij, R. Kikuchi, T. Matsui, T. Fukunaga, K. Eguchi, A comparative study of solid acids in hydrolysis and steam reforming of dimethyl ether, Applied Catalysis A: General. 333 (2007) 114–121. doi:10.1016/j.apcata.2007.09.014.

[164] N. Shimoda, K. Faungnawakij, R. Kikuchi, K. Eguchi, A study of various zeolites and CuFe2O4 spinel composite catalysts in steam reforming and hydrolysis of dimethyl ether, International Journal of Hydrogen Energy. 36 (2011) 1433–1441. doi:10.1016/j.ijhydene.2010.10.088.

[165] L. Gradisher, B. Dutcher, M. Fan, Catalytic hydrogen production from fossil fuels via the water gas shift reaction, Applied Energy. 139 (2015) 335–349. doi:10.1016/j.apenergy.2014.10.080.

[166] I. Sierra, J. Ereña, A.T. Aguayo, J.M. Arandes, M. Olazar, J. Bilbao, Co-feeding water to attenuate deactivation of the catalyst metallic function (CuO-ZnO-Al2O3) by coke in the direct

synthesis of dimethyl ether, Applied Catalysis B: Environmental. 106 (2011) 167–173. doi:10.1016/j.apcatb.2011.05.021.

[167] A. Collin, K.-E. Wirth, M. Ströder, Experimental characterization of the flow pattern in an annular fluidized bed, The Canadian Journal of Chemical Engineering. 86 (2008) 536–542. doi:10.1002/cjce.20056.

[168] S.M. Son, U.Y. Kim, I.S. Shin, Y. Kang, S.H. Kang, B.T. Yoon, et al., Analysis of gas flow behavior in an annular fluidized-bed reactor for polystyrene waste treatment, Journal of Material Cycles and Waste Management. 11 (2009) 138–143. doi:10.1007/s10163-008-0226-0.

[169] V. (2013) ECI Symposium Series, ed., Experimental investigations of hydrodynamics of a spout fluidized bed with draft plates, in: The 14th International Conference on Fluidization – From Fundamentals to Products, 2013.

[170] M.T. Shah, R.P. Utikar, G.M. Evans, M.O. Tade, V.K. Pareek, Effect of Inlet Boundary Conditions on Computational Fluid Dynamics (CFD) Simulations of Gas–Solid Flows in Risers, Industrial & Engineering Chemistry Research. 51 (2011) 1721–1728. doi:10.1021/ie200940f.

[171] R.K. Sinnott, Chemical Engineering Design: Chemical Engineering, Volume 6, 6 (2005) 1056.

[172] A. kayode, Coker, Ludwig's Applied Process Design for Chemical and Petrochemical Plants, Volume 1, 4th ed., Elsevier Inc., Oxford, 2007.

Appendix A: User Defined Function (UDF) for the DME-SR Process

```
// Steam reforming of DME which includes two steps (1) Hydrolysis of DME and methanol steam reforming, methanol decomposition and water gas shift reaction

/*----------------------------------------------------------------------------*/
#include "udf.h"
#include "mem.h"
#include "math.h"

#define CH 7.6e-07 /*catalyst site concentration (mol/kg)*/
#define cwgs 11.2
#define Rgas 8.314 /*J/mol/K*/
#define tavg 693 /*K*/
#define Af(dme) 1.2343e+10 /*s-1bar-1.(mol/gcat)*/
#define Ef(dme) 6.6520e+03 /*J/mol*/
#define Ac(R)        9.3907e+05 /*s-1bar-1.(mol/gcat)*/
#define Ec(R)  4.9786e+04 /*J/mol*/
#define Sdme -86.317   /*J/mol/K*/
#define Hdme -4.0128e+04 /*J/mol*/
#define Smeoh -1.3391e+02 /*J/mol/K*/
#define Hmeoh -6.9305e+04 /*J/mol*/
#define cns 1.0e+03 /*convert mol to kmol*/
#define A1 1.15e+06 /* m3/s/kg */
#define B1 9.41e+05 /* m3/s/kg*/
#define A2 7.09e+07 /*mol/s/kg*/
#define teta 1.1 /* steam to methanol ratio */
#define CR 5.5 /*reforming constant for MeOH-SR*/
#define CD 5.5 /*reforming constant for decomposition*/
#define c_w 4  /* steam/CO molar ratio*/

/* Search the index for each species */
static const real activation_energy_shift = -35000; /*J/mol */
static const real act_energy_MSR = -84100; /* J/mol*/
static const real act_energy_D = -111200; /*J/mol*/
static cxboolean init_flag = TRUE;

static real mw[MAX_PHASES][MAX_SPE_EQNS];
```

```
static int INDEX_PHASE_CO = 0,INDEX_SPECIES_CO = 0,
           INDEX_PHASE_CH3OCH3 = 0,INDEX_SPECIES_CH3OCH3 = 0,
           INDEX_PHASE_H2 = 0, INDEX_SPECIES_H2 = 0,
           INDEX_PHASE_CO2 = 0, INDEX_SPECIES_CO2 = 0,
           INDEX_PHASE_CH3OH = 0, INDEX_SPECIES_CH3OH = 0,
           INDEX_PHASE_H2O = 0, INDEX_SPECIES_H2O = 0;

DEFINE_ADJUST(DME_reforming,domain)
{

  int n, ns;
  Domain *subdomain;

  /*int n_phases = DOMAIN_N_DOMAINS(domain);*/


  if(init_flag)
   {

#if !RP_HOST
     /* search all the species and saved the Molecular Weight */
     sub_domain_loop(subdomain, domain, n)
       {
         Material *m_mat, *s_mat;
         if (DOMAIN_NSPE(subdomain) > 0)
           {
             m_mat = Pick_Material(DOMAIN_MATERIAL_NAME(subdomain),NULL);
             mixture_species_loop(m_mat,s_mat,ns)
               {
                 if (0 == strcmp(MIXTURE_SPECIE_NAME(m_mat,ns),"co"))
                   {
                     INDEX_PHASE_CO = n;
                     INDEX_SPECIES_CO = ns;
                   }
                 else if (0 == strcmp(MIXTURE_SPECIE_NAME(m_mat,ns),"ch3och3"))
                   {
                     INDEX_PHASE_CH3OCH3 = n;
```

```
                    INDEX_SPECIES_CH3OCH3 = ns;
                                                    }
else if (0 == strcmp(MIXTURE_SPECIE_NAME(m_mat,ns),"h2"))
                    {
                      INDEX_PHASE_H2= n;
                      INDEX_SPECIES_H2 = ns;
                    }
                   else if (0 == strcmp(MIXTURE_SPECIE_NAME(m_mat,ns),"co2"))
                    {
                      INDEX_PHASE_CO2 = n;
                      INDEX_SPECIES_CO2 = ns;
                    }
                   else if (0 == strcmp(MIXTURE_SPECIE_NAME(m_mat,ns),"ch3oh"))
                    {
                      INDEX_PHASE_CH3OH = n;
                      INDEX_SPECIES_CH3OH = ns;
                    }
                   else if (0 == strcmp(MIXTURE_SPECIE_NAME(m_mat,ns),"h2o"))
                    {
                      INDEX_PHASE_H2O = n;
                      INDEX_SPECIES_H2O = ns;
                    }

CX_Message ("\n --- %d %d, %d %d, %d %d, %d %d,%d %d, %d %d, %d %d, %d %d, %d %d, %d
%d,%d %d, %d %d, %d %d, %d %d, %d %d \n");
INDEX_PHASE_CO = 0,INDEX_SPECIES_CO = 0;
INDEX_PHASE_CH3OCH3, INDEX_SPECIES_CH3OCH3,
INDEX_PHASE_H2, INDEX_SPECIES_H2,
INDEX_PHASE_CO2, INDEX_SPECIES_CO2,INDEX_PHASE_CH3OH,
INDEX_SPECIES_CH3OH,
INDEX_PHASE_H2O, INDEX_SPECIES_H2O;
mw[n][ns] = MATERIAL_PROP(s_mat,PROP_mwi);
                  }
              }
            else
              {
                s_mat = Pick_Material(DOMAIN_MATERIAL_NAME(subdomain),NULL);
```

```
            mw[n][0] = MATERIAL_PROP(s_mat,PROP_mwi);
          }
        }

#endif
 init_flag = FALSE;
/* to calculate some commonly used values here in order to save the CPU time */
 enum
{
A,
B,
C,
D,
E,
F,
G,
H_M,
I,
Z,
R,
J,
K,
L,
T,
N_REQUIRED_UDM
};

DEFINE_HET_RXN_RATE(hydrolysis,c,t,hr,mw,yi,rr,rr_t)
{
        Thread **pt = THREAD_SUB_THREADS(t);
        Thread *tp = pt[0]; /* gas phase */
        Thread *ts = pt[1]; /* solid phase */

        real p_DME;/* partial pressure of DME*/
        real p_MeOH; /* partial pressure of MeOH*/
        real p_H2O; /* partial pressure of H2O*/
        real rate_coefficient_kc;
```

```
real rate_coefficient_kf;
real rate_coefficient_kcdme;
real rate_coefficient_kfdme;
real equilibrium_constant_Kpmeoh;
real equilibrium_constant_Kpdme;
real n_conc;
real con_for_dme;
real con_cons_dme;

p_DME =
_R(c,pt[0])*UNIVERSAL_GAS_CONSTANT*C_T(c,tp)*yi[INDEX_PHASE_CH3OCH3][INDEX_
SPECIES_CH3OCH3]/mw[INDEX_PHASE_CH3OCH3][INDEX_SPECIES_CH3OCH3]/(100000);/
*bar*/
p_MeOH =
C_R(c,pt[0])*UNIVERSAL_GAS_CONSTANT*C_T(c,tp)*yi[INDEX_PHASE_CH3OH][INDEX_S
PECIES_CH3OH]/mw[INDEX_PHASE_CH3OH][INDEX_SPECIES_CH3OH]/(100000);/*bar*/
p_H2O =
C_R(c,pt[0])*UNIVERSAL_GAS_CONSTANT*C_T(c,tp)*yi[INDEX_PHASE_H2O][INDEX_SPE
CIES_H2O]/mw[INDEX_PHASE_H2O][INDEX_SPECIES_H2O]/(100000);/*bar*/

/*reparametrization of rate and equilibrium constants*/

rate_coefficient_kc=rate_coefficient_kf = exp((log(Ac(R))-((Ec(R))/(Rgas*tavg)))-
((Ec(R)/Rgas)*((1/C_T(c,tp))-(1/tavg))));

rate_coefficient_kcdme=rate_coefficient_kfdme=exp((log(Af(dme))-((Ef(dme))/(Rgas*tavg)))-
((Ef(dme)/Rgas)*((1/C_T(c,tp))-(1/tavg))));

equilibrium_constant_Kpmeoh = exp(((Smeoh/Rgas)-((Hmeoh)/(Rgas*tavg)))-
((Hmeoh/Rgas)*((1/C_T(c,tp))-(1/tavg))));

equilibrium_constant_Kpdme =1/(exp(((Sdme/Rgas)-((Hdme)/(Rgas*tavg)))-
((Hdme/Rgas)*((1/C_T(c,tp))-(1/tavg)))));

n_conc
=(((rate_coefficient_kf*equilibrium_constant_Kpmeoh*p_MeOH)+(rate_coefficient_kcdme*equilibri
um_constant_Kpdme*p_DME))/((rate_coefficient_kc*p_H2O)+(rate_coefficient_kfdme*p_DME)));
```

```
con_for_dme = n_conc*rate_coefficient_kfdme*p_MeOH*CH;

        con_cons_dme = rate_coefficient_kcdme*equilibrium_constant_Kpdme*p_DME*CH;

*rr = -((n_conc*rate_coefficient_kfdme*p_MeOH*CH)-
(rate_coefficient_kcdme*equilibrium_constant_Kpdme*p_DME*CH))*C_UDMI(c,t,Z);
/*kmol/m3/s*/


        C_UDMI(c,t,A) = rate_coefficient_kcdme*equilibrium_constant_Kpdme*p_DME;

        C_UDMI(c,t,B) =
rate_coefficient_kfdme*p_MeOH*(((rate_coefficient_kf*equilibrium_constant_Kpmeoh*p_MeOH)+(
rate_coefficient_kcdme*equilibrium_constant_Kpdme*p_DME))/((rate_coefficient_kc*p_H2O)+(rate
_coefficient_kfdme*p_DME)));

C_UDMI(c,t,C)=(1/(exp(((Sdme/Rgas)-((Hdme)/(Rgas*tavg)))-((Hdme/Rgas)*((1/C_T(c,tp))-
(1/tavg))))));//Kpdme

C_UDMI(c,t,D)=exp(((Smeoh/Rgas)-((Hmeoh)/(Rgas*tavg)))-((Hmeoh/Rgas)*((1/C_T(c,tp))-
(1/tavg))));//kpmeoh

C_UDMI(c,t,E)= exp((log(Af(dme))-((Ef(dme))/(Rgas*tavg)))-((Ef(dme)/Rgas)*((1/C_T(c,tp))-
(1/tavg))));//kfdme=kcdme

C_UDMI(c,t,F)=exp((log(Ac(R))-((Ec(R))/(Rgas*tavg)))-((Ec(R)/Rgas)*((1/C_T(c,tp))-
(1/tavg))));//kc=kf

C_UDMI(c,t,G)=C_R(c,pt[0])*UNIVERSAL_GAS_CONSTANT*C_T(c,tp)*yi[INDEX_PHASE_H2
O][INDEX_SPECIES_H2O]/mw[INDEX_PHASE_H2O][INDEX_SPECIES_H2O]/(100000);//ph2o

        C_UDMI(c,t,H_M)=C_R(c,pt[0])*UNIVERSAL_GAS_CONSTANT*C_T(c,tp)*yi[INDEX_P
HASE_CH3OH][INDEX_SPECIES_CH3OH]/mw[INDEX_PHASE_CH3OH][INDEX_SPECIES_C
H3OH]/(100000);//pmeoh
```

```
C_UDMI(c,t,I)=C_R(c,pt[0])*UNIVERSAL_GAS_CONSTANT*C_T(c,tp)*yi[INDEX_PHASE_CH3OCH3][INDEX_SPECIES_CH3OCH3]/mw[INDEX_PHASE_CH3OCH3][INDEX_SPECIES_CH3OCH3]/(100000);//pdme

C_UDMI(c,t,Z)=((C_R(c,pt[2])*C_VOF(c,pt[2])*C_VOLUME(c,pt[2]))/(C_VOLUME(c,pt[0])*cns));/*kg/m3/s*/

C_UDMI(c,t,R)= -(rate_coefficient_kfdme*p_MeOH*(((rate_coefficient_kf*equilibrium_constant_Kpmeoh*p_MeOH)+(rate_coefficient_kcdme*equilibrium_constant_Kpdme*p_DME))/((rate_coefficient_kc*p_H2O)+(rate_coefficient_kfdme*p_DME)))-(rate_coefficient_kcdme*equilibrium_constant_Kpdme*p_DME))*CH*C_UDMI(c,t,Z);
}

/* Water gas shift reaction for DME-SR */

DEFINE_HET_RXN_RATE(water_gas,c,t,hr,mw,yi,rr,rr_t)
{
    Thread **pt = THREAD_SUB_THREADS(t);
    Thread *tp = pt[0]; /* gas phase */
    Thread *ts = pt[1]; /* solid phase */

    real p_CO;   /* partial pressure of CO*/
    real p_H2O; /* partial pressure of H2O*/
    real p_CO2;/* partial pressure of CO2*/
    real p_H2;/* partial pressure of CO2*/
    real Keq;
    real kwgs;/*rate constant of water gas shift*/ /*mol/m_3/s/K/Pa_2*/



    p_CO =
    C_R(c,pt[0])*UNIVERSAL_GAS_CONSTANT*C_T(c,tp)*yi[INDEX_PHASE_CO][INDEX_SPECIES_CO]/mw[INDEX_PHASE_CO][INDEX_SPECIES_CO];/*Pa*/
    p_H2O =
C_R(c,pt[0])*UNIVERSAL_GAS_CONSTANT*C_T(c,tp)*yi[INDEX_PHASE_H2O][INDEX_SPECIES_H2O]/mw[INDEX_PHASE_H2O][INDEX_SPECIES_H2O];/*Pa*/
```

```
        p_CO2 =
C_R(c,pt[0])*UNIVERSAL_GAS_CONSTANT*C_T(c,tp)*yi[INDEX_PHASE_CO2][INDEX_SPE
CIES_CO2]/mw[INDEX_PHASE_CO2][INDEX_SPECIES_CO2];/*Pa*/
        p_H2 =
        C_R(c,pt[0])*UNIVERSAL_GAS_CONSTANT*C_T(c,tp)*yi[INDEX_PHASE_H2][INDEX_
SPECIES_H2]/mw[INDEX_PHASE_H2][INDEX_SPECIES_H2];/*Pa*/

        Keq = exp((4577.8/C_T(c,tp))-4.33);

        kwgs = 1.74e+17*(1-0.1540*c_w+0.008*c_w*c_w)*pow(C_T(c,tp),-
8.5)*exp(activation_energy_shift/(Rgas*C_T(c,tp)));

        //c_w
=(C_R(c,pt[0])*yi[INDEX_PHASE_H2O][INDEX_SPECIES_H2O]/mw[INDEX_PHASE_H2O][IN
DEX_SPECIES_H2O])/(C_R(c,pt[0])*yi[INDEX_PHASE_CO][INDEX_SPECIES_CO]/mw[INDEX
_PHASE_CO][INDEX_SPECIES_CO]);


        *rr = (cwgs*kwgs*((p_CO*p_H2O-p_CO2*p_H2)/Keq))/1000;

}

/* MeOH Steam Reforming */

DEFINE_HET_RXN_RATE(MeOH_SR,c,t,hr,mw,yi,rr,rr_t)
{
        Thread **pt = THREAD_SUB_THREADS(t);
        Thread *tp = pt[0]; /* gas phase */
        Thread *ts = pt[1]; /* solid phase */

        real krs;
        real conc_meoh;

        krs = (CR*((A1)+B1*log(teta))*exp(act_energy_MSR/(Rgas*C_T(c,pt[0])))); /*m_3/kg/s*/
```

```
   conc_meoh=
(yi[INDEX_PHASE_CH3OH][INDEX_SPECIES_CH3OH]*C_R(c,pt[0])/mw[INDEX_PHASE_CH
3OH][INDEX_SPECIES_CH3OH]); /*concentration of meoh (kmol/m3)*/


        *rr = C_VOF(c,pt[1])*C_R(c,pt[1])*krs*conc_meoh; /* kmol/m3*/

        C_UDMI(c,t,J) = (CR*((A1)+B1*log(teta))*exp(act_energy_MSR/(Rgas*C_T(c,pt[0]))));

        C_UDMI(c,t,K) =
C_VOF(c,pt[1])*C_R(c,pt[1])*(CR*((A1)+B1*log(teta))*exp(act_energy_MSR/(UNIVERSAL_GAS
_CONSTANT*C_T(c,pt[0]))))*conc_meoh;

}

/* MeOH Decomposition*/
/* MeOH Decomposition*/
DEFINE_HET_RXN_RATE(Decomposition,c,t,hr,mw,yi,rr,rr_t)
{
        Thread **pt = THREAD_SUB_THREADS(t);
        Thread *tp = pt[0]; /* gas phase */
        Thread *ts = pt[1]; /* solid phase */

        real kd;

        kd = (CD*A2*exp(act_energy_D/(Rgas*C_T(c,pt[0])))); /*mol/kg/s*/

        *rr = (C_VOF(c,pt[1])*C_R(c,pt[1])*kd)/(1000); /* kmol/m3 (1/1000 was to convert to kmol)*/

        C_UDMI(c,t,L) = (CD*A2*exp(act_energy_D/(Rgas*C_T(c,pt[0]))));

        C_UDMI(c,t,T) = exp(act_energy_D/(Rgas*C_T(c,pt[0])));
}
```

Appendix B: User Defined Function (UDF) for the DME Adsorption

```
/*adsorption model for rate kinetics 1 */
/*-------------------------------------------------------------------------------*/
#include "udf.h"
#include "mem.h"
#include "math.h"

real k = 0.003; /* rate constant */

static int INDEX_PHASE_CH3CL=0, INDEX_SPECIES_CH3CL=0,
                INDEX_PHASE_CH3OCH3 = 0, INDEX_SPECIES_CH3OCH3 = 0;

DEFINE_HET_RXN_RATE(sorption_rate,c,t,hr,mw,yi,rr,rr_t)
{
        Thread **pt = THREAD_SUB_THREADS(t);
        Thread *tp = pt[0]; /* gas phase */
        Thread *ts = pt[1]; /* solid phase */

        real CONC_DME_EQUI =
yi[INDEX_PHASE_CH3OCH3][INDEX_SPECIES_CH3OCH3]*C_R(c,pt[0])/mw[INDEX_PHASE
_CH3OCH3][INDEX_SPECIES_CH3OCH3];

        real DME =
yi[INDEX_PHASE_CH3OCH3][INDEX_SPECIES_CH3OCH3]*C_R(c,pt[1])/mw[INDEX_PHASE
_CH3OCH3][INDEX_SPECIES_CH3OCH3];

        *rr = -k*(CONC_DME_EQUI-DME)*C_VOF(c,ts);

}

/*adsorption model for rate kinetics 2 */
/*-------------------------------------------------------------------------------*/
#include "udf.h"
#include "mem.h"
#include "math.h"
```

```
#define MW_DME 0.04607 //kg/mol
#define MW_GASDME 46.07// kg/kmol of DME
#define Rho_DME 2.06
#define CONSTANT_N 2
#define FREUNDCONS 0.46 //mol/kg of solid
#define DMEoneBAR 0.043
real k =0.003; //m-3 kmol-1 s-1


//static cxboolean init_flag = TRUE;
//static real mw[MAX_PHASES][MAX_SPE_EQNS];
static int INDEX_PHASE_CH3CL=0, INDEX_SPECIES_CH3CL=0,
                INDEX_PHASE_CH3OCH3 = 0, INDEX_SPECIES_CH3OCH3 = 0;
//int curr_ts;
//curr_ts = N_TIME;

DEFINE_HET_RXN_RATE(kinetics_adsorption,c,t,hr,mw,yi,rr,rr_t)
{
    Thread **pt = THREAD_SUB_THREADS(t);
    Thread *tp = pt[0]; /* gas phase */
    Thread *ts = pt[1]; /* solid phase */

real CONEQUI;
real conc_ADS;


CONEQUI=
FREUNDCONS*pow((yi[INDEX_PHASE_CH3OCH3][INDEX_SPECIES_CH3OCH3]*C_R(c,pt[0
])/mw[INDEX_PHASE_CH3OCH3][INDEX_SPECIES_CH3OCH3]),CONSTANT_N); //Freundlich
model for gas adsorbed at equilibrum
//concentration adsorbed
conc_ADS =
yi[INDEX_PHASE_CH3OCH3][INDEX_SPECIES_CH3OCH3]*C_R(c,pt[1])/mw[INDEX_PHASE
_CH3OCH3][INDEX_SPECIES_CH3OCH3];

        *rr = -k*(CONEQUI-conc_ADS)*C_VOF(c,pt[1]); //kmol/m3s
 }
```

Appendix C: List of Publications

- Elewuwa, F and Makkawi, Y (2015) Hydrogen Production by Steam Reforming of DME in a Large Scale CFB Reactor. Part I: Computational Model and Predictions. *International Journal of Hydrogen*. 40(46), 15865–15876.

- Elewuwa, F and Makkawi, Y (2016) Hydrogen Production by Steam Reforming of DME in a Large Scale CFB Reactor. Part 2: Parametric analysis. *International Journal of Hydrogen*. (Submitted)

- Elewuwa, F and Makkawi, Y (2016) CFD Modelling of Dimethyl Ether (DME) Adsorption in Large Scale Fluidized Bed System. (Under preparation)